Investigating the roles of cytoskeletal regulators Cylicin 1, Cylicin 2 and actin-related protein M1 in sperm development and function

Dissertation

zur

Erlangung des Doktorgrades (Dr. rer. nat.)

der

Mathematisch-Naturwissenschaftlichen Fakultat

der

Rheinischen Friedrich-Wilhelms-Universitat Bonn

vorgelegt von

Anđela Kovačević

aus

Kotor, Montenegro

Bonn, 2025

Angefertigt mit Genehmigung der Mathematisch-Naturwissenschaftlichen Fakultät der Rheinischen Friedrich-Wilhelms-Universität Bonn

Gutachter/Betreuer: Prof. Dr. Hubert Schorle

Gutachter: Prof. Dr. Oliver Gruß

Tag der Promotion: 10.12.2025

Erscheinungsjahr: 2026

The contents of this thesis have been partially published in:

Schneider S., Kovacevic A., Mayer M., Dicke AK., Arévalo L., Koser SA, Hansen JN, Young S., Brenker C., Kliesch S., Wachten D., Kirfel G., Strünker T., Tüttelmann F., Schorle H. (2023) Cylicins are a structural component of the sperm calyx being indispensable for male fertility in mice and human *eLife* 12:RP86100 DOI: 10.7554/eLife.86100.3

Kovacevic A., Ordziniak E., Umer N., Arevalo L., Hinterlang LD., Ziaeipour S., Suvilla S., Merges GE, Schorle H. (2025) Actin-related protein M1 (ARPM1) required for acrosome biogenesis and sperm function in mice *BioArxiv* DOI: 10.1101/2025.03.27.645694 (currently in review with *Development*).

LIST OF ABBREVIATIONS

Abbreviation	Meaning
ACTL7A	Actin-like protein 7a
ACTL11	Actin-like protein 11
ACTRT1	Actin-related protein 1
ACTRT2	Actin-related protein 2
AOA	Assisted oocyte activation
AR	Acrosomal Reaction
ARPs	Actin related proteins
ART	Assisted reproductive technology
ARPM1 (ACTRT3)	Actin Related Protein M1 (Actin-related protein 3)
BCA	Bicinchoninic acid assay
BSA	Bovine serum albumin
bp	Base pairs
Cas9	CRISPR associated 9
CAPZA3	F-actin-capping Protein subunit Alpha 3
CAPZB	F-actin-capping Protein subunit Beta
CCIN	Calicin
cDNA	Complementary DNA
CEP131	Centrosomal protein 131
CMA3	Chromomycin A3
CRISPR	Clustered regularly interspaced short palindromic repeats
Cylc	Cylicins
CYLC1	Cylicin 1
CYLC2	Cylicin 2
DAPI	4,6-diamidin-2-phenylindol

DEPC	diethyl pyrocarbonat
DNA	deoxyribonucleic acid
DTT	1,4-dithiothreit
e.g.	*exempli gratia*; Latin: for example
EDTA	ethylenediaminetetraacetic acid
EN	eosin-nigrosine
et al.	*et alii, aliae, alia*; latin: and others
EtBr	ethidium bromide
EtOH	ethanol
F-actin	filamentous actin
FA	Formic acid
FDR	False Discovery Rate
fwd	forward
g	gram
G-actin	globular actin
GFP	green fluorescent protein
GM130	Golgi matrix protein 130
GO	gene ontology
HEK cell	human embryonic kidney cell
HEPES	4-(2-hydroxyethyl)-1-piperazineethanesulfonic acid
HOOK1	Hook microtubule tethering protein 1
HPLC	high performance liquid chromatography
HRP	horseradish peroxidase
HTCA	head-tail coupling apparatus
i.u.	international unit
IAM	inner acrosomal membrane
ICSI	intracytoplasmatic sperm injection

IEP	Isoelectric point
IF	immunofluorescence
IFT	intraflagellar transport
IFT88	intraflagellar transport protein 88
IHC	immunohistochemistry
IMT	intramanchette transport
IP	immunoprecipitation
IVF	in vitro fertilization
kb	kilo base pairs
KCl	potassium chloride
kDA	kilo Dalton
KO	knockout
LC-MS/MS	liquid chromatography – tandem mass spectrometry
LRT	Likelihood ratio test
M	molar
MAP	Microtubule associated protein
MBP	Multiple band protein
MeOH	methanol
MERGE	Male Reproductive Genomics study cohort
min	minute
ml	milliliter
mM	millimolar
mRNA	messenger RNA
ms	millisecond
MS	mass spectrometry
MTOC	microtubule organizing center
NaCl	sodium chloride

NE	Nuclear envelope
ng	Nanogram
NHS	Normal Horse Serum
ns	not significant
OAM	outer acrosomal membrane
ODF2	outer dense fiber protein 2
ON	overnight
PAGE	polyacrylamide gel electrophoresis
PAS	periacrosomal sheath
PAS (staining)	periodic acid schiff
PBS	phosphate-buffered saline
PCA	Principal Component Analysis
PCR	polymerase chain reaction
PFN3	Profilin 3
PGCs	primordial germ cells
PNA	Peanut agglutinin
PT	perinuclear theca
qRT-PCR	quantitative real time polymerase chain reaction
rev	reverse
RIPA	radioimmunoprecipitation assay buffer
RNA	ribonucleic acid
rpm	revolutions per minute
RT	Room temperature
SAL	subacrosomal layer
SC	Sertoli cells
s.d.	standard deviation
SDS	sodium dodecyl sulfate

sec	second(s)
SPATA31	Spermatogenesis-associated protein 31
SPEM3	SPEM family member 3
SSCs	spermatogonial stem cells
TBS	Tris-buffered saline
TEM	transmission electron microscopy
TGN46	Trans Golgi network protein 2 (TGOLN 2)
TRIM27	Tripartite Motif Containing 27
ZPBP	Zona pellucida binding protein
UV	ultraviolet
WES	Whole Exome Sequencing
WT	wild type
µg	microgram
µl	microliter
µm	micrometer
µM	micromolar
°C	Grade Celsius

TABLE OF CONTENTS

LIST OF FIGURES

LIST OF TABLES

Summary

Mammalian germ cells express a vast set of genes specific to the testis, required for the development of sperm cells with their unique structure and function. Sperm-specific cytoskeletal regulators play essential roles in male fertility. Although emerging studies have been investigating these genes, the roles of many of them remain to be elucidated.

Cylicins are testis-specific genes, exclusively expressed during spermiogenesis in mammals. Two Cylicins are identified in mouse and human testis: Cylicin 1 (*Cylc1/CYLC1*) and Cylicin 2 (*Cylc2/CYLC2*). Cylicins are cytoskeletal proteins with lysine-rich repeats, and they are localized in the perinuclear theca (PT) of spermatids and mature sperm. To investigate the roles of Cylicins in male fertility, *Cylc1*- and *Cylc2*-deficient mouse lines were established using CRISPR/Cas9 gene editing. *Cylc1*-deficiency caused male subfertility, while *Cylc2*$^{-/-}$, *Cylc1*$^{-/y}$*Cylc2*$^{+/-}$ and *Cylc1*$^{-/y}$ *Cylc2*$^{-/-}$ male mice were infertile. The most prominent phenotypical observation upon loss of Cylicins in the impaired assembly of posterior region of the PT – calyx. Furthermore, reduced counts of epididymal sperm and severe morphological abnormalities of the sperm head and tail resulted in reduced sperm motility. Proteomics analysis revealed that loss of Cylicins leads to drastic changes in abundance of various proteins within the sperm cytoskeletal compartment, suggesting that Cylicins have a role in maintenance of the sperm head structure and protein composition. Of note, an infertile patient carrying with a hemizygous variant in *CYLC1* and a heterozygous variant in *CYLC2*, and with morphological anomalies of the sperm was identified, highlighting the relevance of Cylicins in human sperm.

Next, a mouse model with a null allele for *Arpm1* was analyzed. Actin-related protein M1 (ARPM1) is a testis-specific member of Actin-related protein family which can be found in the PT of round to elongating spermatids in mouse. *Arpm1*-deficient male mice were subfertile, displaying morphological anomalies of the acrosome in roughly 50% of the sperm cells. Loss of ARPM1 leads to deregulation of *cis*- and *trans*-Golgi trafficking which are required for proper acrosome development during spermiogenesis. Co-immunoprecipitation revealed that ARPM1 interacts with other proteins that localize in the PT (ACTRT1, ACTRT2, ACTL7A) and the sperm surface protein ZPBP, additionally to its already known interaction with PFN3. Based on these results, the role of ARPM1 as a structural component of the PT was proposed to contribute to the cytoskeletal scaffold that connects acrosome and sperm nucleus. In addition, ARPM1 stabilizes the localization of ZPBP to facilitate fertilization and it tethers PFN3 which regulates Golgi-trafficking during acrosome biogenesis.

Taken together the results of this research project represent a significant step forward in elucidating the role of PT proteins in sperm function and male fertility.

1. INTRODUCTION

1.1. Male infertility

The term infertility describes the inability to conceive after a period of 12 months of regular, unprotected intercourse in heterosexual couples (*World Health Organization* – WHO). It's estimated that infertility affects 8-12% of couples in the world (Mascarenhas et al., 2012). Infertility can be caused by female-, male-, or couple-related factors. Overall, men contribute to roughly 50% of infertility cases (Vander Borght & Wyns, 2018). Male infertility can be caused by a variety of factors (environmental, genetic, metabolic) but is mostly related to abnormal development and/or function of spermatozoa. Endocrine disorders and disruptors, urogenital tract infections, obstructions of the reproductive tract, medications and environmental toxins are some of the potential causes of male fertility issues. It is estimated that around 15%–30% of male infertility cases are caused by known genetic factors including chromosomal aberrations (aneuploidies or Y chromosome microdeletions) and single-gene mutations (Krausz & Riera-Escamilla, 2018). Male infertility is diagnosed based on the analysis of semen parameters including physical and chemical aspects of the ejaculate (color, viscosity, pH) and parameters regarding sperm cells (cell count, motility, morphology) according to the WHO Gudelines (*WHO Laboratory Manual for the Examination and Processing of Human Semen*, 2021). Most severe form of male infertility is azoospermia – a condition in which no sperm cells can be found in the ejaculate. Asthenozoospermia is characterized by reduced sperm motility while teratozoospermia refers to the reduced percentage of morphologically normal sperm cells found in the ejaculate (Mascarenhas et al., 2012). Idiopathic male infertility, in which a man is infertile despite his normal semen and hormonal parameters, occurs in 10-20% of cases (Winters & Walsh, 2014). Elucidating roles of testis-specific genes which are involved in sperm development and/or function helps with identifying causes of male infertility and choosing the appropriate treatment.

1.2. Mouse and human testes

Testes or testicles are male reproductive organs that have two main functions: production of mature male gametes (gametogenesis) and secretion of androgen hormones (endocrine function) in mammals. Mouse testicles have an ovoid shape and are localized on both sides of the abdomen. Human testicles are oval shaped organs localized in the scrotum. Each testis is covered by a fibrous capsule called the tunica albuginea and is divided into 200 to 400 lobes. Each lobe contains up to 10 coiled tubules, called seminiferous tubules, which represent a functional unit of mammalian testis (**Figure 1**). The seminiferous tubules are highly

organized and composed of seminiferous epithelium (Utiger, 2024). Spermatogenesis – the development of male germ cells - occurs in the seminiferous tubules.

Sertoli cells are testicular somatic cells that extend from the basal membrane to the lumen of seminiferous tubules, providing structural and molecular support for the differentiating germ cells that surround them. Proximally to the basal membrane of the seminiferous tubule, Sertoli cells create tight junctions among each other, establishing a physical barrier between the vascularized basal membrane and haploid germ cells located towards the lumen of the tubules. Since haploid germ cells are genetically different from somatic cells present in the rest of the body, they are susceptible to immune reactions as they could be recognized as ´foreign´. Testis-blood barrier formed by Sertoli cells prevents vascularization and thus immune reactions in the haploid compartment of the seminiferous tubules (Jeffrey B. Kerr & David De Kretser, 2010).

Leydig cells are localized outside of the seminiferous tubules, in the interstitial compartment and are testosterone producing cells that are under hormonal regulation by the hypothalamic-pituitary axis. Testosterone production in Leydig cells plays a crucial role in many physiological processes in males, including spermatogenesis, sexual development, secondary sexual characteristics and behavior (Zhou et al., 2019).

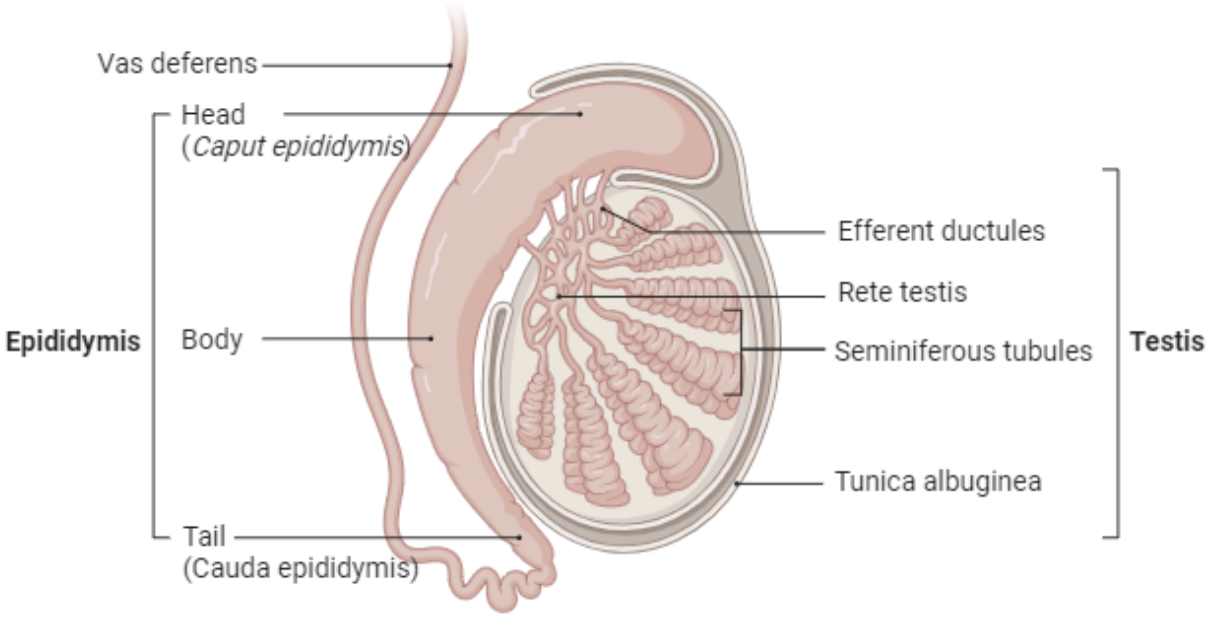

Figure 1: **Graphical representation of mammalian male reproductive organs.** Schematic representation depicts mammalian testis with seminiferous tubules, rete testis and efferent ductules, as well as the epididymis containing tail, body and head. Created with BioRender.com

1.3. Spermatogenesis

Spermatogenesis is the process of differentiation and development of male gametes, which occurs in seminiferous tubules of the testis. Each seminiferous tubulus contains multiple populations of immature germ cells arranged specifically within the epithelium. In mice, one cycle of seminiferous epithelium consists of 12 stages determined by the composition of immature germ cells present and usually noted with roman numbers (**Figure 2**). The entire process of spermatogenesis in mice can be divided into three phases: mitotic phase, meiotic phase and spermiogenesis. In mice, one seminiferous cycle lasts 8.6 days but it must be repeated 4 times for the mature sperm to form, lasting 34.5 days in total (Oakberg, 1956). In humans, one cycle lasts approximately 16 days, while the whole spermatogenesis takes 74 days (Amann, 2008; Heller & Clermont, 1964).

1.3.1. Mitosis

During embryonic development primordial germ cells (PGCs) give rise to gonocytes, which enter spermatogenesis and form the initial pool of spermatogonial stem cells (SSCs) located at the basal membrane of the seminiferous tubule (Phillips et al., 2010). In rodents, undifferentiated type A spermatogonia can be divided into different subtypes based on their localization along the basal membrane. First, single type A spermatogonia (A_s) undergo a mitotic division to produce two paired type A spermatogonia (A_{pr}) (Oakberg, 1956, 1971). After a completed cytokinesis, these cells give rise to new A_s enabling the self-renewal of the pool. A portion of A_{pr} produce a family of aligned type A spermatogonia (A_{al}) which remain connected via cytoplasmatic bridges creating a syncytium and entering the differentiation process simultaneously. Large A_{al} chains differentiate into A1 spermatogonia, which divide and create A2, A3, A4, intermediate and B spermatogonia, depending on the stage of the seminiferous cycle (**Figure 2**). Finally, type B spermatogonia enter another mitotic division giving rise to diploid spermatocytes, which enter meiosis. In human and nonhuman primates, there are only three spermatogonial stem cell types in the testes including A_{dark} and A_{pale} spermatogonia and B spermatogonia (Clermont & Leblond, 1959). A_{dark} spermatogonia are small, round cells with dense chromatin, located on the basal membrane of seminiferous tubules. A_{pale} spermatogonia are larger and have pale, elongated nuclei, containing granulated chromatin. Type B spermatogonia divide by mitosis and enter meiotic divisions.

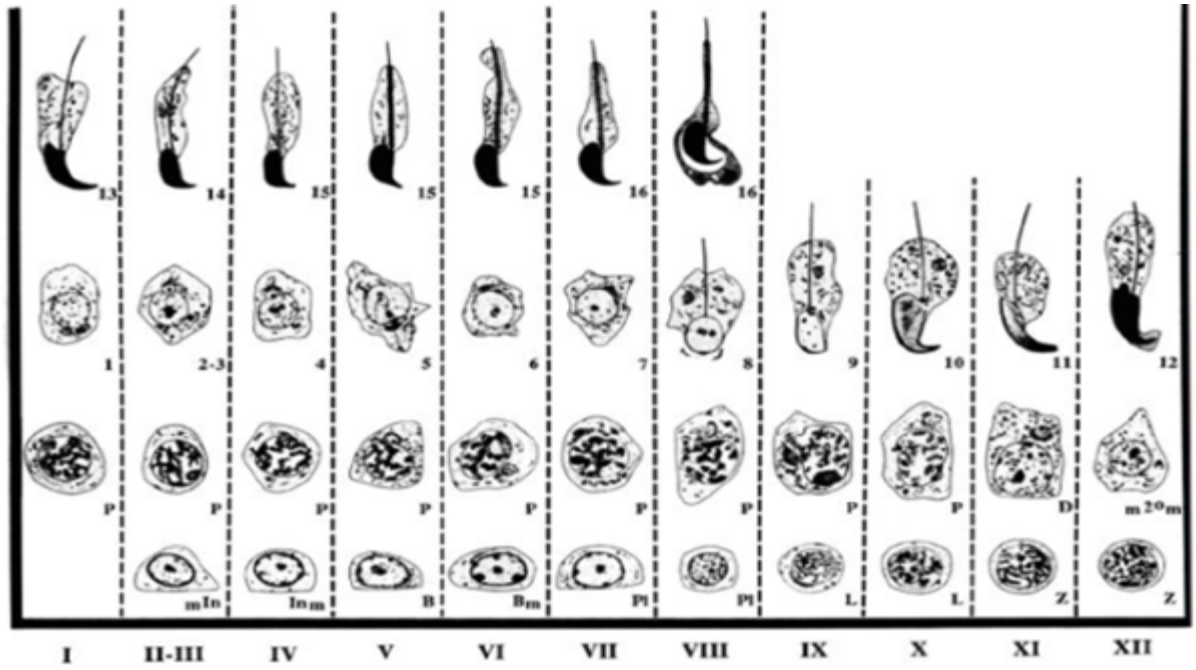

Figure 2: Schematic representation of 16 stages of spermatogenesis in mice. The vertical columns designated by the Roman numerals depict the stages. Arabic numbers depict the steps of spermiogenesis. The specific phases of cell development are type A spermatogonia in mitosis (mIn), intermediate spermatogonia in mitosis (Inm), type B spermatogonia (B), type B spermatogonia in mitosis (Bm), preleptotene spermatocytes (Pl), leptotene spermatocytes (L), zygotene spermatocytes (Z), pachytene spermatocytes (P), diplotene spermatocytes (D) and secondary spermatocytes in meiosis(m2°m). Modified from Russell et al., 1993.

1.3.2. Meiosis

Diploid spermatocytes (2n, 4c) start the meiotic phase of spermatogenesis consisting of two meiotic divisions (**Figure 3**). During meiosis I, double strand DNA breaks form on sister chromatids followed by crossing over and the separation of the homologues chromosomes resulting in haploid secondary spermatocytes (1n, 2c) (Baudat & de Massy, 2007). During meiosis II, the spermatocytes undergo another division to separate sister chromatids resulting in 4 haploid daughter cells (1n, 1c) (de Kretser et al., 1998). These haploid, round spermatids do not divide anymore but enter the spermiogenesis phase in which they undergo a series of morphological changes and differentiate into mature sperm.

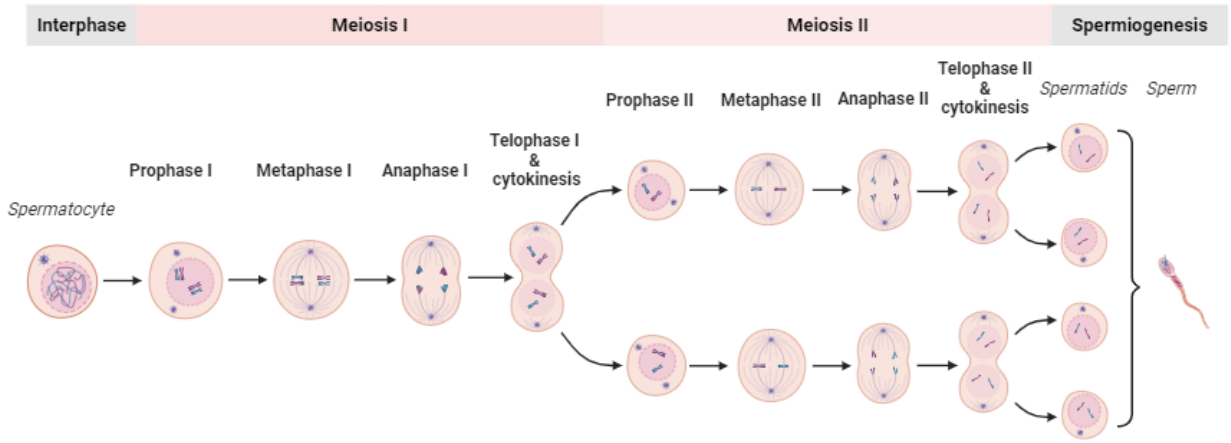

Figure 3: **Schematic representation of meiotic divisions of male germ cells.** During meiosis I diploid spermatocytes divide into secondary haploid spermatocytes. During meiosis II, haploid spermatocytes divide, and sister chromatids separate resulting in four haploid spermatids. Created with BioRended.com

1.3.3. Spermiogenesis

During a process consisting of 16 steps in mice (designated in Arabic numbers), haploid round spermatids undergo drastic morphological changes, gradually elongate and develop sperm-specific accessory structures such as the acrosome and flagellum (Leblond & Clermont, 1952) (**Figure 2**).

A crucial event of spermiogenesis is the acrosome biogenesis, which occurs in four phases described in detail in the next chapter. During the initial phase of the spermiogenesis, centrioles migrate to one pole of the round spermatid, opposite of the growing acrosome, where they attach to the membrane and form a primary cilium, which will further develop into the axoneme, the principal structure of the sperm flagellum (Avidor-Reiss et al., 2020) (**Figure 4**). In the next phase, distal centrioles play a role in flagellum development but later disintegrate in murine sperm. Proximal centrioles remain close to the nucleus and start assembling the head-tail coupling apparatus (HTCA) (Fawcett & Phillips, 1969). As the axoneme grows, accessory structures of the flagellum including mitochondria, outer dense fibers, fibrous sheath and annulus are assembled to build the flagellum. Flagellum development is a continuous process, which takes place throughout entire spermiogenesis (Russell et al., 1993). As the spermatids elongate, a transient microtubular structure called manchette is formed while chromatin undergoes hypercondensation.

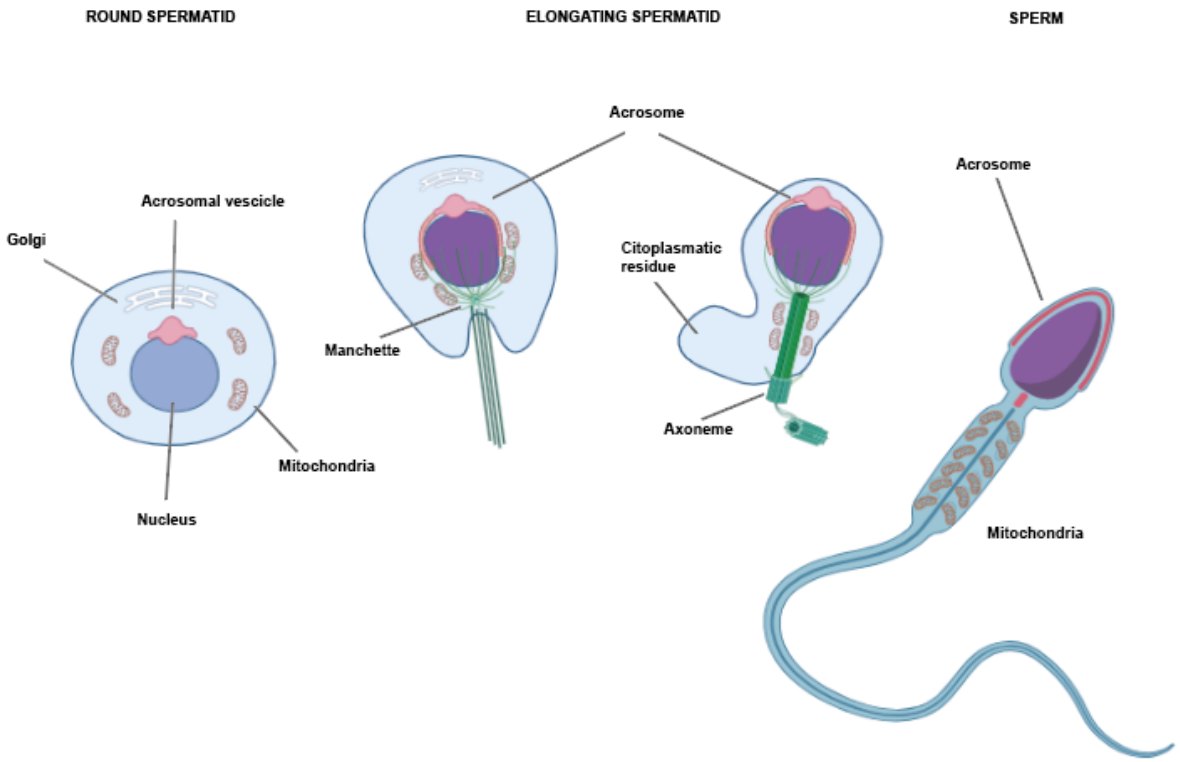

Figure 4: Graphical illustration of spermatid differentiation during spermiogenesis. Round spermatid, elongating spermatids and mature sperm are depicted. Acrosome biogenesis, manchette assembly and flagellum development are illustrated. Different colors of the nucleus represents different stages of chromatin compaction: in round spermatids chromatin is loosely compacted (blue nucleus); in mature sperm chromatin is hypercondensed (dark purple) Created with BioRender.

During spermiogenesis, chromatin remodeling is initiated, and majority of histones are replaced by protamines. In round spermatids, histones are acetylated and replaced by sperm-specific histones such as H2A.L2 (Govin et al., 2007; Luense et al., 2019; Montellier et al., 2013). This allows for transition proteins 1 and 2 (TNP1 and TNP2) binding, which act as intermediators in histone to protamine transition (Goudarzi et al., 2014). In humans and mice, two protamines are required for proper chromatin compaction: protamine 1 (PRM1) and protamine 2 (PRM2) (Chauviere et al., 1992). After protamines are recruited, TNP-histone complexes are removed from DNA, and are evicted from the sperm head with the excess cytoplasm at the end of spermatogenesis. Finally, sperm DNA is condensed, reducing the size of the sperm nucleus 10-fold compared to the nuclei of somatic cells (Pogany et al., 1981; Tres & Kierszenbaum, 1975). The excess of cytoplasm is removed from the sperm cell in the form of residual bodies, which get phagocytosed by surrounding Sertoli cells. Finally, at step 16 of spermiogenesis, sperm cells assume their final morphology and get released into the lumen of seminiferous tubule in a process called spermiation. Of note, sperm shape and length vary among species and while human sperm head is oval, mice have falciform sperm head (Lüpold & Pitnick, 2018).

1.3.4. Sperm maturation

After spermiogenesis, sperm cells are spermiated into the lumen of seminiferous tubule, but even though the morphological differentiation is completed, spermatozoa are not yet mature nor able to fertilize the egg. To gain the fertilization ability, sperm cells go through the post-gonadal differentiation process in the epididymal tract. In the efferent ducts that connect testis to the caput epididymis, the concentration of sperm cells increases while changes in the ionic composition of the luminal fluid occur (Dacheux et al., 2016). Epididymal epithelium secrets specific lysosomes (epididymosomes), which transport proteins important for fertilization ability of the sperm (Gervasi & Visconti, 2017). Following ejaculation, spermatozoa undergo further changes during their transit through female reproductive tract (Austin, 1952; Chang, 1951). This process is called capacitation and consists of a series of biochemical rather than morphological changes that enable the sperm to penetrate and fertilize the egg. During capacitation, chemical changes of the sperm tail allow more efficient motility, while modifications of the sperm head membrane facilitate acrosome reaction and egg penetration. Due to biochemical changes, sperm membrane becomes more penetrable to Ca^{2+} ions causing their influx and promoting the motility (hyperactivation) (Visconti et al., 1998).

1.4. Acrosome and acrosome biogenesis

Acrosome is a lysosome-derived organelle unique to sperm cells of many species and highly conserved through evolution (Berruti & Paiardi, 2011). It is located at the anterior pole of the sperm head and forms a cap-like envelope around the nucleus. Acrosomal membrane can be divided into outer acrosomal membrane (OAM) beneath the plasma membrane at the front of the sperm head, and inner acrosomal membrane (IAM), which is connected to the nuclear membrane. Acrosomes contain hydrolytic and proteolytic enzymes, which are released when OAM fuses to the plasma membrane upon contact with the egg (Topfer-Petersen, 1999; Yanagimachi, 2011). This process called acrosome reaction (AR) is fundamental for the successful fertilization as it enables penetration of the sperm across the protective layers of the female gamete and thus the fusion of the sperm and the egg (Ikawa et al., 2010).

Acrosome biogenesis occurs during spermiogenesis, and it can be subdivided into four phases: *i)* Golgi phase (step 1-3 spermatids), *ii)* Cap phase (step 4-7 spermatids), *iii)* acrosome phase (step 8-12 elongating spermatids) and *iv)* maturation phase (step 13-16) (**Figure 5**) (Clermont & Leblond, 1959). Golgi apparatus is essential during the initial phases of acrosome biogenesis representing the main site for vesicle formation and trafficking. During the first (Golgi) phase of acrosome development, small proacrosomal vesicles deriving from

trans-Golgi network, fuse and form a large acrosomal granule at one pole of the round spermatid. During the Cap phase, the acrosomal granule grows and fills up with glycoproteins originating from the Golgi apparatus, as it flattens over the nucleus forming a cap-like structure. During the acrosome phase as the spermatid elongates, the acrosome condensates and becomes tightly attached to the nuclear envelope (EN). During the final maturation phase the spermatid assumes final shape and the acrosome anchors itself to the anterior part of the sperm head (Khawar et al., 2019).

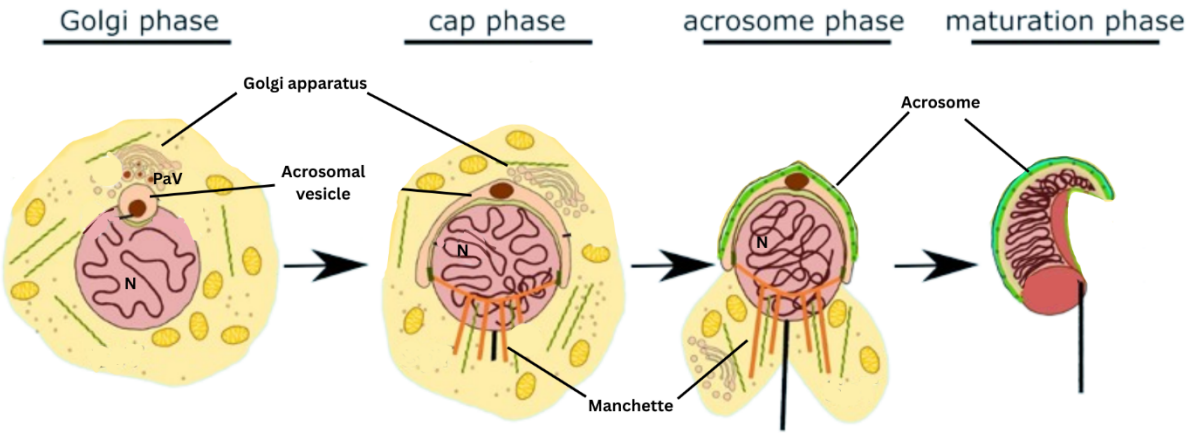

Figure 5: Schematic representation of four phases of acrosome biogenesis in mouse. During Golgi phase, proacrosomal vesicles (PaV) fuse to form one big acrosomal vesicle. During the cap phase, the acrosomal vesicle flattens and spreads over the nucleus forming a cap-like structure. During the acrosome phase, acrosome is tightly attached to the nuclear envelope and it elongates along with the spermatid. Finally, during the maturation phase, the elongation of the spermatid is completed, and the acrosome covers the apical portion of the nucleus. Modified from (Zakrzewski et al., 2021).

1.5. Sperm cytoskeleton

Dynamic changes of spermatid cytoskeleton and testis-specific cytoskeletal regulators are essential for male fertility. Importance lies in microtubule organization and regulation during spermiogenesis. Microtubules are major components of the cytoskeleton of eucaryotic cells and are composed of α- and β-tubulin heterodimers, which polymerase and create linear proto-filaments (Desai & Mitchison, 1997). α- and β-tubulin dimers assemble in a head to tail manner establishing the polarity of microtubules. The end of the microtubules with α-tubulin exposed is defined ‘minus end’ and is usually stable. The minus ends of the microtubules de-polymerize slowly and can be attached to microtubule organizing centers (MTOC). On the contrary, ’plus ends’ with β-tubulin exposed are more dynamic and can rapidly polymerize and de-polymerize (Teixidó-Travesa et al., 2012). Nucleation or development of a microtubule generally happens in MTOCs such as centrosomes (Lüders & Stearns, 2007) while their dynamic is regulated by Microtubule Associated Proteins (MAPs) that can stabilize the

microtubule or cap at their ends to prevent polymerization (O'Donnell & O'Bryan, 2014). Additionally, MAPs can also regulate movement and transport of cargoes along the microtubule. Microtubules often undergo post-translational modifications of their tubulin subunits to modulate their specific function within the cell.

As discussed above, regulation of microtubule dynamics is essential during spermiogenesis because various microtubule-associated platforms are involved in spermatid remodeling. In round spermatids, microtubules appear to be randomly distributed within the cell and not anchored to one specific MTOC. However, as the spermatid elongates, it acquires a distinct polarity with nucleus and acrosome localizing at the anterior pole opposite to HTCA and developing flagellum at the posterior pole of the cell. This polarization of the spermatids involves trafficking of cargo along microtubular platforms: intramanchette transport (IMT) and intraflagellar transport (IFT). Microtubules are also an essential component of mammalian cilia and flagella, including the sperm tail where they form a typical 9+2 axonemal structure. The formation of the sperm tail involves the transport of cargos along microtubular platform of IFT (Kierszenbaum, Rivkin, & Tres, 2011).

1.5.1. Manchette

Manchette is a transient microtubular structure (**Figure 4, Figure 5**), that is crucial for spermatid differentiation as it represents a basis for microtubular trafficking of cargos (IMT). This structure can be first observed in step 8 spermatids as a microtubular platform that spreads between the perinuclear ring and the developing axoneme (O'Donnell & O'Bryan, 2014). The perinuclear ring serves as a nucleation site for the development of manchette microtubules, which are free and more dynamic at the caudal part. As the spermatid elongates, manchette microtubules form a skirt-like structure on the posterior pole of the cell, opposite to the developing acrosome. This zipper-like movement of the manchette contributes to the elongation and flattening of the sperm head (Russell et al., 1991). During spermatid differentiation, motor and non-motor proteins utilize manchette microtubules and F-actin filaments to deliver vesicular or non-vesicular cargos to different regions of the cell. One of the motor proteins responsible for manchette movement is kinesin 2, along with other kinesins and dynein which move cargo along microtubular filaments. Manchette contains F-actin filaments as well, which serve as tracks for myosin-mediated cargo transport. Disruptions of manchette assembly and trafficking pathway lead to abnormal manchette elongation and its delayed removal causing abnormal sperm development, morphological defects of the sperm head and flagellum leading to male infertility (Kierszenbaum, Rivkin, & Tres, 2011).

1.5.2. Acroplaxome

Acroplaxome is a sperm-specific cytoskeletal plate located at the anterior region of the sperm head. This cytoskeletal scaffold consists of the marginal ring mainly formed by F-actin filaments and Keratin 5. The acroplaxome has a principal role in anchoring the inner acrosomal membrane (IAM) to the nuclear envelope (NE) during spermatid elongation. Additionally, during acrosome biogenesis, Golgi-derived proacrosomal vesicles move along the F-actin filaments of the acroplaxome and fuse to form the acrosomal granule (Kierszenbaum et al., 2003).

1.5.3. Perinuclear theca

The Perinuclear theca (PT) is a sperm-specific cytoskeletal structure that surrounds the nucleus of developing spermatids and mature spermatozoa. It's a highly condensed cytosolic layer resistant to non-ionic detergent extraction. Functionally and structurally, PT can be divided into two regions: the subacrosomal layer (SAL) which is located between inner acrosomal membrane and nuclear envelope, while postacrosomal sheath (PAS) is found at the caudal portion of the sperm head, between plasmalemma and nuclear envelope (Oko & Maravei, 1994). A large portion of the PT located in the posterior part of the sperm head is the calyx which contains sperm-specific, very basic cytoskeletal proteins such as Calicin and the Cylicins (Hess et al., 1993) (**Figure 6**). Actin-capping proteins CAPZA3 and CAPZB, which bind to barbed ends of actin filaments and prevent their further polymerization or degradation also localize in the sperm calyx (Bülow et al., 1997).

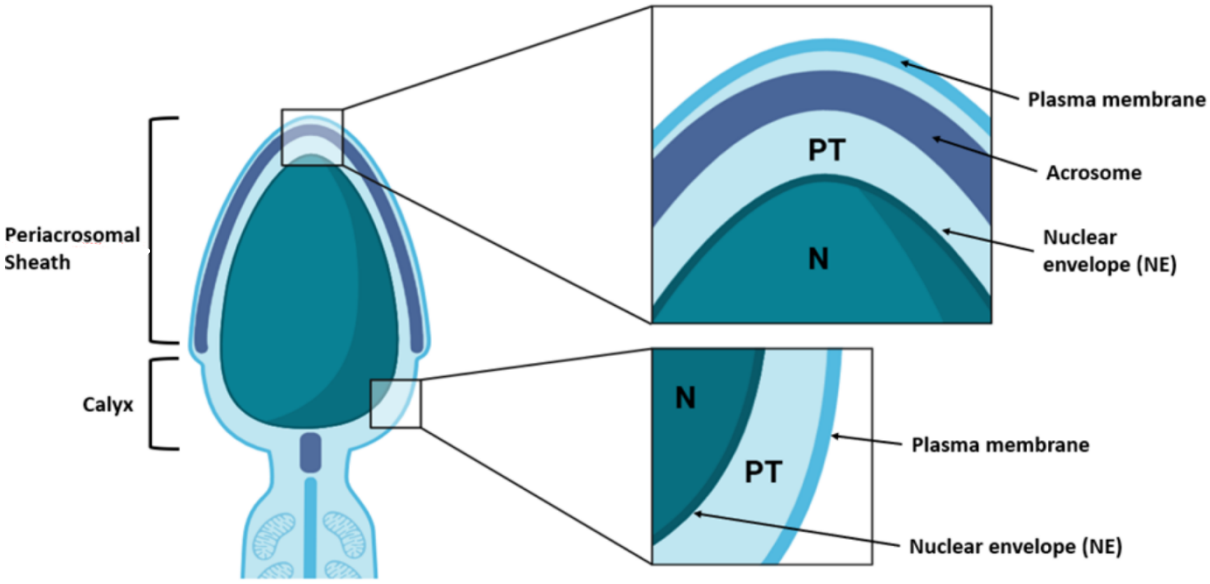

Figure 6: **Graphical representation of human sperm head**. Acrosome (dark blue) and periacrosomal sheath are visible at the anterior part of the sperm head while calyx region of perinuclear theca lies in the posterior part of the sperm head. N = nucleus; PT = perinuclear theca; NE= nuclear envelope. Created with Biorender.

1.6. Perinuclear theca proteins

The PT acts as a main cytoskeletal scaffold of mature sperm and its composition reflects the unique role and morphology of sperm cells. Rather than conventional cytoskeletal proteins, in PT protein lysates many sperm-specific cytoskeletal proteins can be found (Oko & Sutovsky, 2009). Molecular complexity of PT was shown through extensive proteomic analyses of murine and bovine PT lysates that revealed 500–800 different proteins (Zhang et al., 2022a). Emerging studies from recent years have been elucidating the role of different PT-specific proteins in knockout mouse models as well as human patients. For example, the loss of PT-specific protein Calicin (CCIN) causes infertility in male mice. The enlarged space between the IAM and the NE and increased thickness of the acroplaxome are observed in spermatids and mature sperm of *Ccin*-deficient mice. CCIN deficiency leads to sperm nuclear surface subsidence - the invagination of the nuclear surface caused by defective acroplaxome structure (Zhang et al., 2022a). Interactome analysis revealed that CCIN interacts with itself as well as other PT proteins such as SPACA1 and ACTL7A and several NE proteins including lamin B receptor (LBR). According to these results, CCIN has a role in acroplaxome development and anchoring of the acrosome to the nuclear envelope (Zhang et al., 2022a).

In addition to sperm-specific cytoskeletal proteins, PT contains several signaling molecules essential for sperm-egg interaction such as SPACA1, ZPBP and PLCζ1, as well as de novo synthesized core histones involved in chromatin remodeling of the male pronucleus at early post-fertilization stages (Hamilton et al., 2021; Oko & Sutovsky, 2009; Sutovsky et al., 2003).

1.6.1. Cylicins

Cylicins are highly basic, testis-specific proteins found in PT of mammalian sperm (Hess et al., 1993, 1995). They belong to a family of Multiple Band Proteins (MBP) which were characterized for the first time by Longo et al. (1987). Two Cylicin genes were identified in most species: Cylicin1 (*Cylc1*) and Cylicin2 (*Cylc2*). In mice and human, CYLC1/*Cylc1* gene is X-linked. CYLC2 in humans localizes on chromosome 9, while in mice it maps on chromosome 4. Cylicins are characterized by a peculiar sequence rich in repetitive lysine-lysine-aspartic acid (KKD) and lysine-lysine-glutamic acid (KKE) peptide motifs which contribute to an isoelectric point (IEP) >pH 10. The central part of the molecule contains repeating units of up to 41 amino acids which are predicted to form short α-helices (Hess et al., 1993). Both Cylicins have similar molecular and domain characteristics, but CYLC2 has a shorter amino-terminal portion than CYLC1 (**Figure 7**).

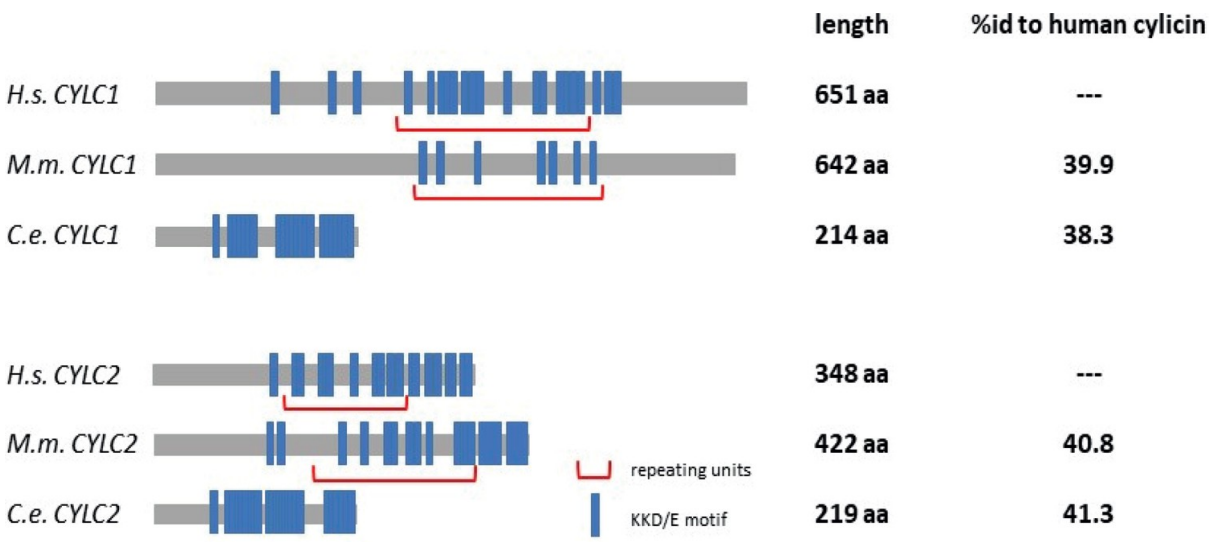

Figure 7: **Comparison of CYLC1 and CYLC2 amino acid sequences in *Caenorhabditis elegans* and *Mus musculus* to *Homo sapiens***. KKD/E motifs are highlighted in blue and repeating units are marked by red brackets. Modified from (Schneider and Kovacevic et al., 2023). Analysis was performed by Dr. Simon Schneider.

Both Cylicins are expressed in round and elongating spermatids and in compacted sperm in mice (**Figure 8**) (Lukassen et al., 2018). Similarly, in human testis, expressions of both Cylicins are limited to haploid cells, mainly spermatids and compacted sperm (**Figure 8 C**) (Guo et al., 2018a). Hess et al. (1993, 1995) demonstrated that CYLC1 and CYLC2 localize in the posterior region of human and bovine sperm head – the calyx region. Actin-binding properties of CYLC2 in boar sperm were analyzed by Rousseaux - Prévost et al. (2003). Although they were predicted to act as cytoskeletal regulators of the sperm in mammals, the exact role of the Cylicins in male fertility remained to be elucidated in this study.

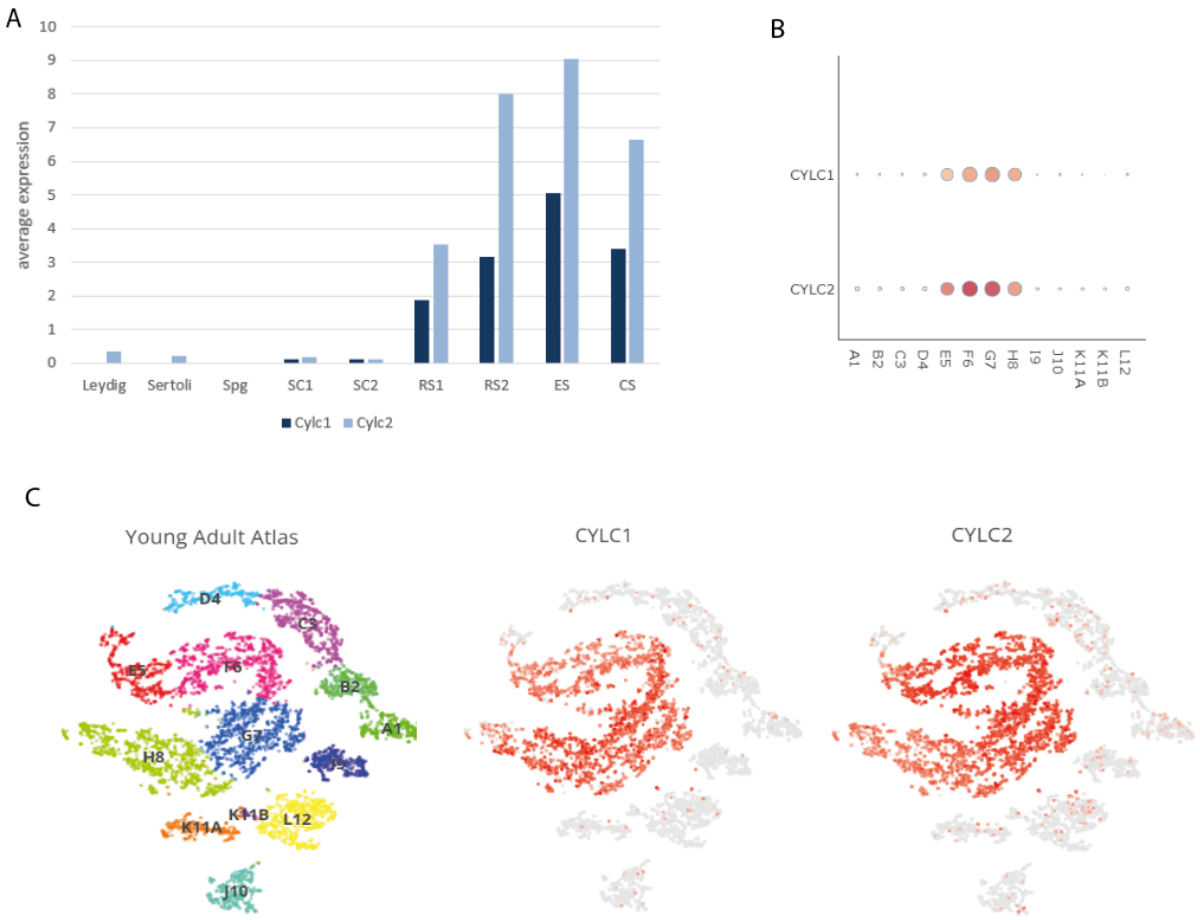

Figure 8: **Expression pattern of Cylicins in mouse and human. A**) Average expression of *Cylc1* and *Cylc2* in different testicular cell populations in mouse: Spg: spermatogonia, SC1: Spermatocyte 1; SC2: Spermatocyte 2, RS1: round spermatid 1; RS2: round spermatid 2; ES: elongating spermatid, CS: compacted sperm. Source: Lukassen et al., 2018 **B-C)** Expression pattern of *CYLC1* and *CYLC2* across different cell populations of human testis. A1: spermatogonial stem cells (SSCs), B2: differentiating spermatogonia, C3: early primary spermatocytes, D4: late primary spermatocytes, E5: round spermatids, F6: elongating spermatids, G7: sperm "1" H8: sperm "2". Red indicates high expression while gray indicates low or no expression. Similarly, dot color and size in the dot plot are related to the average expression. Data extracted from *Human Testis Atlas* database (Guo et al., 2018a).

1.6.2. Actin-related proteins and ARPM1

Actin-related proteins (Arps) are a superfamily of proteins which share sequence similarities with conventional actin and are involved in different cellular processes. Arps are evolutionally conserved from yeast to human (Goodson & Hawse, 2002) and share between 17 and 60% amino acid homology with conventional actins (Schafer & Schroer, 1999). Different Arps have distinct roles in different cellular processes such as actin polymerization, dynein motor function, as well as chromatin remodeling within the nucleus (Blessing et al., 2004). Arps can be found in the cytoplasm where they form complexes with actin-binding proteins and serve as cytoskeletal regulators. Most Arps are ubiquitously expressed; however, some members of the family have testis-specific expression in mice and human (Hara et al., 2008). For example, Actin-like 7a (ACTL7A) is a testis-specific Arp which has a role in acrosome biogenesis as well as formation of subacrosomal F-actin filaments (Ferrer et al., 2023; Y. Zhang et al., 2023). In murine and human sperm, ACTL7A localizes in the periacrosomal region of the PT, however, in mouse sperm it can also be detected in the tail (Fu et al., 2012). *Actl7a*-deficient male mice are infertile, with abnormalities of the sperm head morphology, including defective acrosome and its detachment from the nuclear envelope. Off note, similar phenotype was observed in human infertile patients with variants in *Actl7a* gene (Wang et al., 2021; Xin et al., 2020; X. Zhou et al., 2022). Furthermore, Actin-related proteins ACTRT1 and ACTRT2 are localized in the calyx region of mature sperm (Heid et al., 2002). Male mice deficient for ACTRT1 are subfertile, with mild morphological defects of the sperm head and acrosome detachment from the nucleus (Zhang et al., 2022b). Pathogenic variants in *ACTRT1* gene cause acephalic spermatozoa syndrome and male infertility in human patients (Sha et al., 2021).

Actin-related protein M1 (ARPM1) also known as Actin-related protein T3 (ACTRT3) has been described to localize in both cytoplasmatic and nuclear fraction of testis protein extracts (Hara et al., 2008). Interestingly, in late round spermatids and early elongating spermatids, ARPM1 localizes at the subacrosomal portion of the cell, while in the testicular sperm it's found in the postacrosomal calyx region of PT (Hara et al., 2008). According to single cell RNA-sequencing of adult mouse testis (Lukassen et al., 2018a), *ArpM1* is expressed starting from round spermatids and its mRNA levels peak in elongating spermatids (**Figure 9A**). Human ARPM1 is mainly expressed in round and elongating spermatids of young adult human testicular tissue (**Figure 9 B-C**) (Guo et al., 2018a). Off note, ARPM1 has been identified as a molecular interactor of a small cytoskeletal protein called Profilin 3 (PFN3), found specifically in the testis (Hara et al., 2008; Umer et al., 2021). Male mice deficient for *Pfn3* are subfertile, with acrosome malformations. The molecular role of ARPM1 and the phenotypical analysis of *Arpm1*-deficient mice are reported in this thesis.

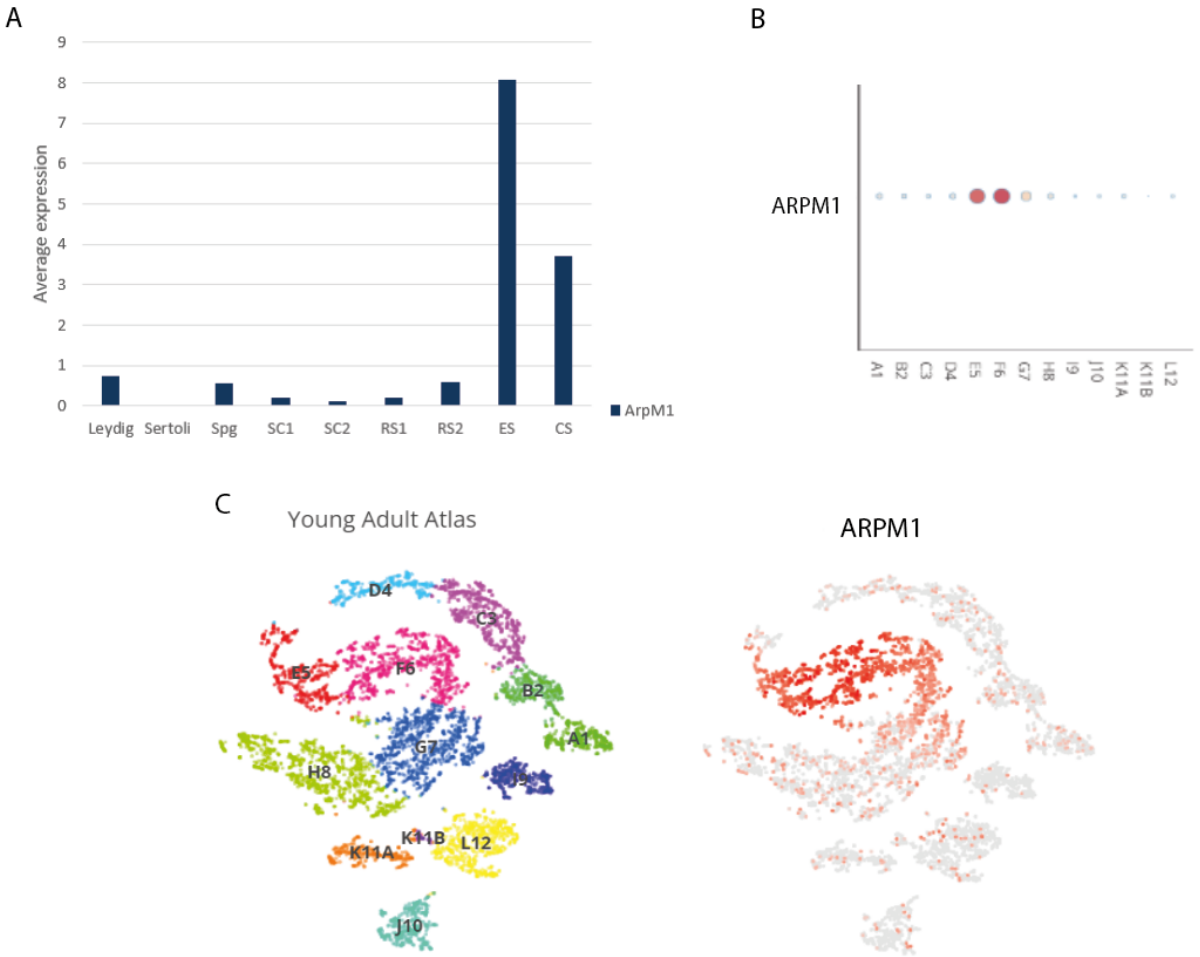

Figure 9: Expression pattern of *Arpm1/ARPM1* in mouse and human. A) Average expression *Arpm1* in different testicular cell populations in mouse: Spg: spermatogonia, SC1: Spermatocyte 1; SC2: Spermatocyte 2, RS1: round spermatid 1; RS2: round spermatid 2; ES: elongating spermatid, CS: compacted sperm. Source: Lukassen et al., 2018. **B-C)** Expression pattern of *ARPM1* (*ACTRT3*) across different cell populations of human testis. A1: spermatogonial stem cells (SSCs), B2: differentiating spermatogonia, C3: early primary spermatocytes, D4: late primary spermatocytes, E5: round spermatids, F6: elongating spermatids, G7: sperm "1" H8: sperm "2". Red indicates high expression while gray indicates low or no expression. Similarly, dot color and size in the dot plot are related to the average expression. Data extracted from *Human Testis Atlas* database (Guo et al., 2018a).

1.7. Aim of the research

For this thesis, two research projects were conducted, using CRISPR/Cas9 gene edited mouse lines deficient for *Cylc1*, *Cylc2* and *Arpm1* to elucidate the function of three genes in male fertility.

First, fertility analysis of *Cylc1*- and *Cylc2*-deficient male mice was performed to investigate the effect of loss of CYLC1 and CYLC2 respectively. Next, two lines were combined to analyze the double *Cylc*-deficiency. Detailed morphological analysis of the epididymal sperm and testicular tissue from all genotypes was performed, with the aim to elucidate the effect of the loss of one, two or three functional *Cylc* alleles on sperm development and function. Semen analysis of a patient carrying variants in both *CYLC1* and *CYLC2* genes was performed, and morphology of his sperm cells was analyzed in detail and compared to sperm from a healthy donor to demonstrate the relevance of Cylicins in human male fertility.

In the second project of this thesis, *Arpm1*-deficient mouse model was established in order to investigate the role of ARPM1. Fertility analysis was performed, elucidating the relevance of ARPM1 in male fertility in mice. Phenotypical analysis of sperm and testis was performed in detail to decipher the cause of male subfertility observed in *Arpm1*-deficient mice. Finally, to understand molecular function and interaction partners of ARPM1, an in-vitro co-immunoprecipitation approach was established, representing a relevant step forward towards unraveling the role of ARPM1 and PT-protein network in general.

2. MATERIALS

2.1. Equipment

Description	Model/Cat.number	Supplier
Adjustable micropipettes	Research	Eppendorf AG, Hamburg, Germany
Bacterial incubator	Innova 4000	New Brunswick Scientific, Edison, USA
Balance	Precision Balance BP211S	Sartorius, Göttingen, Germany
	Balance DA AI 300	
Blot imaging system	ChemiDoc™ MP	Bio-rad, Hercules, USA
Cell culture incubator	Heracell 210i CO_2 incubator	Hera Safe
Centrifuges	Multifuge 3 S-R	Kendro, Hanau, Germany
	5417R	Eppendorf AG, Hamburg, Germany
	5415D	Eppendorf AG, Hamburg, Germany
	FastGene® Mini Centrifuge NG002R	Nippon Genetics Europe GmbH, Düren, Germany
Confocal microscopes	VisiScope	Vistron Systems, Puchheim,Germany
Counting chamber	Neubauer improved	Marienfeld, Lauda-Konigshofen, Germany
DNA SpeedVac	DNA110	Savant, Farmingdale, USA
Electrophoresis power supply	Consort EV243	Peqlab, Erlangen, Germany
Electroporator	Gene Pulser II	Bio-rad, Hercules, USA
Gel electrophoresis	40-1214	Peqlab, Erlangen, Germany

chambers	B1	Peqlab, Erlangen, Germany
Heating plate	OTS 40.2025	Medite, Burgdorf, Germany
High speed cameras	acA1920-155ucMED	Basler AG, Ahrensburg, Germany
	ORCA-Flash4.0 V3, C13220-20 CU	Hamamatsu, Hamamatsu City, Japan
HPLC system	Dionex Ultimate nano	Dionex GmbH, Idstein, Germany
Magnetic separation rack	S1509S	New England Biolabs, Massachusetts, USA
Magnetic stirrer	MR3001	Heidolph, Schwabach, Germany
Mass spectrometer	Orbitrap Fusion Lumos	Thermo Fisher Scientific, Bremen, Germany
Microcentrifuge	VWR MiniStar silverline	VWR, Radnor, USA
Microplate absorbance reader	iMark™	Bio-Rad, Hercules, USA
Microplate shaker	980121EU	VWR, Radnor, USA
Microscopes	DM IRB	Leica, Wetzlar, Germany
	IX71	Olympus, Hamburg, Germany
	DM5500 B	Leica Microsystems, Wetzlar, Germany
Microtome	Microm HM 325	Microm GmbH, Walldorf, Germany
Orbital shaker and incubator	Innova 4000	New Brunswick Scientific, New Jersey, USA
PAGE Handcast system	Mini-PROTEAN® Tetra Handcast Syytem	Bio-rad, Hercules, USA
PCR cycler	2720 Thermal Cycler	Applied Biosystems

pH meter	FiveEasyTMFE20	Mettler Toledo AG, Schwerzenbach, Switzerland
Pipette Controllers	Accu-jet® pro	BRAND, Wertheim, Germany
	IntegraPipetboy 2	INTEGRA Biosciences, Biebertal, Germany
Polyacrylamide gel electrophoresis (PAGE) chamber	Mini-PROTEAN® Tetra Cell	Bio-rad, Hercules, USA
Real-time PCR system	ViiA 7 Real Time PCR System™	Applied Biosystems
Sample Mixer	HulaMixer™	Thermo Fisher, Waltham, USA
Semi-dry transfer system	Trans-Blot® Turbo™ Transfer System	Bio-Rad, Hercules, USA
Sonicator	Bioruptor®	Diagenode SA, Belgium
Spectrophotometers	NanoDrop™ 1000	Peqlab, Erlangen, Germany
	NanoDrop ONE™	Thermo Fisher, Waltham, USA
Sterile hood	BSB 6A	Gelaire® Flow Laboratories, Meckenheim, Germany
Thermomixer	Thermomixer compact	Thermo Fisher, Waltham, USA
Tissue embedding station	Tissue-Tek®	Sakura Finetek, Heppenheim, Germany
Tissue sample processor	Tissue-Tek® VIP	Sakura Finetek, Heppenheim, Germany
Trans-illuminating dissection microscope	SZ61	Olympus Corporation, Tokyo, Japan
	SZX2-ILLTS	Olympus Corporation, Tokyo, Japan

	MS 5	Leica, Microsystems, Wetzlar, Germany
Transmission electron microscope	Verios 460L (FEI) with a STEM III-detector	Thermo Fisher Scientific, Waltham, MA, USA
	Crossbeam 550 with a retractable STEM detector	Zeiss, Oberkochen, Germany
Ultramicrotome	PowerTome	RMC Boeckeler
UV imaging system	GEL iX20	INTAS Science Imaging Instruments GmbH, Gottingen, Germany
Vortexer	Vortex-Genie® 2	Scientific Industries, New York, USA
	Bio-Vortex V1	Peqlab, Erlangen, Germany
Water bath	TW8	Julabo, Seelbach, Germany
Wet blot transfer system	Mini Trans-Blot® Cell	Bio-Rad, Hercules, USA

2.2. Consumables

Description of the product	**Manufacturer**
1.5 ml / 2 ml / 5 ml reaction tubes	Sarstedt, Nümbrecht, Germany
1.5 ml low bindng tubes	Sarstedt, Nümbrecht, Germany
15 ml / 50 ml centrifuge tubes	Corning, Arizona, USA
	Labsolute Th.Geyer GMBH, Renningen, Germany
96-well BCA plate flat bottom	Brand GmbH & Co. KG, Wertheim, Germany
384-well PCR plate	4titude ltd., Ockley, United Kingdom
Amicon® Ultra 50K‐0.5 Centrifugal Filter Device	Merck, Darmstadt, Germany

Axygen® PCR® strip tubes	Corning Inc., New York, USA
Bacteria culture tube 13 ml	Sarstedt, Nümbrecht, Germany
C18 ZipTips	Merck Millipore, Darmstadt, Germany
Carboxylate-coated magnetic beads (Sera-Mag SpeedBeads)	GE Healthcare (cat. no. 45152105050250; 65152105050250)
Cell culture flasks	Sarstedt, Nümbrecht, Germany
Cover slips (18 x18 mm, 24 x 40 mm, 24 x 60 mm)	Medite, Burgdorf, Germany
Cryo tubes	Thermo Fisher Scientific, Waltham, MA, USA
Filter paper (blotting paper)	Bio-rad, Hercules, USA
Filter tips	Nerbe plus GmbH, Winsen, Germany
Microscope slides	Marienfeld GmbH, Lauda-Konigshofen, Germany
Multiwell dishes cell culture grade	TPP, Trasadingen, Switzerland
Paraplast Plus	McCormick Scientific, St. Louis, MO, USA
Petridishes	Sarstedt, Nümbrecht, Germany
Pipette tips	Greiner, Kremsmuenster, Austria
qPCR seal	4titude ltd., Ockley, United Kingdom
Roti® PVDF 0.45 µm pore size	Carl Roth, Karlsruhe, Germany
Serological pipettes	Corning Incorporated, Corning, NY, USA Sarstedt, Nümbrecht, Germany
Sterile filters, 0.45 µm surfactant-free cellulose acetate membrane (SFCA)	Corning Incorporated, Corning, NY, USA
Whatman paper	Macherey-Nagel, Duren, Germany

2.3. Chemicals

Description of the product	Cat.number	Manufacturer
1,4-dithiothreit (DTT)	3483-12-3	Carl Roth, Karlsruhe, Germany
2-Mercaptoethanol	60-24-2	Carl Roth, Karlsruhe, Germany
2-propanol	67-63-0	VWR, Radnor, USA
2,4,6-Tris (dimethylaminomethyl) phenol	90-72-2	Serva, Heidelberg, Germany
Aceton	67-64-1	VWR, Radnor, USA
Agarose	A9539-500G	Sigma-Aldrich, St. Louis, USA
Albumin fraction V (BSA)	9048-46-8	AppliChem, Darmstadt, Germany
Ampicillin (Amp)	69-52-3	AppliChem, Darmstadt, Germany
Ammonium persulfate (APS)	7727-54-0	Carl Roth, Karlsruhe, Germany
Calcium chloride	10043-52-4	Merck, Darmstadt, Germany
Chloroform	67-66-3	Sigma-Aldrich, St. Louis, USA
Chromomycin A3	7059-24-7	Merck, Darmstadt, Germany
cOmplete™ ULTRA Tablets, Mini Protease Inhibitor Cocktail	05 892 970 001	Roche, Basel, Suisse
Coomassie Brillant Blue G250	6104-58-1	Biomol, Hamburg, Germany
Diethyl pyrocarbonate (DEPC)	1609-47-8	Sigma-Aldrich, St. Louis, USA
Entellan®	1079610100	Merck, Darmstadt, Germany

Eosin Y	-	Merck, Darmstadt, Germany
Eosin Y solution 0.5 % in H2O	17372-87-1	Carl Roth, Karlsruhe, Germany
Ethanol (EtOH) absolute	64-17-5	VWR, Radnor, USA
Ethidium bromide (EtBr) solution 1%	1239-45-8	Carl Roth, Karlsruhe, Germany
Ethylenediaminetetraacetic acid (EDTA)	60-00-4	AppliChem, Darmstadt, Germany
Fluoroshield™ with DAPI	F6057	Sigma-Aldrich, St. Louis, USA
GelRed® Prestain Plus 6X DNA Loading Dye	41011	Biotium, Fremont, CA
Glacial acetic acid	64-19-7	AppliChem, Darmstadt, Germany
Glucose	50-99-7	AppliChem, Darmstadt, Germany
Glycine	56-40-6	Carl Roth, Karlsruhe, Germany
HEPES	7365-45-9	Sigma-Aldrich, St. Louis, USA
Hoechst (bisbenzimide)	H 33342	Sigma-Aldrich
Hydrochloric acid	7647-01-0	VWR, Radnor, USA
Isofluran-Piramal	-	Piramal healthcare, Northumberland, UK
Lipofectamine™ 3000	L30000015	Thermo Fisher, Waltham, USA
Methanol (MeOH)	67-56-1	VWR, Radnor, USA
MitoTracker Red CMXRos	9082	Cell Signaling Technology, Cambridge, UK
Nigrosine	8005-03-6	Carl Roth, Karlsruhe, Germany

Non-fat dried milk powder	2A011831	AppliChem, Darmstadt, Germany
Peanut agglutinin (PNA)-fluorescein isothiocyanate (FITC) Alexa 615 Fluor 488 conjugate	L21409	Thermo Fisher Invitrogen, Waltham, USA
Pierce Protease and Phosphatase inhibitor Mini Tablets, EDTA free	88669	Thermo Fisher Scientific, Rockford, USA
PBS tablets	-	AppliChem, Darmstadt, Germany
Potassium acetate	127-08-2	AppliChem, Darmstadt, Germany
Potassium dihydrogen phosphate (KH2PO4)	7778-77-0	Carl Roth, Karlsruhe, Germany
Rotiphorese	-	Carl Roth, Karlsruhe, Germany
Sodium chloride (NaCl)	7647-14-5	AppliChem, Darmstadt, Germany
Sodium dodecyl sulphate (SDS)	151-21-3	VWR, Radnor, USA
Sodium hydrogen carbonate (NaHCO3)	144-55-8	Carl Roth, Karlsruhe, Germany
Sodium hydroxide	1310-73-2	VWR, Radnor, USA
Tetramethylethylendiamine (TEMED)	110-18-9	Carl Roth, Karlsruhe, Germany
tri-sodium citrate (dihydrate)	6132-04-3	Merck, Darmstadt, Germany
Tris hydrochloride	1185-53-1	Carl Roth, Karlsruhe, Germany
Tris(hydroxymethyl)aminomethane	77-86-1	VWR Radnor (now Avantor), USA
Triton® X-100	9036-19-5	AppliChem, Darmstadt, Germany

TRIzol™	-	Invitrogen™, Thermo Fisher Scientific, Waltham, USA
Tween® 20	9005-64-5	AppliChem, Darmstadt, Germany
Urea	57-13-6	Merck, Darmstadt, Germany
Xylene	1330-20-7	VMP Chemiekontor, Siegburg, Germany
Yeast extract	8013-01-2	Merck, Darmstadt, Germany
β-mercaptoethanol	60-24-2	Carl Roth, Karlsruhe, Germany

2.4. Buffers and Solutions

Buffer or solution	**Recipe/supplier**
Alkaline lysis buffer (HotShot)	25 mM NaOH, 0.2 mM EDTA; pH 12
Bouin fixing solution	Carl Roth, Karlsruhe, Germany
Destaining solution (Coomassie Brilliant Blue)	40% MeOH, 10% acetic acid in ddH2O
DreamTaq Green Buffer	Thermo Fisher, Waltham, USA
DNA Lysis Buffer	2 ml 5 M NaCl, 1 ml 1 M Tris-HCl, pH 8.0, 5 ml 0.5 M EDTA, pH 8.0, 5 ml 10% (m/v) SDS, ddH_2O to 100 ml
Eosin-Nigrosin staining solution	0.67 g eosin Y (color index 45380), 0.9 g sodium chloride, 10 g nigrosin (color index 50420), 100 ml ddH2O
Fixation solution for Coomassie Brilliant Blue	50% MeOH, 10% acetic acid in ddH2O
Fixation solution for sperm cells	MetOH, acetic acid (2:1)
Fixation solution for TEM	3% (v/v) glutaraldehyde in 0.1 M cacodylate buffer, pH 7.4

Heamalum, acidic (Mayer)	Waldeck, Munster, Germany
LB medium 5x	25 g tryptone/pepton, 2.5 g yeast extract, 12.5 g sodium chloride, 500 ml ddH_2O
Lysogeny broth (LB)-agar	25 g tryptone/pepton, 2.5 g yeast extract, 12.5 g sodium chloride, 8 g agar, 500 ml ddH_2O
Mouse anesthesia	8.5 ml 0.9% NaCl, 1 ml 10% Ketamine, 0.5 ml 2% Xylazine
Miniprep Buffer P1	10 ml 1 M Tris HCl pH 8.0, 0.58 g EDTA, 1 µl 100 mg/ml RNase per ml, up to 100 ml with ddH_2O
Miniprep Buffer P2	1.6 g NaOH, 2 g SDS, 200 ml ddH_2O
Miniprep Buffer P3	58.89 g KAc pH 5.5, 200 ml ddH_2O
M-PER™ Mammalian Protein Extraction Reagent	Thermo Fisher, Waltham, USA
Neutralizing buffer (HotShot)	40 mM Tris-HCl; pH 4
PBS x10	10.9 g Na_2HPO_4, 3.2 g NaH_2PO_4, 90 g NaCl, 1 L ddH_2O
PageRuler™ prestained protein ladder	26616, Thermo Fisher, Waltham, USA
PageRuler™Plus prestained protein ladder	Thermo Fisher, Waltham, USA
PHEM bufffer	600 mM PIPES-Na, 250 mM HEPES-Na, 100 mM EGTA, 20 mM $MgCl_2$, pH 6.9
Radioimmunoprecipitation assay (RIPA) buffer (10x)	Cell Signaling Technology, Cambridge, UK
Reaction buffer ($MgCl_2$) for DNAse I	Thermo Fisher, Waltham, USA
Roti®-Load 1, reducing, 4x conc.	Carl Roth, Karlsruhe, Germany
SDS loading buffer 5x	110 mM Tris/HCl pH 6.8, 20% Glycerol, 3.8% SDS, 8% β-mercaptoethanol, 0.05% bromophenol blue
SDS running buffer x10	VWR, Radnor, USA
Transfer buffer (x10)	24.2 g Tris(hydroxymethyl)aminomethane, 144.1 g glycine, 5 ml SDS 20%, ddH_2O ad 1 l

Tris-acetate-EDTA (TAE) buffer (50x)	292 g Tris(hydroxymethyl)aminomethane, 18.6 g EDTA, 57.1 ml glacial acetic acid, ddH_2O ad 1 l
Tris-EDTA buffer pH 9.0	1.21 g TRIS base, 0.37 g EDTA, 1 L ddH_2O, 0.5 ml Tween 20
Tri-Sodium citrate buffer pH 6.0	2.94 g tri-sodium citrate dihydrate, 1 L ddH_2O, HCl (to adjust pH), 0.5 ml Tween 20

2.5. Antibodies

Antibody	**Supplier**	**Cat.number**	**IF dilution**	**IHC dilution**	**WB dilution**
α-tubulin	Abcam	AB7291	-	-	1:5000
α-tubulin	Merck-Millipore	16-232	1:1000	-	-
ACTL7A	Proteintech	17355-I-AP	1:500	-	1:500
ACTRT1	Sigma	HPA003119	1:200	-	1:500
ACTRT2	Proteintech	16992-I-AP	1:500	-	1:1000
ARPM1	Proteintech	27580-1-AP	1:500	1:500	1:500
β-actin	Sigma	219386	-	-	1:500
CAPZA3	Progen	GP-SH4	1:500	-	-
CCIN	Progen	GP-SH3	1:500	-	-
CYLC1 (mouse)	Davids Biotechnology (Regensburg, Germany	Custom made polyclonal antibody	1:1000 (sperm cells) 1:500 (testis)	1:500	1:1000
CYLC1 (human)	Santa-Cruz	sc-166400	1:500		
CYLC2	Davids Biotechnology (Regensburg, Germany	Custom made polyclonal antibody	1:1000 (sperm cells) 1:500 (testis)	1:500	1:1000

GM130	BD Bioscience	610823	1:500	-	-
HA-tag	Proteintech	81290-1-RR	1:500	-	1:5000
HOOK1	Proteintech	10871-1-AP	1:500	-	-
Myc-tag	Proteintech	16286-1-AP	1:500	-	1:1000
PFN3	Provided by Prof. Dr. Walter Witke (University of Bonn)	-	1:250	1:250	1:100
PLCζ	Invitrogen	PA5-50476	1:100	-	-
SP56	Invitrogen	MA1-10866	1:500	-	-
TGN46	Invitrogen	MA5-32532	1:500	-	1:500
ZPBP	Proteintech	15835-1-AP	1:500	-	.

2.6. Media and cell culture reagents

Medium/reagent	**Recipe/supplier**
DMEM	Gibco®/Life Technologies, Carlsbad, USA
DPBS	Gibco®/Life Technologies, Carlsbad, USA
Fetal Bovine Serum (FBS)	Gibco®/Life Technologies, Carlsbad, USA
HEK cell medium	DMEM + GlutaMAX; 10% FBS, 1% penicillin/streptomycin; 1% L-glutamine; 1% Non-Essential Amino Acids; 1% sodium pyruvate
L-Glutamine 200 mM (100x)	Gibco®/Life Technologies, Carlsbad, USA
MEM Non-essential Amino Acids 100x	Gibco®/Life Technologies, Carlsbad, USA
Penicillin/Streptomycin	Gibco®/Life Technologies, Carlsbad, USA
Sodium pyruvate 100 mM	PAN Biotech
Trypsin	Gibco®/Life Technologies, Carlsbad, USA

TYH medium	138 mM NaCl, 4.8 mM KCl, 2 mM CaCl2, 1.2 mM KH2PO4, 5.6 mM glucose, 1 mM MgSO4, 10 mM HEPES, 10 mM Llactate, 0.5 mM sodium pyruvate, pH 7.4

2.7. Kits

Name	**Manufacturer**
DynabeadsTM Antibody Coupling Kit	Thermo Fisher, Waltham, USA
Dynabeads™ Co -Immunoprecipitation Kit	Thermo Fisher, Waltham, USA
GeneRuler™ 1 kb DNA ladder	Thermo Fisher, Waltham, USA
GeneRuler™ 100 bp plus DNA ladder	Thermo Fisher, Waltham, USA
ImmPACT® Vector® Red alkaline phosphatase substrate- (SK-5105)	Vector Laboratories, Newark, CA, USA
Maxima H Minus Reverse Transcriptase	Thermo Fisher, Waltham, USA
Maxima SYBR Green qPCR Mater Mix	Thermo Fisher, Waltham, USA
NucleoBond® Xtra Maxi Kit	Thermo Fisher, Waltham, USA
NucleoSpin® Gel and PCR Clean-up	Thermo Fisher, Waltham, USA
Pierce™ BCA protein assay kit	Thermo Fisher, Waltham, USA
Pierce™ HA Tag IP/ Co-IP Kit	Thermo Fisher, Waltham, USA
Pierce™ Myc Tag IP/Co-IP Kit	Thermo Fisher, Waltham, USA
Subcellular Protein Fractionation Kit for Cultured cells #78840	Thermo Fisher, Waltham, USA
SuperSignal™ West Femto Maximum Sensitivity Substrate	Thermo Fisher, Waltham, USA
VectaFluor™ Anti-Mouse IgG, DyLight® 594 Kit, R.T.U- (DI-2794)	Vector Laboratories, Newark, CA, USA
VectaFluor™ Duet Double Labeling Kit, DyLight® 594 Anti-Rabbit IgG, DyLight® 488 Anti-Mouse IgG- (DK8828)	Vector Laboratories, Newark, CA, USA
VectaFluor™ Horse Anti-Rabbit IgG, DyLight® 488 Antibody Kit- (DI-1788)	Vector Laboratories, Newark, CA, USA

VECTASTAIN® ABC-AP Kit, Alkaline Phosphatase (Rabbit IgG)- (AK-5001)	Vector Laboratories, Newark, CA, USA
WESTAR NOVA 2.0 Western Blot Substrate	Cyanagen s.r.l., Bologna, Italy

2.8. Plasmids

Plasmid name	**Source**
pEGFP_N3	Clonetech (6080-1)
pCMV_HA-C	Clonetech (635690)
pCMV_Myc-C	Clonetech (635689)
pCMV_Myc-C_ACTRT1	Constructed by Leo Hinterlang (Bachelor thesis, 2024)
pCMV_Myc-C_ACTRT2	
pCMV_Myc-C_ACTL7A	
pCMV_Myc-C_PFN3	Constructed by Eva Ordziniak (Master thesis, 2024)
pCMV_Myc-C_ZPBP	
pCMV_Myc-C_SPEM2	

2.9. Oligonucleotides

2.9.1. Protospacers and guide RNA sequences

Name	**Sequence (5´-3´)**	**Reference**
Mm.Cas9.CYLC1.sg1	GGTTTATCCATACGTGAGT	(Schneider et al., 2023)
Mm.Cas9.CYLC1.sg2	GGCTTAGGTGATGCTCTAAA	
Mm.Cas9.CYLC2.1.AB	AAGGGAGAGTCGAAAAGCGT	
Mm.Cas9.CYLC2.1.AF	GGATCCAAGGATAAAGTGTC	
Arpm1_Guide2_exon1	CCGGTCCAAGGGCCATACGG	Kovacevic et al. 2025 (Biorxiv)
Arpm1_Guide4_exon2	CGGAAAGGAAAATATCAGTG	

2.9.2. Genotyping primers

Gene	Direction	Sequence (5´-3´)	Mouse line	Reference
Cylc1	fwd	TATACACACAATCCACAATCTTGAAAT	B6-*Cylc1*Δ	(Schneider, Kovacevic et al., 2023)
	rev_1	TCACTTCAAAATCCAACTTGTCCT		
	rev_2	TGCCTAGTATTTCAGGTTCCCC		
Cylc2	fwd	ACCACCATTATGGATGCACCG	B6-*Cylc2*Δ	(Schneider, Kovacevic et al., 2023)
	rev_1	AGTGTTTCTTGTGAGCTCGTTG		
	rev_2	GGCTGAATCTTTACCCTTAGGT		
Arpm1	fwd	GACGCGACATTACCAACACCTGT	B6-*Arpm1*Δ2295 B6-*Arpm1*Δ2299	Kovacevic et al. 2025 (Biarxiv)
	rev_1	TGATGGATAGGAAGCTCCTGCGCTCC		
	rev_2	AAAGCATCTCTGGTGTACAATGTTGGG		

2.9.3. qRT-PCR primers

Name	Sequence (5´-3´)
*Cylc1*_fwd	GGGGAAAAATAAGCTCATGTGTAG
*Cylc1*_rev	TTCAGGTTCCCCATTGGTTA
*Cylc2*_fwd	GCATTTCCCAAACCACCAAGG
*Cylc2*_rev	AACGGATGGTCTCTCGGATATT
*β-actin*_fwd	TGTTACCAACTGGGACGACA
*β-actin*_rev	GGGTGTTGAAGGTCTCAAA

2.9.4. cDNA PCR primers

Name	Sequence (5´-3´)
18F	ACCAGTGGTGATCGACAACG
196R	AATTCTGCAGCCGTGATCCA
161R	TTGATCACCCACACACAGCT
121F	CCTGCCAATACTGCCGTACA
40F	TCGGGAATGATCAAGGCGG
189R	CAGCCGTGATCCACATGTCT

2.9.5. PCR cloning primers

Name	Sequence (5´-3´)
OV fwd_EcoR1_ACTRT1	AAAAGAATTCATGCTTGATCCAGCTAGATTAGAT
OV rev_XhoI_ACTRT1	TTTTCTCGAGAAAAGCATTTTCTTTGAACCACAAATG
OV fwd_EcoR1_ACTRT2	AAAAGAATTCATGTTTAACCCACTGGTACTAGATTC
OV rev_XhoI_ACTRT2	TTTTCTCGAGAGAAGCACCGCCTCTGGAC
OV_fwd_EcoRI_ACTL7A	AAAAGAATTCATGTCTCTGGATGGTGTGTG
OV_rev_KpnI_ACTL7A	TTTTGGTACCGAAGCACCTTCTGTAGAGGA
OV_fwd_ApaI_ARPM1	AAAAGGGCCCATGAGCGGCTACCAGCCAC
OV_rev_KpnI_ARPM1	TTTTGGTACCAAAGCATCTCTGGTGTACAATGTTGG
OV_fwd_EcoRI_PFN3	AAAAGAATTCATGAGTGACTGGAAGGGCTACATCAGTGC
OV_rev_KpnI_PFN3	TTTTGGTACCAGAGCACTGCTCACGCAGCCCACCAA
OV_fwd_EcoRI_ZPBP	AAAAGAATTCATGTGTACCCAAGCTGGGTCCCAA
OV_fwd_EcoRI_SPEM2	AAAAGAATTCATGGAAAACCAGCTGTGGCAGAACA
OV_rev_XhoI_SPEM2	TTTTCTCGAGAGTTAAGTTTCCCTGTCCGGCTTCTA

2.9.6. Plasmid sequencing primers

Name	Sequence (5´-3´)
Rev_M13_seq	CAGGAAACAGCTATGACC
Fwd_783F_seq	TAGAAGACACCGGGACCGAT

2.9.7. Sanger sequencing primers

Name	Sequence (5´-3´)
CYLC1 (NM_021118.3)_fwd	ACTGATGCTGACTCTGAACCG
CYLC1 (NM_021118.3)_rev	CCTTCGAGTCACAAAGTTGTCA
CYLC2 (NM_001340.5)_fwd	CTGTCGAGGTGGATTCTAAAGC
CYLC2 (NM_001340.5)_rev	TGCATCCTTCTTTGCATCCT

2.10. Enzymes

Enzyme	Supplier
DNase I, RNase free	Thermo Fisher, Waltham, USA
DreamTaq DNA Polymerase	Thermo Fisher, Waltham, USA
Restriction enzymes: BglII; ApaI; EcoRI; KpnI; SalI; XhoI; XmiI;	Thermo Fisher, Waltham, USA
RiboLock RNase Inhibitor	Thermo Fisher, Waltham, USA
RNase A, DNase free	AppliChem, Darmstadt, Germany
T4 DNA ligase	Thermo Fisher, Waltham, USA

2.11. Bacteria

Enzyme	Ref. number	Supplier
NEB® Stable Competent *E. coli*	C2987H	New England Biolabs, Ipswich, USA
NEB® 5-alpha Competent *E. coli*	C3040H	New England Biolabs, Ipswich, USA

NEB® Turbo Competent *E. coli*	C2984H	New England Biolabs, Ipswich, USA

2.12. Cell lines

Cell line	**Reference**
HEK-293T	RRID: CVCL_0063

2.13. Software

Software	**Application**	**Source**
Adobe Illustrator	Vector graphic software	www.adobe.com
Biorender	Graphical illustration	www.biorender.com
Endnote	Reference management software	https://www.endnote.com
Ensembl	Genome database	http://www.ensembl.org
Gene ontology	Enrichment analysis on gene/protein sets	www.geneontology.org
Geneious Prime	Sequence analysis software	https://www.geneious.com
gnomAD	Genome Aggregation Database	https://gnomad.broadinstitute.org/sd
GraphPad Prism	Statistical analysis	https://www.graphpad.com/
ImageJ	Image analysis and vector graphics software	http://imagej.nih.gov/ij/
Mascot Server 2.8.3	Peptide identification software	Matrix Science Ltd, London, UK
Mendeley	Reference management software	www.mendeley.com

NCBI	collection of databases; National Center for Biotechnology Information (NCBI)	http://www.ncbi.nlm.nih.gov/
Nuclear_Morphology_Analysis_1.1 8.1_standalone (Plug in for ImageJ)	Nuclear morphology image analysis software	(Skinner et al., 2019)
Proteome Discoverer software 2.5.0.400 and 3.1.0.638	mass spectrometry raw data processing	Thermo Fisher, Waltham, USA
R	Statistical computing software	https://www.r-project.org
SpermQ	Flagellar beat analysis	(Hansen et al., 2018)
STRING	Protein-Protein Interaction Networks search tool	https://string-db.org
SwissProt	Protein sequence database	https://www.sib.swiss/swissprot
UniProt (2023/04)	Mouse reference proteome database	https://www.uniprot.org
Venny 2.1.0	Venn diagram generating page	https://bioinfogp.cnb.csic.es/tools/venny/index.html
VisiView software	imaging software	Vistron Systems GmbH, Puchheim, Germany
Zeiss SmartSEM	Electron microscopy imaging software	https://www.zeiss.com/microscopy/en/products/software/zeiss-smartsem.html

3. METHODS

3.1. Animals

3.1.1. Ethics statement

All animal experiments in this study were performed according to the German law of animal protection and with the approval of the local institutional animal care committees (Landesamt für Natur, Umwelt und Verbraucherschutz, North Rhine-Westphalia; approval IDs: AZ84-02.04.2013.A429, AZ81- 02.04.2018.A369).

3.1.2. Animal keeping

All mice used in this study were housed with 12 hours day/night rhythm and fed *ad libitum*. For organ dissection and further experiments animals were sacrificed by cervical dislocation. Mice aged between 8 and 15 weeks were used for analysis.

3.1.3. Generation of gene-edited mouse lines

Cylc1/Cylc2

CRISPR/Cas9-mediated gene editing in zygotes of the hybrid mouse strain B6D2F1 was used by Dr. Simon Schneider, to generate *Cylc1*- and *Cylc2*-deficient mouse lines (Schneider et al., 2016). Guide sequences are depicted in 9.2.1. *Cylc2*-deficient mice were generated by electroporation of ribonucleoprotein (RNP) complexes into zygotes using a GenePulser II electroporation device (Bio-Rad, Feldkirchen, Germany). Established mouse lines were registered with Mouse Genome Informatics: Cylc1em1Hsc (MGI: 7341368), Cylc2em1Hsc (MGI:6718280). Mouse lines were maintained as congenic strains on C57Bl/6J background.

Arpm1

Two *Arpm1*-deficient mouse lines (Δ2295 and Δ2298) were generated by Dr. Naila Umer using CRISPR/Cas9 mediated gene editing in zygotes of the hybrid strain B6D2F1. Two guide RNAs targeting exon 1 and exon 2 were designed causing a 1.7kb deletion resulting in a frameshift and a nonfunctional, highly truncated protein. Guide sequences are depicted in 9.2.1. Two independent founder animals were generated and mated to C57Bl/6J WT mice to establish the lines. Mouse lines were registered with Mouse Genome Informatics: Actrt3<em1Hsc> MGI:6718284.

3.1.4. Fertility analysis

In order to assess their fertility, male mice aged between 8-12 weeks from all genotypes of all lines analyzed in this study were mated 1:1/1:2 to WT C57BL/6J females of reproductive age. Female mice were checked for copulatory plugs daily. Plug-positive females were separated

from males and monitored for pregnancies and litters. At least five plugs per male were assessed and the percentage of plugs that resulted in live litter was calculated. Pups born in each litter were counted to calculate average litter size per genotype.

3.1.5. Mouse dissection and morphological analysis

Male mice used in this study were sacrificed for organ collection. Animals were weighted and male reproductive organs (testis and epididymis including caput, corpus and cauda) were collected immediately. Both testes were weighted and either fixed in Bouin or 4% PFA or snap frozen and stored at -80°C for further use. Cauda epididymis were collected in PBS and used for epididymal sperm isolation. Tail tips of each animal were collected and stored at -80°C.

3.1.6. *In-vitro* fertilization assay

For *in vitro* fertilization assay, C57Bl/6J WT females were super-ovulated at 12 weeks of age. Sperm extracted from both cauda epididymis of WT and *Arpm1*$^{-/-}$ male mice were incubated in 200 µl of FertiUp and distributed among drops containing oocytes. The number of oocytes and embryos was monitored at 0 h, 24 h, 48 h, 72 h and 96 h after fertilization.

3.2. Nucleic Acid Analysis

3.2.1. Genomic DNA extraction

To determine genotypes of all newborn pups, genomic DNA was extracted from ear punch biopsies using the HotShot method previously described by Truett et al., 2000. Briefly, 75 µl of alkaline lysis buffer was added to a small tail tissue piece while 50 µl of alkaline lysis buffer was used for ear punches. Samples were heated to 95°C for 30-60 mins while shaking at 350-400 rpm. The tissues were then cooled to 4°C and 75 µl or 50 µl of neutralization buffer is added for tail tissues or ear punches respectively. Samples were briefly mixed and DNA extracts were further used in genotyping PCRs.

3.2.2. Mouse genotyping PCR

Genotyping PCRs were performed using 1-2 µl of HotShot lysate mixed with 0.2 µl of DreamTaq Polymerase, 5 µl 10x DreamTaq buffer, 2 µl dNTP mix (10 mM) and 1 µl of each primer (10 mM). The reaction mix was adjusted to a final volume of 50 µl with $_{dd}$H2O. Genotyping primers used in this study are listed in 2.9.2. PCR products were separated on 1% agarose gels using EtBr or GelRed stain.

Cycling conditions:

Arpm1 genotyping: 94°C, 2 min; 35x (94°C, 30 sec; 66°C, 30 sec; 72°C, 45 sec); 5 min 72°C. product sizes: WT: 272 bp, *Arpm1Δ2295:* 315 bp, *Arpm1Δ2298:* 319 bp

Cylc1 genotyping: 95°C, 2 min; 30x (95°C, 30 sec; 60°C, 30 sec; 72°C, 45 sec); 72°, 5 min; expected product sizes: WT: 427 bp, Δ*Cylc1:* 264 bp

Cylc2 genotyping: 95°C, 2 min; 30x (95°C, 30 sec; 60°C, 30 sec; 72°C, 30 sec; 72°, 10 min; expected product size WT: 376 bp, Δ*Cylc2:* 286 bp

3.2.3. RNA isolation from mouse testis

RNA was isolated from one testis from 3 mice of each genotype using TRIzol according to manufactures instructions. Briefly, the testicular tunica was removed, and each testis was homogenized in 1 ml TRIzol using glass homogenizer. After 5 min incubation at RT, 200 µL chloroform was added to each sample and incubated again for 3 min. Samples were centrifuged at 10,600 rpm for 15 min at 4°C and the supernatant was mixed with 500 µL isopropanol, incubated 10 min at RT and again pelleted at 10,600 for 10 min at 4°C. Isolated RNA was washed with 75% EtOH in DEPC H2O twice and air-dried. RNA was dissolved in 100 µL DEPC H2O at 55°C for 15 min and stored at -80°C until use. RNA concentrations were determined using NanoDrop.

3.2.4. Removal of genomic DNA and cDNA synthesis

1 µg RNA per sample was digested using 1 µl DNase I and 1 µl of 10x Reaction Buffer. Mixture was incubated for 30 min at 37°C. After adding 1 µl of EDTA, samples were incubated for 10 min at 65°C. The samples were then further used as a template for Whole cDNA synthesis using Maxima H Minus Reverse Transcriptase Kit according to manufacturer's instructions. For 11 µl of RNA template, 1 µl of primers, 1 µl of dNTP mix (10mM) and 2.5 µl of DEPC H2O was used. The mix was incubated at 65°C for 5 min and centrifuged briefly. Next, 1 µl of Maxima H Minus Reverse Transcriptase with 4 µl of 5x RT buffer was added, as well as 0.5 µl of RiboLock RNase inhibitor. After brief centrifugation, samples were incubated at 25°C for 10 min and at 65°C for 30 min. Reaction was terminated by heating at 85°C for 5 min and samples were stored at -20°C.

3.2.5. Polymerase chain reaction on cDNA

For *Arpm1*-deficient mouse line, PCR was performed on genomic cDNA to demonstrate the presence of truncated transcripts in *Arpm1*$^{-/-}$ mice. Testicular RNA was extracted as described in previous paragraph and cDNA was synthesized. PCR was performed using approximately 100 ng of cDNA from each genotype. PCR mix was composed of: DreamTaq Buffer (5 µl),

dNTPs (1 µl), primer 1 (1 µl), primer 2 (1 µl), Taq polymerase (0.2 µl), 100 ng cDNA (2 µl), ddH2O (to 50 µl). Different primer combinations used to amplify potential transcripts are listed in **Table 1**.

Table 1: PCR Primer combinations and product sizes

Primer combination	**WT product size**	**Δ2295 *Arpm1*$^{-/-}$ product size**	**Δ2298 *Arpm1*$^{-/-}$ product size**
A: 18F + 196R	1,050	179	183
B: 18F + 161R	145	No product	No product
C: 121F + 196R	122	No product	No product
D: 40F + 189R	1021	150	154

Cycling conditions:

A and **D**: 95°C, 60 sec; 30x (95°C, 30 sec; 60°C, 30 sec; 72°C, 45 sec); 5 min 72°C.

B and **C**: 95°C, 60 sec; 30x (95°C, 30 sec; 60°C, 30 sec; 72°C, 30 sec); 5 min 72°C.

3.2.6. Quantitative reverse transcription - polymerase chain reaction (qRT PCR)

Testis tissue RNA extracted with TRIzol was further used for the analysis of relative expression of genes studied. qRT-PCR was performed using Maxima SYBR Green PCR Master Mix on ViiA 7 Real Time PCR System. Each genotype was analyzed in 3 replicates. Normalization was performed using β-actin was used as a housekeeping gene. Primers used for qRT-PCR are shown in 2.9.3.

3.3. Protein biochemistry

3.3.1. Protein isolation from mouse testis

To isolate proteins for western blot analysis, mouse testis were homogenized in 1:10 RIPA buffer (1 ml per 100 mg tissue) supplemented with protease inhibitors and incubated on ice for 15 min. Samples were then sonicated for 5 min and centrifuged for 30 min at 14,000 rpm at 4°C. The supernatant was stored at -20°C and used for downstream applications. Protein concentrations were quantified using NanoDrop or BCA Assay

3.3.2. Isolation of subcellular compartment proteins from sperm cells

For analysis of sperm cell proteins by western blot and mass spectrometry, proteins were isolated from epididymal sperm using the “Subcellular Fractionation Kit” for Cultured cells

according to the manufacturer's instructions, with some modifications. Five subcellular protein fractions were isolated: membrane protein fraction, cytoplasmic protein fraction, soluble nuclear fraction, chromatin bound fraction, and cytoskeletal protein fraction. Briefly, epididymal sperm cells were washed in ice-cold PBS and centrifuged at 500 × *g* for 5 min at 4°C. Supernatant was removed and pellet was resuspended in 400 µl of Cytoplasmatic Extraction Buffer (CEB). After 10 min incubation tubes were centrifuged again at 500 × *g* for 5 min. Supernatant was transferred to a clean, pre-chilled tube on ice (cytoplasmatic fraction). Nextm 400 µl of ice-cold Membrane Extraction Buffer (MEB) was added to the pellet, incubated for 10 min at 4°C with gentle shaking and centrifuged at 3000 × *g* for 5 min. Supernatant was transferred to a clean tube on ice (membrane protein fraction) and 200 µl of ice-cold Nuclear Extraction Buffer (NEB) was added to the pellet. After incubating for 30 min at 4°C with gentle shaking, samples were centrifuged at 5000 × *g* for 5 min. Supernatant was transferred to a clean pre-chilled tube (soluble nuclear extract). Chromatin-bound extraction buffer was prepared adding $CaCl_2$ and MNase to the NEB and 200 µl was added to the pellet. Samples were incubated at RT for 15 min and centrifuged at 16 000 × *g* for 5 min. Supernatant was transferred to a clean tube and 200 µl of Pellet Extraction Buffer (PEB) was added to the pellet. After centrifugation at 16 000 × *g* for 5 minutes, supernatant that contains cytoskeletal proteins was transferred to a clean tube. Protein concentrations of all extracts were quantified using NanoDrop or BCA Assay and samples were stored at -80°C. Cytoskeletal protein fractions were used for western blot and mass spectrometry analysis.

3.3.3. BCA Assay

Protein extracts from testis tissues and mature sperm were quantified using Pierce BCA Protein Assay Kit according to manufacturer´s instructions for the 96-well microplate procedure. Briefly, 25 µl of each sample in duplicate was pipetted into a well and 200 µl of working solution (BCA Reagent A: BCA Reagent B = 50:1) was added. The microplate was placed on a shaker for 1 min and incubated at 37°C for 30 min. Measurements were performed using microplate absorbance reader and the quantification of protein concentrations is based on biuret reaction. Briefly, proteins in alkaline solution cause reduction of Cu^{2+} to Cu^{+} while BCA reagent chelates with generated Cu^{+} ions. This results in the formation of a purple reaction product with an absorption at maximum 562 nm. The absorption increases linearly with protein concentration and can be used to quantify protein concentration.

3.3.4. SDS-PAGE

For protein analysis, 20 µg of protein extracts diluted in 1x Roti load and boiled at 95°C for 5 min. Samples were run on a 12% SDS gel with a 5% stacking gel and separated by electrophoresis using 1 x SDS Running buffer. Proteins were run on the stacking gel at 70 V

while they were separated in resolving gel at 90-110 V. PageRuler Prestained Protein Ladder or PageRuler Prestained Plus Protein Ladder were used as a marker. Proteins were then transferred to methanol-activated PVDF membranes using the Trans-Blot Turbo System (Bio-Rad).

3.3.5. Western Blot

After transferring the proteins, PVDF membranes were blocked using TBST with either 5% milk or 3% BSA in for 1 h at RT. After washing in TBST, the membranes were incubated with primary antibody diluted in blocking buffer at 4°C ON. Antibodies and dilutions used are listed in 2.5. Membranes were then washed again in TBST and incubated with secondary antibodies in blocking buffer for 1 h at RT. Following washing in TBST, the signals were detected with WESTARNOVA2.0 chemiluminescent substrate or SuperSignalTM West Femto Maximum Sensitivity Substrate on the ChemiDoc MP Imaging system.

3.3.6. Proteomics

Peptide preparation

Sperm cytoskeletal protein fractions were extracted as described in 3.3.2 and the protein content was determined by BCA assay. 28 µg protein were reduced, alkylated and digested according to the Preomics iST-NHS kit protocol. Samples were incubated with 0.25 mg of TMTpro isobaric labeling reagent (18plex) at RT for 1 h, followed by quenching with 10 µl 5% hydroxylamine. Pooled peptides were dried in a vacuum concentrator and dissolved in 20 mM ammonium formate. Reversed phase fractionation at elevated pH was achieved on a Reprosil 100 C18 column (3 µm 125 x 4 mm, Dr. Maisch GmbH, Ammerbuch-Entringen, Germany). Fractions were combined into six pools and dried in a vacuum concentrator.

LC/MS measurements

Peptides were dissolved in 0.1% formic acid (FA) and separated on a Dionex Ultimate 3000 RSLC nano HPLC system (Dionex GmbH, Idstein, Germany). 1 µg was injected onto a C18 analytical column (self-packed 400 mm length, 75 µm inner diameter, ReproSil-Pur 120 C18-AQ, 3 µm, Dr. Maisch). Peptides were separated during a 240 min gradient from 5% to 35% solvent B (90% acetonitrile, 0.1% FA) at 300 nl/min. The nanoHPLC was coupled online to an Orbitrap Fusion Lumos mass spectrometer (ThermoFisher Scientific, Bremen, Germany). Peptide ions between 330 and 1600 m/z were scanned in the Orbitrap detector. In a top-speed method, peptides were subjected to collision induced dissociation for identification (CID: 0.7 Da isolation, normalized energy 30%) and fragments analyzed in the linear ion trap with AGC target 50% and maximum fill time 35 ms, rapid mode. Fragmented peptide ions were excluded from repeat analysis for 30 s. Top 10 fragment ions were chosen for synchronous precursor

selection and fragmented with higher energy CID (HCD: 2 Da MS2 isolation, 65% collision energy) for detection of reporter ions in the Orbitrap analyzer (range 100-500 m/z, resolution 50,000, maximum fill time 86 ms, AGC target 200%).

Data analysis

Raw data processing and database search were performed with Proteome Discoverer software 3.1.0.638 (Thermo Fisher Scientific). Peptide identification was done with an in-house Mascot server version 2.8.3 (Matrix Science Ltd, London, UK). MS data were searched against Uniprot mouse reference proteome database (2023/04) and contaminants database (Hao lab[1]). Precursor Ion m/z tolerance was 10 ppm, fragment ion tolerance 0.5 Da (CID). Tryptic peptides with up to two missed cleavages were searched. $C_6H_{11}NO$-modification of cysteines (delta mass of 113.08406) and TMTpro on N-termini and lysines were set as static modifications. Oxidation was allowed as dynamic modification of methionine. Mascot results were evaluated by the Percolator algorithm version 3.05[2] as implemented in Proteome Discoverer. Spectra with identifications above 1% q-value were sent to a second round of database search with semi tryptic enzyme specificity (one missed cleavage allowed). Protein N-terminal acetylation, methionine oxidation, TMTpro, and cysteine alkylation were then set as dynamic modifications. Actual FDR values were 0.7% (peptide spectrum matches) and 1.0% (peptides and proteins). Reporter ion intensities (most confident centroid) were extracted from the MS3 level, with SPS mass match >65%.

3.4. Sperm analysis

3.4.1 Isolation of mouse epididymal sperm

Sperm cells were isolated from the cauda epididymis via the swim-out method (Schneider et al., 2016). Briefly, both caudae were dissected from a mouse and immersed in 1ml PBS at 37°C. Caudae were then cut multiple times and squeezed using forceps and incubated at 37°C for 30 min. The medium was pipetted multiple times and then collected. A small portion of sperm cells was used for sperm count at 1:40 dilution using Thoma counting chamber. After centrifugation at 1200 rpm for 5 min at 4°C, sperm cells were snap frozen and stored at -80°C. Alternatively, the cells were fixed in 4% PFA or in Methanol and acetic acid solution (2:1).

3.4.2. Eosin-Nigrosine (EN) staining

Sperm swim-out solution was mixed with EN stain 1:1 and incubated for 30 sec. 30 µl of the mix was smeared on a microscopic slide, air-dried and mounted with Entellan. For each genotype used in this study, a minimum of 200 sperm per animal from at least 3 animals were

analyzed under a light microscope. Sperm cells were counted and the ratio between pink stained (non-viable) and white unstained (viable) cells was calculated.

3.4.3. Nuclear morphology analysis

Sperm cells fixed in Methanol and acetic acid solution were dropped on microscopic slides and mounted with ROTI Mount FluorCare DAPI. For the nuclear morphology analysis, images were collected at 100x magnification using a fluorescent microscope. A minimum of 100 sperm heads per animal were analyzed. Images were analyzed using the ImageJ plugin ´Nuclear_ Morphology_ Analysis_ 1.18.1_standalone´ (Skinner et al., 2019). The minimum detection area was set to 1.000 pixels, while the maximum detection area was 7.000 pixels.

3.4.4. Sperm motility assessment

For the motility analysis, epididymal sperm was collected in 1 ml sterile filtered THY medium for 15 min at 37°C and diluted 1:20 - 1:50 in 3% BSA. 30 µl of dilution were pipetted onto a microscopic slide and covered with a cover slip. Samples were evaluated using an inverted microscope with a heated slide holder (37°C). A high-speed camera was used to record short videos of swimming sperm at 100 frames/sec for 2 sec. Videos were analyzed using ImageJ by producing a ´z project´ to distinguish motile from immotile sperm. 100 cells per animal were analyzed.

3.4.5. High resolution microscopy of the flagellar beat

Fresh sperm samples collected in THY buffer were diluted 1:100 and inserted into a custom-made observation chamber (Hansen et al., 2018). Briefly, the observation chamber was composed of a custom-made metal mechanical holder, in which a glass cover slip was placed. After placing a drop of sperm suspension in the center of the cover slip, another cover slip was placed on top and on its edges three layers of adhesive tape (Tesafilm®, Tesa, Norderstedt, Germany) were placed. Finally, a chamber with a depth of 150 µm was obtained. This way, swimming was still permitted under the cover glass. Image sequences of live mouse sperm were acquired using dark field at an inverted microscope (IX71; Olympus, Hamburg, Germany), equipped with a dark-field condenser and a high-speed camera. Final magnification ×16 was obtained using a ×10 objective (NA 0.4, UPlanFL; Olympus, Hamburg, Germany) with an additional ×1.6 magnifying lens (Olympus, Hamburg, Germany). Three WT and three *Cylc2*$^{-/-}$ animals were used. Image sequences were analyzed using SpermQ plug-in for Image as described by (Hansen et al., 2018).

3.5. Microscopy

3.5.1. Histology

After dissection, Bouin or 4% PFA fixed mouse testis tissues were washed in 70% ethanol, paraffinized, embedded and sectioned at 3-5 µm using microtome. For histological analysis, the sections were deparaffinized with Xylene 2x10 min and re-hydrated in decreasing ethanol row (100%, 90%, 80%, 70%). For PAS staining, tissue sections were incubated with Periodic acid (0.5%) for 10 min, rinsed with H_20 and for 20 min with Schiff reagent. For H&E staining, tissue sections were treated with Hemalum solution acid (Henricks and Mayer) and Eosin Y solution (Carl Roth). In both procedures, stained sections were dehydrated in increasing ethanol row (70%, 80%, 90%, 100%) and mounted using Entellan (Sigma-Aldrich). Slides were imaged at ×20, ×40 and ×63 magnification using a Leica DM5500 B microscope.

3.5.2. Immunofluorescence/immunohistochemistry

Bouin fixed testis tissue sections were used for IHC staining. After deparaffinizing, heat-activated antigen retrieval was performed using citrate buffer (pH 6.0) or Tris-buffer (pH 9.0) for 15 min at 500 W. For sperm immunofluorescence, mature sperm cells extracted from cauda epididymis were fixed with methanol acetic acid (3:1), dropped on glass slides, and air dried. After washing in PBS twice, all samples were permeabilized using 0.1% Triton X-100 for 10 min at RT. The samples were then blocked with 5% BSA for 30 min, followed by blocking with NHS (Vectorlabs, Burlingame, CA, USA; DI-1788) for 30 min at RT. All primary antibodies were incubated ON at 4°C. Antibodies and dilutions are listed in 2.5. The respective secondary antibodies were incubated for 1 h at RT using VectaFluor Labeling Kit DyLight 488 and DyLight 594. Slides were mounted with DAPI containing mounting medium (ROTImount FluorCare DAPI).

For squash tubule samples used for manchette labelling, fresh testes from three animals of each genotype were transferred to PBS immediately after dissection. Seminiferous tubules were isolated, dissected and placed on a microscope slide. Tubules were then pressed on a slide using a coverslip, quickly frozen in liquid nitrogen, and fixed in 90% ethanol for 5 min. Squash testis samples were stored at -80°C until further use for the staining of α-tubulin and HOOK1.

For the analysis of acrosome morphology, PNA-FITC Alexa Fluor 488 conjugate was used on the Bouin fixed testis tissues and epididymal sperm fixed in 4% PFA, for 20 min at RT. After permeabilization in 0.1% Triton X-100 for 10 min at RT and blocking in 5% BSA for 30 min, the samples were incubated with PNA-FITC 5 µg/ml for 30 min at RT. The slides were mounted using DAPI containing mounting medium. For CMA3 staining 10 µl of epididymal sperm fixed

in methanol and acetic acid (3:1) was dropped on glass slides and air dried. The slides were covered in CMA3 solution and incubated for 20 min in a humid chamber at RT. Slides were washed in PBS twice and mounted with DAPI containing mounting medium. All stainings were performed on a minimum of three animals per genotype.

3.5.3. Immunofluorescence staining on HEK239T cells

For staining experiments, HEK293T cells were grown on glass coverslips in a 24 well plate. 24 h after transfection cells were fixed in 4% PFA for 15 min and washed in PBS. After permeabilization with 0.3% Triton X-100 for 10 minutes, cells were washed in PBS and blocked with NHS for 20 minutes, followed by blocking with 5% BSA for 30 minutes. Primary antibodies were incubated at 4°C ON at dilutions listed in 2.5. After PBS wash, cells were incubated with secondary horse anti-rabbit antibody DyLight™ 594 for 1 h at RT. To counterstain the nuclei, cells were incubated with 0.01 mg/ml Hoechst for 10 minutes and washed in PBS. Coverslips were mounted on glass slides using Fluoroshield™.

3.5.4. Trasmission Electron Microscopy

- **Cylicin project**

For TEM fresh epididymal sperm and testis tissue from *Cylc*-deficient mice were used. The samples were washed in PBS and fixed in 3% glutaraldehyde at 4°C ON. After washing in 0.1 M cacodylate buffer and the samples were fixed again in 2% osmium tetroxide at 4% for 2 h. After dehydration in an ascending ethanol row, the samples were contrasted in 70% ethanol 0.5% uranyl acetate for 1.5 h at 4°C. The samples were then washed in propylenoxide, three times for 10 min at RT and embedded in Epon C at 70°C for 48 hr. Ultra-thin (70 nm) sections were examined using a Verios 460L microscope (FEI) with a STEM III-detector.

- ***Arpm1* project**

Sperm cells and testis samples from *Arpm1*-deficient mice were fixed with 4% PFA and 2.5% glutaraldehyde in PBS ON. After washing in cacodylate buffer, the samples were incubated with 1% osmium tetroxide and 0.8% ferricyanate in cacodylate buffer for 2 h. Samples were washed with cacodylate buffer and pelleted at 600 g before dehydration in ethanol row and propylene oxide. The dehydration step with 70% ethanol was done including 0.5% uranyl acetat for 1 h. The samples were infiltrated with propylene oxide/Epon mixtures (1:1, 1:2) and infiltrated with pure Epon at 60°C for 48 h. Ultra/thin (70 nm) sections were cut using an ultramicrotome (RMC Boeckeler Powertome) and collected on formvar-carbon-coated TEM copper slot girds. TEM grids were counterstained with uranyl acetate and lead citrate before imaging transmitted electrons with a Crossbeam 550 (Zeiss) and a retractable STEM detector.

SmartSEM software (Zeiss) was used to acquire images at 30 kV acceleration voltage with 150 pA current in imaging mode.

3.6. Cloning

3.6.1. PCR amplification

For cloning, initial PCRs were performed on cDNA (or gDNA in case of *Pfn3*) to amplify the gene of interest. PCR mix included: DreamTaq Polymerase (0.2 µl), 10x DreamTaq buffer (5 µl), 10 mM dNTP mix (1 µl), primer each (0.5 µl), cDNA / gDNA (1 µl), ddH_2O (to 50 µl). PCR products were purified using the NucleoSpin Gel and PCR-Clean-up Kit according to the manufacturer´s protocol. Concentrations of the PCR products were measured using a NanoDrop One.

Cycling conditions:

Actl7a, Actrt1, Actrt2: 95°C, 10 sec; 25x (95°C, 45 sec; 60°C, 60 sec; 72°C, 2 min); 5 min 72°C

Arpm1: 95°C, 3 min; 35x (95°C, 45 sec; 60°C, 60 sec; 72°C, 2 min); 10 min 72°C

Pfn3: 95°C, 5 min; 35x (95°C, 30 sec; 63°C, 30 sec; 68°C, 30 sec); 7 min 68°C

Spem2: 95°C, 30 sec; 35x (95°C, 45 sec; 62°C, 30 sec; 68°C, 80 sec); 7 min 68°C

Zpbp: 95°C, 30 sec; 15x (95°C, 45 sec; 60°C, 30 sec; 68°C, 80 sec); 22x (95°C, 45 sec; 60°C, 30 sec; 68°C, 80 sec); 7 min 68°C

3.6.2. Vector Cloning

Vectors and purified PCR products of each gene were digested using Restriciton Enzymes listed in 2.10, according to the manufacturer´s protocol. Vectors and PCR products were then ligated ON at 16°C in a reaction containing: 10x Ligation Buffer (1 µl), plasmid 500 ng/µl Stock (2 µl), T4 Ligase (1 µl), dH_2O (to 10 µl), and the amount of PCR product calculated using formula:

$$X\ ng\ of\ PCR\ product = \frac{(Y\ bp\ PCR\ product) * (50\ ng\ plasmid)}{(size\ in\ bp\ of\ plasmid)}$$

3.6.3. Transformation of competent *E.Coli* bacteria

Chemically competent *E. coli* strain (C2987H, C3040H, C2984H) was incubated with 5 µl of ligation product for 30 min on ice. Bacteria were heat-shocked at 42°C for 1 minute and cooled on ice for 5 min. Next, 950 µl of recovery medium was added and suspension was incubated for 1 h at 37°C, on a shaker. Bacteria were plated onto LB agar plates containing 100 µg/ml ampicillin and incubated ON at 37°C. Finally, colonies were picked and transferred to 3 ml LB medium containing 100 mg/ml ampicillin and incubated ON 37°C, at 220 rpm.

3.6.4. Plasmid isolation

1.5 ml of bacteria culture was used for plasmid isolation. Bacteria culture was centrifuged at 14,000 rpm for 40 s and resuspended in 150 µl P1 buffer (supplemented with RNase A 1:1000). Next, 300 µl of P2 Buffer was added, followed by adding 150 µl P3 buffer. Samples were centrifuged at 14,000 rpm for 5 min and supernatant was transferred to fresh tube containing 1 ml cold EtOH and incubated at -20°C for 10 min. DNA was pelleted at 14,000 rpm for 15 min at 4°C and washed with 80% EtOH. Air-dried pellets were dissolved in 40 µl RNase free H_2O.

3.6.5. Sequencing

For each established plasmid, two samples containing 5 µl of plasmid DNA (50-100 ng/µl) each combined with 5 µl of forward sequencing primer (5 µM) or 5µl of reverse sequencing primer (5 µM) were sent to Eurofins Genomics for “LightRun” Sequencing. Primers used for sequencing are listed in 2.9.6.

3.6.6. Plasmid preparation

For plasmid preparation, bacteria were cultured in 250 ml LB medium containing ampicillin. Plasmids were isolated using Nucleobond Xtra Maxi Plus Kit according to manufacturer’s protocol. Plasmids were further used for transfections and stored at -20°C.

3.7. Cell culture

HEK293TCells were grown at 37°C and 7.5% CO2 in DMEM supplemented with 10% fetal bovine serum, 1% L-Glutamine, 1% Penicillin/Streptomycin, 1% Non-Essential Amino Acids and 1% Sodium Pyruvate. Cell lines were regularly checked for the presence of mycoplasma contamination.

3.7.1. Transfection

HEK293T cells at 60-70% confluency were transfected with 2.5 µg plasmid with Lipofectamin™ 3000 according to manufacturer's instructions. As control for transfection efficiency pEGFP_N3 Plasmid was used. Protein extractions and immunofluorescent staining were performed 24-48h after transfection.

3.8. Co-immunoprecipitation

Co-Immunoprecipitation was performed using Pierce® HA IP Kit or Pierce® c-Myc Tag IP Kit. The provided c-Myc-tagged positive control or HA-tagged positive control were diluted in 150 µl of TBS. Anti-HA agarose or anti-Myc agarose were resuspended and dispensed in corresponding columns. After ON incubation at 4°C in HulaMixer™, spin columns were placed in a collection tube and the flow through was ensured through 10 s pulse centrifugation. Elution was performed by adding 25 µl 2x non-reducing sample buffer, incubation at 95°C for 5 min and followed by pulse centrifugation for 10 s. Input, flow-through and eluate were analysed by Western blotting.

3.9. Human patient analysis

All experiments including human samples were conducted in collaboration with Prof. Dr. Frank Tüttelmann and Prof. Dr. Timo Strünker at the Centre of Reproductive Medicine and Andrology (CeRA), University of Münster, Germany.

3.9.1. Study cohort and ethical approval

In this thesis, the MERGE (Male Reproductive Genomics study) cohort was analysed. At the time of the study the cohort comprised data from of more than 2030 men, from CeRA in Münster, Germany. Most of the cohort participants have severe oligozoospermia (<5 Mill./ml sperm concentration), crypto- or azoospermia or notable sperm morphological defects (≥5 Mill./ml sperm concentration, <4% normal forms). Common causes for infertility such as oncologic diseases, AZF deletions, or chromosomal aberrations were ruled out in advance. Patients with aetiologically still unexplained infertility underwent whole exome sequencing (WES). Cohort analysis was performed by Dr. Sophie Koser, Dr. Ann-Kristin Dicke and Prof. Dr. Frank Tüttelmann. All participants gave written informed consent according to the protocols approved by the Ethics Committee of the Medical Faculty Münster (Ref. No. MERGE: 2010-578-f-S) in accordance with the Declaration of Helsinki in 1975.

3.9.2. Whole exome sequencing and data analysis

DNA extracted from patients' peripheral blood lymphocytes was used for WES as previously described (Wyrwoll et al., 2020). Data obtained from 2066 infertile men was filtered for rare (≤0.01 minor allele frequency, gnomAD) variants located within the coding sequence or the adjacent 15 bp of flanking introns in *CYLC1* and *CYLC2*. For patients with either bi-allelic *CYLC2* variants or a combination of *CYLC1* and *CYLC2* variants, the whole exome dataset was screened to rule out other potential genetic causes. Variants detected were classified according to the guidelines by the American College of Medical Genetics and Genomics-Association for Molecular Pathology (ACMG-AMP) (Richards et al., 2015) adapted to recent recommendations as outlined in (Wyrwoll et al., 2024).

3.9.3. Sanger sequencing

Sanger sequencing with variant-specific primers was performed for validation and segregation purposes. Primers used for Sanger sequencing are listed in 2.9.7.

3.9.4. Analysis of the human semen samples

Ejaculate samples from a healthy donor and patient M2270 were analyzed according to WHO guidelines (*WHO Laboratory Manual for the Examination and Processing of Human Semen*, 2021). Sperm cells were fixed in methanol and acetic acid (3:1) for immunofluorescence staining. Samples were permeabilized with 0.1% Triton X-100. After blocking with 5% BSA for 30 min, slides were incubated with primary antibodies for 3 h at RT. Secondary antibodies were incubated for 1 h, followed by mounting with DAPI containing medium.

3.10. Statistical analysis

For all analyses, mean values ± s.d. were calculated, if not stated otherwise. Statistical significance was determined by one-way ANOVA using Bonferroni correction or a two-tailed, unpaired Student's t-test. The value of $P<0.05$ was considered significant and is indicated in the graphs (*$P<0.05$; **$P<0.005$; ***$P<0.001$; ***$P<0.0001$). All experiments were conducted as biological replicates unless otherwise stated, and N of replicates is provided in Methods section and/or figure legends.

3.11. Data representation

All images shown in this thesis (photomicrographs and transmission electron micrographs) represent raw images, and except for adjustments in size, cropping and white balance were not otherwise manipulated. Graphs were prepared using GraphPad Prism or R. Visualizations of graphs and figures were prepared using Adobe Illustrator.

4. RESULTS I

Parts of the results have been published in:

Schneider S., Kovacevic A., Mayer M., Dicke AK., Arévalo L., Koser SA, Hansen JN, Young S., Brenker C., Kliesch S., Wachten D., Kirfel G., Strünker T., Tüttelmann F., Schorle H. (2023) Cylicins are a structural component of the sperm calyx being indispensable for male fertility in mice and human *eLife* 12:RP86100 DOI: 10.7554/eLife.86100.3

4.1. CRISPR/Cas9 gene editing results in *Cylc1*- and *Cylc2*-deficient mouse lines

Mouse lines deficient for either or both *Cylc1* and *Cylc2* generated by Dr. Simon Schneider (Schneider et al., 2020) were used in this study. For *Cylc1*, two sgRNAs targeting exon 5 were designed and deletion of 1.585 kb comprising 85% of the coding sequence resulting in a frameshift was established (**Figure 10 A**). For *Cylc2*, two guide RNAs targeting exon 4/5 of the gene were designed leading to a deletion of 1.145 kb (**Figure 10 A**). Importantly, in both generated lines, the majority of the functional domains with repetitive, lysine-lysine-aspartic acid (KKD) and lysine-lysine-glutamic acid (KKE) peptide motifs were depleted. Deletions were confirmed by PCR (**Figure 10 B**).

The intercross between *Cylc1*- and *Cylc2*-deficient mouse lines resulted in *Cylc1*$^{-/y}$ *Cylc2*$^{+/-}$ and *Cylc1*$^{-/y}$ *Cylc2*$^{-/-}$ male mice. Quantitative reverse transcription-polymerase chain reaction (qRT-PCR) performed on testicular cDNA confirmed the absence of *Cylc1* and/or *Cylc2* transcripts in *Cylc*-deficient mice (**Figure 11 A**). In *Cylc2*$^{+/-}$ and *Cylc1*$^{-/y}$ *Cylc2*$^{+/-}$ testicular tissue, the amount of *Cylc2* transcripts was reduced to 50%. Of note, neither loss of *Cylc1* nor *Cylc2* resulted in upregulation of *Cylc2* or *Cylc1*, respectively. Additionally, the lack of CYLC1 and CYLC2 in cytoskeletal protein fractions of the mature sperm cells from the respective knockout was confirmed by Western blot analysis (**Figure 11 B**). Mass spectrometry analysis of cytoskeletal fractions of epididymal sperm revealed reduced abundance of CYLC1 in samples from all mice lacking a functional *Cylc1* allele and in sperm from *Cylc2*$^{-/-}$ male mice as well (**Supplementary figure S1**). Similarly, a reduced abundance of CYLC2 peptides was observed in sperm from *Cylc2*$^{-/-}$ and *Cylc1*$^{-/y}$ *Cylc2*$^{-/-}$ male mice, as well as in samples from *Cylc1*$^{-/y}$ and *Cylc1*$^{-/y}$ *Cylc2*$^{+/-}$ mice (**Supplementary figure S2**).

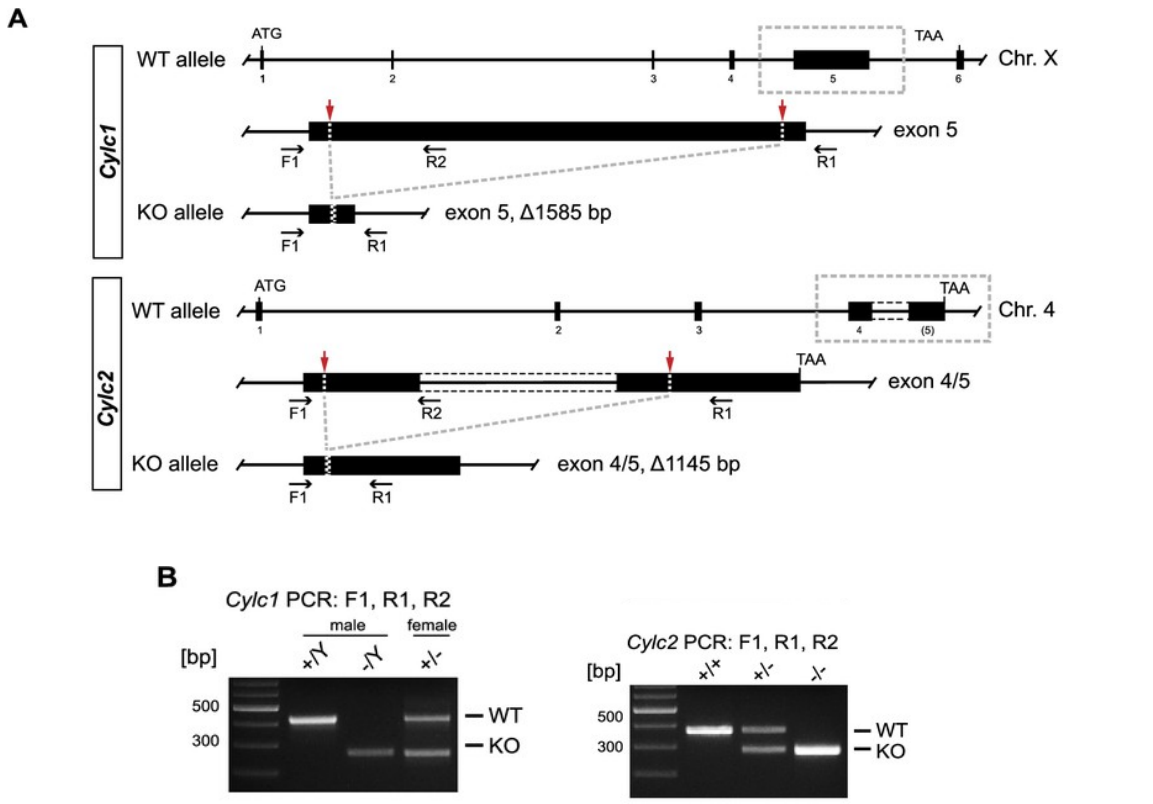

Figure 10: Generation of *Cylc1*- and *Cylc2*- deficient mouse lines. A) Schematic representation of the targeting strategy for CRISPR/Cas9-mediated generation of *Cylc1*- and *Cylc2*-deficient alleles performed by Dr. Simon Schneider. Targeting sites of guide RNAs are depicted by red arrows. Genotyping primer binding sites are depicted by black arrows. **B)** Representative genotyping PCR of *Cylc1*- and *Cylc2*-deficient mice. Modified from Schneider, Kovacevic et al., 2023.

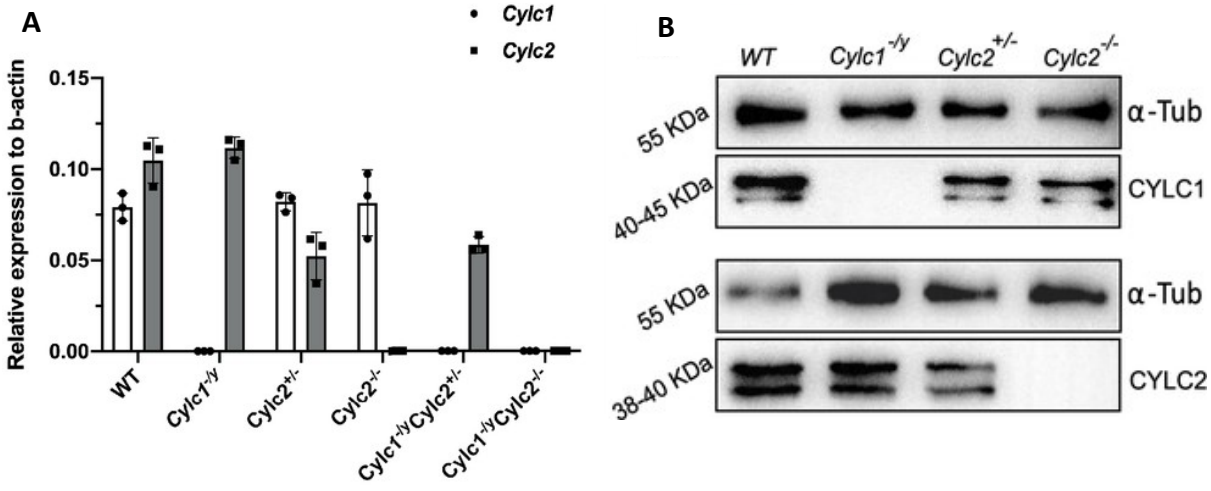

Figure 11: Validation of *Cylc*-deficiency. A) Relative expressions of *Cylc1* and *Cylc2* in testicular tissue of WT, *Cylc1*$^{-/y}$, *Cylc2*$^{+/-}$, *Cylc2*$^{-/-}$, *Cylc1*$^{-/y}$ *Cylc2*$^{+/-}$ and *Cylc1*$^{-/y}$ *Cylc2*$^{-/-}$ mice analyzed by qRT-PCR. n=3 **B**) Immunoblot against CYLC1 and CYLC2 on cytoskeletal protein fractions from WT, *Cylc1*$^{-/y}$, *Cylc2*$^{+/-}$ and *Cylc2*$^{-/-}$ testes. α-Tubulin was used as load control. Modified from Schneider, Kovacevic et al., 2023.

4.2. Cylicins are indispensable for male fertility in mice

Next, fertility analysis of *Cylc*-deficient male mice was performed. Mating *Cylc1*$^{-/y}$ male mice with WT C57Bl/6J females resulted in significantly reduced pregnancy rates (16%) and litter sizes (2.2) when compared to WT males (70% pregnancy rate and mean litter size of 7), indicating that these males are subfertile. Pregnancy rates (75%) and litter sizes (7.5) of *Cylc2*$^{+/-}$ male mice were not altered remaining comparable to the ones obtained in WT male mice. *Cylc2*$^{-/-}$ male mice were infertile, with no pregnancies observed. Interestingly, *Cylc1*$^{-/y}$ *Cylc2*$^{+/-}$ male mice are infertile suggesting that at least two functional *Cylc* alleles are required for male fertility preservation in mice. *Cylc1*$^{-/y}$ *Cylc2*$^{-/-}$ male mice lacking were infertile (**Figure 12 A, B**).

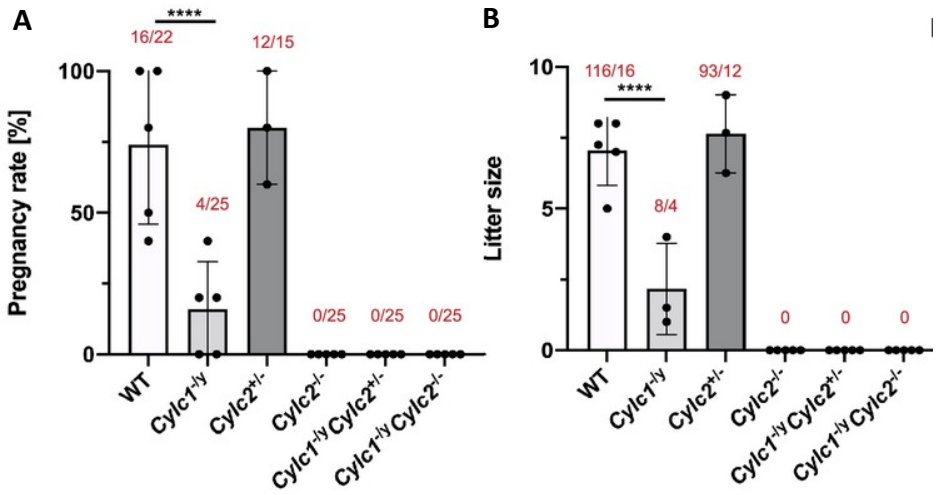

Figure 12: Fertility analysis of *Cylc*-deficient male mice. A) Pregnancy rates (%) and **B**) mean litter sizes of *Cylc*-deficient male mice in comparison to WT matings. Mean values ± s.d. are shown. Black dots represent mean values obtained for each male mouse included in the analysis. Total number of offspring per total number of pregnancies as well as total number of pregnancies per total number of plugs are depicted above each bar. Modified from Schneider, Kovacevic et al., 2023.

Testis weight and gross testicular morphology were unaltered in all analyzed animals (**Figure 13 A, B**). Hematoxylin and Eosin (H&E) staining of testicular tissue sections revealed that all stages of spermatogenesis were present and appeared unaltered in all genotypes (**Figure 13 B**). Epididymal sperm count in *Cylc1*$^{-/y}$ and *Cylc2*$^{+/-}$ male mice was reduced by 40–47% compared to WT, while in *Cylc2*$^{-/-}$ and *Cylc1*$^{-/y}$ *Cylc2*$^{+/-}$ male mice epididymal sperm count was reduced by 65%. In *Cylc1*$^{-/y}$ *Cylc2*$^{-/-}$ males, sperm counts were most affected as indicated by an 85% of less cells counted (**Figure 14 A**). Eosin-Nigrosine staining was used to analyze the viability of the epididymal sperm cells: cells which were stained pink were considered non-viable due to a damaged membrane. The quantification revealed that the viability of *Cylc2*$^{-/-}$ and *Cylc1*$^{-/y}$*Cylc2*$^{-/-}$ sperm was reduced by approx. 15% compared to WT sperm (**Figure 14 B**).

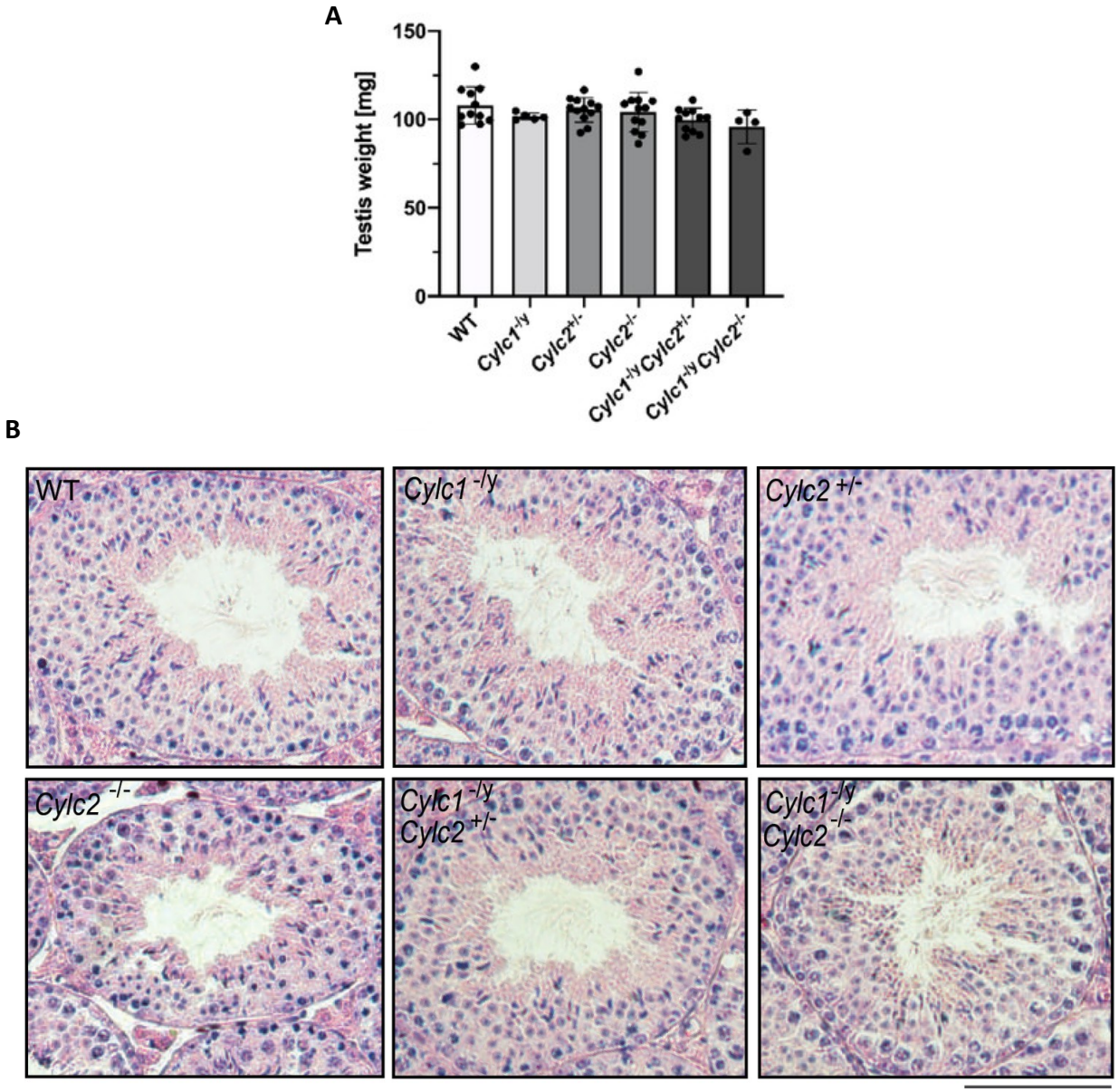

Figure 13: Testis weight and tissue architecture of *Cylc*-deficient mice. A) Testis weight (mg) of WT, *Cylc1*$^{-/y}$, *Cylc2*$^{+/-}$, *Cylc2*$^{-/-}$, *Cylc1*$^{-/y}$ *Cylc2*$^{+/-}$, and *Cylc1*$^{-/y}$ *Cylc2*$^{-/-}$ males. Mean values ± s.d. are shown; black dots represent data points for individual males. **B**) H&E-stained testicular tissue sections of WT, *Cylc1*$^{-/y}$, *Cylc2*$^{+/-}$, *Cylc2*$^{-/-}$, *Cylc1*$^{-/y}$ *Cylc2*$^{+/-}$ and *Cylc1*$^{-/y}$ *Cylc2*$^{-/-}$ male mice. Scale bar: 100 µm. Modified from Schneider, Kovacevic et al., 2023.

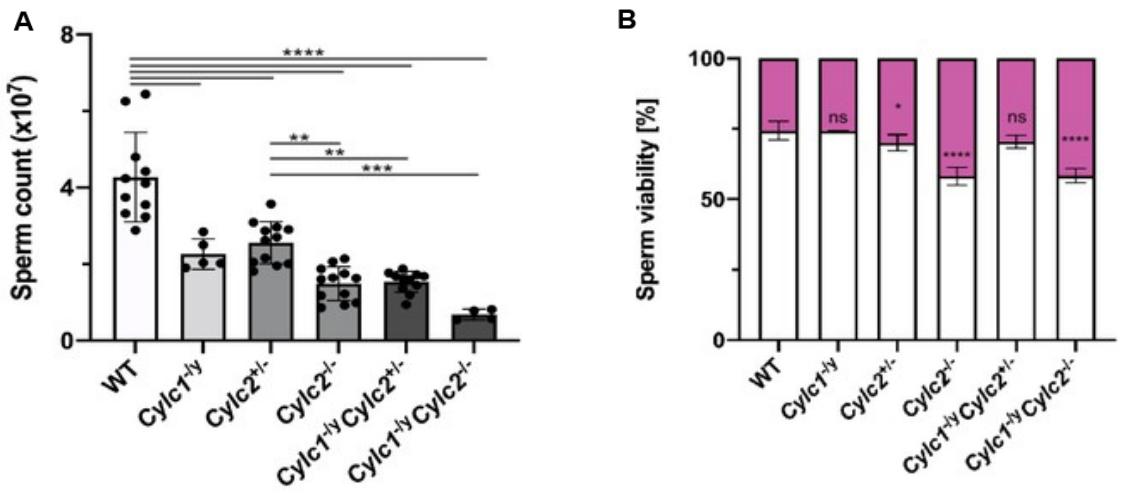

Figure 14: Epididymal sperm analysis of *Cylc*-deficient mice. A) Epididymal sperm count (×10^7) of WT, *Cylc1*$^{-/y}$, *Cylc2*$^{+/-}$, *Cylc2*$^{-/-}$, *Cylc1*$^{-/y}$ *Cylc2*$^{+/-}$, and *Cylc1*$^{-/y}$ *Cylc2*$^{-/-}$ mice. Mean values ± s.d. are shown; black dots represent data points for individual animals. **B**) Viability of the epididymal sperm stained with Eosin-Nigrosine. The percentage of Eosin negative (viable) and Eosin positive (inviable) sperm is shown. Data is represented as mean ± s.d. n=3. Modified from Schneider, Kovacevic et al., 2023.

4.3. Cylicins are localized in the perinuclear theca of murine sperm

We raised polyclonal antibodies against CYLC1 and CYLC2 in order to study their localization and role in male fertility in more detail. Immunofluorescence staining of Bouin-fixed testicular sections of WT mice revealed the presence of both CYLC1 and CYLC2 in the haploid germ cells (**Figure 15**). Of note, both CYLC1 and CYLC2 are first detectable in the perinuclear theca of round spermatids, particularly in the periacrosomal region, co-localizing with the acrosomal matrix marker SP56 (**Figure 16**). During the following stages of spermiogenesis, as the spermatids elongate, localization of both Cylicins shifts towards the posterior part of the cell, while SP56 remains at the growing acrosome (**Figure 16**). Importantly, signal was absent in CYLC1 stained tissues of *Cylc1*$^{-/y}$, *Cylc1*$^{-/y}$ *Cylc2*$^{+/-}$ and *Cylc1*$^{-/y}$ *Cylc2*$^{-/-}$ male mice, while CYLC2 wasn´t detectable in *Cylc2*$^{-/-}$ and *Cylc1*$^{-/y}$ *Cylc2*$^{-/-}$ tissue sections (**Figure 15**).

In mature sperm, CYLC1 and CYLC2 localize in the calyx – the posterior region of sperm PT (**Figure 16 B, Figure 17**). As expected, CYLC1 signal was absent from the sperm cells from *Cylc1*$^{-/y}$, *Cylc1*$^{-/y}$ *Cylc2*$^{+/-}$ and *Cylc1*$^{-/y}$ *Cylc2*$^{-/-}$ mice while CLYC2 was undetected in *Cylc2*$^{-/-}$ and *Cylc1*$^{-/y}$ *Cylc2*$^{-/-}$ sperm. This demonstrates that the antibodies raised are specific to CYLC1 and CYLC2 and do not cross-react. Interestingly, in sperm from *Cylc2*$^{+/-}$ and *Cylc2*$^{-/-}$ mice, CLYC1 was mislocalized and appeared irregularly scattered throughout the sperm head. Similarly, CYLC2 lost its proper calyx localization in *Cylc1*$^{-/y}$ *Cylc2*$^{+/-}$ sperm, suggesting that CLYC1 is required for the regular localization of CYLC2 in the calyx of PT, and vice versa (**Figure 17**).

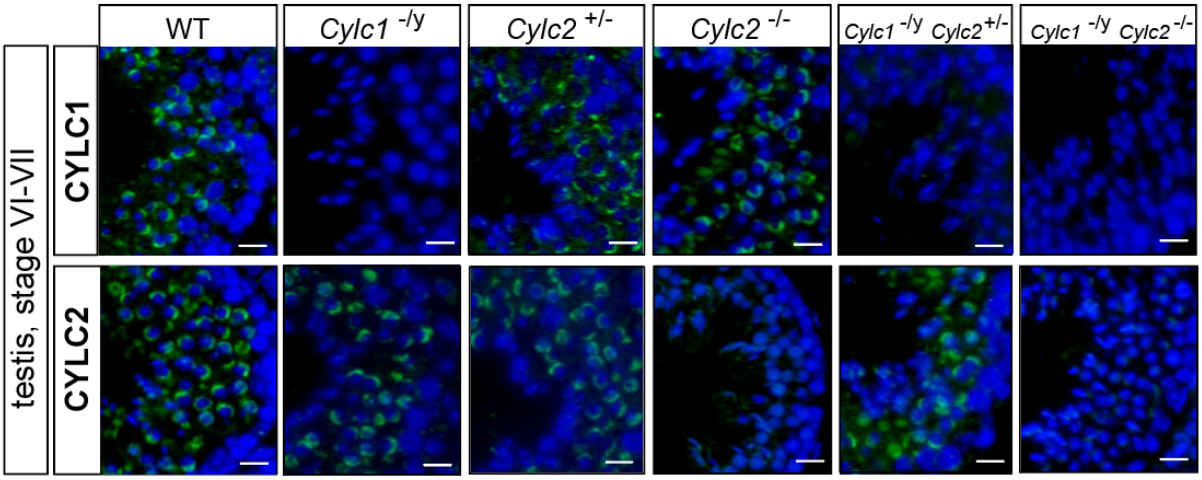

Figure 15: Localization of CYLC1 and CYLC2 in murine testis. Immunofluorescent staining of testicular tissue sections from WT, *Cylc1*$^{-/y}$, *Cylc2*$^{+/-}$, *Cylc2*$^{-/-}$, *Cylc1*$^{-/y}$ *Cylc2*$^{+/-}$, and *Cylc1*$^{-/y}$ *Cylc2*$^{-/-}$ mice against CYLC1 and CYLC2. Both CYLC1 and CYLC2 are detectable in haploid cells only. In *Cylc1*$^{-/y}$, *Cylc1*$^{-/y}$ *Cylc2*$^{+/-}$, and *Cylc1*$^{-/y}$ *Cylc2*$^{-/-}$ tissue sections, CYLC1 signal is not detected. In *Cylc2*$^{-/-}$ and *Cylc1*$^{-/y}$ *Cylc2*$^{-/-}$ tissues CYLC2 signal is not detected. Nuclei were counterstained with DAPI. Scale bar: 5 µm. n=3. Modified from Schneider, Kovacevic et al., 2023.

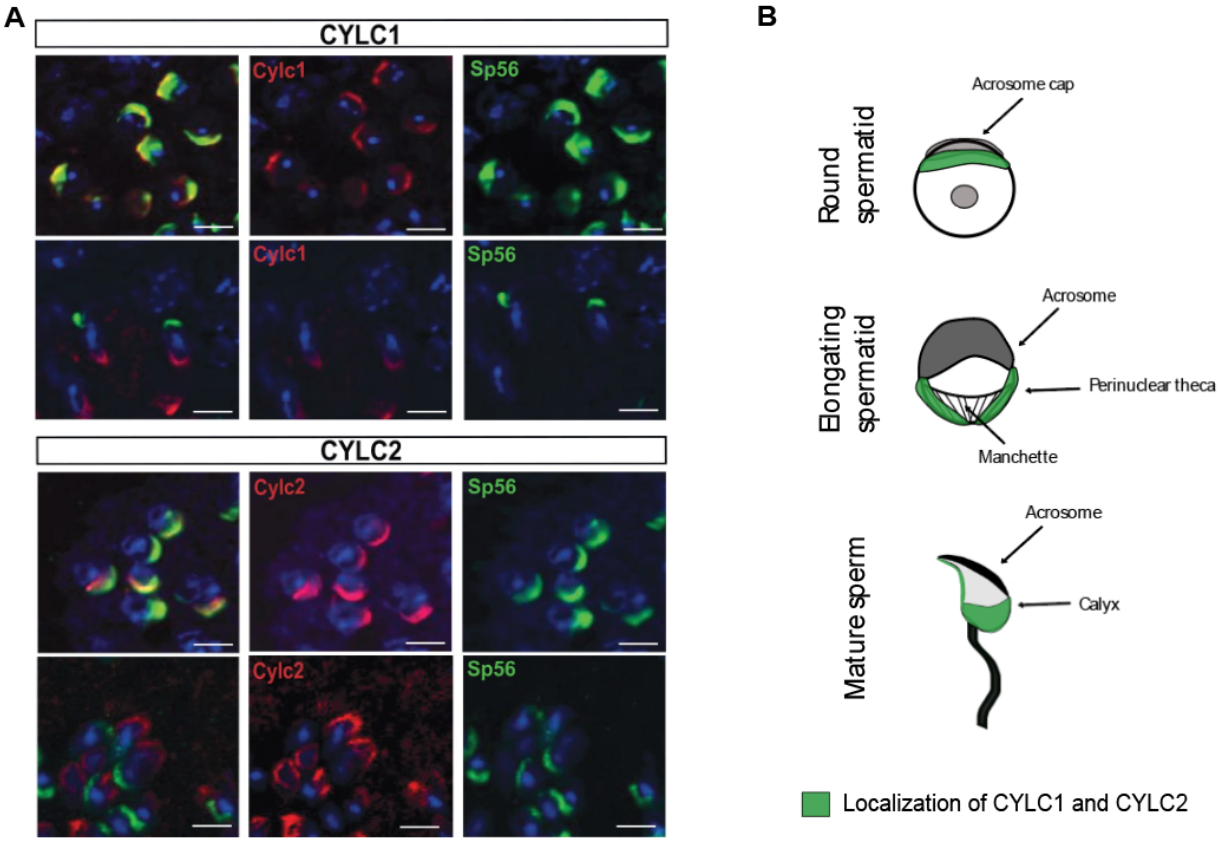

Figure 16: Localization pattern of CYLC1 and CYLC2 during spermiogenesis. A) Immunofluorescence staining against the acrosomal matrix marker SP56 (green) and CYLC1 or CYLC2 (red) in round and elongating spermatids. Nuclei were stained with DAPI. Scale bar: 5 µm. **B**) Schematic illustration of both CYLC1 and CYLC2 (green) localization during spermiogenesis. Modified from Schneider, Kovacevic et al., 2023.

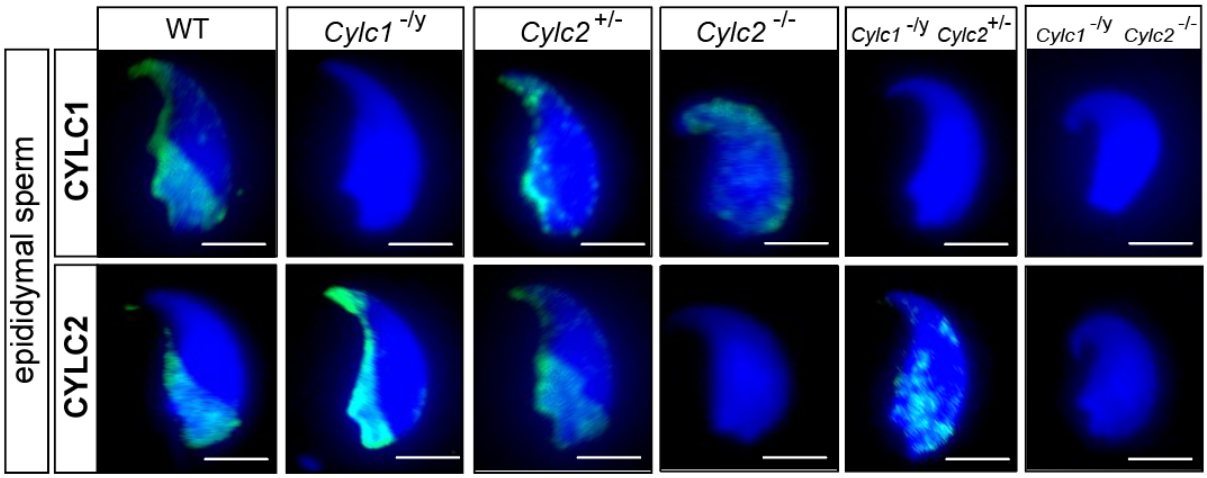

Figure 17: Localization of CYLC1 and CYLC2 in murine epididymal sperm. Immunofluorescent staining of epididymal sperm from WT, *Cylc1*$^{-/y}$, *Cylc2*$^{+/-}$, *Cylc2*$^{-/-}$, *Cylc1*$^{-/y}$ *Cylc2*$^{+/-}$ and *Cylc1*$^{-/y}$ *Cylc2*$^{-/-}$ mice against CYLC1 and CYLC2. Both CYLC1 and CYLC2 are detectable in the calyx region of the PT. In *Cylc1*$^{-/y}$, *Cylc1*$^{-/y}$ *Cylc2*$^{+/-}$, and *Cylc1*$^{-/y}$ *Cylc2*$^{-/-}$ sperm cells CYLC1 signal is not detected, while in *Cylc2*$^{-/-}$ sperm, CYLC1 lost the typical calyx localization and is irregularly scattered throughout the sperm head. In *Cylc2*$^{-/-}$ and *Cylc1*$^{-/y}$ *Cylc2*$^{-/-}$ sperm cells CYLC2 signal is not detected, while CYLC1 is irregularly scattered throughout the sperm head. Nuclei were counterstained with DAPI. Scale bar: 5 µm. Modified from Schneider, Kovacevic et al., 2023.

4.4. *Cylc*-deficiency severely affects sperm morphology in mice

4.4.1. Effect of *Cylc*-deficiency on sperm nuclear morphology

To check for defects in sperm nuclear morphology DAPI-stained sperm samples were analyzed in detail using Nuclear Morphology software plug-in for Image J (**Figure 18 A**). *Cylc1*$^{-/y}$, *Cylc2*$^{+/-}$ and *Cylc1*$^{-/y}$ *Cylc2*$^{+/-}$ sperm showed no alterations of the nuclear shape when compared to WT (**Figure 18 B, C**). However, nuclei of *Cylc2*$^{-/-}$ sperm appeared smaller on average, with shorter hooks, increased circularity and reduced elongation (**Figure 18 B, C**). Similarly, *Cylc1*$^{-/y}$ *Cylc2*$^{-/-}$ sperm nuclei appeared smaller as well, and with drastically reduced elongation and increased circularity (**Figure 18 B, C**). This indicates that the loss of both CYLC1 and CYLC2 causes abnormal shape of the sperm nucleus which could contribute to defects of sperm motility and thus male fertility.

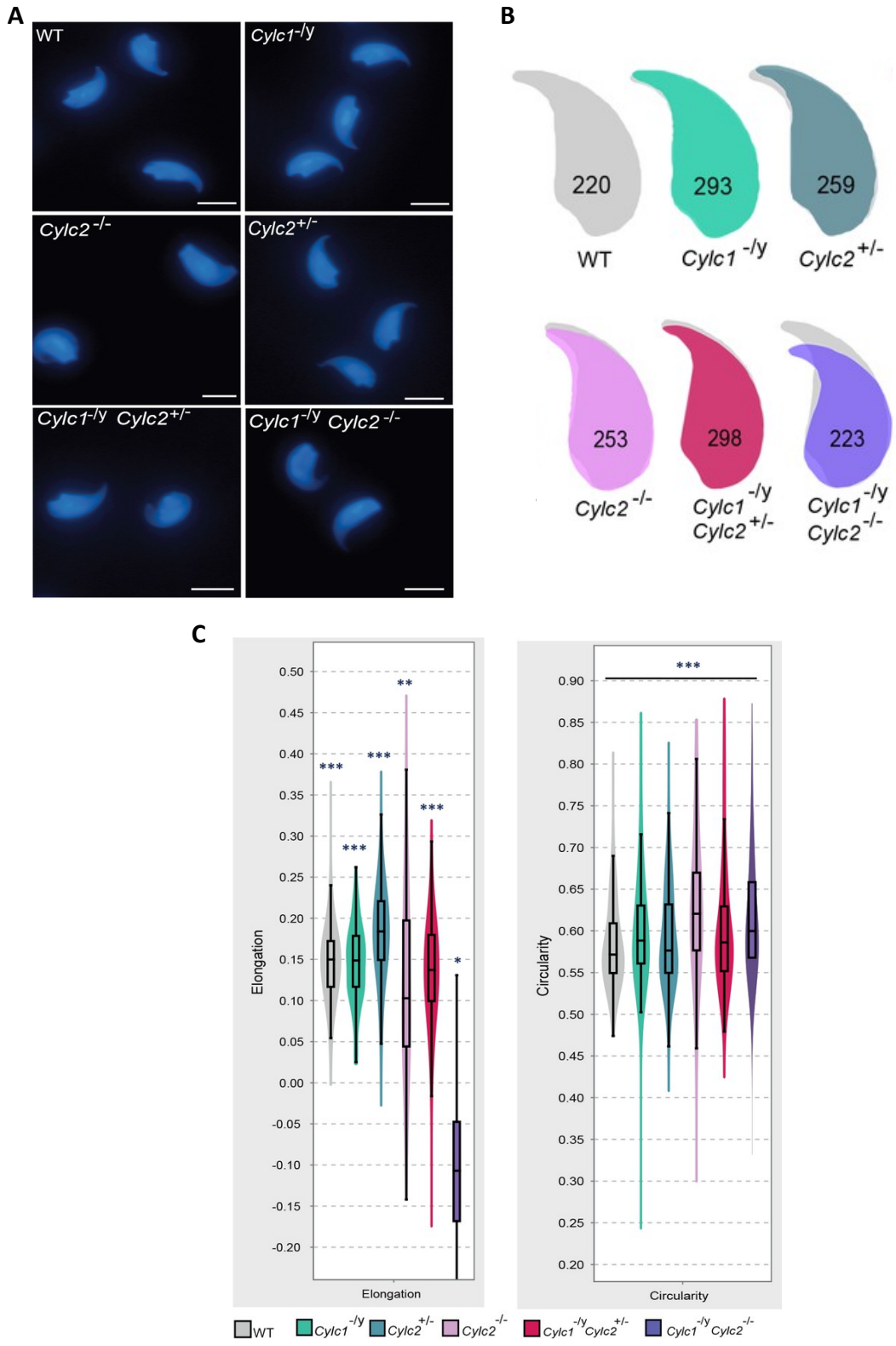

Figure 18: Nuclear morphology of *Cylc*-deficient sperm. A) DAPI stained sperm nuclei of WT, *Cylc1*$^{-/y}$, *Cylc2*$^{+/-}$, *Cylc2*$^{-/-}$, *Cylc1*$^{-/y}$ *Cylc2*$^{+/-}$, and *Cylc1*$^{-/y}$ *Cylc2*$^{-/-}$ male mice. Scale bar: 5 µm. **B**) Nuclear morphology of WT, *Cylc1*$^{-/y}$, *Cylc2*$^{+/-}$, *Cylc2*$^{-/-}$, *Cylc1*$^{-/y}$ *Cylc2*$^{+/-}$ and *Cylc1*$^{-/y}$ *Cylc2*$^{-/-}$ sperm. Number of cells analyzed for each genotype is shown **C**) Elongation and circularity of nuclei from WT, *Cylc1*$^{-/y}$, *Cylc2*$^{+/-}$, *Cylc2*$^{-/-}$, *Cylc1*$^{-/y}$ *Cylc2*$^{+/-}$, and *Cylc1*$^{-/y}$ *Cylc2*$^{-/-}$ sperm. The minimum detection area was set to 1.000 pixels, the maximum detection area was 7.000 pixels. Modified from Schneider, Kovacevic et al., 2023.

4.4.2. *Cylc*-deficiency leads to acrosome and flagellum abnormalities

For the first morphological analysis, epididymal sperm cells were imaged at a bright field microscope. Sperm cells from *Cylc1*$^{-/y}$, *Cylc2*$^{+/-}$ and *Cylc1*$^{-/y}$ *Cylc2*$^{+/-}$ mice had regular morphology of the head and tail, comparable to the WT. Interestingly, in samples from *Cylc2*$^{-/-}$ and *Cylc1*$^{-/y}$ *Cylc2*$^{-/-}$ mice, coiling of the flagella and bending of the sperm head were observed, with some cells having tails entirely wrapped around the sperm head (**Figure 19**).

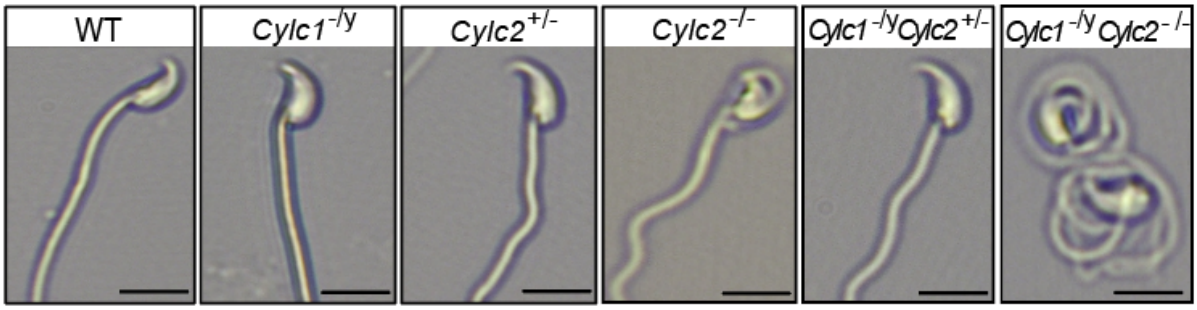

Figure 19: Morphology of *Cylc*-deficient epididymal sperm. Bright-field microscopy of sperm from WT, *Cylc1*$^{-/y}$, *Cylc2*$^{+/-}$, *Cylc2*$^{-/-}$, *Cylc1*$^{-/y}$*Cylc2*$^{+/-}$ and *Cylc1*$^{-/y}$*Cylc2*$^{-/-}$ mice. Coiling of the flagellum and its wrapping around the sperm head is visible in *Cylc2*$^{-/-}$ and *Cylc1*$^{-/y}$ *Cylc2*$^{-/-}$. Scale bar: 10 µm. Modified from Schneider, Kovacevic et al., 2023.

For a more detailed analysis of sperm morphology, we used peanut agglutinin (PNA)-fluorescein isothiocyanite (FITC) lectin as an acrosome marker, MITOred, to visualize mitochondria in the flagellum and DAPI to counter stain the nucleus. In WT and *Cylc2*$^{+/-}$ sperm, acrosome appears as a smooth, cap-like structure that lies on the apical part of the nucleus, while the flagellum is protruding from the caudal portion of the sperm head (**Figure 20 A**). Interestingly, in *Cylc1*$^{-/y}$ mice, malformations of the acrosome were detected in around 38% of mature sperm, while their flagellum appeared unaltered and properly connected to the head. Malformations of the acrosome were observed in 76% of *Cylc2*$^{-/-}$ sperm cells, while flagellum defects including bending of the neck region, coiling of the flagellum and its wrapping around the sperm head appeared in 80% of sperm (**Figure 20 A, B**). These morphological alterations were observed in 70% of *Cylc1*$^{-/y}$ *Cylc2*$^{+/-}$ sperm and in 92% of *Cylc1*$^{-/y}$ *Cylc2*$^{-/-}$ sperm (**Figure 20 A, B**). Additionally, severe malformations and misplacement of the acrosome were found in sperm from *Cylc1*$^{-/y}$ *Cylc2*$^{-/-}$ mice, with PNA-lectin signal detectable all over the sperm cell, including the flagellum (**Figure 20 A, B**).

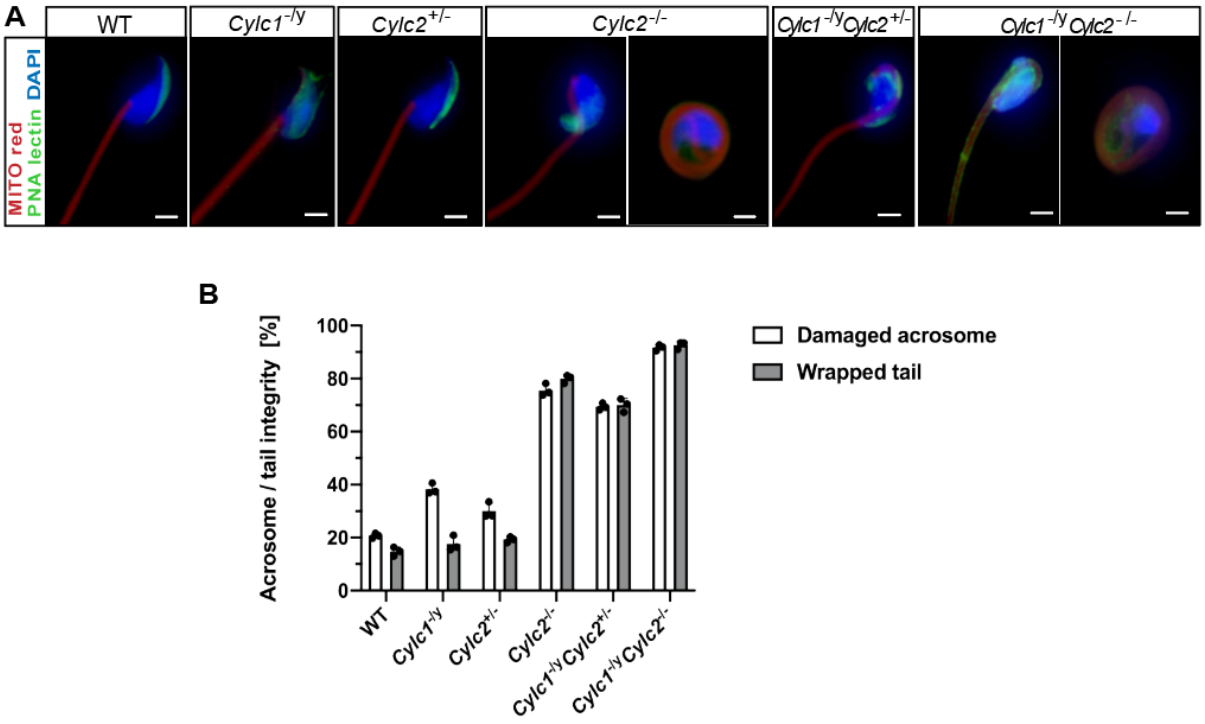

Figure 20: Acrosome and flagellum analysis of *Cylc*-deficient sperm. A) Immunofluorescence staining of epididymal sperm PNA-lectin (green) was used as an acrosome marker and MITOred (red) was used to stain flagella. Nuclei were counterstained with DAPI. Scale bar: 5 µm. **B**) Quantification of abnormal acrosomes and coiled flagella of WT, *Cylc1*$^{-/y}$, *Cylc2*$^{+/-}$, *Cylc2*$^{-/-}$, *Cylc1*$^{-/y}$ *Cylc2*$^{+/-}$, and *Cylc1*$^{-/y}$ *Cylc2*$^{-/-}$ mice is shown. n=3. Modified from Schneider, Kovacevic et al., 2023.

Detailed morphological analysis of epididymal sperm using transmission electron microscopy (TEM) further confirmed the observed morphological defects (**Figure 21, Supplementary figure S3**). In *Cylc2*$^{-/-}$ sperm coiling of the tail and dislocation of the head-tail connecting piece from the basal plate, resulting in parallel positioning of head and tail were observed (**Figure 21**, **Supplementary figure S3**, white arrowheads). Furthermore, *Cylc2*$^{-/-}$ sperm head and portions of the tail were surrounded by one continuous membrane including excess of cytoplasm. In *Cylc2*$^{-/-}$ sperm loosening of the peri-acrosomal region and its detachment from the nucleus were observed (**Figure 21**, **Supplementary figure S3,** green arrowheads). Off note, *Cylc1*$^{-/y}$ sperm cells did not display any apparent morphological abnormalities, with intact PT and acrosome as well as the normal head-tail connecting region (**Figure 21**). Interestingly, nuclei of sperm from *Cylc1*$^{-/y}$ and *Cylc2*$^{-/-}$ animals appeared with normal electron density comparable to WT, indicating that *Cylc*-deficiency does not affect chromatin remodeling. Holes in the nuclei of some sperm cells from *Cylc2*$^{-/-}$ mice were observed but were likely due to cell death caused by severe morphological abnormalities, rather than representing nuclear defects caused by *Cylc2*-deficiency (**Supplementary figure S3**). Finally, a prominent defect in *Cylc2*$^{-/-}$ sperm was the abnormalities of the posterior region of the PT and absence of calyx structure (**Figure 21**, **Supplementary figure S3,** red arrowheads).

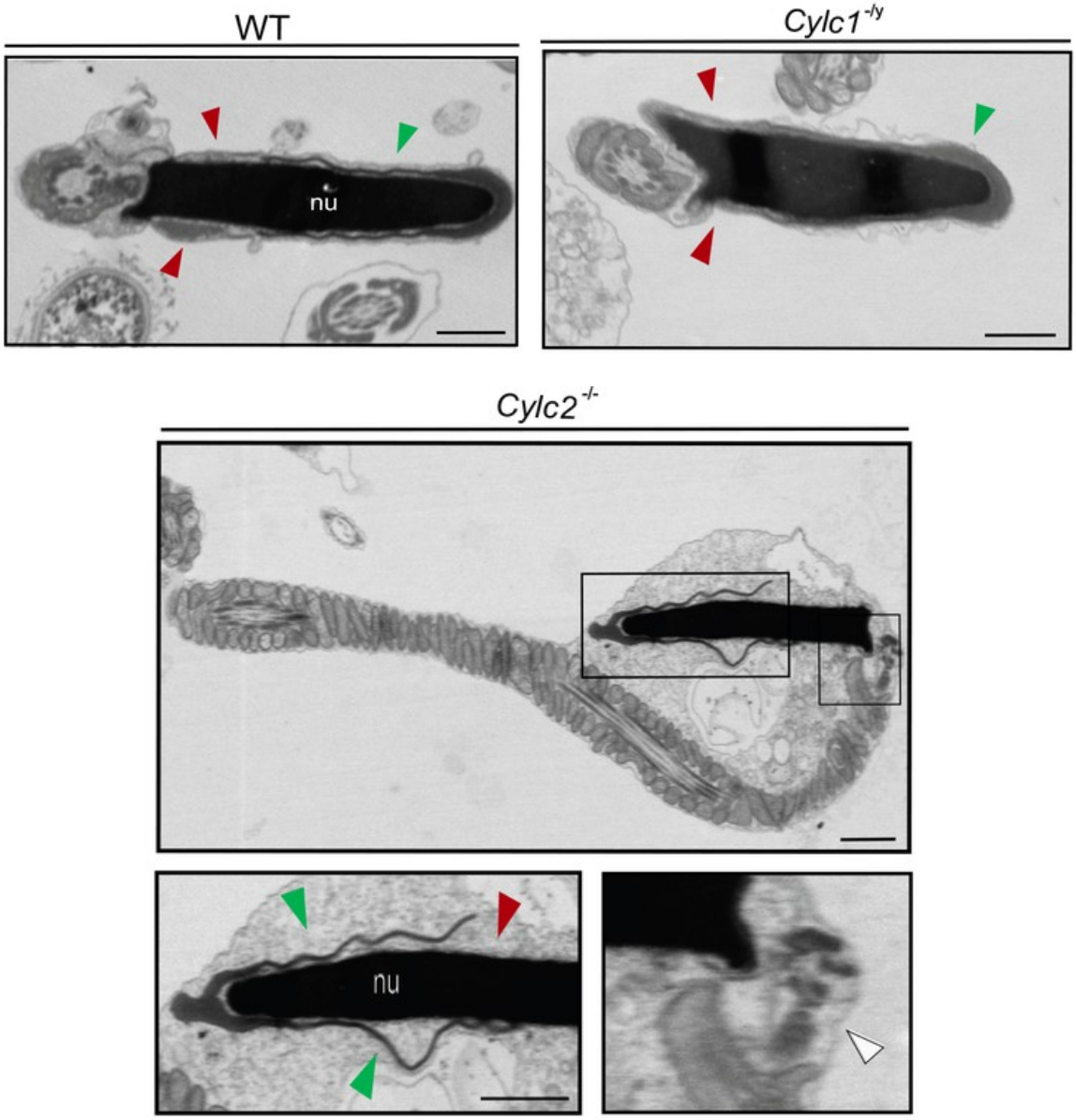

Figure 21: TEM micrographs of WT, *Cylc1*$^{-/y}$ and *Cylc2*$^{-/-}$ epididymal sperm. Acrosome appears detached from the nucleus in *Cylc2*$^{-/-}$ sperm (green arrowheads), while the calyx is missing entirely (red arrowheads). The head-tail connecting piece aberration is shown by white arrowheads. Nuclei (nu) are equally electron dense in all genotypes. Scale bar: 1 µm. See also Supplementary figure S3. Modified from Schneider, Kovacevic et al., 2023.

To investigate the effects of flagellar defects on motility, the swimming of epididymal sperm activated in TYH medium from all genotypes was analyzed. In WT, *Cylc1*$^{-/y}$ and *Cylc2*$^{+/-}$ male mice, around 60% of sperm cells were motile (**Figure 22 A**). Not surprisingly, the motility of *Cylc2*$^{-/-}$ sperm was drastically reduced to only 7% motile sperm and to only 2% in *Cylc1*$^{-/y}$ *Cylc2*$^{-/-}$ male mice. Interestingly, the few motile sperm cells found in *Cylc2*-deficient mice were not progressive but were swimming in circular trajectories *in-situ*, which is likely due to defects of the head-tail connecting piece and the sperm head bending over the tail. Finally, the reduction of sperm motility was observed in *Cylc1*$^{-/y}$ *Cylc2*$^{+/-}$ mice as well, with 27% of motile sperm cells (**Figure 22 A**).

Next, to analyze the flagellar beat of non-capacitated WT and *Cylc2*$^{-/-}$ sperm in detail, SpermQ software was used (Hansen et al., 2018). Interestingly, a reduced amplitude of the initial flagellar beat and reduced average curvature of the flagellum during a single beat was detected, suggestive of the stiffness in the neck region of *Cylc2*$^{-/-}$ sperm (**Figure 22 B**). Overall, the flagellar beat of *Cylc2*$^{-/-}$ sperm cells was similar to WT cells, however, interruptions during which midpiece and initial principal piece appeared stiff were observed. These interruptions occurred only on the open-hook side and their duration varied from beat to beat. Finally, a high-frequency beating occurs at the flagellar tip, probably consuming higher amounts of energy. Of note, the axoneme structure at the midpiece of *Cylc2*$^{-/-}$ sperm was unaltered, with the typical 9+2 microtubular composition, suggesting that the alterations of the flagellar beat are not caused by axoneme deformities but rather originate from the observed structural defects of the sperm head and head-tail connecting piece (**Figure 23**).

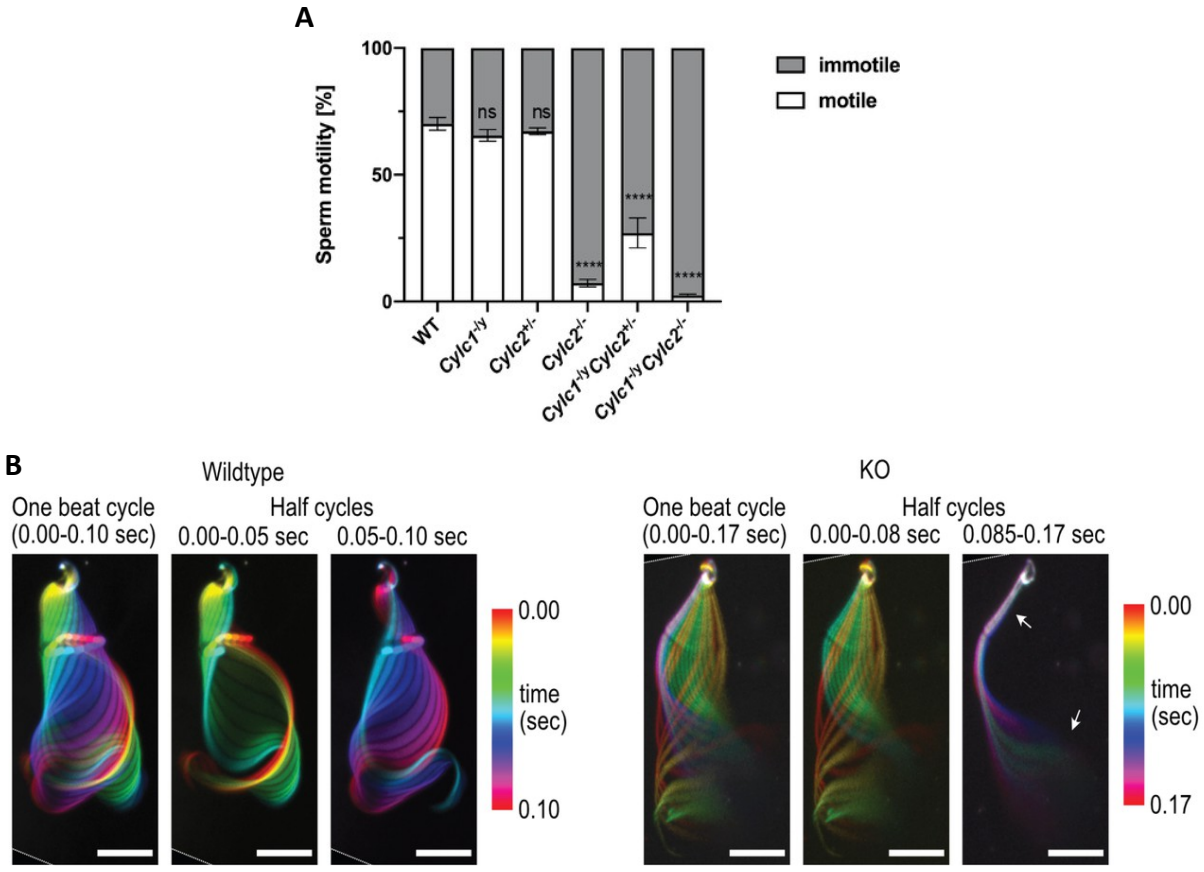

Figure 22: Motility of *Cylc*-deficient epididymal sperm. A) Quantification of motile and immotile epididymal sperm activated in TYH medium. Mean values ± SD are shown. **B**) Full and half-beat cycle time-lapse plots of the flagellar beat of WT and *Cylc2*$^{-/-}$ sperm. In *Cylc2*$^{-/-}$ sperm, the stiffness of the midpiece and high oscillations of the end piece were observed in one direction of the beat. Modified from Schneider, Kovacevic et al., 2023. Flagellar beat analysis was performed together with Dr. Jan Hansen. Flagellar beat analysis can be observed in videos published in Schneider, Kovacevic et al., 2023.

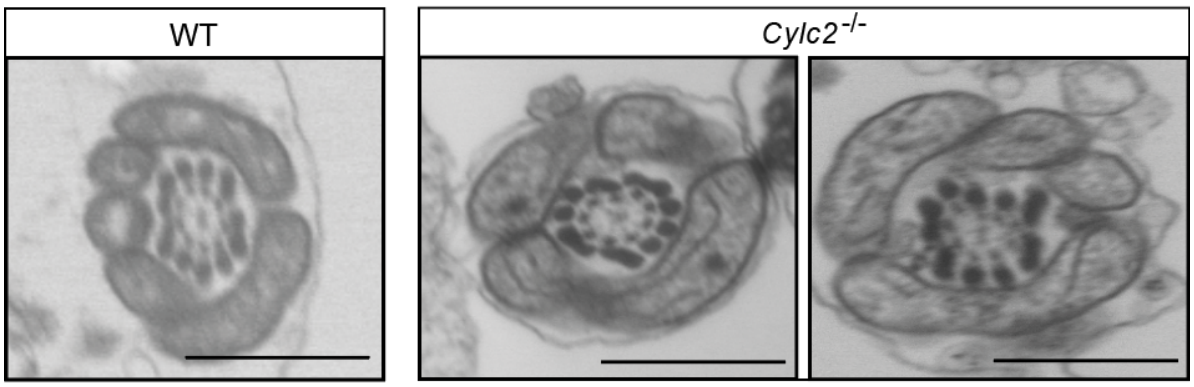

Figure 23: Cross-sections of axonemal structures of WT and *Cylc2*$^{-/-}$ sperm. TEM micrographs of WT and *Cylc2*$^{-/-}$ sperm axonemes at the midpiece region of sperm flagellum. The axonemes of *Cylc2*$^{-/-}$ sperm were unaltered. Scale bar: 500 nm. Modified from Schneider, Kovacevic et al., 2023.

4.4.3. Cylicins are required for proper calyx morphology

As observed in TEM micrographs of the epididymal sperm Cylc2-deficiency caused abnormalities of the PT and absence of the calyx region (**Figure 21, Supplementary figure S3,** red arrowheads). Instead of surrounding the nucleus entirely, the PT in *Cylc2*$^{-/-}$ sperm appeared interrupted and lacked its caudal part completely. In *Cylc1*$^{-/y}$ sperm cells, PT and calyx region appeared intact (**Figure 21, Supplementary figure S3,** red arrowheads).

To study calyx defects caused by *Cylc*-deficiency in more detail, other calyx-specific proteins, CCIN (Zhang et al., 2022a) and CAPZA3 (Geyer et al., 2009), which co-localize with CYLC1 and CYLC2 in epididymal sperm were analyzed. In *Cylc1*$^{-/y}$ and *Cylc2*$^{+/-}$ sperm, CCIN localization remained unaltered, being detected in the calyx and in the ventral portion of PT (**Figure 24 A, B**). However, in sperm of mice lacking two or three *Cylc* alleles, CCIN lost its calyx localization and appeared distributed randomly in the sperm cell. Of note, in 91% of *Cylc2*$^{-/-}$ sperm, CCIN signal is found in the sperm tail or with random distribution throughout the sperm head, without the typical calyx localization (**Figure 24 A, B**). Similarly, in 91% of *Cylc1*$^{-/y}$ *Cylc2*$^{+/-}$ and 98% of *Cylc1*$^{-/y}$*Cylc2*$^{-/-}$ sperm, the localization of CCIN was significantly altered, with the signal being distributed across the sperm head and tail (**Figure 24 A, B**).

Actin-capping proteins CAPZα3 (CAPZA) and CAPZβ3 (CAPZB) form a heterodimer that localizes in the calyx (Wear & Cooper, 2004a). Immunofluorescence staining revealed that the localization of CAPZα3 remained unaltered in *Cylc1*$^{-/y}$ and *Cylc2*$^{+/-}$ mice compared to WT mice (**Figure 24 A, C**). In 84% of *Cylc2*$^{-/-}$ sperm cells, CAPZA3 localizes correctly to the caudal portion of the head, however it can be found in the apical portion of the PT suggesting to its mislocalization. Interestingly, in *Cylc1*$^{-/y}$ *Cylc2*$^{+/-}$ sperm CAPZA3 maintained its correct calyx localization in around 30% of sperm. In *Cylc1*$^{-/y}$ *Cylc2*$^{-/-}$ deficient mice 92% of spermatozoa showed aberrant and random distribution of CAPZA3 across the sperm head rather than in the regular calyx region (**Figure 24 A, C**). Interestingly, contrary to CCIN, CAPZA3 was never detected in the sperm tail, and it remained localized in the sperm head. Off note, both CCIN and CAPZA3 stainings indicate that in epididymal sperm from *Cylc1*$^{-/y}$ mice, calyx region appears thinner compared to the calyx of WT sperm (**Figure 24**). These results suggest that loss of Cylicins impairs the formation of calyx, which might contribute to morphological anomalies of the sperm described initially.

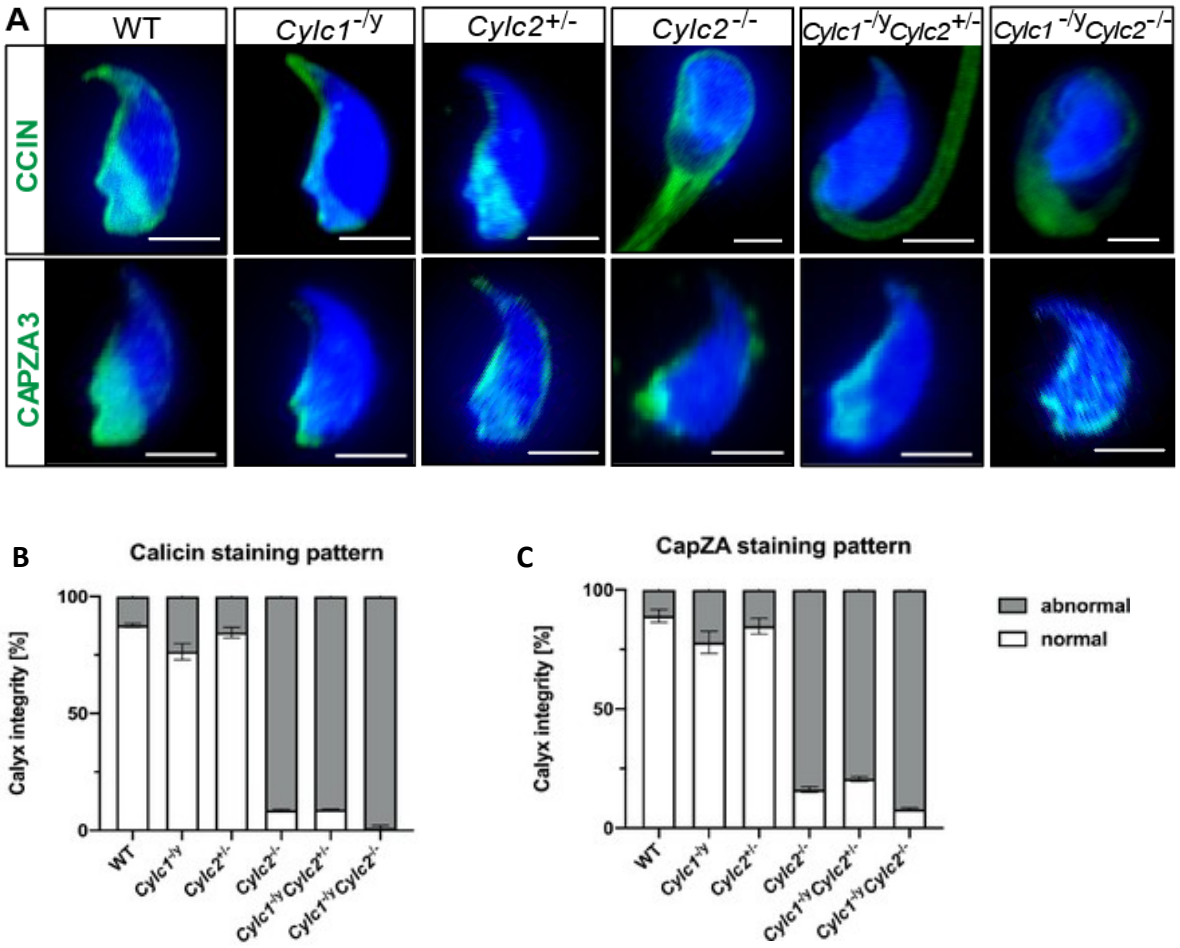

Figure 24: Analysis of calyx structure in *Cylc*-deficient sperm. A) Immunofluorescent staining against PT proteins CCIN (upper panel) and CAPZA3 (lower panel) in WT, *Cylc1*$^{-/y}$, *Cylc2*$^{+/-}$, *Cylc2*$^{-/-}$, *Cylc1*$^{-/y}$ *Cylc2*$^{+/-}$, and *Cylc1*$^{-/y}$ *Cylc2*$^{-/-}$ sperm. Nuclei were counterstained with DAPI. Scale bar: 5 µm. **B)** Quantification of sperm with abnormal CCIN staining pattern in WT, *Cylc1*$^{-/y}$, *Cylc2*$^{+/-}$, *Cylc2*$^{-/-}$, *Cylc1*$^{-/y}$ *Cylc2*$^{+/-}$, and *Cylc1*$^{-/y}$ *Cylc2*$^{-/-}$ mice **C)** Quantification of sperm with abnormal CAPZA3 staining pattern in WT, *Cylc1*$^{-/y}$, *Cylc2*$^{+/-}$, *Cylc2*$^{-/-}$, *Cylc1*$^{-/y}$ *Cylc2*$^{+/-}$, and *Cylc1*$^{-/y}$ *Cylc2*$^{-/-}$ mice. Mean values ± SD are shown. Modified from Schneider, Kovacevic et al., 2023.

4.5. *Cylc*-deficiency causes defects of spermiogenesis

4.5.1. Cylicins are required for proper acrosome biogenesis

To study the origin of the defects in sperm morphology, spermiogenesis of *Cylc*-deficient mice was analyzed in detail. First, acrosome biogenesis was investigated by PNA-lectin and PAS staining of testicular tissue sections (**Figure 25, Supplementary figure S4**). During the first phase of acrosome biogenesis (Golgi phase), proacrosomal vesicles deriving from the Golgi apparatus start to aggregate into a single granule at one pole of round spermatids. In all genotypes, this proacrosomal granule was unaltered and observed as small dot on the surface of round spermatids in PNA stained testis tissues (**Figure 25**). Next, during cap phase, growing acrosomes flatten to cover the apical part of the nucleus forming a cap-like structure. The acrosomal cap appeared smooth and regularly distributed on the perinuclear region of round spermatids of WT and *Cylc2*$^{+/-}$ mice. However, in some of the round spermatids from *Cylc2*$^{-/-}$ and *Cylc1*$^{-/y}$ mice, growing acrosomal caps were irregular, with visible gaps (**Figure 25**). Finally, in *Cylc1*$^{-/y}$ *Cylc2*$^{+/-}$ and *Cylc1*$^{-/y}$ *Cylc2*$^{-/-}$ mice, the damage of acrosomal caps affected most of the round spermatids where deformities or irregular localization of acrosome were observed (**Figure 25**). Next, at acrosome phase, while spermatids elongate, acrosomes develop along the nucleus forming an arrow-like structure. In many elongating spermatids of all *Cylc*-deficient mice irregular acrosomes were detected. In testis samples of *Cylc2*$^{-/-}$ and *Cylc1*$^{-/y}$ *Cylc2*$^{-/-}$ mice detachment of the acrosome from the nuclear envelope was observed suggesting that Cylicins are required for the attachment of the developing acrosome to the nuclear envelope during spermiogenesis (**Figure 25**). These results suggest that the previously observed morphological defects of *Cylc*-deficient epididymal sperm originate from the early stages of spermiogenesis.

Next, TEM analysis of testicular tissue was performed in step 6 round spermatids of both WT and *Cylc2*$^{-/-}$ testis. The Golgi phase appeared unaltered with morphologically normal acrosomal granules (**Figure 26 A**). During steps 7-8 the spermatids start to elongate, and the growing acrosomes flatten over the nucleus. However, in *Cylc2*$^{-/-}$ spermatids, an increased distance between the developing acrosome (**Figure 26 B**, green arrowheads) and microtubules on the posterior part of the cell (**Figure 26 B**, red arrowheads) was observed at the central region called perinuclear ring. As spermiogenesis progressed, in spermatids at step 9-10 microtubules appeared longer on one side of the nucleus. The displacement of the acrosome to the side and its detachment from the nuclear envelope was observed, as well as the formation of a gap in the PT (**Figure 26 C, D**). In step 16 spermatids, the calyx was absent, while an excess of cytoplasm surrounded the nucleus and flagellum (**Figure 26 F**, white arrowhead), while remains of manchette microtubules are still present (yellow arrowhead).

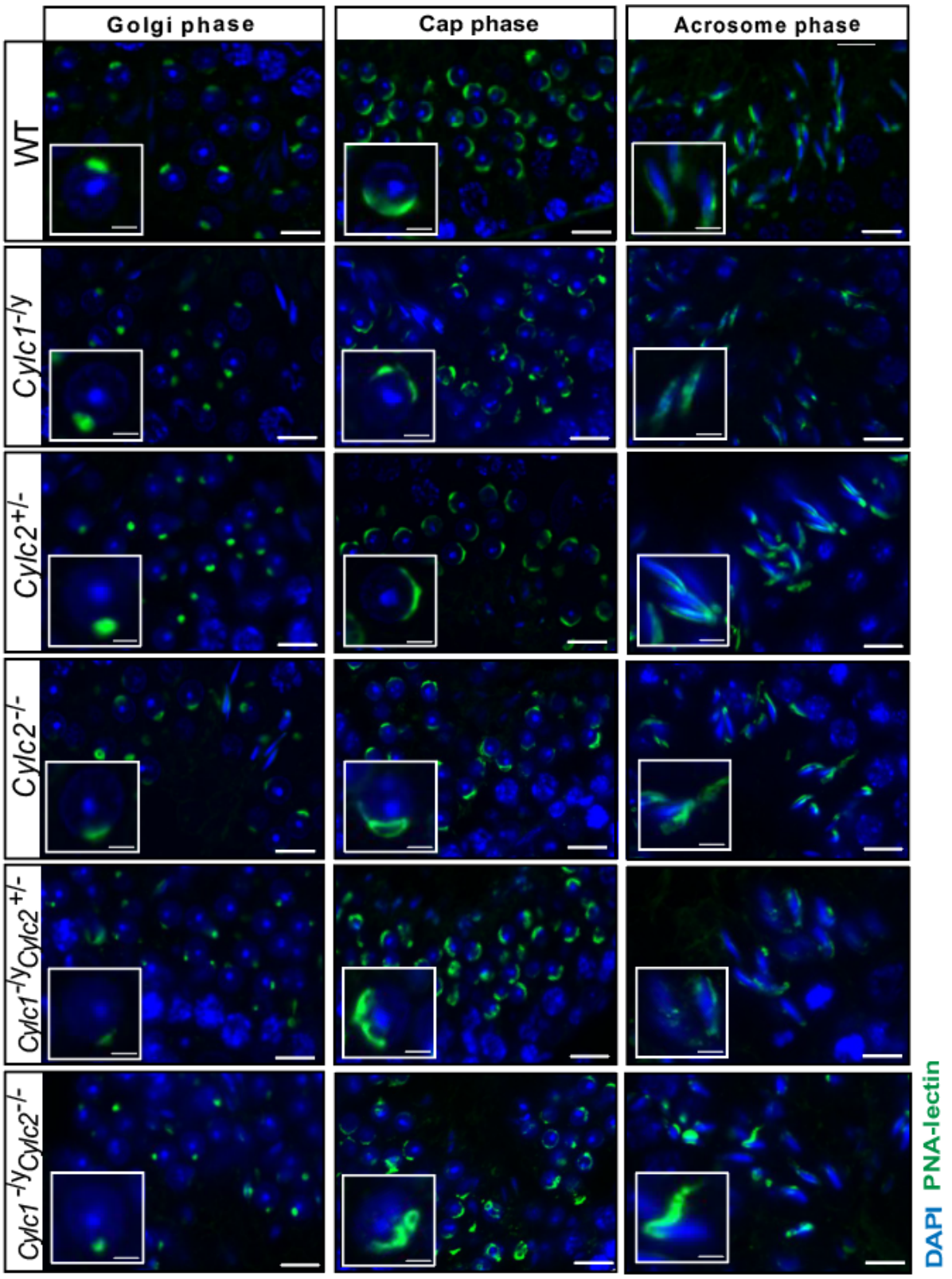

Figure 25: Analysis of acrosome biogenesis in testicular tissue of *Cylc*-deficient mice. PNA-lectin (green) immunofluorescence staining of testicular tissue sections of WT, *Cylc1*$^{-/y}$, *Cylc2*$^{+/-}$, *Cylc2*$^{-/-}$, *Cylc1*$^{-/y}$ *Cylc2*$^{+/-}$, and *Cylc1*$^{-/y}$ *Cylc2*$^{-/-}$ mice. Round spermatids at stage I-IV featuring Golgi phase of acrosome biogenesis are visible in the left panel. Round spermatids in cap phase (stage V–VIII) are shown in the middle panel. Elongating spermatids in acrosomal phase (stage IX–XI) are visible in the right panel. Nuclei were counterstained with DAPI. n=3 Scale bar: 10 µm. Inserts show representative single spermatids at higher magnification (scale bar: 2 µm). Modified from Schneider, Kovacevic et al., 2023.

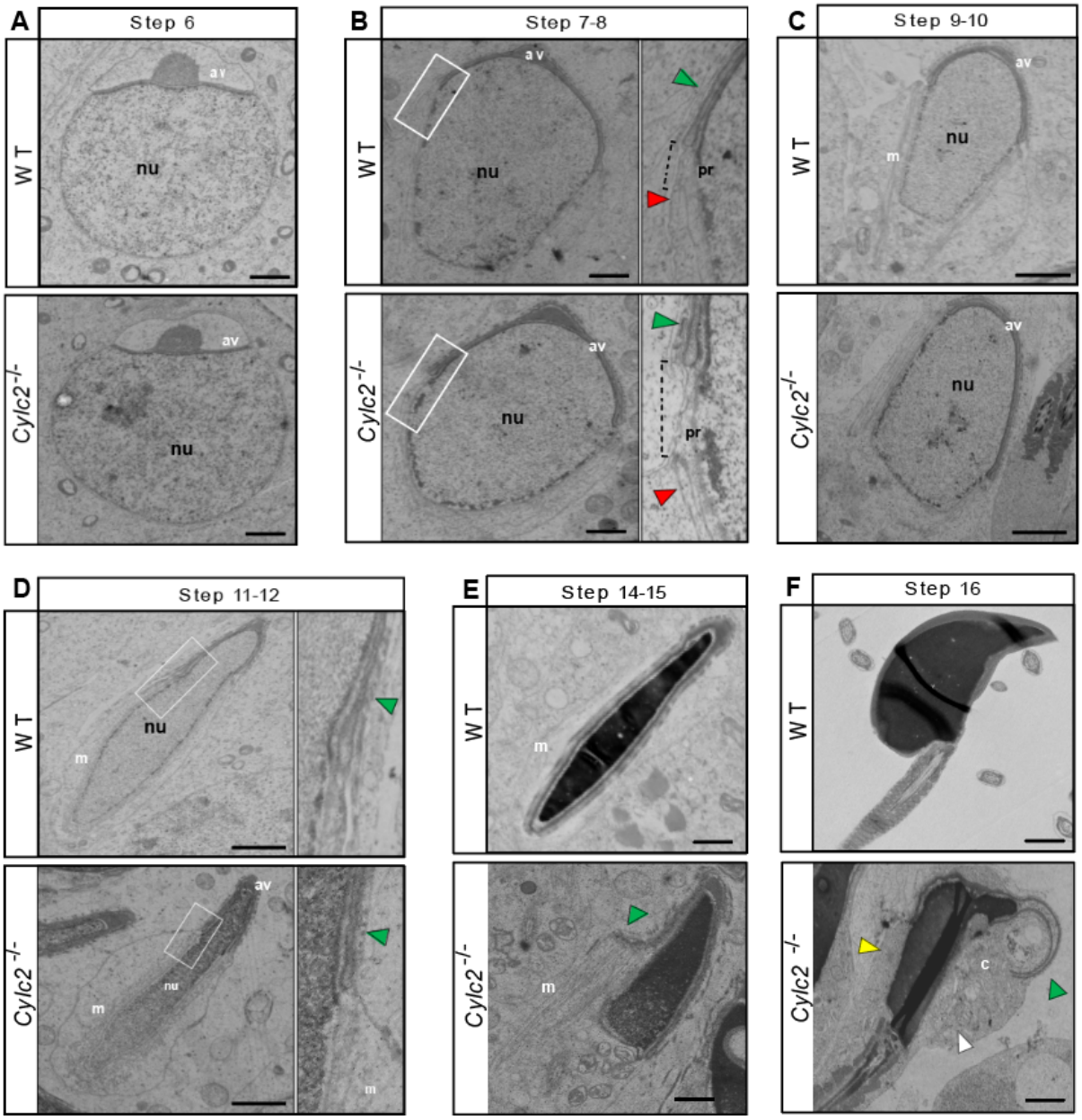

Figure 26: TEM micrographs of testicular tissues of WT and *Cylc2*$^{-/-}$ mice. Representative single spermatids from step 6 (**A**); step 7-8 (**B**); step 9-10 (**C**); step 11-12 (**D**); step 14-15 (**E**) and step 16 (**F**). Green arrowheads = acrosome; red arrowheads = manchette; white arrowhead = cytoplasm; yellow arrowhead = remaining microtubules after manchette disassembly. **nu**: nucleus; **av**: acrosomal vesicle; **pr:** perinuclear ring; **m**: manchette microtubules; **cy**: cytoplasm. Modified from Schneider, Kovacevic et al., 2023.

Finally, in TEM samples of testis tissue from *Cylc2*-deficient mice, many damaged and degrading cells with perforated nuclei and detached structures were observed having (**Supplementary figure S5**). Phagosomes containing cellular remains were observed far away from the lumen at the basal membrane of the tubuli, suggesting that the cells that suffer most severe structural damage are being removed likely by Sertoli cells. This clearance of malformed cells explains the reduction of epididymal sperm count in *Cylc*-deficient genotypes.

4.5.2. Abnormal manchette elongation and disassembly are caused by *Cylc*-deficiency

While investigating acrosome development in TEM micrographs of *Cylc2*$^{-/-}$ spermatids, abnormalities of the manchette were observed as well. Manchette is a transient microtubular platform for protein transport during sperm head elongation, which is required for proper sperm head shaping and sperm development. To study manchette assembly and morphology in all genotypes, immunofluorescence staining against acetylated α-tubulin on squash testis samples was performed and spermatids were staged for step-to-step comparison (**Figure 27 A**). In step 8 spermatids of all genotypes, assembly of manchette microtubules was not altered. After the manchette assembles, it starts elongating toward the neck region during step 9. At steps 10-11, this microtubular structure assumes the typical skirt-like form at the caudal region of the cells. Until this point, the manchette assembly was unaltered in all genotypes. In spermatids from *Cylc1*$^{-/y}$ and *Cylc2*$^{+/-}$ mice and regular manchette development persisted in further steps of spermiogenesis. Starting from step 12, excessive manchette elongations could be observed in spermatids from *Cylc2*$^{-/-}$, *Cylc1*$^{-/y}$ *Cylc2*$^{+/-}$ and *Cylc1*$^{-/y}$ *Cylc2*$^{-/-}$ mice (**Figure 27 A**). This excessive elongation became more prominent at step 13 spermatids. Manchette length in step 10-13 spermatids was measured and the mean was obtained, showing that the average manchette length was 76–80 nm in WT, *Cylc1*$^{-/y}$ and *Cylc2*$^{+/-}$ spermatids, while for *Cylc2*$^{-/-}$ and *Cylc1*$^{-/y}$ *Cylc2*$^{-/-}$ spermatids mean manchette length was up to 100 nm (**Figure 27 B**). Of note, in *Cylc1*$^{-/y}$ *Cylc2*$^{+/-}$ spermatids an intermediate phenotype with a mean manchette length of 86 nm was observed (**Figure 27 B**). In some *Cylc2*-deficient spermatids a displacement of the manchette to the ventral side of the nucleus was observed along with its excessive elongation (**Figure 27 A**). In step 16 spermatids the manchette was disassembled normally in WT, *Cylc1*$^{-/y}$, and *Cylc2*$^{+/-}$ male mice (**Figure 27 A**). However, *Cylc2*$^{-/-}$, *Cylc1*$^{-/y}$ *Cylc2*$^{+/-}$ and *Cylc1*$^{-/y}$ *Cylc2*$^{-/-}$ spermatids showed a persistent α-tubulin signal, indicating that disassembly of the manchette is delayed or incomplete. In TEM micrographs of testicular tissues from *Cylc2*$^{-/-}$ male mice, abnormal elongation of manchette microtubules in step 14-15 spermatids can be observed, while in WT manchettes are disassembled already and the PT appeared as a unique structure that compactly surrounds the nucleus (**Figure 26 F**, **yellow arrowhead**). Another manchette marker is HOOK1, which binds to microtubules and regulates protein trafficking during endocytosis and spermiogenesis. Co-staining of the spermatids against acrosome marker PNA lectin and HOOK1 as manchette marker, showed that abnormal manchette elongation occurs simultaneously with the anomalies in the developing acrosome during spermatid elongation in *Cylc2*$^{-/-}$ male mice (**Figure 28 A**). Images of immunofluorescent co-staining against HOOK1 and PNA lectin were used to make schematic representation of spermatid elongation in *Cylc2*$^{-/-}$ compared to WT mice (**Figure 28**

B). As the spermatid elongates, *Cylc2*$^{-/-}$ acrosomes detach and grow further from the nucleus, while manchette elongates excessively (**Figure 28 B**).

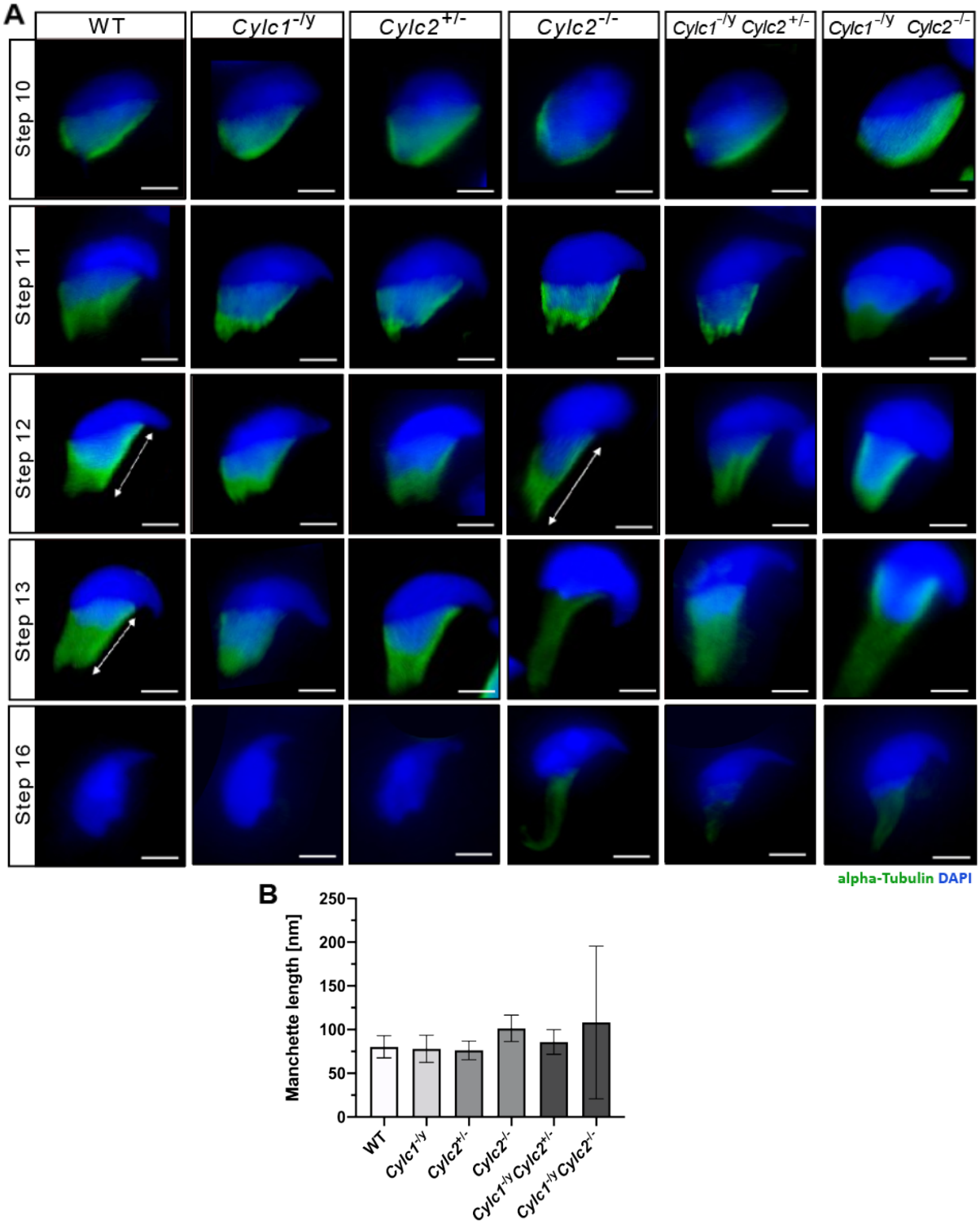

Figure 27: Manchette formation in *Cylc*-deficient spermatids. A) Immunofluorescence staining against α-tubulin in squash testis samples of WT, *Cylc1*$^{-/y}$, *Cylc2*$^{+/-}$, *Cylc2*$^{-/-}$, *Cylc1*$^{-/y}$ *Cylc2*$^{+/-}$ and *Cylc1*$^{-/y}$ *Cylc2*$^{-/-}$ mice. Single spermatids in different steps of spermiogenesis were shown for step-to-step comparison. Scale bar: 5 µm. **B**) Quantification of manchette length in WT, *Cylc1*$^{-/y}$, *Cylc2*$^{+/-}$, *Cylc2*$^{-/-}$, *Cylc1*$^{-/y}$, *Cylc2*$^{+/-}$, and *Cylc1*$^{-/y}$ *Cylc2*$^{-/-}$ spermatids at steps 10–13. Modified from Schneider, Kovacevic et al., 2023.

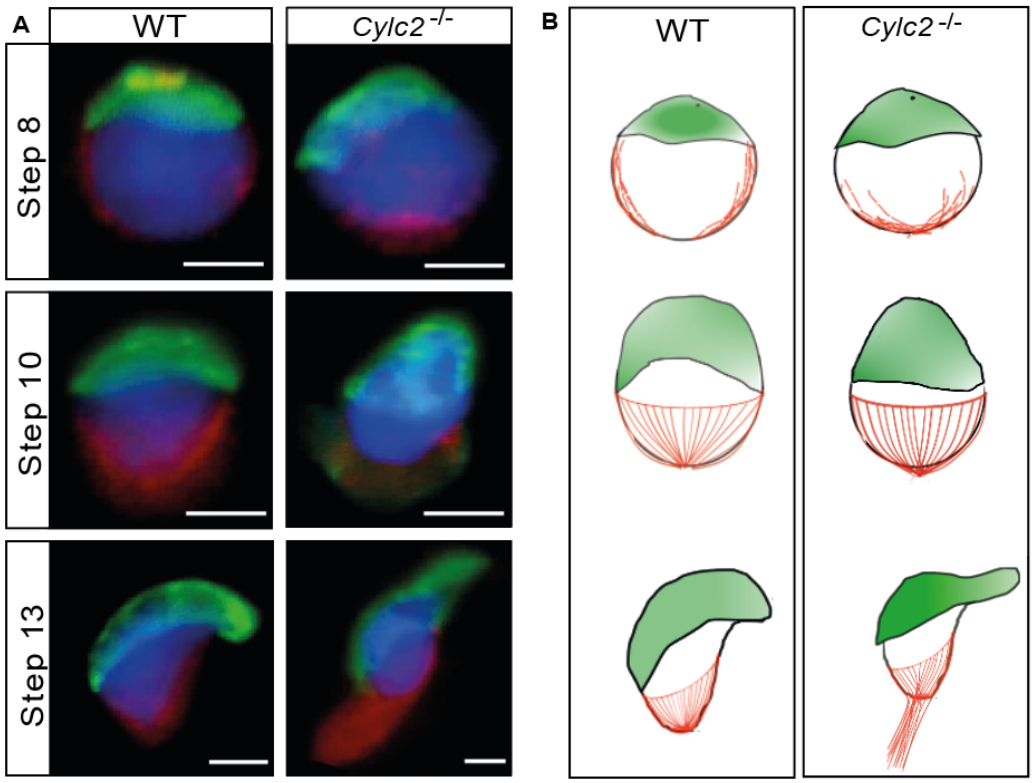

Figure 28: Acrosome and manchette development in *Cylc2*$^{-/-}$ mice. **A)** Co-staining of manchette with HOOK1 (red) and acrosome with peanut agglutinin (PNA)-lectin (green) in round, elongating and elongated spermatids of WT and *Cylc2*$^{-/-}$ mice. Scale bar: 3 µm. **B)** Schematic representation of spermiogenesis with acrosomal structure depicted in green and manchette microtubules in red. Modified from Schneider, Kovacevic et al., 2023.

4.6. Proteomic analysis of the cytoskeletal compartment of *Cylc*-deficient sperm

To investigate in more detail the effect of *Cylc*-deficiency on cytoskeletal compartment of mature sperm cells, Mass Spectrometry analysis was performed on subcellular protein fractions corresponding to sperm cytoskeleton of all six genotypes. First, Principal Component Analysis (PCA) was performed to capture the maximal variance in the data (**Figure 29**). In a PCA plot, samples (dots) that are closer to each other in the plot are more similar. The size of the dot for each sample indicates its contribution to variance in the dataset. All three WT samples analyzed were clustered close to each other indicating high similarity between them. Very similar were samples from *Cylc2*$^{+/-}$, *Cylc2*$^{-/-}$ and *Cylc1*$^{-/y}$ *Cylc2*$^{-/-}$ male mice. Although *Cylc1*$^{-/y}$ and *Cylc1*$^{-/y}$ *Cylc2*$^{-/-}$ samples had one outlier each, overall PCA was considered good, without significant differences between samples from the same group (**Figure 29**).

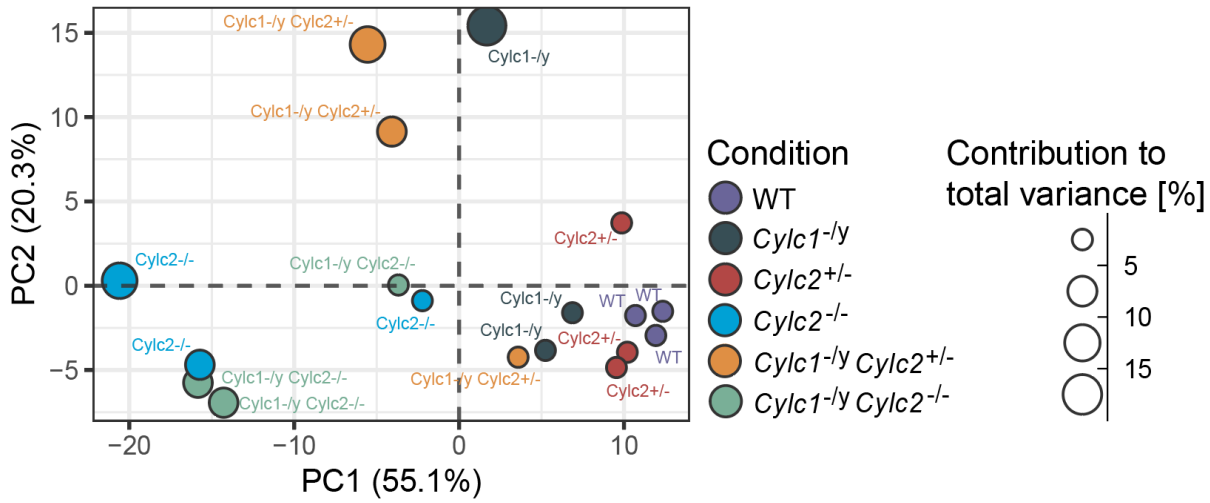

Figure 29: PCA plot of the proteomics analysis of cytoskeletal compartment of *Cylc*-deficient sperm. PC1 (55.1%) and PC2 (20.3%) are the first and second principal components accounting for the highest amount of variance in the dataset. The values on the axes indicate how much each sample differs from the "center" of the dataset along these two main components. Each dot represents a different sample in the dataset. The size of the dot represents its contribution to the total variance. Larger dots contribute more to the overall variance in the dataset. Measurements were performed by Dr. Marc Sylvester; Bioinformatics data analysis was performed by Dr. Andreas Buness and Dr. Farhad Shakeri.

In the heatmap shown in **figure 30**, the 100 most significantly depleted or enriched proteins are depicted, with red boxes indicating higher and blue boxes indicating lower protein abundances. As expected, CYLC1 showed lower abundance in *Cylc1*$^{-/y}$, *Cylc1*$^{-/y}$ *Cylc2*$^{+/-}$ and *Cylc1*$^{-/y}$ *Cylc2*$^{-/-}$ sperm compared to WT and *Cylc2*$^{+/-}$. Interestingly, CYLC1 appeared less abundant in *Cylc2*$^{-/-}$ sperm as well. Similarly, CYLC2 was significantly depleted in sperm from *Cylc1*$^{-/y}$, *Cylc2* $^{-/-}$, *Cylc1*$^{-/y}$ *Cylc2*$^{+/-}$ and *Cylc1*$^{-/y}$ *Cylc2*$^{-/-}$ mice compared to WT and *Cylc2*$^{+/-}$. As described previously, the RNA level of *Cylc1* and *Cylc2* were not altered in testis from *Cylc2*$^{-/-}$ and *Cylc1*$^{-/y}$ male mice, respectively (**Figure 11 A**).

Among the most significantly depleted proteins in *Cylc*-deficient sperm are many PT-specific proteins such as ACTL11, ACTRT3 (ARPM1), ACTRT2, CAPZB, CAPZA3, ACTL7A, SPEM3, CCIN and different isoforms of SPATA31. This severe depletion of PT proteins indicates that CYLC1 and CYLC2 might interact with these proteins and are required for the maintenance of the molecular complex responsible for the structure of PT. In *Cylc1*$^{-/y}$ sperm, the most significantly enriched proteins belonged to different metabolic processes, while in samples from *Cylc2*$^{-/-}$ and *Cylc1*$^{-/y}$ *Cylc2*$^{-/-}$ sperm, proteins involved in translation and protein folding and degradation are found in addition to those involved in metabolism (**Supplementary figure S6**). This suggests that the enriched proteins are a secondary effect caused by cellular stress due to abnormal development and morphology and are not analyzed in more detail.

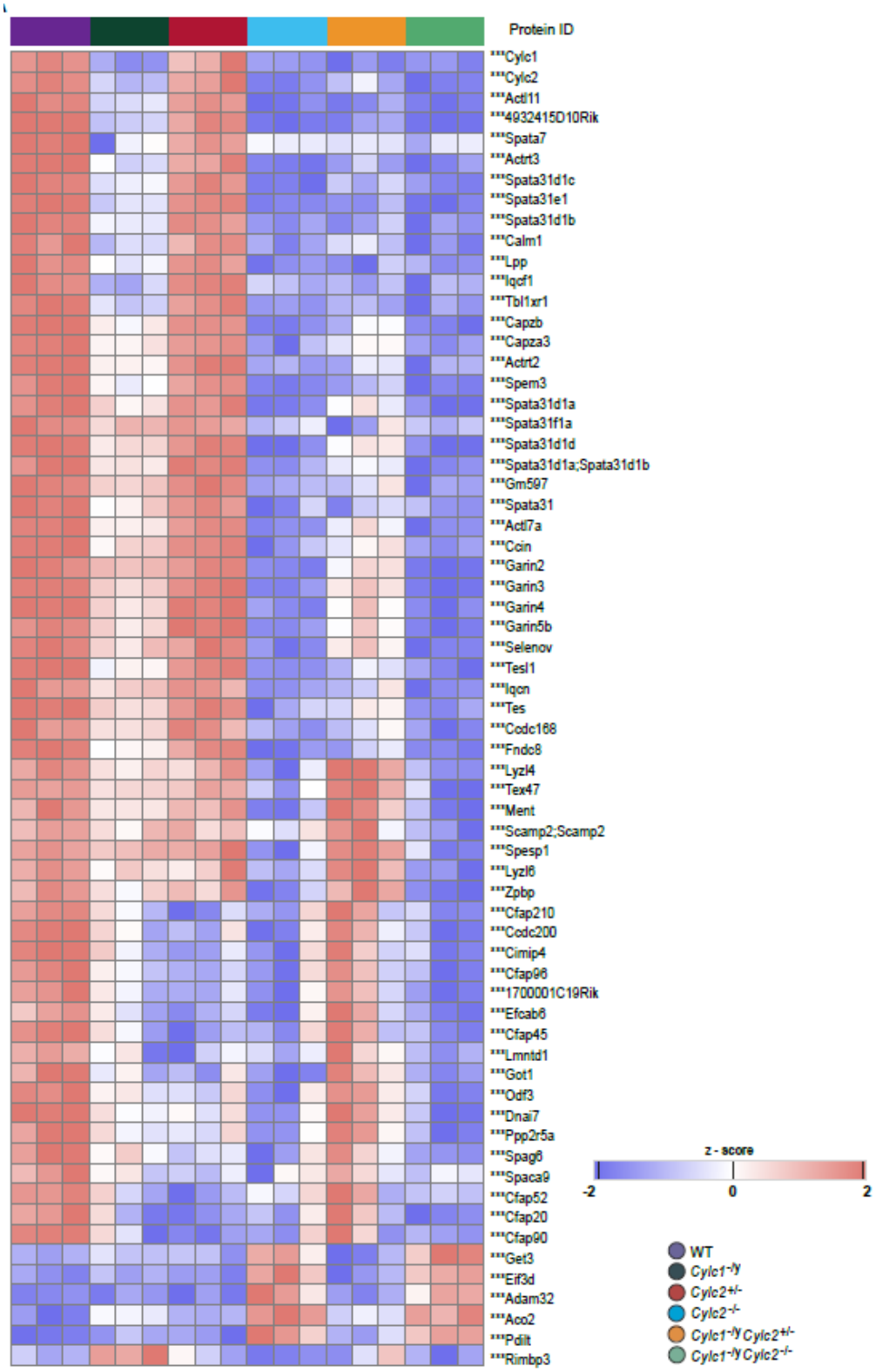

Figure 30: Differentially abundant proteins in Cylc-deficient sperm. Heatmap depicting 100 most significantly depleted or enriched proteins in cytoskeletal protein fractions of WT, *Cylc1*$^{-/y}$, *Cylc2*$^{+/-}$, *Cylc2*$^{-/-}$, *Cylc1*$^{-/y}$, *Cylc2*$^{+/-}$ and *Cylc1*$^{-/y}$ *Cylc2*$^{-/-}$ sperm. Rows represent specific proteins detected with their IDs listed on the right side. Columns depict different genotypes represented by the colored bar at the top. The color intensity of the boxes visually represents relative abundance levels of different proteins where red tones indicate higher and blue tones lower protein abundance. Measurements were performed by Dr. Marc Sylvester; Bioinformatics data analysis was performed by Dr. Andreas Buness and Dr. Farhad Shakeri.

In sperm from *Cylc1*$^{-/y}$ male mice, 44 proteins were significantly less abundant compared to the WT sperm, while 32 proteins were significantly enriched (**Figure 31; Figure 32**). All significantly depleted proteins in sperm from *Cylc1*$^{-/y}$ mice were also significantly lower abundant in *Cylc2*$^{-/-}$ and *Cylc1*$^{-/y}$ *Cylc2*$^{-/-}$ sperm (**Figure 31 A**). Other than CYLC1 itself, among the 10 most significantly depleted proteins in *Cylc1*$^{-/y}$ sperm other PT-specific proteins are found, such as ACTL11, CYLC2, SPEM3 and different isoforms of SPATA31 (**Figure 32**). Interestingly, in *Cylc2*$^{+/-}$ sperm cytoskeletal compartment, no significant differences in protein abundance were observed, while only a slight depletion of proteins from CFAP (Cilia and Flagella associated proteins) family is found (**Figure 33**). More severe effects on the cytoskeletal protein department were observed in *Cylc2*$^{-/-}$ sperm where roughly 600 proteins were significantly depleted and almost 1000 proteins were enriched, overlapping mostly with depleted/enriched proteins found in sperm from *Cylc1*$^{-/y}$ *Cylc2*$^{-/-}$ mice (**Figure 31; Figure 34**). As expected, among the 10 most significantly depleted proteins in *Cylc2*$^{-/-}$ sperm, some of the PT-specific proteins were detected, such as ACTL7A, ACTL11, SPEM3 and different isoforms of SPATA31. Interestingly, in sperm from *Cylc1*$^{-/y}$*Cylc2*$^{+/-}$ male mice only 116 proteins were significantly depleted, with ACTL11, SPEM3 and SPATA31 isoforms among the top 10 (**Figure 35**). As expected, the deficiency of both CYLC1 and CYLC2 caused similar defects of the protein abundance in sperm like the ones observed in *Cylc2*$^{-/-}$ with almost 600 depleted and more than 900 enriched proteins (**Figure 31**; **Figure 36**). ACTL11, ACTL7A, SPEM3 and SPATA31 isoforms were again found among the 10 most significantly depleted proteins, suggesting that these proteins might be potential molecular interactors of CYLC1 and/or CYLC2 in the PT.

Gene Ontology (GO) term enrichment analysis showed that in *Cylc1*$^{-/y}$ sperm, significantly depleted proteins belong mostly to cytoskeletal calyx, with the highest fold-enrichments, F-actin capping protein complex, acrosomal and secretory vesicle and motile cilium (**Figure 37 A**). In *Cylc2*$^{-/-}$ sperm, depleted proteins belong to almost all cellular compartments of the sperm, including different cytoskeletal complexes such as inner and outer dynein arms, microtubule associated complexes, microtubule organizing centers as well as sperm specific organelles such as acrosome, manchette and flagellum (**Figure 37 B**). This suggests that CYLC2 might be required for maintenance of the sperm cytoskeletal structure and its deficiency leads to disruption of all sperm cell compartments. As expected, similar results were obtained in *Cylc1*$^{-/y}$ *Cylc2*$^{+/-}$ sperm (**Figure 37 C**).

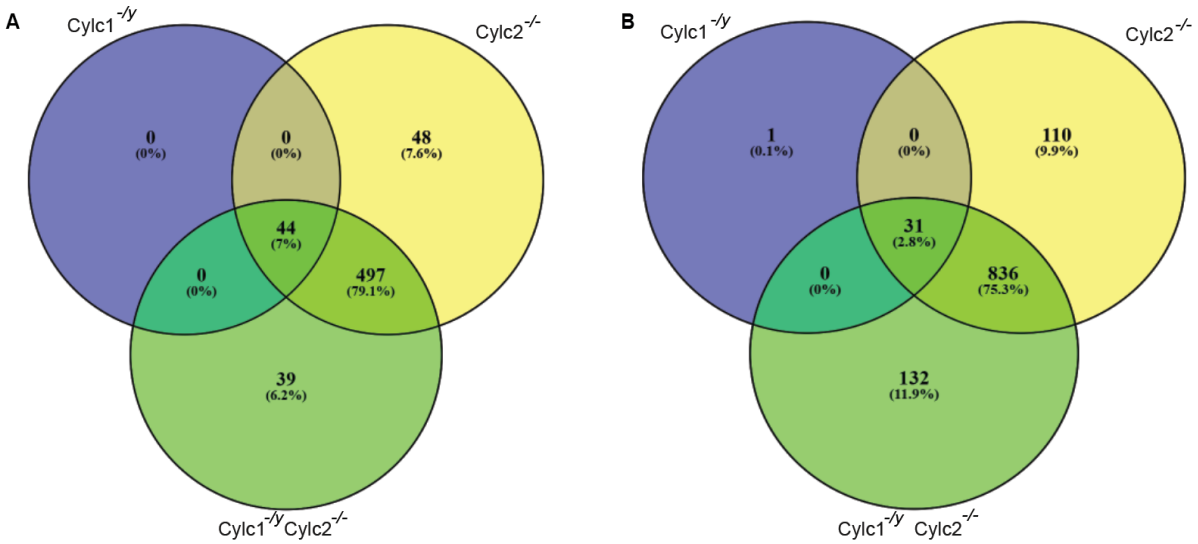

Figure 31: **Protein differential abundance comparison between *Cylc1*$^{-/y}$, *Cylc2*$^{-/-}$ and *Cylc1*$^{-/y}$ *Cylc2*$^{-/-}$ sperm.** **A**) lower abundant and **B**) higher abundant proteins in cytoskeletal fractions from sperm of *Cylc1*$^{-/y}$, *Cylc2*$^{-/-}$ and *Cylc1*$^{-/y}$ *Cylc2*$^{-/-}$ mice compared to sperm from WT mice. Diagrams are generated using Venny 2.1.0. online software. Measurements were performed by Dr. Marc Sylvester; Bioinformatics data analysis was performed by Dr. Andreas Buness and Dr. Farhad Shakeri.

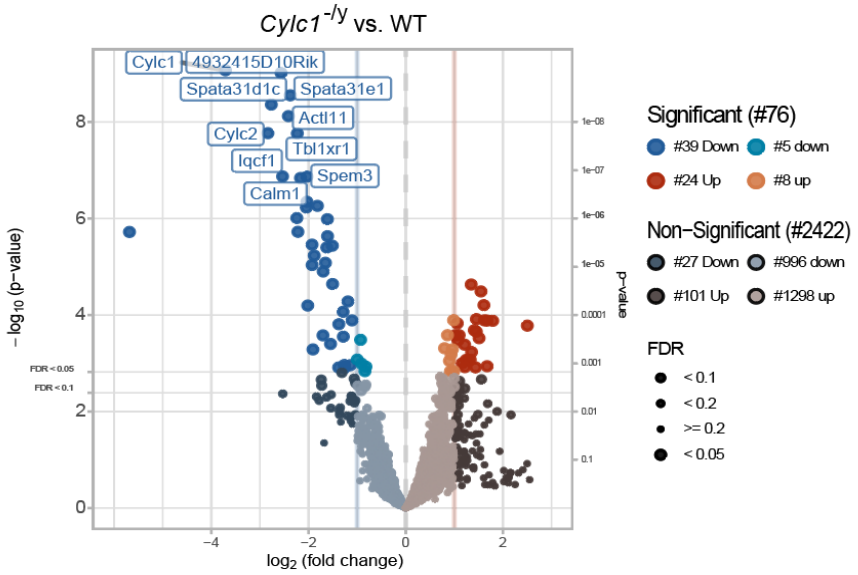

Figure 32: Differentially abundant proteins in *Cylc1*$^{-/y}$ sperm. Volcano plot representing differential protein abundance in cytoskeletal compartment of *Cylc1*$^{-/y}$ sperm compared to WT sperm. Log2 fold change shown in x-axis represents the magnitude of differential abundance. Negative values (blue) represent proteins that are less abundant in *Cylc1*$^{-/y}$ sperm compared to WT, while positive values (red) show enriched proteins. y-axis shows -log10 p-value that represents the statistical significance of the differential abundance. Blue and red dots represent proteins that are significantly depleted or enriched respectively. Gray or pale dots represent proteins that are not significant. The horizontal gray lines represent different FDR (False Discovery Rate) thresholds. Ten most significantly depleted proteins are labelled by name. Measurements were performed by Dr. Marc Sylvester; Bioinformatics data analysis was performed by Dr. Andreas Buness and Dr. Farhad Shakeri.

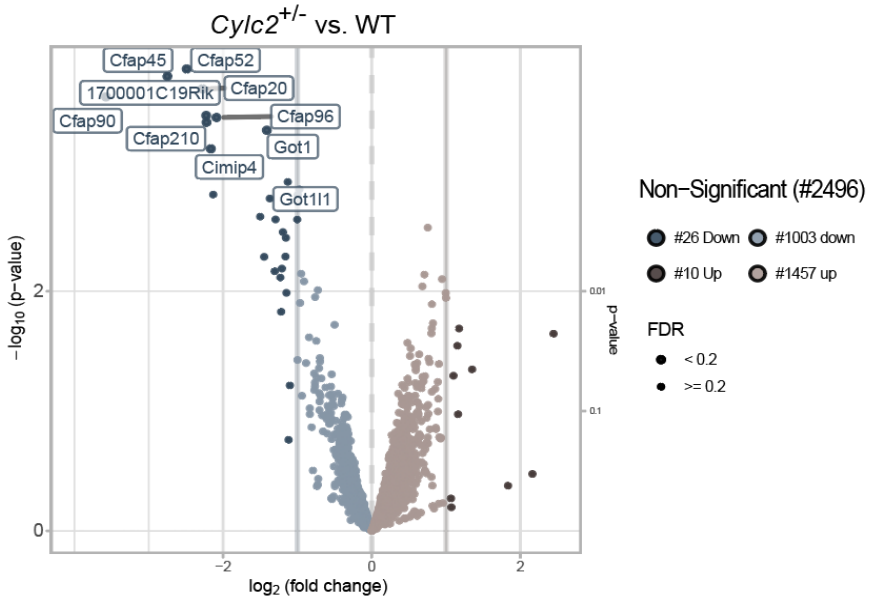

Figure 33: Differentially abundant proteins in *Cylc2*$^{+/-}$ sperm. Volcano plot representing differential protein abundance in cytoskeletal compartment of *Cylc2*$^{+/-}$ sperm compared to WT sperm. Log2 fold change shown in x-axis represents the magnitude of differential abundance. Negative values (blue) represent proteins that are less abundant compared to WT, while positive values (red) show enriched proteins. y-axis shows -log10 p-value that represents the statistical significance of the differential abundance. Gray or pale dots represent proteins that are not significant. The horizontal gray lines represent different FDR (False Discovery Rate) thresholds. Ten most significantly depleted proteins are labelled by name. Measurements were performed by Dr. Marc Sylvester; Bioinformatics data analysis was performed by Dr. Andreas Buness and Dr. Farhad Shakeri.

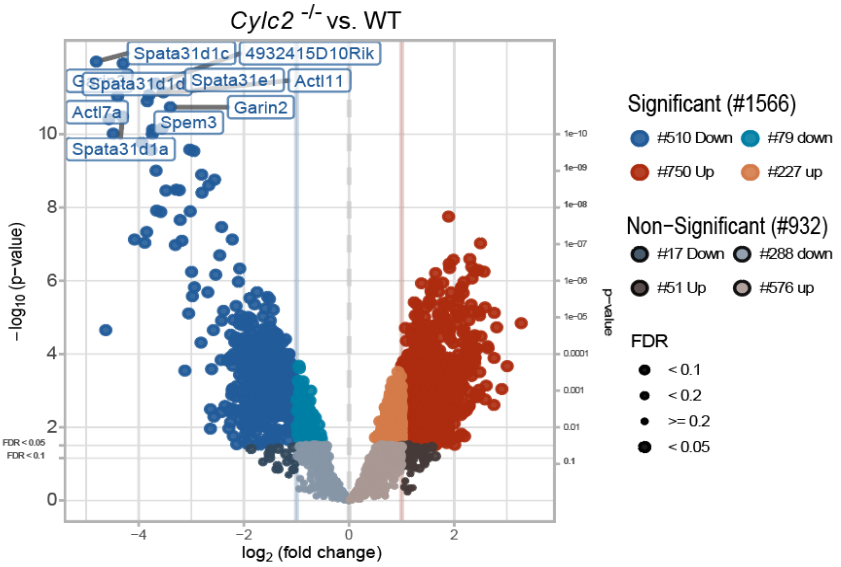

Figure 34: Differentially abundant proteins in *Cylc2*$^{-/-}$ sperm. Volcano plot representing differential protein abundance in cytoskeletal compartment of *Cylc2*$^{-/-}$ sperm compared to WT sperm. Log2 fold change shown in x-axis represents the magnitude of differential abundance. Negative values shown in blue represent proteins that are less abundant in the mutant compared to WT, while positive values depicted in red show enriched proteins. y-axis shows -log10 p-value that represents the statistical significance of the differential abundance. Blue and red dots represent proteins that are significantly depleted or enriched respectively. Gray or pale dots represent proteins that are not significant. Vertical red lines indicate the fold change cutoffs. The horizontal gray lines represent different FDR (False Discovery Rate) thresholds. Ten most significantly depleted proteins are labelled by name. Measurements were performed by Dr. Marc Sylvester; Bioinformatics data analysis was performed by Dr. Andreas Buness and Dr. Farhad Shakeri.

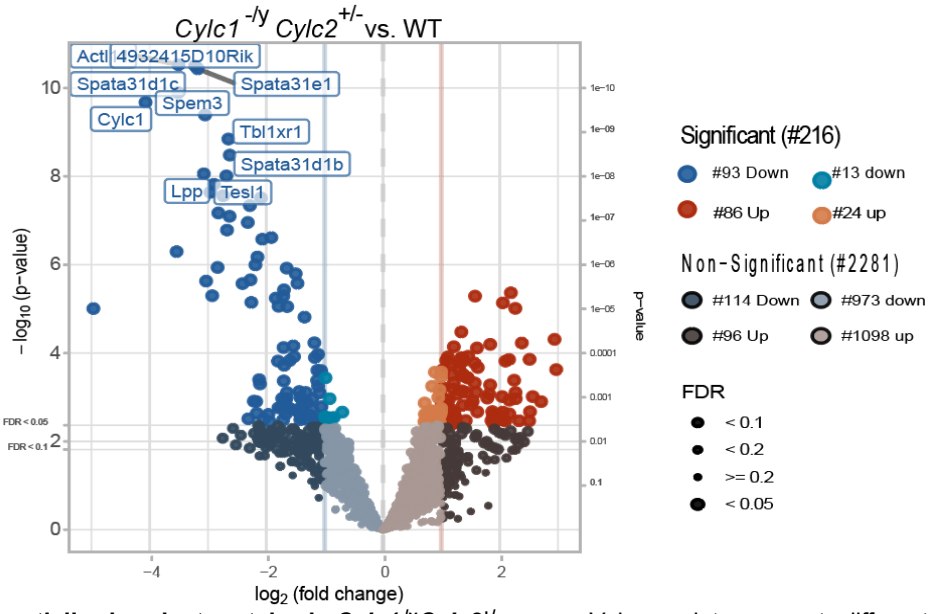

Figure 35: Differentially abundant proteins in *Cylc1*$^{-/y}$*Cylc2*$^{+/-}$ sperm. Volcano plot represents differential protein abundance in cytoskeletal compartment of *Cylc1*$^{-/y}$*Cylc2*$^{+/-}$ sperm compared to WT sperm. Log2 fold change shown in x-axis represents the magnitude of differential abundance. Negative values (blue) represent proteins that are less abundant compared to WT, while positive values (red) show enriched proteins. y-axis shows -log10 p-value that represents the statistical significance of the differential abundance. Blue and red dots represent proteins that are significantly depleted or enriched respectively. Gray or pale dots represent proteins that are not significant. Vertical red lines indicate the fold change cutoffs. The horizontal gray lines represent different FDR (False Discovery Rate) thresholds. Ten most significantly depleted proteins are labelled by name. Measurements were performed by Dr. Marc Sylvester; Bioinformatics data analysis was performed by Dr. Andreas Buness and Dr. Farhad Shakeri.

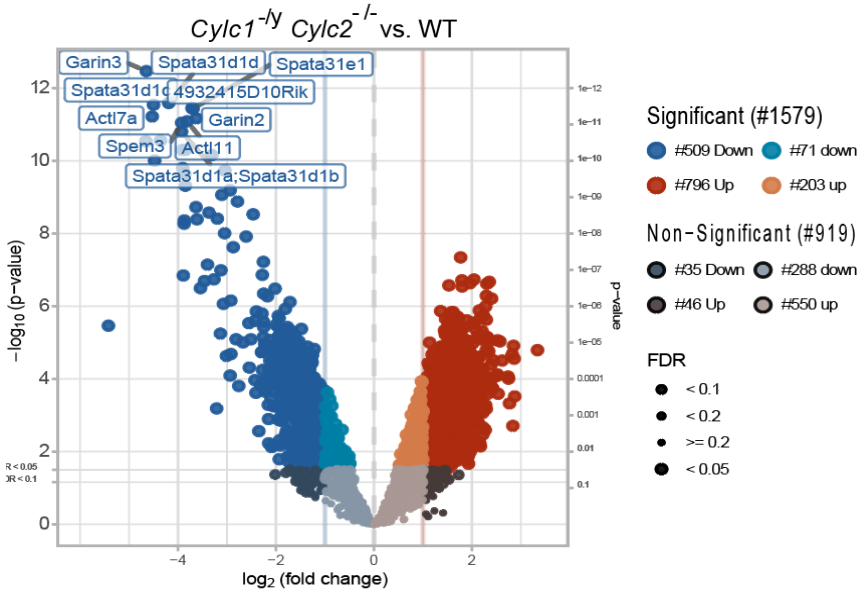

Figure 36: Differentially abundant proteins in *Cylc1*$^{-/y}$*Cylc2*$^{-/-}$ sperm. Volcano plot represents differential protein abundance in cytoskeletal compartment of *Cylc1*$^{-/y}$*Cylc2*$^{-/-}$ sperm compared to WT sperm. Log2 fold change shown in x-axis represents the magnitude of differential abundance. Negative values (blue) represent proteins that are less abundant compared to WT, while positive values (red) show enriched proteins. y-axis shows -log10 p-value that represents the statistical significance of the differential abundance. Blue and red dots represent proteins that are significantly depleted or enriched respectively. Gray or pale dots represent proteins that are not significant. Vertical red lines indicate the fold change cutoffs. The horizontal gray lines represent different FDR (False Discovery Rate) thresholds. Ten most significantly depleted proteins are labelled by name. Measurements were performed by Dr. Marc Sylvester; Bioinformatics data analysis was performed by Dr. Andreas Buness and Dr. Farhad Shakeri.

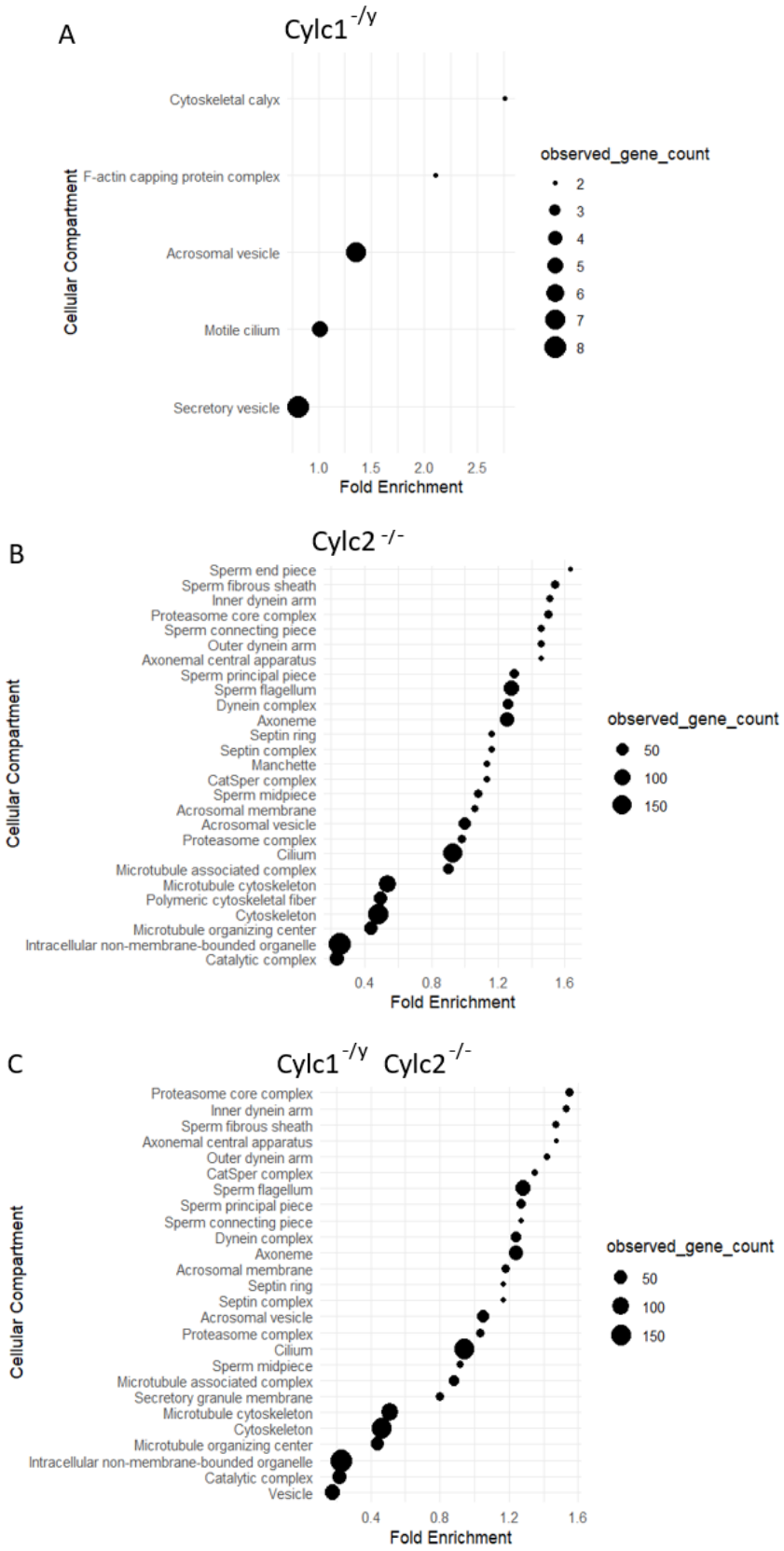

Figure 37: **Enrichment analysis of depleted proteins in Cylc-deficient sperm.** GO term enrichment analysis of significantly depleted proteins in *Cylc1*$^{-/y}$ (**A**), *Cylc2*$^{-/-}$ (**B**) and *Cylc1*$^{-/y}$, *Cylc2*$^{-/-}$ (**C**) sperm cytoskeletal compartments. Y-axis depicts different cellular compartments while x-axis shows Fold Enrichment. The size of the dots represents the observed protein count in each cellular compartment. Measurements were performed by Dr. Marc Sylvester; Bioinformatics data analysis was performed by Dr. Andreas Buness and Dr. Farhad Shakeri.

4.7. Cylicins are required for normal sperm morphology and male fertility in humans

After elucidating the effects of *Cylc*-deficiency on male fertility and sperm development in mice, we next addressed whether infertile men can also display variants in *CYLC1/CYLC2*. Exome sequencing within the MERGE (Male Reproductive Genomics study) cohort was performed by Dr. Ann-Kristin Dicke, Dr. Sophie Koser and Prof. Dr. med. Frank Tüttelmann at the Centre for Reproductive Medicine and Andrology (CeRA) at the University of Münster, Germany. One patient (#M2270) carrying rare (MAF <0.01, gnomAD) missense variants in both *CYLC1* and *CYLC2* was identified (**Figure 38**). This 40-year-old man of German origin and his partner presented at the fertility clinic because of 6 years of unsuccessful attempts to conceive.

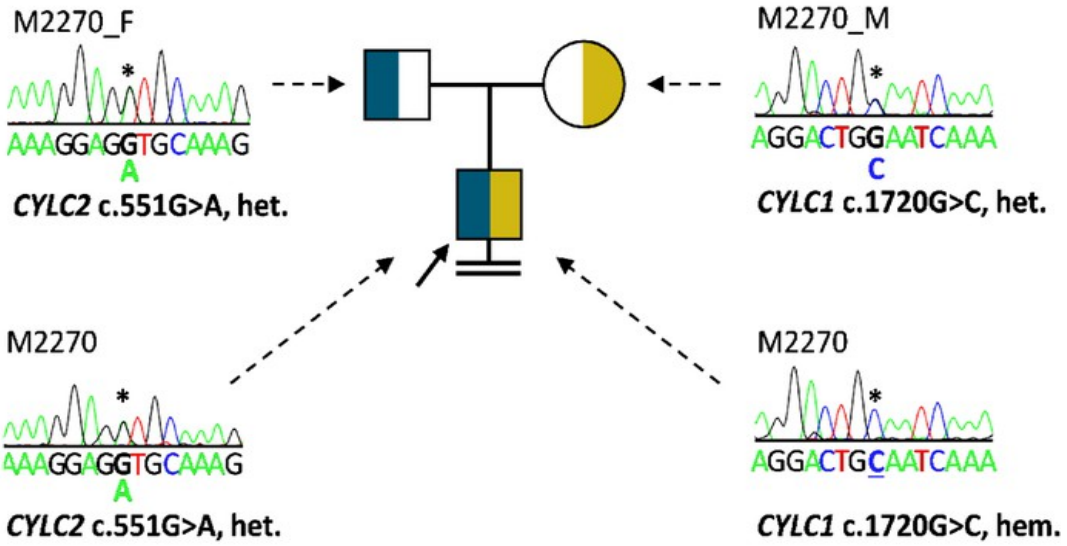

Figure 38: Pedigree of patient #M2270. A heterozygous *CYLC2* variant c.551G>A carried by his father (M2270_F) and the X-linked *CYLC1* variant c.1720G>C in a heterozygous state carried by his mother (M2270_M) are depicted. Asterisks (*) indicate the location of the variants in *CYLC1* and *CYLC2* in the electropherograms. Modified from (Schneider, Kovacevic et al., 2023). Data was obtained by Dr. Sophie Koser and Dr. Ann-Kristin Dicke at the University of Münster.

Pedigree analysis revealed that the patient inherited from his mother the variant c.1720G>C in *CYLC1* leading to an amino acid exchange from glutamic acid to glutamine (p.(Glu574Gln)). Using in silico tools this is predicted to be deleterious (SIFT [Ng & Henikoff, 2003]) or possibly damaging (PolyPhen [Adzhubei et al., 2010]) (**Figure 38**). It maps on exon 4 and affects a region which is predicted to be intolerant to such substitutions (**Figure 39 A**). This variant has a CADD score of 11.91 and it occurs only twice in the gnomAD database (v2.1.1) comprising 141,456 individuals (67,961 XY) being identified once in a hemizygous male and once in a female carrier. Furthermore, #M2270 patient carries the heterozygous variant c.551G>A

in *CYLC2* that is predicted to be tolerated (SIFT) or benign (PolyPhen) with a low CADD score of 0.008. This variant of paternal inheritance is located in exon 5 out of 8 and affects a region in which such variants are likely tolerated (**Figure 38, Figure 39 B**). According to the gnomAD database, this is a rare variant occurring with an allele frequency of 0.0035 in the general population. Interestingly, only three XX individuals are reported to be homozygous for the variant within *CYLC2*. Importantly, no other potentially pathogenic variants in genes associated with sperm morphology were identified by exploring the exome of #M2270.

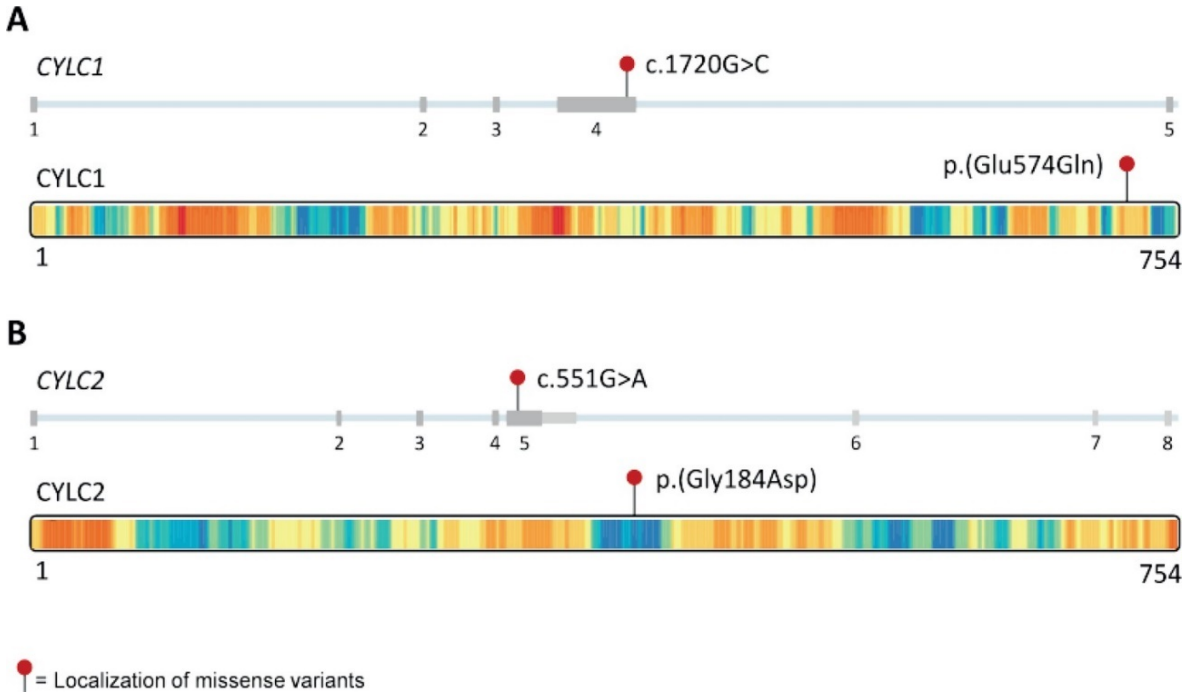

Figure 39: **Localization of the *CYLC1* and *CYLC2* variants identified in #M2270 patient. A**) The *CYLC1* variant affects exon 4 and an intolerant part of the C-terminal region of *CYLC1*. **B)** The missense variant in *CYLC2* detected in #M2270 affects exon 5 and a tolerant part of *CYLC2.* Modified from (Schneider, Kovacevic et al., 2023). Data was obtained by Dr. Sophie Koser and Dr. Ann-Kristin Dicke at the University of Münster.

To investigate the effects of heterozygous variants in *CYLC1* and *CYLC2* genes, semen samples from the patient was collected by Dr. Samuel Young and Prof. Dr. Timo Strünker. First, semen analysis was performed following WHO guidelines (*WHO Laboratory Manual for the Examination and Processing of Human Semen*, 2021) and the results are shown in **Table 2**. The patient had slightly reduced sperm concentration in the semen and a significant reduction of motile spermatozoa (12.5%) was observed. Interestingly, only 2% of the sperm cells showed normal morphology, while 98% of sperm showed head defects (**Table 2**). One ICSI procedure was performed, resulting in 17 fertilized oocytes out of 18 retrieved. This indicates that morphological defects of the sperm can be overcome by ICSI, since the sperm chromatin doesn´t seem to be affected by Cylc-deficiency. However, cryo-single embryo transfer was performed three times in spontaneous cycles, but no pregnancy was achieved.

Table 2: Semen analysis of the patient #M2770

	First visit	Second visit	WHO reference value
Abstinence time (day)	4	5	
Volume (ml)	4.2	5.8	>1.4
Concentration (Mill./ml)	10.5	16.3	>16
Total sperm count (Mill.)	44.1	94.5	>39
Vitality (%)	53	27	>54
Motility:			
a (%)	7	9	a+b > 30
b (%)	5	4	
c (%)	19	8	
d (%)	69	79	
Morphology			
normal (%)	2	2	>4
head defects (%)	98	98	
midpiece defects (%)	63	59	
flagella defects (%)	18	47	

Next, detailed morphological analysis of sperm from semen samples of patient #M2270 compared to sperm from a healthy donor was performed (**Figure 40**). Immunofluorescence staining against CYLC1 revealed its calyx localization in healthy donor's sperm, however, in #M2270, CYLC1 signal could not be detected, indicating the lack of protein (**Figure 40 A**). Bright-field microscopy demonstrated that sperm flagella from #M2270 coiled similarly to flagella of sperm from *Cylc*-deficient mice (**Figure 40 B**). Around 57% of #M2270 sperm displayed abnormal and coiled flagella while in a healthy donor only 6% of flagella were defected (**Figure 40 B, C**). Interestingly, sperm cells counterstained with DAPI revealed that 27% of M2270 flagella carry cytoplasmatic bodies without nuclei, which could be defined as headless spermatozoa (**Figure 40 B** white arrowhead; **Figure 40 C**).

Calyx integrity was investigated by immunofluorescence staining against CCIN (**Figure 41 A**). While spermatozoa of a healthy donor showed a typical, funnel-like calyx structure in the posterior region of PT, in sperm from #M2270, CCIN localized irregularly throughout head and tail. This is comparable to our results in mice and suggests that Cylicins have a role in stabilizing the calyx structure and composition in both mice and human spermatozoa (**Figure 41 A**). Finally, we analyzed the localization of the testis-specific phospholipase C zeta 1

(PLCζ1) which localizes to the postacrosomal region of PT in mammalian sperm (Yoon et al., 2008; Yoon & Fissore, 2007). Immunofluorescence staining of healthy donor's spermatozoa showed a previously described localization of PLCζ1 in the calyx, however, sperm from #M2270 patient showed signal irregularly dispersed through the PT surrounding sperm heads (**Figure 41 B**). These results indicate that *Cylc*-deficiency can lead to severe disruption of PT in human sperm as well. Since PLCζ1 has a role in generating calcium (Ca^{2+}) oscillations that are required for oocyte activation, its disruption leads to fertilization failure and thus male infertility (Yoon & Fissore, 2007).

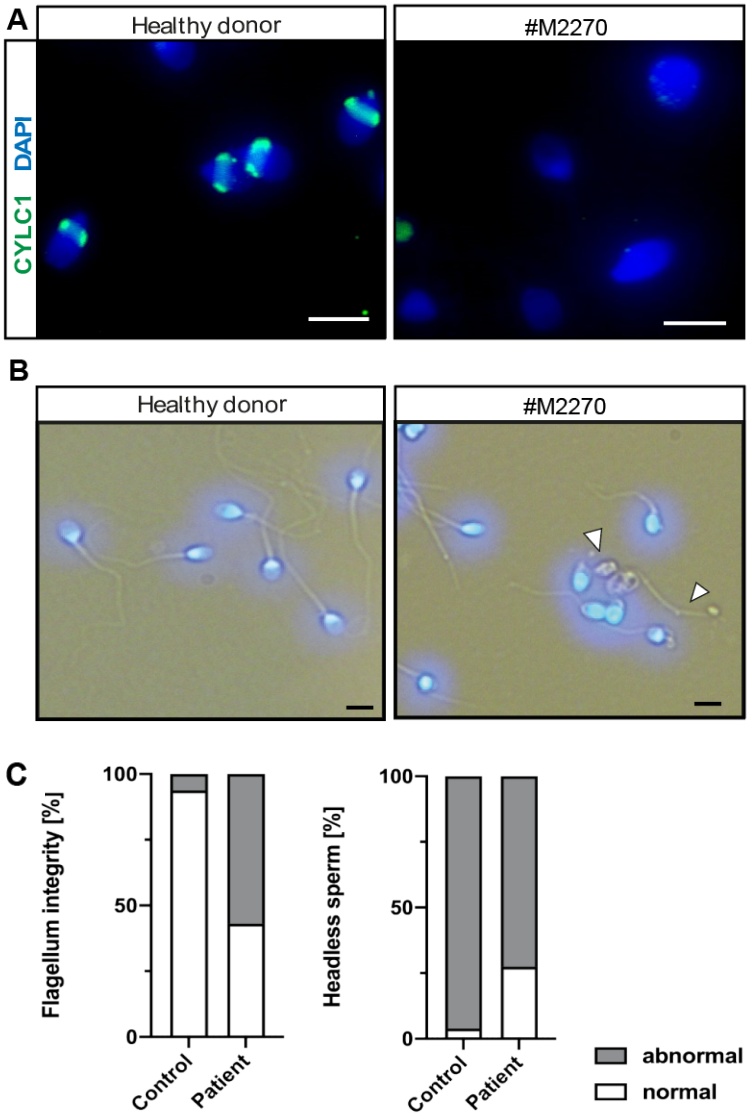

Figure 40: Morphological analysis of human sperm. A) Immunofluorescence staining against CYLC1 in sperm from a healthy donor and patient #M2270. While in donor's sperm CYLC1 localizes in the calyx, in the patient's sperm the signal is absent. Scale bar: 5 µm. **B**) Bright-field microscopy images of the spermatozoa from healthy donor and #M2270 with visible head and tail anomalies such as flagellum coiling. Headless spermatozoa, which carry cytoplasmatic residues without nuclei are depicted with white arrowheads. Nuclei were counterstained with DAPI. Scale bar: 5 µm. **C**) Quantification of flagellum integrity and headless sperm counted in brightfield microscopy images in the semen of patient #M2270 and a healthy donor. Modified from Schneider, Kovacevic et al., 2023. Patient´s semen sample was processed together with Dr. Samuel Young at the University of Münster.

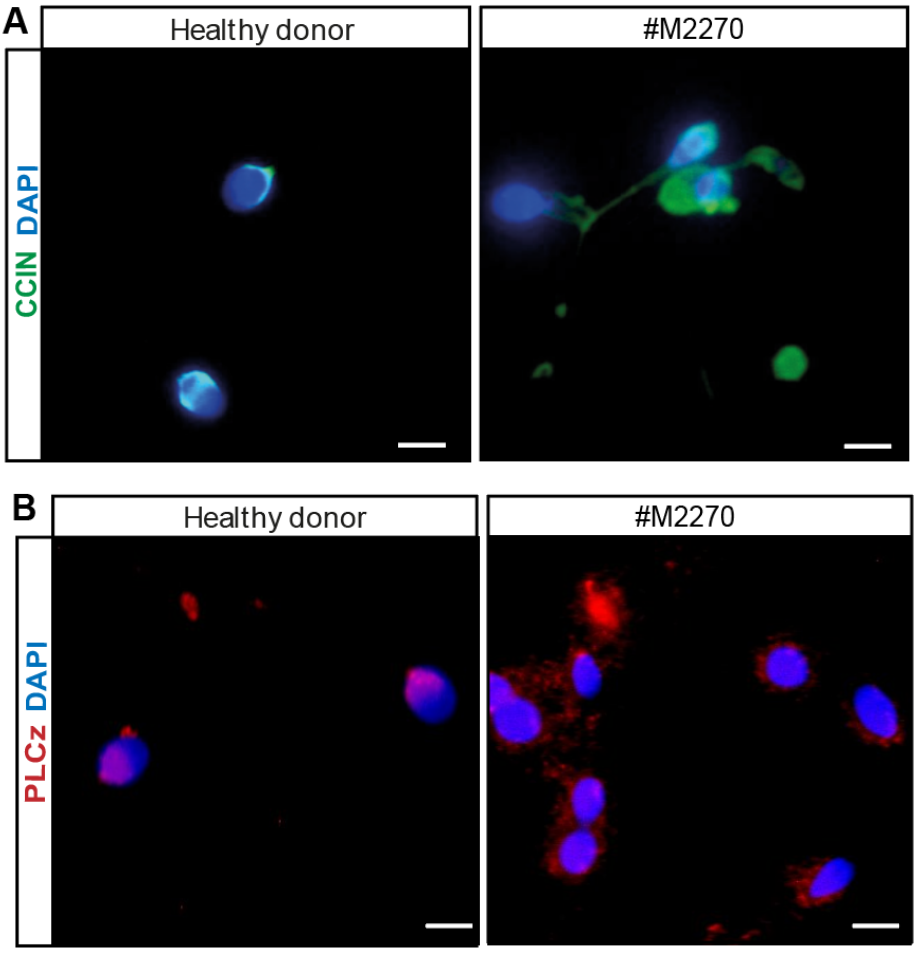

Figure 41: Calyx staining of human sperm. A) Immunofluorescence staining against CCIN in sperm of patient #M2270 and a healthy donor. Nuclei were counterstained with DAPI. Scale bar: 3 µm. **B**) Immunofluorescence staining against PLCζ in sperm of patient #M2270 and a healthy donor. Nuclei were counterstained with DAPI. Scale bar: 3 µm. Modified from Schneider, Kovacevic et al., 2023.

5. RESULTS II

Parts of the results have been published in:

Kovacevic A., Ordziniak E., Umer N., Arevalo L., Hinterlang LD., Ziaeipour S., Suvilla S., Merges GE, Schorle H. (2025) Actin-related protein M1 (ARPM1) required for acrosome biogenesis and sperm function in mice *BioArxiv* DOI: 10.1101/2025.03.27.645694 (currently in review with *Development*).

5.1. CRISPR/Cas9 gene editing results in *Arpm1*-deficient mouse line

Mouse lines deficient for *Arpm1* used in this study were generated by Dr. Naila Umer. Two guide RNAs targeting exon 1 and exon 2 were designed leading to a deletion of 1.7 kb which resulted in a frameshift and a truncated protein (**Figure 42, Figure 43, Supplementary Figure S7**). Two founder animals were generated and mated to C57Bl/6J WT mice to give rise to two lines: Δ2295 and Δ2298 (**Figure 43, Supplementary Figure S7**). Genotyping of animals was performed by PCR, with the WT allele detected as a 272 bp band and knockout alleles from Δ2295 and Δ2298 lines detected at 315 bp and 319 bp respectively (**Figure 44**).

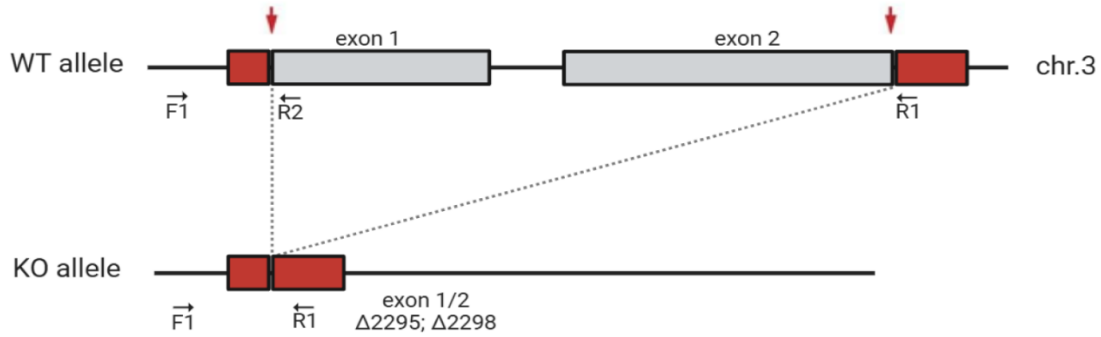

Figure 42: Generation of *Arpm1*-deficient mouse lines. Targeting sites of guide RNAs are depicted by red arrows. Genotyping primer binding sites are depicted by black arrows. The image is created using BioRender.com. *Arpm1*-deficient mouse lines were generated by Dr. Naila Umer who designed the sgRNA. Electroporation was performed by Angela Egert and Andrea Jäger. Modified from Kovacevic et al., 2025, preprint.

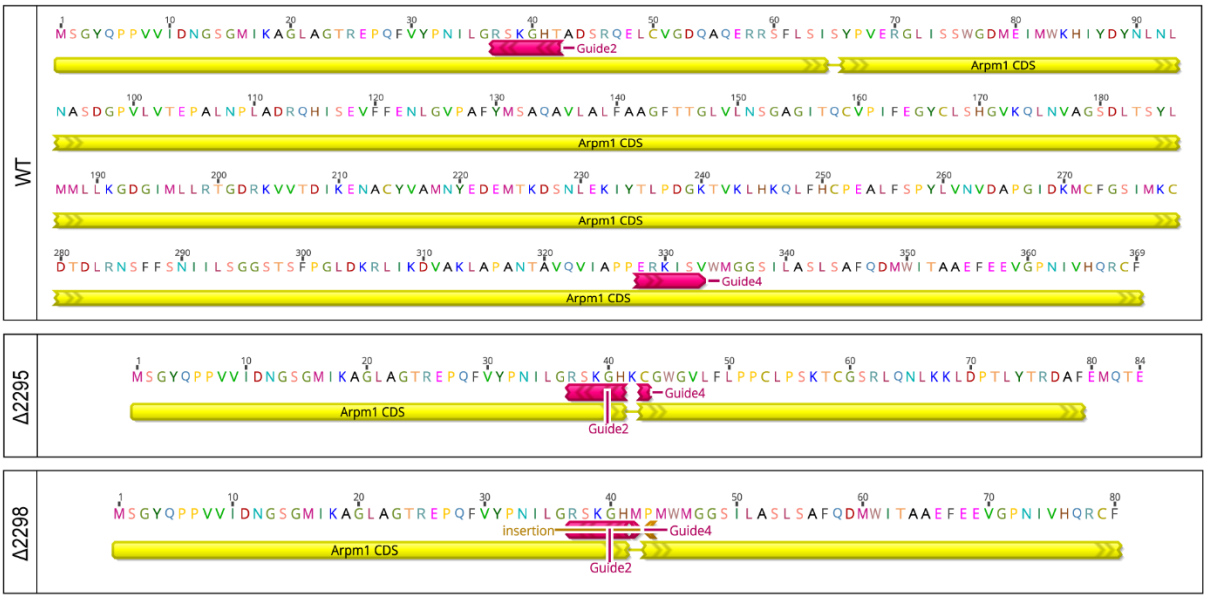

Figure 43: Schematic representation of the amino acid sequence of full length ARPM1 and the truncated proteins in Δ2295 and Δ2298 mouse lines. Binding sites of guide RNA sequences are depicted in red. Sequencing was performed by Dr. Gina E. Merges. Modified from Kovacevic et al., 2025, preprint.

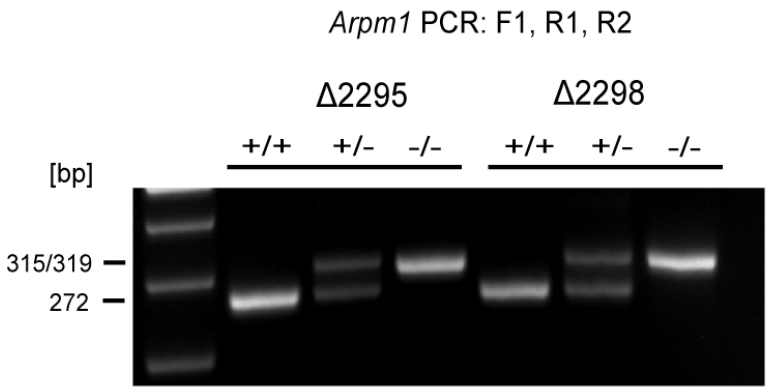

Figure 44: Genotyping PCR of *Arpm1*-deficient mice. Primer F1 and R1 amplify the WT allele (272 bp); Primer F1 and R2 detect the *Arpm1*-knockout allele: 315 bp (Δ2295) and 319 bp (Δ2298) PCR band. Primer sequences used are listed in 2.9.2. Genotyping was performed by Greta Zech. Modified from Kovacevic et al., 2025, preprint.

PCR performed on testicular cDNA revealed the presence of truncated *Arpm1* transcripts in both *Arpm1*$^{-/-}$ lines, while WT transcripts were detected as longer PCR products (**Figure 45 A, D**). PCR using primers designed to bind to the predicted deleted region in *Arpm1* sequence led to a shorter PCR product corresponding to WT sequence, while the truncated transcripts were not amplified (**Figure 45 B, C**). Furthermore, using a polyclonal antibody in testicular protein extracts of WT and *Arpm1*$^{+/-}$ mice a band corresponding to ARPM1 protein was detected at a size of 41 kDa, while the protein was undetectable in *Arpm1*$^{-/-}$ (**Figure 46 A**). IHC staining revealed the presence of ARPM1 in different populations of germ cells in WT and *Arpm1*$^{+/-}$ testicular sections. In *Arpm1*$^{-/-}$ testicular tissue ARPM1 staining was absent (**Figure 46 A**). Immunofluorescence staining of WT and *Arpm1*$^{+/-}$ epididymal sperm revealed that ARPM1 localizes mainly in the calyx region of the perinuclear theca, while ARPM1 signal was absent from *Arpm1*$^{-/-}$ epididymal sperm (**Figure 46 B**).

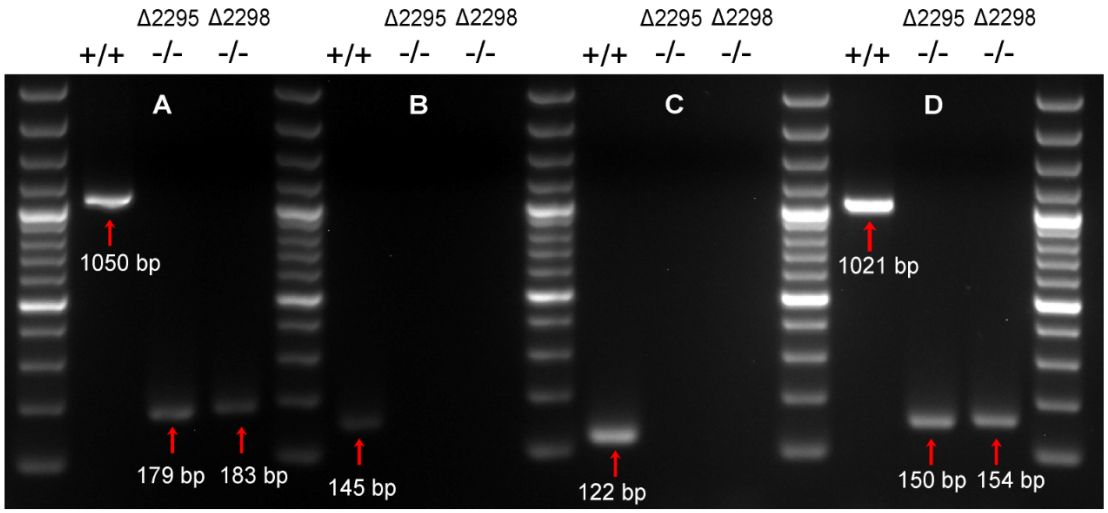

Figure 45: Validation of *Arpm1*-deficient mouse lines. PCR on testicular cDNA showing truncated Arpm1 transcripts in knockout animals from Δ2295 and Δ2298 lines (smaller PCR bands in A and D), compared to the longer WT transcripts. Primer combinations and product sizes are listed in Table 1. Primer sequences used for the PCR on cDNA are listed in 2.9.4. PCR was performed by Greta Zech. Modified from Kovacevic et al., 2025, preprint.

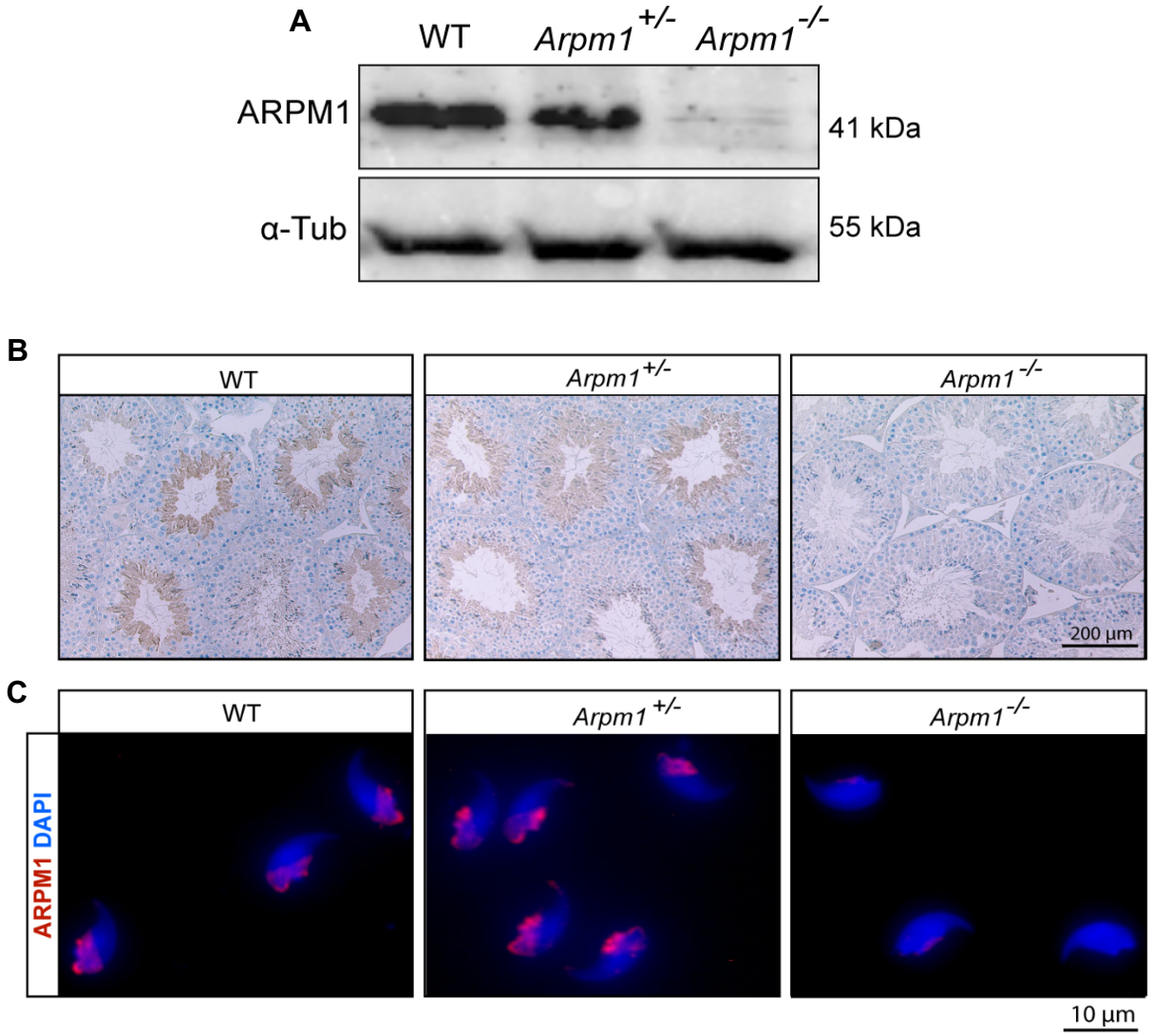

Figure 46: **Analysis of ARPM1 protein levels. A**) WB on testicular protein lysates from WT, *Arpm1*$^{+/-}$ and *Arpm1*$^{-/-}$ mice. Band corresponding to ARPM1 is detected at 41 kDa in WT and *Arpm1*$^{+/-}$ samples and it was absent *Arpm1*$^{-/-}$. α-Tubulin was used as load control (55 kDa). **B**) IHC staining of ARPM1 on testicular tissue sections from WT, *Arpm1*$^{+/-}$ and *Arpm1*$^{-/-}$ male mice. Scale bar: 200 µm. **C**) Immunofluorescent staining of ARPM1 (red) on WT, *Arpm1*$^{+/-}$ and *Arpm1*$^{-/-}$ epididymal sperm cells. Nuclei were counterstained with DAPI (blue). Scale bar: 10 µm. Modified from Kovacevic et al., 2025, preprint.

5.2. ARPM1 is required for male fertility in mice

5.2.1. Loss of ARPM1 leads to male subfertility in mice

To investigate the effect of *Arpm1*-deficiency on male fertility, WT, *Arpm1*$^{+/-}$ and *Arpm1*$^{-/-}$ male mice were mated with C57Bl/6J WT females. Pregnancy rates obtained by *Arpm1*$^{+/-}$ and *Arpm1*$^{-/-}$ male mice were comparable to the ones obtained when mating with WT males (**Figure 47 A**). WT and *Arpm1*$^{+/-}$ male mice produced an average litter size of 7.5, while *Arpm1*$^{-/-}$ male mice were subfertile, with an average litter size of 1.5 (**Figure 47 B**).

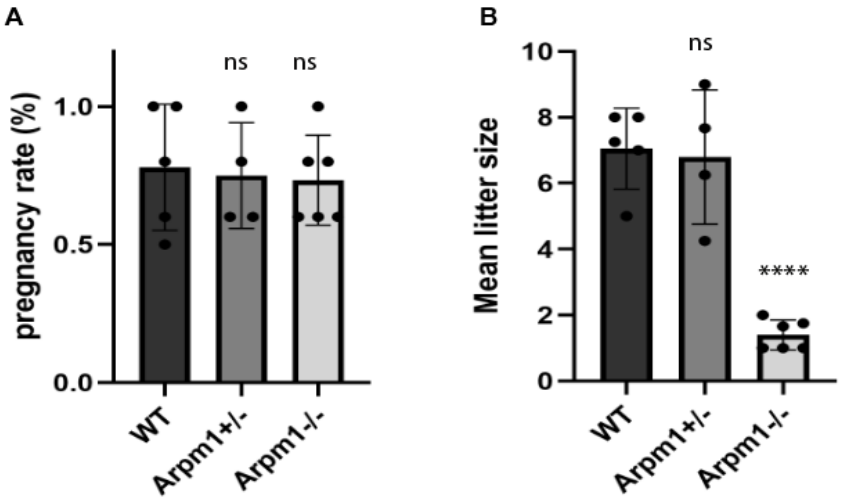

Figure 47: **Fertility analysis of Arpm1-deficient male mice. A**) pregnancy rates (%) and **B**) mean litter sizes of WT, *Arpm1*$^{+/-}$ and *Arpm1*$^{-/-}$ male mice. Columns represent mean values ± s.d. Black dots represent mean values obtained for each male animal included in the analysis. Fertility analysis was performed by Andrea Jäger and Dr. Naila Umer. Modified from Kovacevic et al., 2025, preprint.

Testis weight was slightly reduced in *Arpm1*$^{-/-}$ male mice compared to WT, while the overall aspect of the testis was not affected by *Arpm1*-deficiency (**Figure 48 A, B**). Histological analysis of Papanicolaou (PAS) stained testis tissue sections of all three genotypes revealed that *Arpm1*-deficiency did not cause alterations of seminiferous epithelium. All germ and somatic cell populations of spermatogenesis were detectable in *Arpm1*$^{+/-}$ and *Arpm1*$^{-/-}$ testicular tissue sections (**Figure 49**). Taken together, these results suggest that *Arpm1*-deficiency does not cause defects of the testicular tissue composition, and it does not affect spermatogenesis in mice.

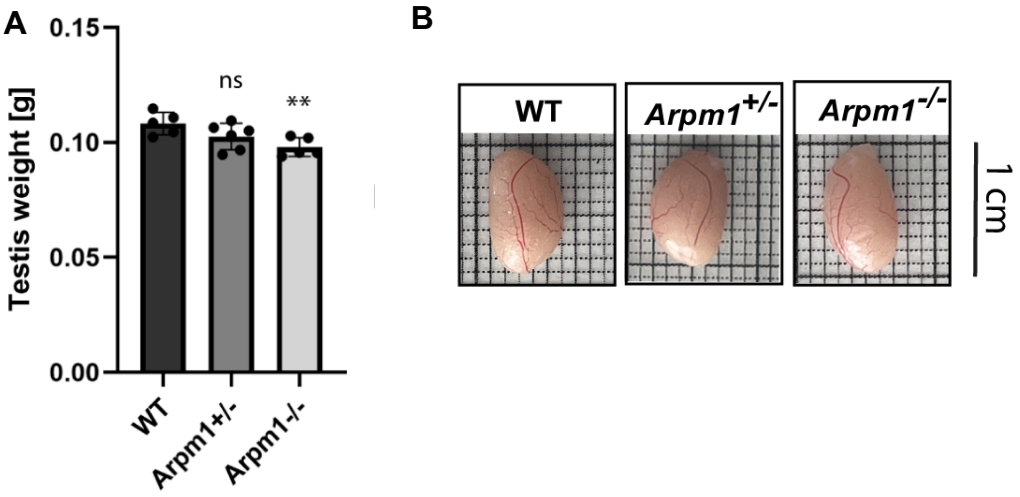

Figure 48: Macroscopic analysis of testes from *Arpm1*-deficient mice. A) Average testis weight (mg) of adult WT, *Arpm1*$^{+/-}$ and *Arpm1*$^{-/-}$ male mice. Columns represent mean values ± s.d. Black dots represent mean values obtained for each male animal included in the analysis. **B**) Comparable photographs of the testes of WT, *Arpm1*$^{+/-}$ and *Arpm1*$^{-/-}$ mice. Scale bar: 1 cm. Modified from Kovacevic et al., 2025, preprint.

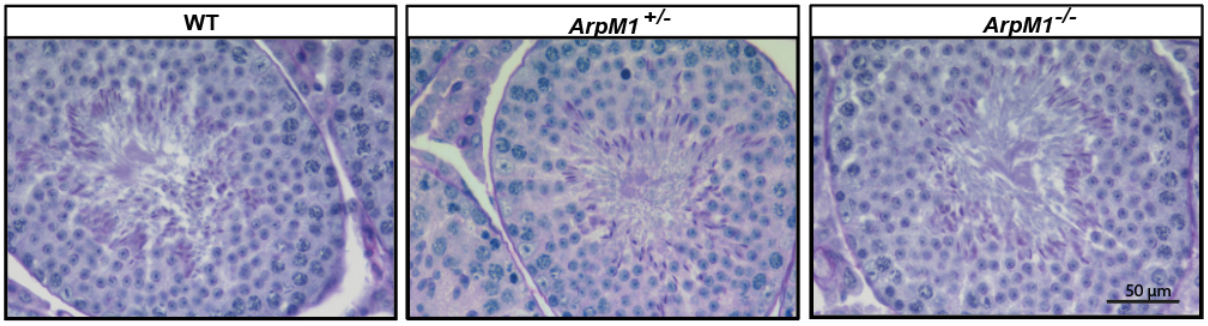

Figure 49: **Testicular tissue architecture of *Arpm1*-deficient male mice.** PAS staining of testis tissue sections from WT, *Arpm1*$^{+/-}$ and *Arpm1*$^{-/-}$ mice depicting all cell populations of the testis, at stage V-VII. Scale bar: 50 µm. Modified from Kovacevic et al., 2025, preprint.

Epididymal sperm count revealed no significant alterations in *Arpm1*$^{+/-}$ mice (4 x 10^7) compared to WT (5 x 10^7). However, in *Arpm1*$^{-/-}$ male mice, epididymal sperm count was reduced to 3 x 10^7 (**Figure 50 A**). Furthermore, Eosin-Nigrosine staining of epididymal sperm, revealed that in *Arpm1*$^{-/-}$ mice only 40% of sperm are viable with intact membranes, compared to 80% in WT and *Arpm1*$^{+/-}$ (**Figure 50 B**). This, taken together with testis tissue histological analysis, suggests that reduced sperm count is likely caused by cell death of non-viable sperm, rather than the spermiogenesis arrest. Interestingly, motility of the epididymal sperm activated in THY medium was not altered in neither *Arpm1*$^{+/-}$ nor *Arpm1*$^{-/-}$ male mice, suggesting that loss of ARPM1 does not affect the swimming of the sperm (**Figure 50 C**).

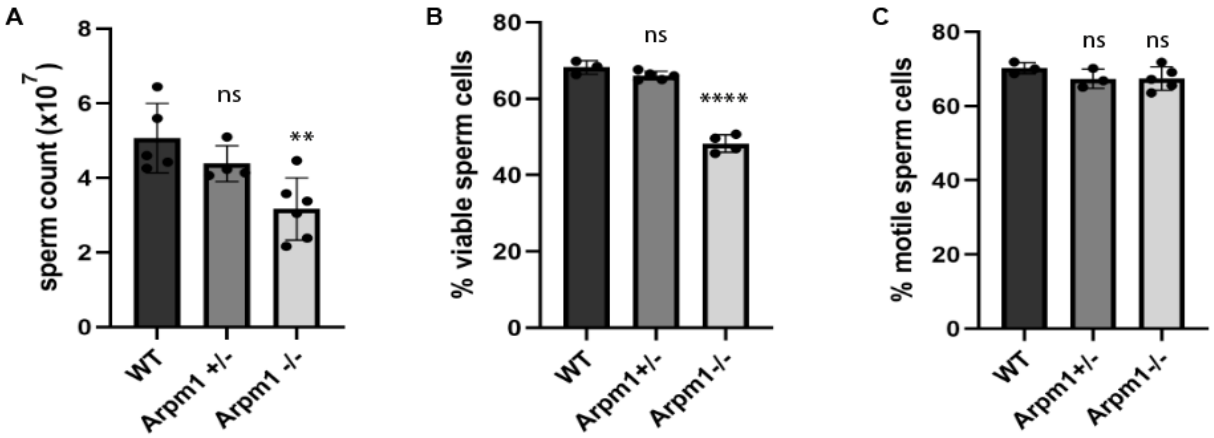

Figure 50: Analysis of epididymal sperm from *Arpm1*-deficient mice. A) Epididymal sperm count (×10^7) of WT, *Arpm1*$^{+/-}$ and *Arpm1*$^{-/-}$ male mice. Columns represent mean values ± s.d. Black dots represent mean values obtained for each animal analysed. **B**) Quantification of viable sperm from WT, *Arpm1*$^{+/-}$ and *Arpm1*$^{-/-}$ male mice investigated by eosin-nigrosine staining. Columns represent mean values ± s.d. Black dots represent mean values obtained for each animal analysed. **C**) Quantification of motile epididymal sperm cells from WT, *Arpm1*$^{+/-}$ and *Arpm1*$^{-/-}$ mice upon activation in TYH medium. Columns represent mean values ± s.d. Black dots represent mean values obtained for each animal analysed. Data was obtained together with Dr. Naila Umer and Sara Suvilla (Master´s thesis 2023). Modified from Kovacevic et al., 2025, preprint.

Morphological analysis of epididymal sperm stained with mitochondria marker MITO-red revealed no alterations of the flagellum in *Arpm1*$^{+/-}$ nor *Arpm1*$^{-/-}$ mice, with regular morphology of the midpiece (**Figure 51**). Next, nuclear morphology of DAPI stained epididymal sperm was assessed using Nuclear Morphology plug-in for ImageJ. Sperm nuclear morphology was not altered in *Arpm1*$^{+/-}$ mice when compared to WT (**Figure 52 A**). Even though *Arpm1*$^{-/-}$ sperm heads displayed proper morphology when observed at the bright field microscope, a slight reduction of their area was depicted by the software, indicating that *Arpm1*-deficiency leads to smaller sperm heads (**Figure 52 B, C**). Chromomycin A3 (CMA3) staining was performed to assess sperm chromatin integrity and protamine deficiency which could be a potential cause of smaller sperm nuclei. Interestingly, no alterations in chromatin compaction in *Arpm1*$^{+/-}$ nor *Arpm1*$^{-/-}$ epididymal sperm were observed, suggesting that, despite the slightly smaller sperm heads in *Arpm1*$^{-/-}$ mice, the loss of ARPM1 does not affect the DNA compaction (**Figure 53 A, B**). This indicates that ARPM1 likely acts as a cytoskeletal regulator outside of the sperm nucleus and is not required for histone to protamine exchange during sperm chromatin condensation.

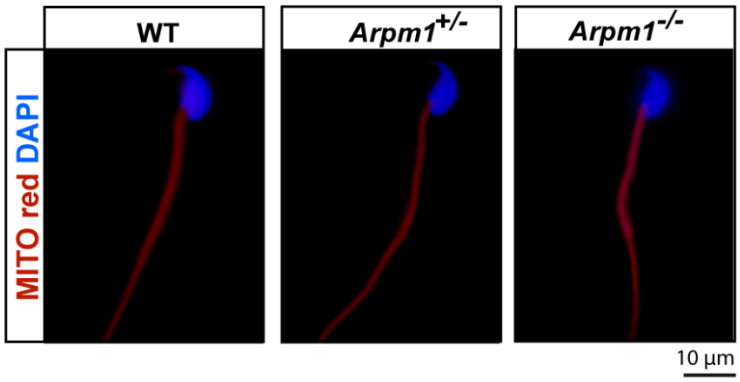

Figure 51: **Flagellum of *Arpm1*-deficient sperm**. MITO-red staining of epididymal sperm from WT, *Arpm1*$^{+/-}$ and *Arpm1*$^{-/-}$ mice showing intact flagella in all genotypes. Nuclei were counterstained with DAPI. Scale bar: 10 µm. Modified from Kovacevic et al., 2025, preprint.

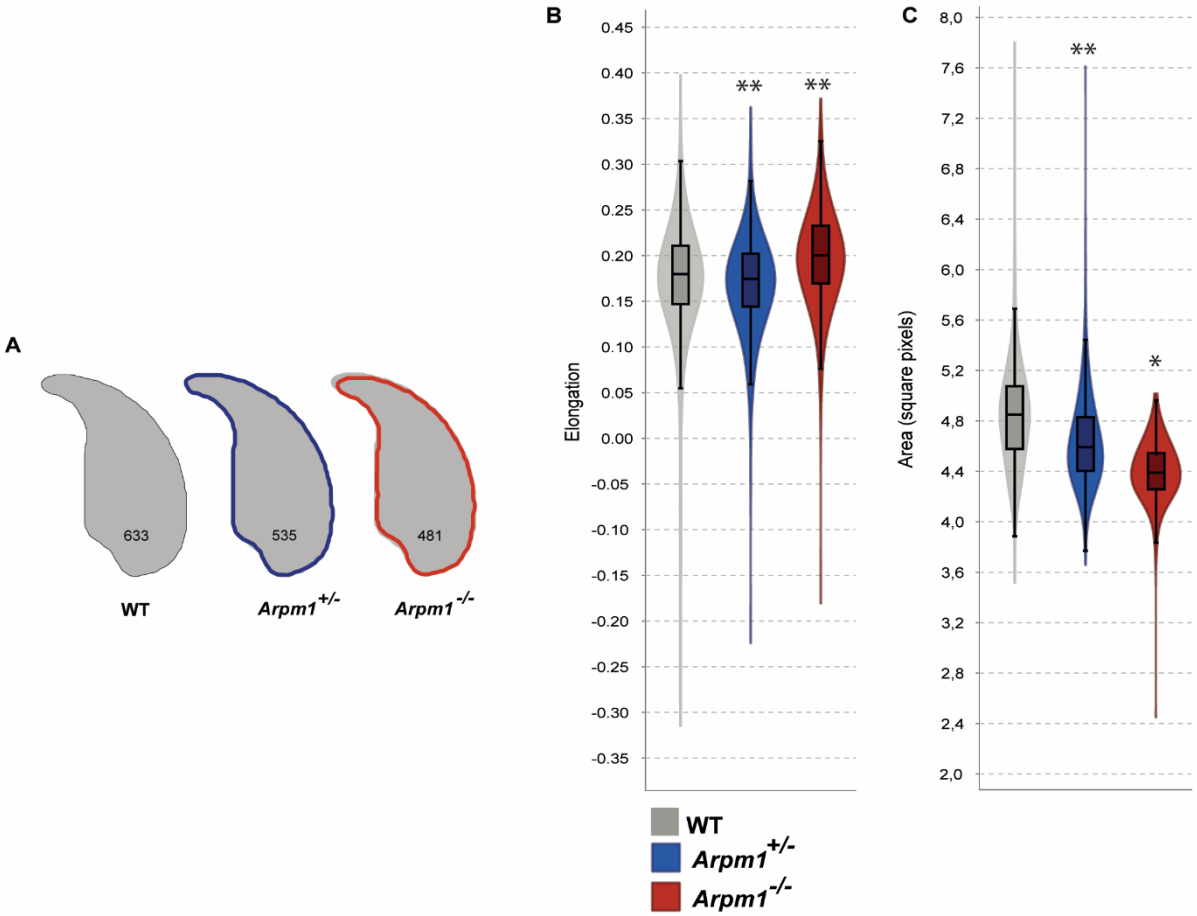

Figure 52: Nuclear morphology of *Arpm1*-deficient sperm. A) Graphical representation of nuclear morphology analysis of *Arpm1*$^{+/-}$ (blue outline) and *Arpm1*$^{-/-}$ (red outline) sperm heads compared to WT (gray). The number of cells analyzed per genotype is shown. **B**) Elongation and **C**) area of nuclei from WT, *Arpm1*$^{+/-}$ and *Arpm1*$^{-/-}$ sperm cells. The minimum detection area was set to 1.000 pixels, while the maximum detection area was 7.000 pixels. (*P<0.05, **P<0.005, ***P<0.001, ****P<0.0001). Modified from Kovacevic et al., 2025, preprint.

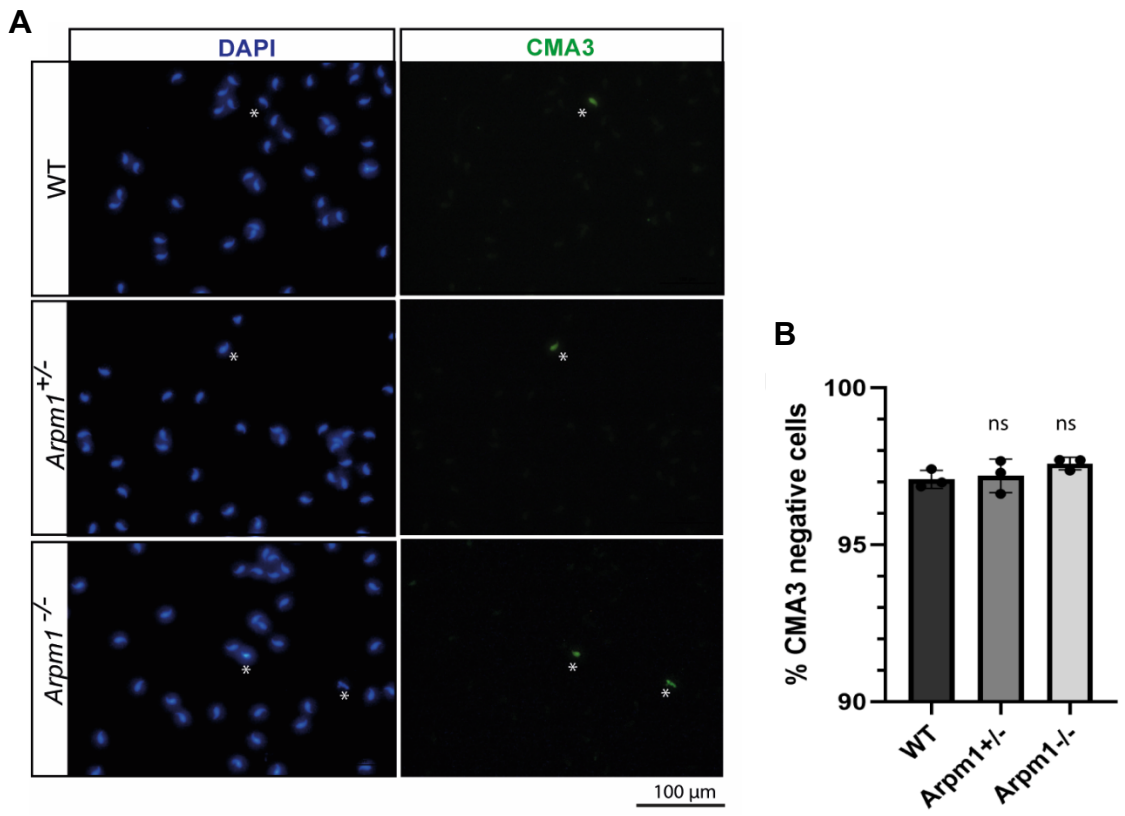

Figure 53: Chromatin compaction in *Arpm1*-deficient sperm. A) CMA3 stained epididymal sperm from WT, *Arpm1*$^{+/-}$ and *Arpm1*$^{-/-}$ mice. CMA3 positive nuclei are depicted with white asterisks. Nuclei were counterstained with DAPI (left panel). Scale bar: 100 µm. **B**) Quantification of CMA3 negative sperm cells from WT, *Arpm1*$^{+/-}$ and *Arpm1*$^{-/-}$ mice. Black dots represent mean values obtained for each animal analysed. n=3. A minimum of 100 sperm cells per animal were analyzed. Modified from Kovacevic et al., 2025, preprint.

5.2.2. Loss of ARPM1 causes lower fertilization rate in-vitro

To investigate whether reduced litter size of *Arpm1*$^{-/-}$ male mice affected fertilization or early embryo development, in vitro fertilization (IVF) experiments were performed. After 24h of incubation in IVF medium, WT sperm fertilized 90% of oocytes out of which 60% reached blastocyst stage (**Figure 54 A, B, C**). Interestingly, when incubated with *Arpm1*$^{-/-}$ sperm, only 35% of oocytes were fertilized and reached the two-cell stage clearly indicating that the *Arpm1*-deficincy causes reduction of fertilization efficiency in male mice (**Figure 54 A, B, C**). Of note, blastocyst rate in relation to the two cell stage embryos remained comparable (65%) in both WT and *Arpm1*$^{-/-}$ mice, suggesting that preimplantation embryo development is not affected by the loss of ARPM1. Sperm cells incubated in IVF medium showed normal swimming behavior and managed to find and bind to oocytes, however, they remained attached to the surface of the oocyte, failing to fertilize it. This demonstrates that loss of ARPM1 interferes with the fertilization ability of the sperm.

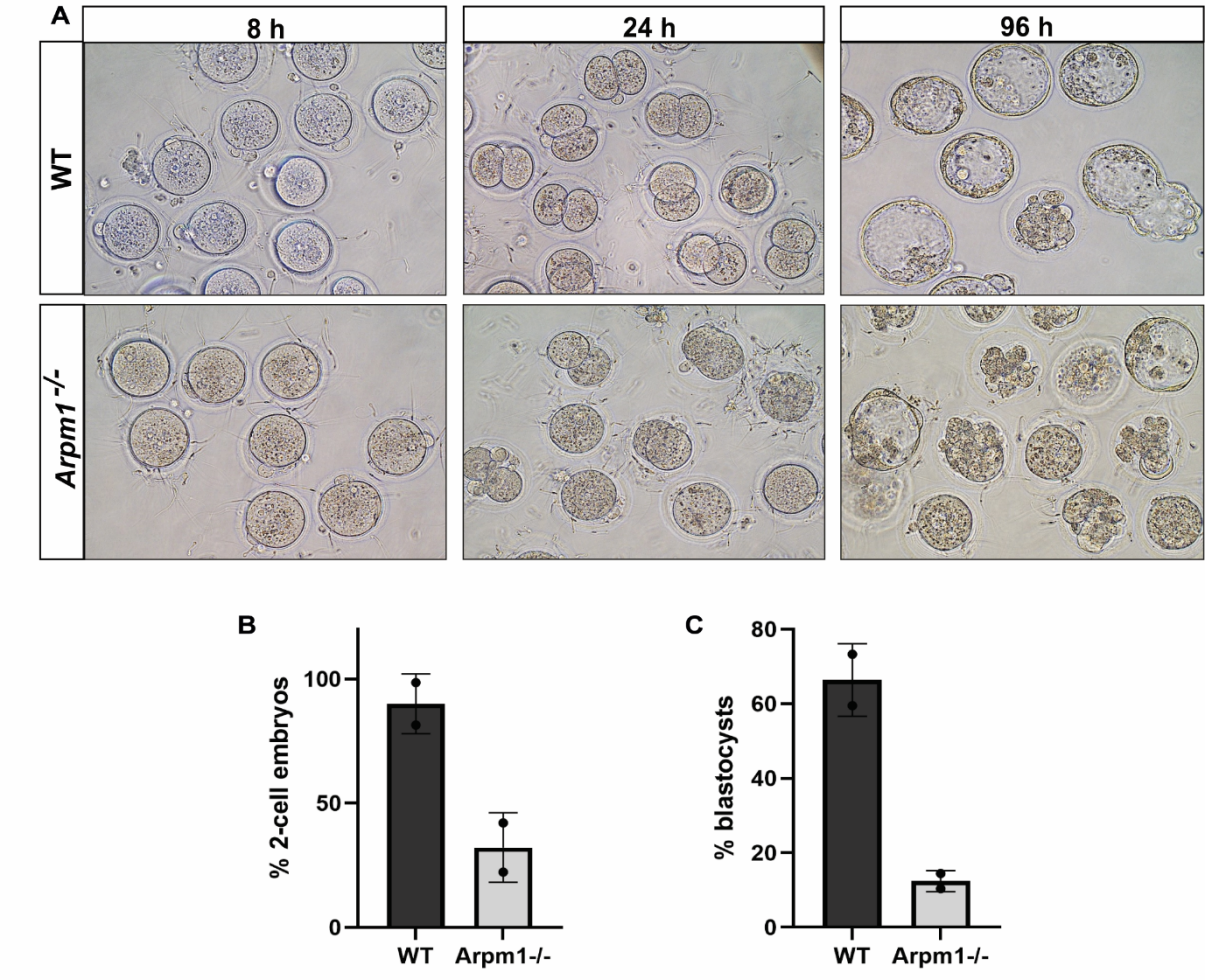

Figure 54: IVF analysis of *Arpm1*-deficient sperm. A) Photographs of embryos at 8h, 24h and 96h after in vitro fertilization of WT oocytes with WT and *Arpm1*$^{-/-}$ sperm. The percentage of two-cell embryos **B**) observed after 24h and **C**) percentage of blastocysts after 96h are shown. Columns represent mean values ± s.d. n=2. IVF analysis was performed together with Angela Egert. Modified from Kovacevic et al., 2025, preprint.

5.3. Loss of ARPM1 causes acrosome defects in mice

5.3.1. *Arpm1*$^{-/-}$ sperm cells have abnormal acrosomes

PNA-FITC staining of epididymal sperm in *Arpm1*$^{-/-}$ mice revealed that acrosomes appeared vacuolized, shortened or not attached to the nuclear membrane. Sperm cells presenting PNA signal only at the very tip of the head, as well as those with only posterior part of the acrosome present were observed (**Figure 55 A**). In WT and *Arpm1*$^{+/-}$ male mice, acrosome defects are found in around 20% of sperm cells while approximately 50% of *Arpm1*$^{-/-}$ sperm displayed acrosomal abnormalities (**Figure 55 B**). Transmission electron microscopy allowed more detailed observation of epididymal sperm. We revealed that in the equatorial region of the *Arpm1*$^{-/-}$ sperm head most acrosomes were partially detached from nuclear envelope (**Figure 56**). On the apical pole of *Arpm1*$^{-/-}$ sperm, acrosomes appear drastically shortened or vacuolized, despite localizing properly on the apical portion of the sperm head. The anchoring of the acrosome at the equatorial region appeared defective (**Figure 56**). Acrosomes from *Arpm1*$^{+/-}$ epididymal sperm were intact and comparable to the WT (**Figure 56**).

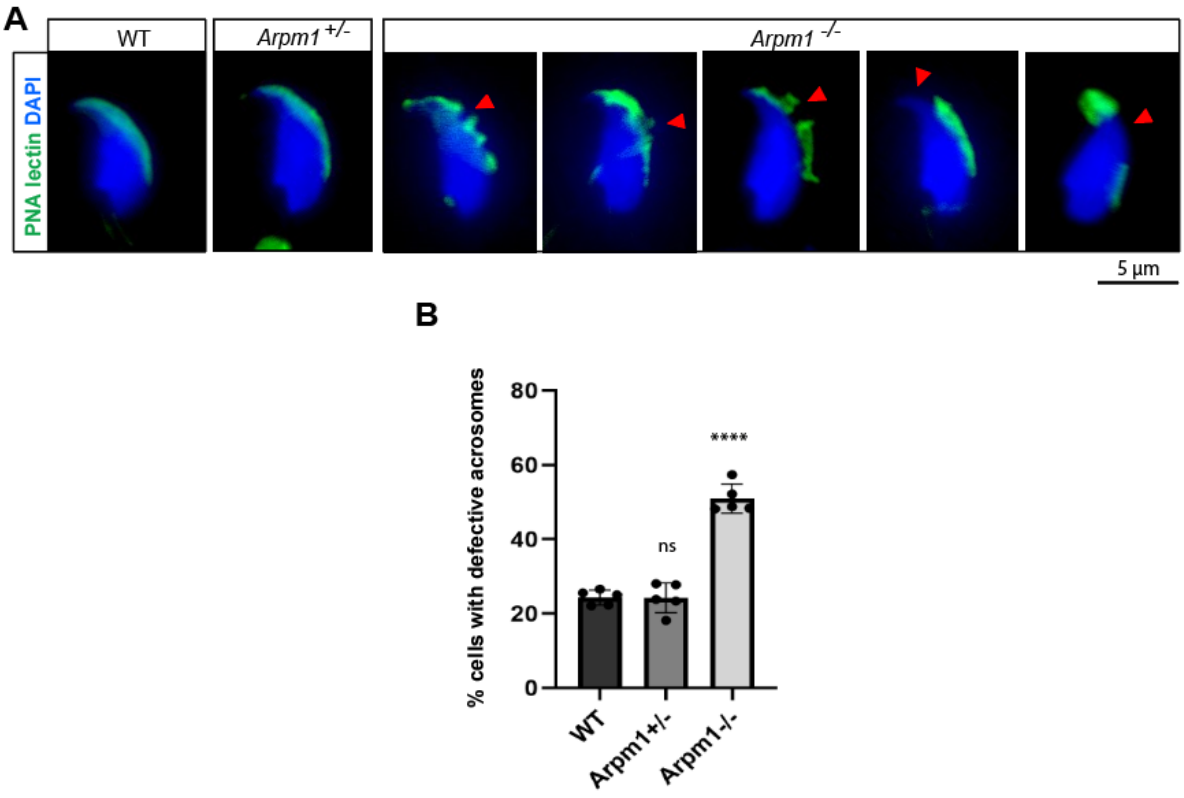

Figure 55: Acrosome of *Arpm1*-deficient epididymal sperm. A) Immunofluorescence staining of WT, *Arpm1*$^{+/-}$ and *Arpm1*$^{-/-}$ epididymal sperm with PNA-lectin (green). Nuclei were counterstained with DAPI. Different acrosome defects in *Arpm1*$^{-/-}$ sperm are depicted with red arrowheads. Scale bar: 5 µm **B**) Quantification of acrosome abnormalities observed in PNA-lectin-stained sperm of WT, *Arpm1*$^{+/-}$ and *Arpm1*$^{-/-}$ mice. Columns represent mean values ± s.d. n=5 Data was obtained together with Eva Ordziniak during her Master´s thesis (2024). Modified from Kovacevic et al., 2025, preprint.

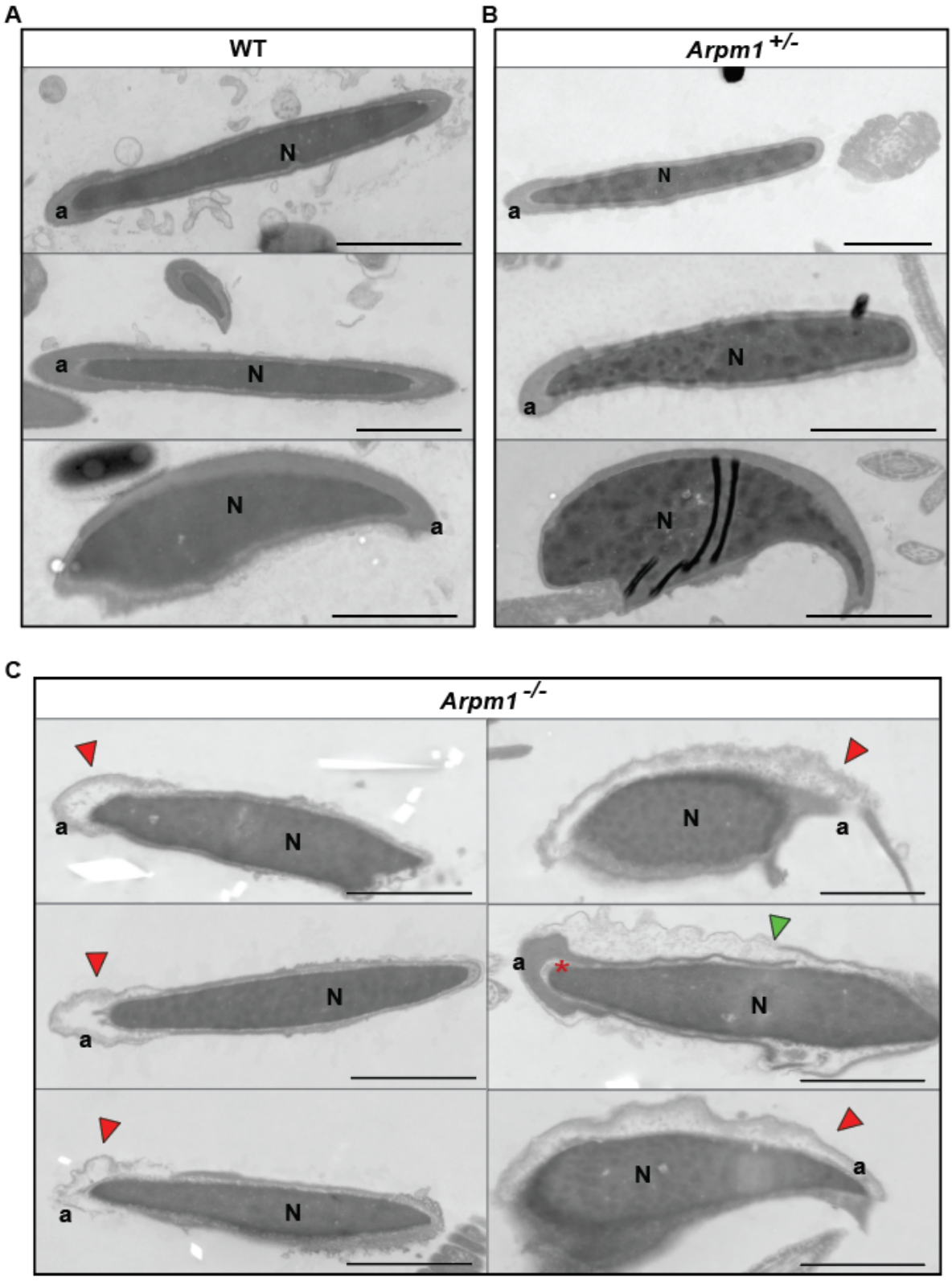

Figure 56: Acrosomes and nuclei of *Arpm1*-deficient sperm visualized by TEM. TEM micrographs of **A**) WT, **B**) *Arpm1*$^{+/-}$ and **C**) *Arpm1*$^{-/-}$ epididymal sperm. Defective acrosomes in *Arpm1*$^{-/-}$ sperm are depicted with red arrowheads. Breakage of the PT at the equatorial ring is shown by a green arrowhead. Red asterisk depicts acrosome detached from the nuclear envelope. N: nucleus; a: acrosome Scale bar: 1 µm. Modified from Kovacevic et al., 2025, preprint.

5.3.2. ARPM1 deficient spermatids have defective acrosome development

PNA-lectin staining was performed on testicular tissue sections from WT, *Arpm1*$^{+/-}$ and *Arpm1*$^{-/-}$ to analyze acrosome development during spermiogenesis. In all three genotypes, regularly formed proacrosomal granules were detectable on poles of round spermatids in Golgi phase (**Figure 57, upper panel**). In spermatids from WT and *Arpm1*$^{+/-}$ mice, acrosome development proceeds with Cap phase in which acrosomal vesicles form smooth cap-like structures on the surface of the nucleus. In *Arpm1*$^{-/-}$ spermatids, the acrosomal vesicles in Cap phase appear disrupted, vacuolized or detached from the nuclear surface (**Figure 57, middle panel; Figure 58 A**). During the Acrosome phase, in elongating spermatids in WT and *Arpm1*$^{+/-}$ testis the acrosomal granules elongate along with the spermatid and gradually flatten to cover the apical portion of the cell, forming an arrow shaped structure. In *Arpm1*$^{-/-}$ testis sections the acrosomes elongate along with the spermatids, however, they appear vacuolized (**Figure 57, lower panel; Figure 58 B,** red arrowhead) and their detachment from the nucleus can be observed (**Figure 57, lower panel; Figure 58 B,** magenta arrowhead).

TEM micrographs of testicular tissue allowed the study of the acrosome in more detail. In round spermatids at step 4-5 of all genotypes, Golgi phase spermatids show regular acrosomal vesicles (**Figure 59 A**). During the Cap phase, Golgi apparatus in *Arpm1*$^{-/-}$ spermatids appeared detached and displaced from the nuclear envelope, while in WT and *Arpm1*$^{+/-}$ spermatids, Golgi adheres to the nuclear surface (**Figure 59 B**). Large vesicles between growing acrosomes and the Golgi apparatus were present in *Arpm1*$^{-/-}$ spermatids, while in WT and *Arpm1*$^{+/-}$ mice, Golgi structure appeared regular, with membranes tightly compacted (**Figure 59 B,** red asterisks). In step 8 elongating spermatids of all three genotypes proper nuclear compaction and manchette formation were observed, however, in *Arpm1*$^{-/-}$ spermatids, an increased gap between manchette and developing acrosome can be observed at the equatorial ring (**Figure 59 C**).

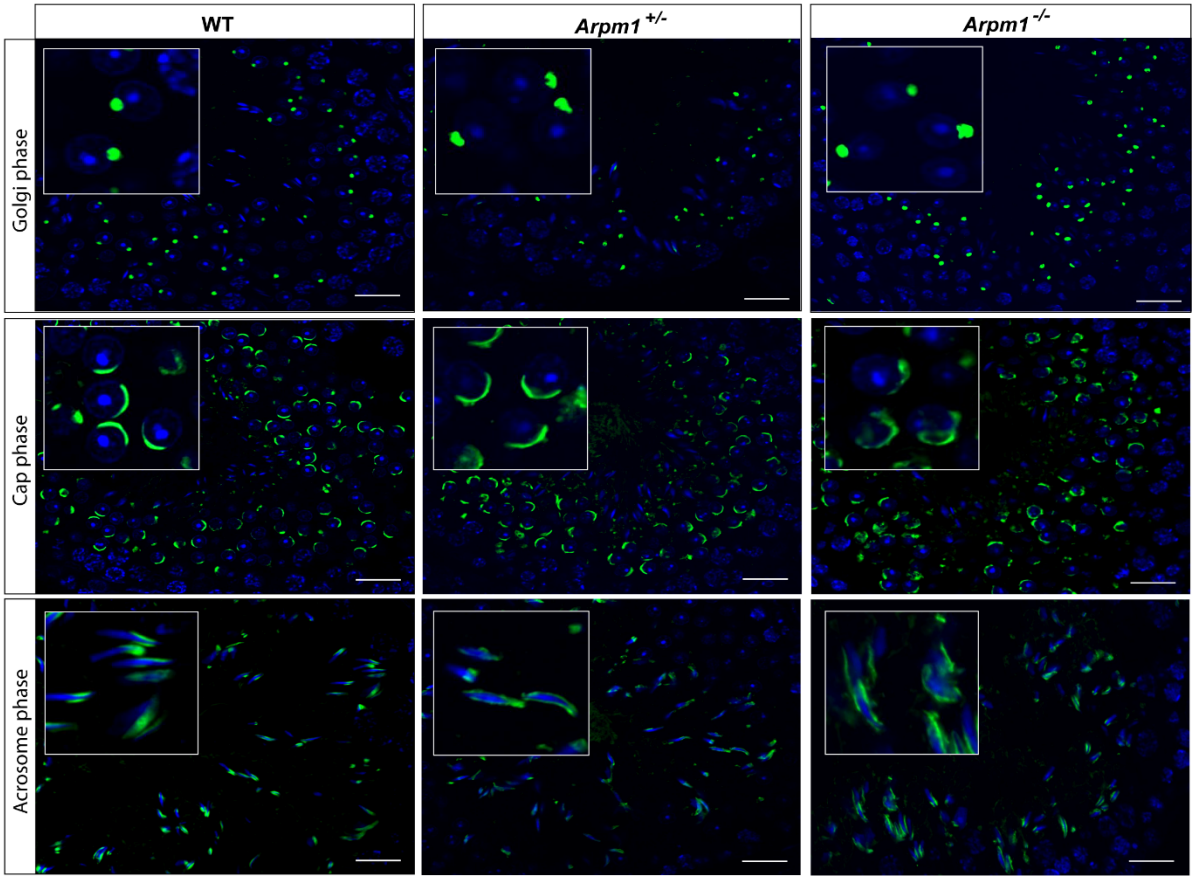

Figure 57: **Acrosome biogenesis in *Arpm1*-deficient testis tissue**.Staining of PNA-lectin in testicular tissue of WT, *Arpm1*$^{+/-}$ and *Arpm1*$^{-/-}$ male mice (green). In Golgi phase acrosomal granule is visible by dot-like signal at the surface of nuclei (upper panel). In Cap phases of WT and *Arpm1*$^{+/-}$ round spermatids acrosomal granule is visible as a cap-like signal on one side of round spermatids (middle panel). In *Arpm1*$^{-/-}$ round spermatids, vacuolized acrosome granules are observed (middle panel). In the acrosomal phase detached acrosomes are visible in *Arpm1*$^{-/-}$ elongating spermatids (lower panel). Nuclei were counterstained with DAPI. Staining was performed on three animals from each genotype. Scale bar: 20 µm. Inserts show representative spermatids present in the main picture at higher magnification. Data was obtained together with Eva Ordziniak during her Master´s thesis (2024). Modified from Kovacevic et al., 2025, preprint.

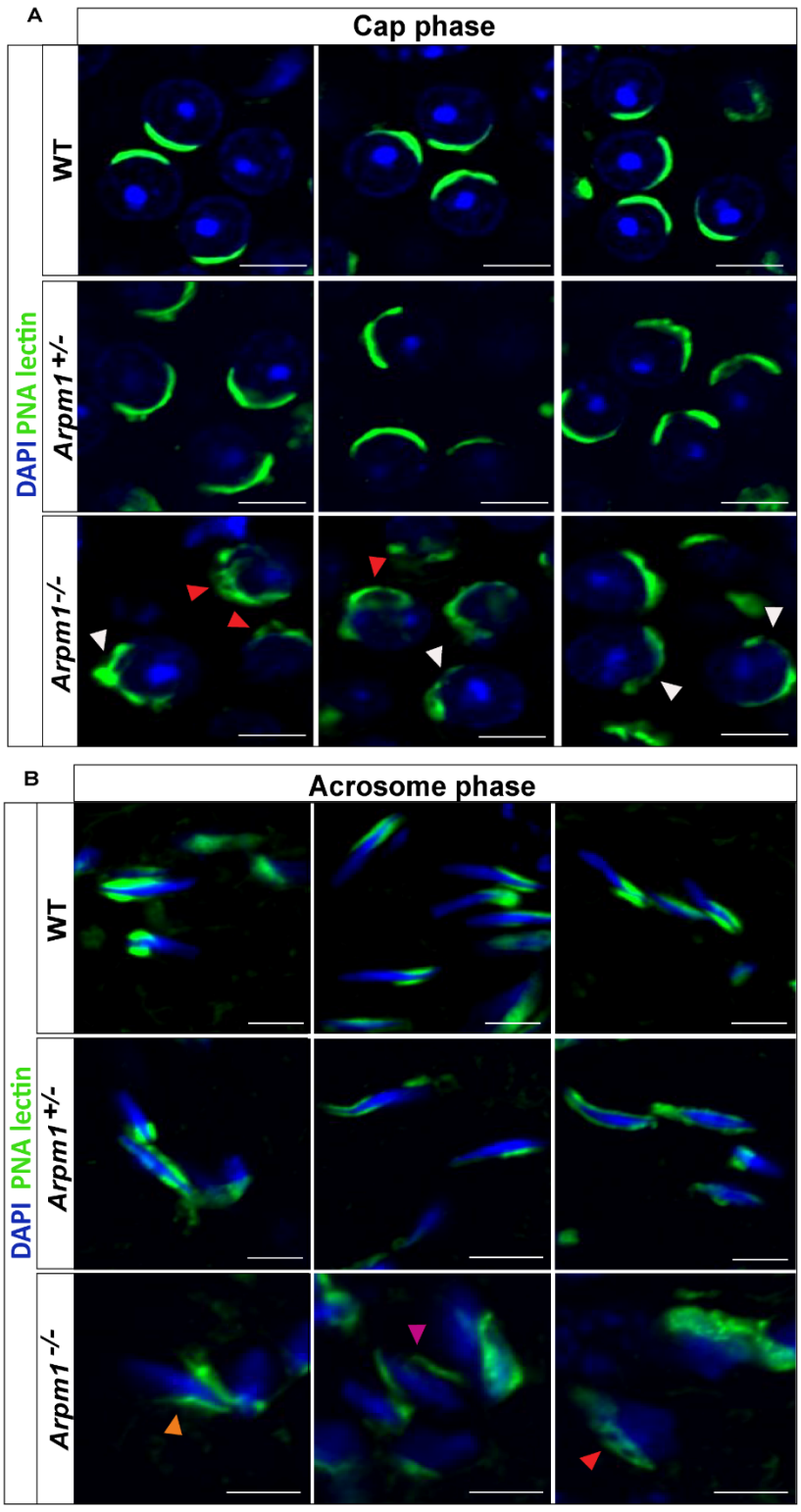

Figure 58: Cap and acrosome phase of acrosome biogenesis in *Arpm1*-deficient mice. Staining of the acrosome marker PNA-lectin in testicular tissue sections of WT, *Arpm1*$^{+/-}$ and *Arpm1*$^{-/-}$ mice (green). **A**) Round spermatids in cap phase of acrosome biogenesis are shown. Red arrowheads depict vacuolized acrosomes; white arrowheads show interrupted acrosomal granules. **B**) Elongating spermatids in acrosome phase are depicted. Red arrowheads depict vacuolized acrosomes; magenta arrowheads depict acrosomes detached from the nuclear envelope. Nuclei were counterstained with DAPI. Staining was performed on three animals from each genotype. Scale bar: 5 µm. Data was obtained together with Eva Ordziniak during her Master´s thesis (2024). Modified from Kovacevic et al., 2025, preprint.

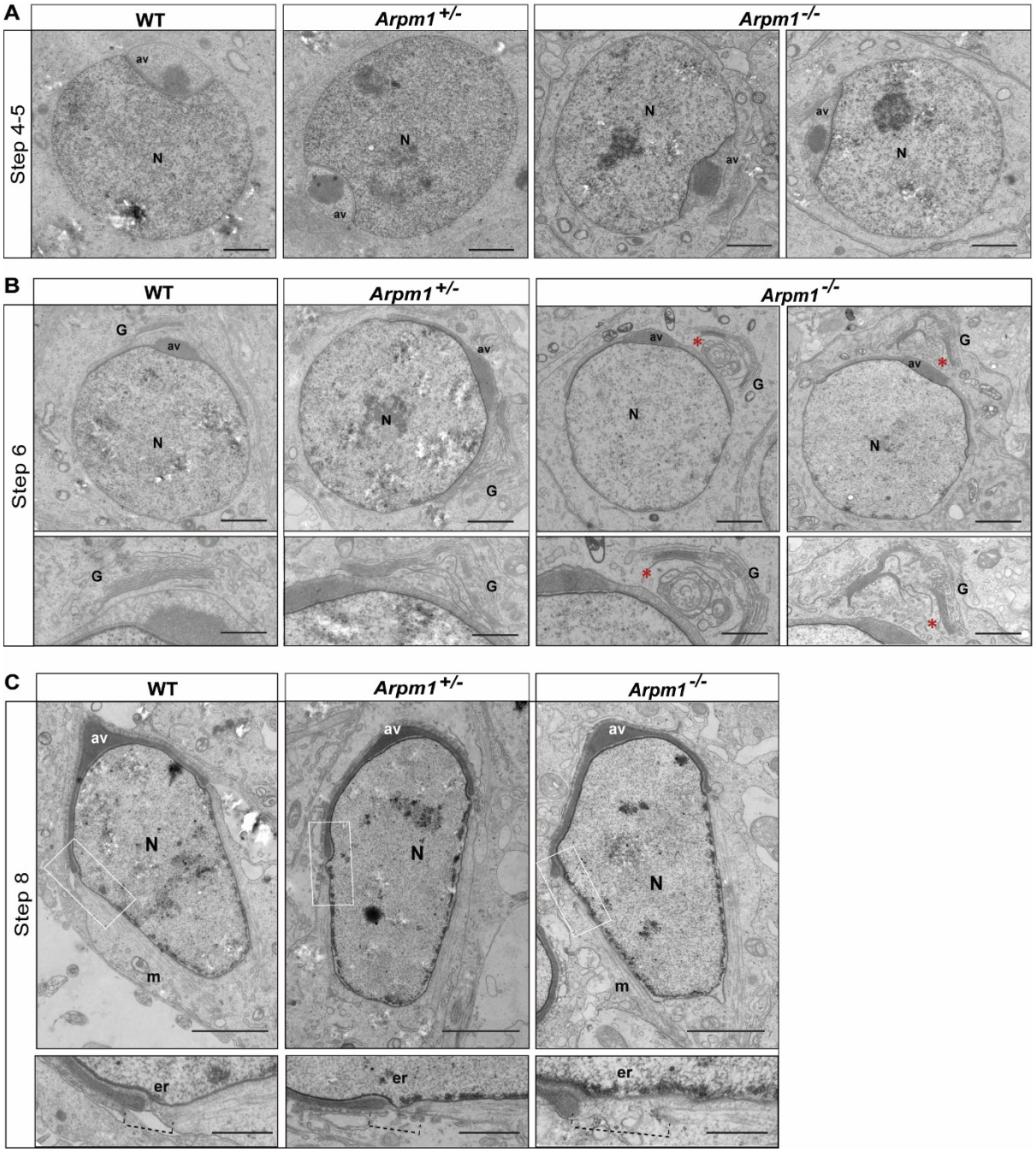

Figure 59: Spermiogenesis of Arpm1-deficient mice visualized by TEM. **A**) TEM micrographs of WT, *Arpm1*$^{+/-}$ and *Arpm1*$^{-/-}$ round spermatids in step 4-5 of spermiogenesis. N: nucleus; av: acrosomal vesicle. Scale bar: 5 µm. **B**) TEM micrographs of WT, *Arpm1*$^{+/-}$ and *Arpm1*$^{-/-}$ round spermatids in step 6 of spermiogenesis. Defective Golgi structures are depicted with red asterisks. N: nucleus; G: Golgi apparatus; av: acrosomal vesicle. Scale bar: 5 µm. Scale bar of the insert: 1 µm. **C**) TEM micrographs of WT, *Arpm1*$^{+/-}$ and *Arpm1*$^{-/-}$ elongating spermatids in step 8 of spermiogenesis. Inserts depict an enlarged gap between acroplaxome and manchette in *Arpm1*$^{-/-}$ spermatids compared to WT and *Arpm1*$^{+/-}$. N: nucleus; G: Golgi apparatus; av: acrosomal vesicle; m: manchette; er: equatorial ring. Scale bar: 5 µm. Scale bar of the insert: 1 µm. Modified from Kovacevic et al., 2025, preprint.

5.3.3. Loss of ARPM1 causes defects in Golgi trafficking during spermiogenesis

Since the vesicle trafficking between Golgi and the developing acrosome is essential for the acrosome development, the defects observed in *Arpm1*$^{-/-}$ round spermatids at TEM suggest that lack of ARPM1 eventually disrupts Golgi trafficking causing abnormal development of the acrosome. To investigate the effect of *Arpm1*-deficiency on Golgi-trafficking, *cis*- and *trans*-Golgi network markers were analysed. GM130 is a 130kDa protein required for vesicle tethering and maintenance of the *cis*-Golgi structural integrity. In murine round spermatids, staining against GM130 forms a cap-like pattern corresponding to the growing acrosomes (Tiwari et al., 2019). Interestingly, in *Arpm1*$^{-/-}$ spermatids, the GM130 signal appeared irregularly dispersed, without distinct localization within the round spermatids, indicating that *Arpm1*-deficiency leads to aberrant *cis*-Golgi trafficking during acrosome biogenesis (**Figure 60**).

TGN46 is a *trans*-Golgi network marker required for the formation of exocytic vesicles and secretion from the *trans*-part of the Golgi network in round spermatids. In testicular tissue sections of WT and *Arpm1*$^{+/-}$ mice, TGN46 is uniformly detected throughout round spermatids (**Figure 61 A**). However, in *Arpm1*$^{-/-}$ testis tissues, the staining pattern of TGN46 appeared irregular with lower signal intensity in round spermatids compared to WT and *Arpm1*$^{+/-}$ tissue samples (**Figure 61 A**). Similarly, protein levels of TGN46 were reduced in lysates from *Arpm1*$^{-/-}$ testis compared to WT and *Arpm1*$^{+/-}$ (**Figure 61 B**). Depletion of TGN46 in many different cell populations causes delayed or defective formation of post-Golgi vesicles, which in spermatids correspond to pro-acrosomal granules (Potelle et al., 2016). These results indicate that loss of ARPM1 causes defects in Golgi-derived proacrosomal vesicles leading to acrosome malformations. Similar results were observed in *Pfn3*-deficient male mice (Umer et al., 2021), indicating that the PFN3-ARPM1 protein complex is required for acrosome biogenesis by regulating Golgi-trafficking.

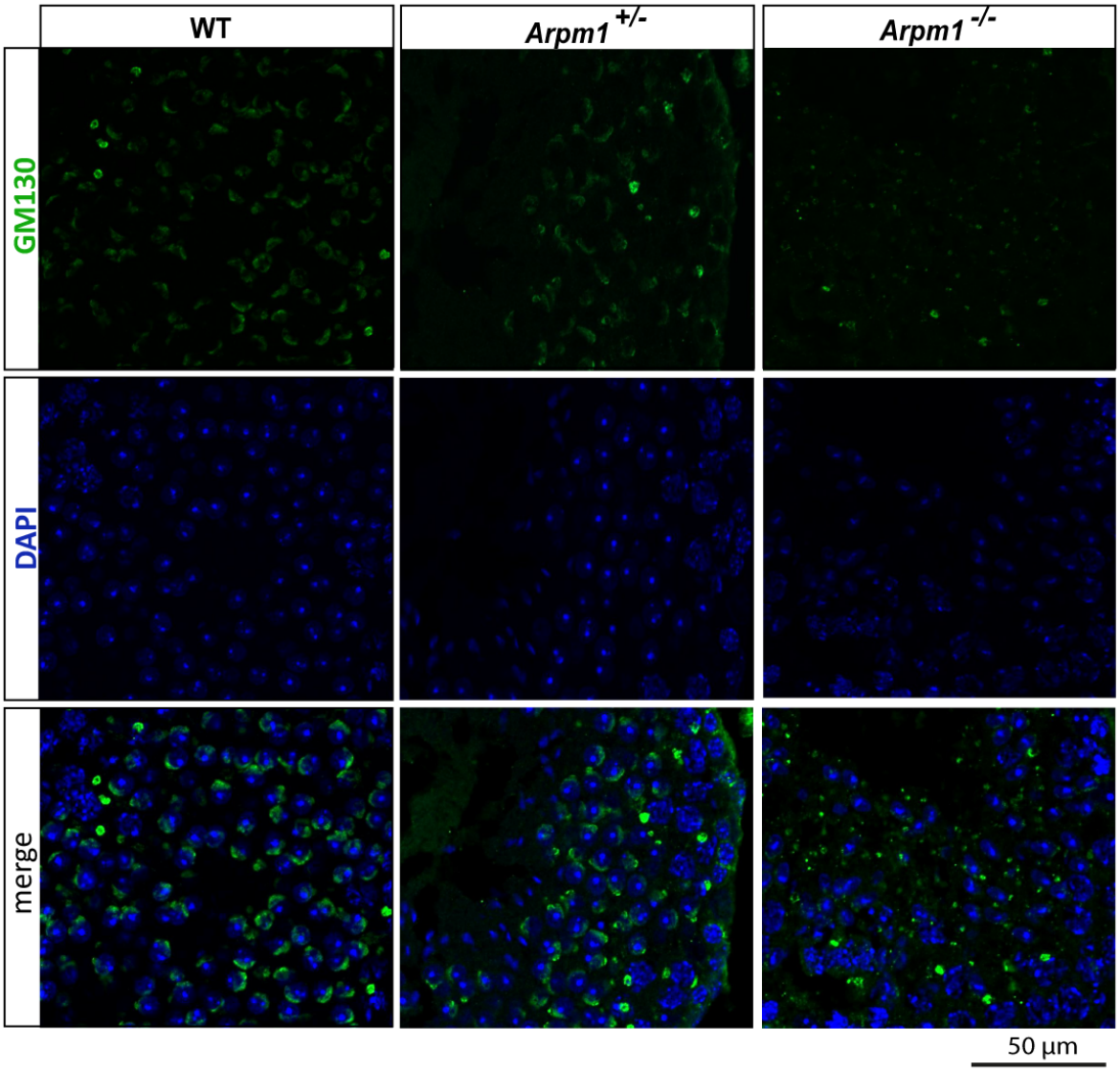

Figure 60: GM130 localization in *Arpm1*-deficient testis. Immunofluorescence staining of testicular tissue sections from WT, *Arpm1*$^{+/-}$ and *Arpm1*$^{-/-}$ male mice against GM130 *cis*-Golgi marker (green). In WT and *Arpm1*$^{+/-}$ round spermatids, GM130 signal forms a cap-like pattern over the nucleus. In *Arpm1*$^{-/-}$ round spermatids GM130 signal is scattered irregularly. Nuclei were counterstained with DAPI (blue). Scale bar: 50 µm. Data was obtained together with Sara Suvilla during her Master´s thesis (2023). Modified from Kovacevic et al., 2025, preprint.

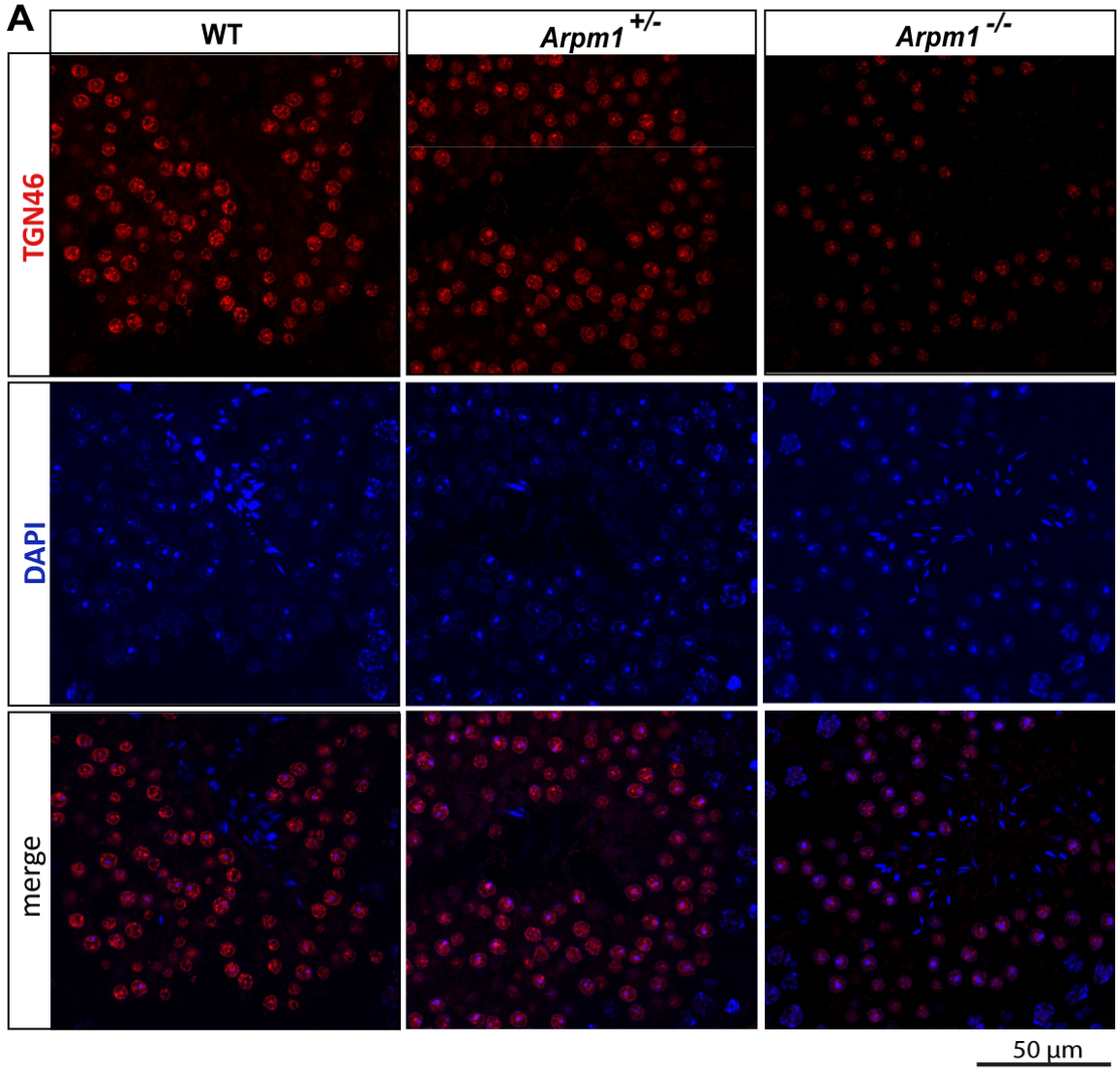

Figure 61: TGN46 distribution in *Arpm1*-deficient testis. A) Immunofluorescence staining of testicular tissue sections from WT, *Arpm1*$^{+/-}$ and *Arpm1*$^{-/-}$ male mice against TGN46 *trans*-Golgi marker (red). In *Arpm1*$^{-/-}$ round spermatids TGN46 signal was less intense compared to WT and *Arpm1*$^{+/-}$ round spermatids. Nuclei were counterstained with DAPI (blue). Scale bar: 50 µm. **B**) Immunoblot against TGN46 on protein lysates from WT, *Arpm1*$^{+/-}$ and *Arpm1*$^{-/-}$ testes. The band is detected between 70-80 kDa. α-Tubulin was used as load control (55 kDa). Data was obtained by Sara Suvilla during her Master´s thesis (2023). Modified from Kovacevic et al., 2025, preprint.

5.4. ARPM1 is part of PT protein network

5.4.1. ARPM1 interacts with other PT-specific proteins

As reported previously, ARPM1 interacts with PFN3, but it co-precipitates with many unidentified proteins as well (Hara et al., 2008). Based on the localization of ARPM1 in the PT of spermatids and mature sperm, several potential molecular interactors were identified from the literature. To study potential interactions between ARPM1 and other PT-specific proteins, an *in vitro* system was established as described in Master thesis of Eva Ordziniak. Briefly, combinations of expression plasmids containing coding sequence of genes of interest, either HA- or Myc-tagged were transfected transiently in HEK293T cells. Immunofluorescent staining of transfected cells was used to demonstrate the transfection efficiency (**Figure 62 A**). Interestingly, ARPM1, ACTRT1, ACTRT2, ACTL7A and ZPBP signals were detected in cytoplasm of HEK293T cells, surrounding their nuclei. PFN3 and SPEM2 were detected overlapping with DAPI signal. Due to the lack of commercially available antibody against SPEM2 at the time this study was conducted, staining was performed only against Myc-tag. Non-transfected HEK239T cells were stained with the same antibodies specific for the protein of interest as well as antibodies against Myc- or HA-tag, and no signal was detected, confirming the specificity of the antibodies as well as the transfection efficiency (**Figure 62 B**).

Co-transfection followed by co-immunoprecipitation analysis confirmed the interaction between ARPM1 and PFN3 which has been previously described (Hara et al., 2008; Umer et al., 2021). Furthermore, ARPM1 co-precipitated with ACTRT1, ACTRT2 and ACTL7A which are other members of Arp family with testis-specific expression pattern, localizing in the PT of spermatids and mature sperm. Finally, ARPM1 co-immunoprecipitated with Zona pellucida binding protein (ZPBP), a sperm surface protein required for the binding to the zona pellucida of the egg and thus required for fertilization (Lin et al., 2007). ARPM1 does not interact with SPEM2 - a testis-specific protein required for acrosome biogenesis and cytoplasm eviction (Li et al., 2024) (**Figure 63**).

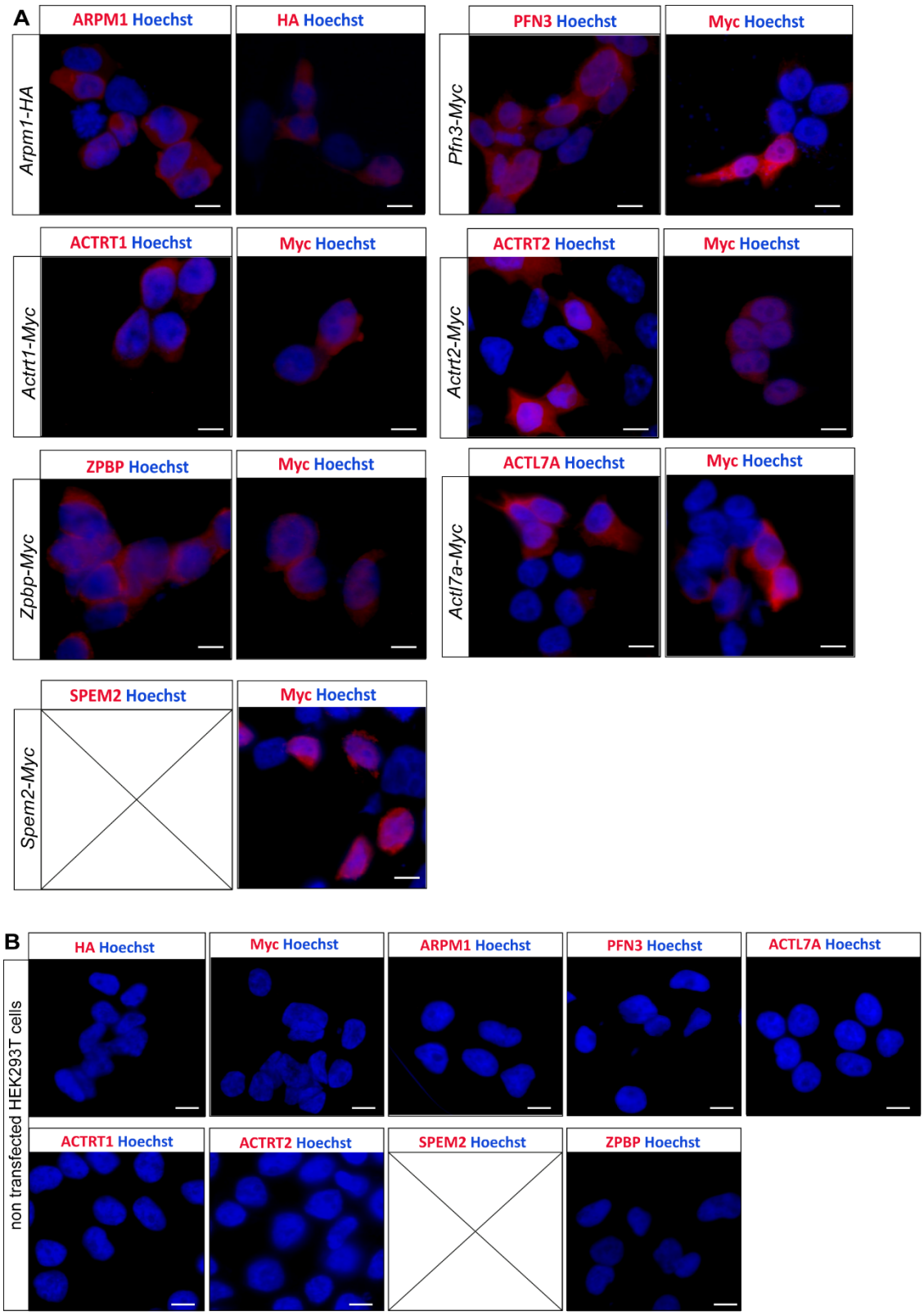

Figure 62: Validation of transfection in HEK293T cells. A) Immunofluorescent staining of transfected HEK293T cells against specific antibodies (ARPM1, PFN3, ACTRT1, ACTRT2, ACTL7A and ZPBP) and their respective Myc- or HA-tag. Nuclei were counterstained with Hoechst 3458. Scale bar: 10 µm. **B**) Immunofluorescent staining against HA-tag, Myc-tag, ARPM1, PFN3, ACTL7A, ACTRT1, ACTRT2 and ZPBP on non-transfected HEK293T cells. Nuclei were counterstained with Hoechst 3458. Scale bar: 10 µm. Transfections and stainings were performed together with Dr. Gina Merges and Eva Ordziniak. Modified from Kovacevic et al., 2025, preprint.

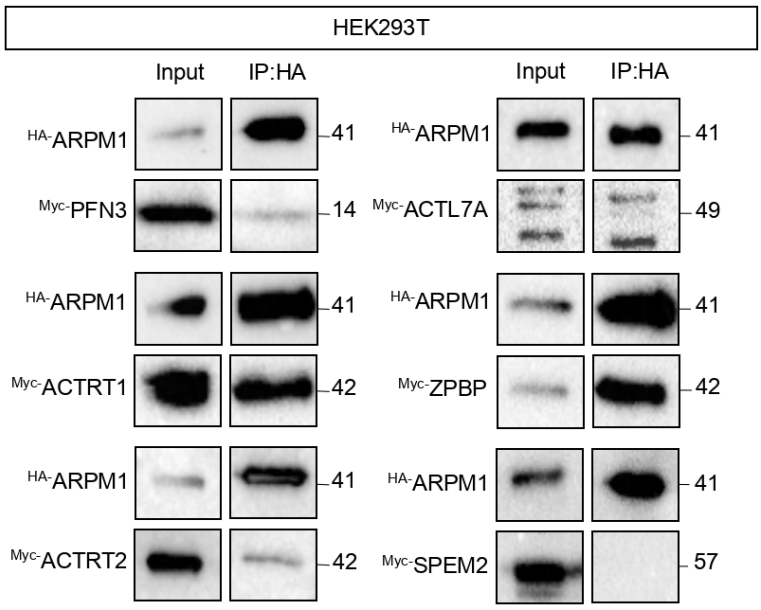

Figure 63: **Co-IP assay on protein lysates from co-transfected HEK293T cells**. ARPM1 co-precipitates with PFN3, ACTRT1, ACTRT2, ACTL7A and ZPBP. The interaction between ARPM1 and SPEM2 was not detected. Co-immunoprecipitation was performed by Eva Ordziniak during her Master´s thesis (2024). Modified from Kovacevic et al., 2025, preprint.

In order to analyze the effect of *Arpm1*-deficiency on its interaction partners in the PT, their localization and protein levels were investigated. ACTRT1 and ACTRT2 normally localize in the calyx of mature sperm in WT mice (**Figure 64 A**). In *Arpm1*$^{-/-}$ sperm, ACTRT1 is found in the calyx, however, the signal appeared weaker indicating lower protein abundance (**Figure 64 A**). Slightly reduced protein levels of ACTRT1 in *Arpm1*$^{-/-}$ testicular protein lysates were detected by immunoblotting, confirming the reduction of ACTRT1 protein abundance upon loss of ARPM1 (**Figure 64 B**). *Arpm1*-deficiency did not affect neither the localization of ACTRT2 in epididymal sperm nor its protein levels in testicular lysates (**Figure 64 A, B**). ACTL7A localizes in the PT of WT sperm, with a typical accumulation in the equatorial ring region. In *Arpm1*$^{-/-}$ sperm, ACTL7A signal is present, however, it appears equally distributed along the PT, without the equatorial ring accumulation site (**Figure 64 A**). As detected by immunoblotting, ACTL7A protein levels remained unaltered, suggesting that ARPM1 might be required for the proper localization of ACTL7A but *Arpm1*-deficiency does not lead to its depletion (**Figure 64 B**). Finally, a mislocalization of Zona pellucida binding protein (ZPBP) required for sperm to oocyte binding and fertilization (Lin et al., 2007) is observed in epididymal sperm from *Arpm1*$^{-/-}$ mice. ZPBP normally localizes in the acrosomal region of the sperm head, however in *Arpm1*$^{-/-}$ sperm it accumulates in the posterior part of the sperm head, in calyx and equatorial region (**Figure 64 A**). This suggests that ARPM1 is required for the proper localization of ZPBP in epididymal sperm.

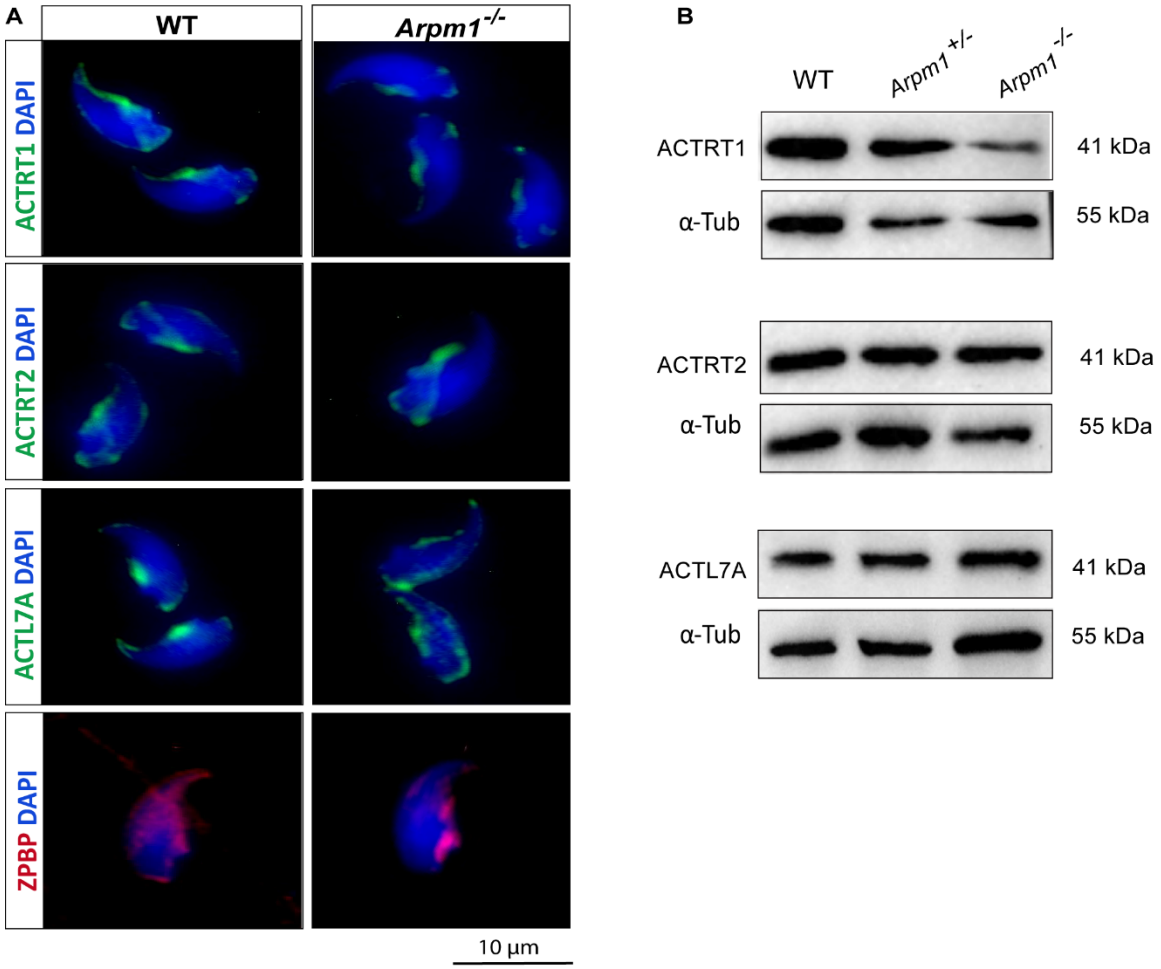

Figure 64: Analysis of PT proteins in *Arpm1*-deficient mice. A) Immunofluorescence staining of PT-specific proteins that interact with ARPM1 on WT and *Arpm1*$^{-/-}$ epididymal sperm. ACTRT1 and ACTRT2 are localized in the calyx of both WT and *Arpm1*$^{-/-}$ sperm. ACTL7A shows irregular distribution in the PT of *Arpm1*$^{-/-}$ sperm compared to WT. ZPBP accumulates in the calyx of *Arpm1*$^{-/-}$ epididymal sperm instead of the acrosomal portion as seen in WT sperm. Nuclei were counterstained with DAPI. Scale bar: 10 µm. **B**) Westen Blot against PT-specific proteins ACTRT1, ACTRT2 and ACTL7A on whole testis protein lysates of WT, *Arpm1*$^{+/-}$ and *Arpm1* $^{-/-}$ mice. α-tubulin (55 Da) was used as load control. Modified from Kovacevic et al., 2025, preprint.

5.4.2. ARPM1-PFN3 complex is required during spermiogenesis

Immunohistochemical staining of testicular tissue sections revealed a reduction of PFN3 signal in testis from *Arpm1*$^{-/-}$ mice (**Figure 65 A**). Similarly, western blot analysis revealed a strong reduction of PFN3 protein levels in *Arpm1*$^{-/-}$ testicular protein lysates, suggesting that the loss of ARPM1 might cause destabilization and depletion of PFN3 (**Figure 65 B**). Additionally, in WT epididymal sperm, PFN3 signal can be detected in the PT surrounding the nucleus. In *Arpm1*$^{-/-}$ sperm PFN3 signal is strongly reduced and detectable only at the tip of the sperm head (**Figure 65 C, red arrowhead**). Interestingly, *Pfn3*-deficient mice displayed loss of ARPM1 in testicular protein lysates as well (Umer et al., 2021).

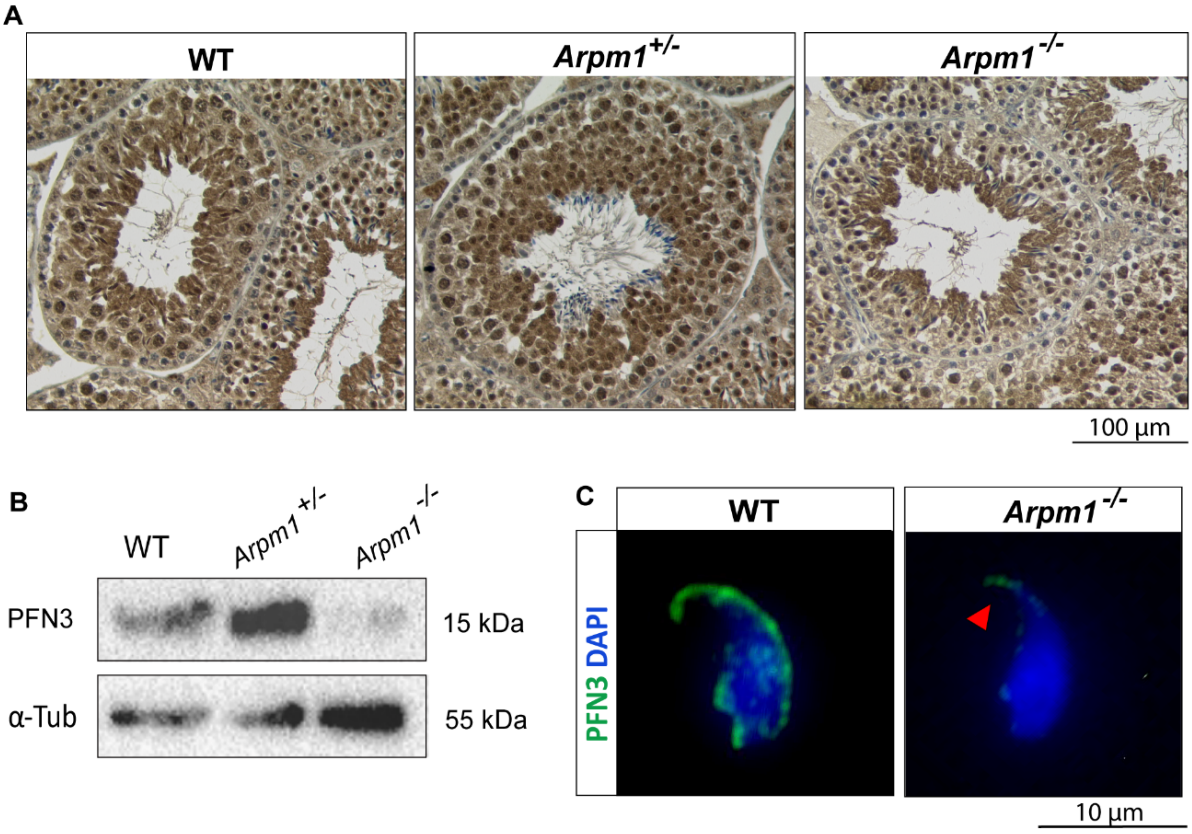

Figure 65: PFN3 localization and protein levels in Arpm1-deficient mice. A) Immunohistochemical staining of testicular tissue sections from WT, *Arpm1*$^{+/-}$ and *Arpm1*$^{-/-}$ mice against PFN3. Scale bar: 100 µm **B**) Western blot against PFN3 on testicular protein lysates of WT, *Arpm1*$^{+/-}$ and *Arpm1*$^{-/-}$ mice. Band corresponding to PFN3 is detected at 14-15 kDa. α-tubulin (55 kDa) was used as load control. **C**) Immunofluorescence staining against PFN3 in WT and *Arpm1*$^{-/-}$ epididymal sperm. Red arrowhead indicates PFN3 signal at the tip of the *Arpm1*$^{-/-}$ sperm head. Nuclei were counterstained with DAPI. Scale bar: 10µm. Modified from Kovacevic et al., 2025, preprint.

6. DISCUSSION

Parts of the discussion have been published in:

Schneider S., Kovacevic A., Mayer M., Dicke AK., Arévalo L., Koser SA., Hansen JN, Young S., Brenker C., Kliesch S., Wachten D., Kirfel G., Strünker T., Tüttelmann F., Schorle H. (2023) Cylicins are a structural component of the sperm calyx being indispensable for male fertility in mice and human *eLife* DOI: 10.7554/eLife.86100.3

Kovacevic A., Ordziniak E., Umer N., Arevalo L., Hinterlang LD., Ziaeipour S., Suvilla S., Merges GE, Schorle H. (2025) Actin-related protein M1 (ARPM1) required for acrosome biogenesis and sperm function in mice *BioArxiv* DOI: 10.1101/2025.03.27.645694 (currently in review with *Development*).

In research projects reported in this thesis, three different genes required during in spermiogenesis were investigated using gene-edited mouse models. While patients carrying variants in the studied genes have been identified, mouse models remain an essential research model due to the difficulty of obtaining human testicular tissue samples for research purposes. Additionally, genes analyzed in this study are evolutionarily conserved across species suggesting the essential function in both mice and human (Schneider, Kovacevic et al., 2023, Kovacevic et al., 2025). In the first part of this study, *Cylc1-*, *Cylc2-* as well as double *Cylc1/Clyc2*-deficient mice were analyzed in detail to elucidate the role of CYLC1 and CYLC2 during spermiogenesis. An infertile patient carrying variants in both genes was identified supporting the relevance of our mouse models. Next, *Arpm1*-deficient mice were analyzed providing further insight into the complex cytoskeletal scaffold within the sperm head in mice.

6.1. Cylicins are structural components of sperm, required for male fertility in mice and human

Cylc1-, *Cylc2-,* and *Cylc1/2*-deficient mouse lines were analyzed revealing that the loss of Cylicins impairs male fertility in mice. *Cylc1*$^{-/y}$ male mice were subfertile, with reduced litter sizes. Fertility was not affected in *Cylc2*$^{+/-}$ male mice, while *Cylc2*$^{-/-}$, *Cylc1*$^{-/y}$ *Cylc2*$^{+/-}$ and *Cylc1*$^{-/y}$ *Cylc2*$^{-/-}$ males displayed infertility, suggesting that at least 2 functional *Cylc* alleles are required for male fertility in mice.

CYLC1 and CYLC2 localize in the periacrosomal region of round spermatids with their signal shifting to the postacrosomal portion of PT during spermatid elongation. After completed

spermiogenesis, both CYLC1 and CYLC2 are localized in the calyx of mature sperm. Similar localization pattern of Cylicins has been previously described in human, boar, and bovine sperm and testis (Hess et al., 1993, 1995; Longo et al., 1987). Other PT-specific proteins such as CCIN and CAPZB/CAPZA3 have shown similar localization during spermiogenesis and in mature sperm, suggesting the potential interactions between different PT proteins (Bülow et al., 1997; Lécuyer et al., 2000; Zhang et al., 2022a). We observed severe defects of the sperm head architecture upon loss of two or three functional *Cylc* alleles, with defective acrosome biogenesis and structure. Starting from cap phase of acrosome development, a detachment of the acrosome from NE was observed in round spermatids from *Cylc*-deficient mice, leading to severe morphological malformations of the acrosome in mature sperm. Furthermore, *Cylc*-deficiency leads to a significant reduction in protein abundance of other PT components such as CCIN, CAPZB/CAPZA3, different isoforms of SPATA31 and members of Arp superfamily, indicating that CYLC1 and CYLC2 might interact with other PT proteins. Interestingly, *Cylc2*-deficiency caused a significant depletion of more sperm cytoskeletal proteins compared to the deficiency of *Cylc1*, which reflects well the infertility or subfertility observed in *Cylc1*-deficient and *Cylc2*-deficient male mice respectively. In *Cylc1*$^{-/y}$ sperm cells, significantly less abundant proteins belong mostly to the calyx and acrosome. Off note, morphological defects of the sperm upon loss of CYLC1 have been found only at the level of calyx and acrosome while the flagellum and the manchette remained intact, suggesting that CYLC1 has a role exclusively in the PT compartment of murine spermatids and sperm. In epididymal sperm from *Cylc2*$^{-/-}$ and *Cylc1*$^{-/y}$ *Cylc2*$^{-/-}$ mice, proteins which were significantly lower abundant compared to WT sperm belong to different cytoskeletal complexes of the sperm head and tail as well as the IMT machinery, indicating that the loss of CYLC2 affects not only the PT, but causes defects in overall sperm morphology including the flagellum and head-tail connecting region. The underlying reason for this might be an essential role of CYLC2 in protein transport during spermiogenesis. Further experiments including Co-immunoprecipitation on different germ cell populations from the testis as well as the epididymal sperm, followed by Mass spectrometry analysis should be performed to investigate whether CYLC2 has different interaction partners and thus distinct roles throughout the various stages of sperm development.

In a recently published study, it was demonstrated that CYLC1 interacts with itself and other PT proteins, namely ACTRT1, ACTRT2, ACTL7A, CAPZA3 and CCIN. Upon loss of CYLC1, the interaction between ACTRT1 and ACTL7A was partially disrupted, suggesting its role as a molecular glue within the PT-protein complex (Jin et al., 2024). Furthermore, CCIN is an indispensable component of the IAM-PT-NE complex and is required to maintain bidirectional connections with other PT proteins and keep the acroplaxome tightly connected to the nuclear envelope (Zhang et al., 2022a). In epididymal sperm from *Ccin*-deficient mice, nuclei and

acrosomes appeared vacuolized, with destabilized PT causing nuclear subsidence (Zhang et al., 2022a). Next, CAPZ complex consisting of actin-capping protein Zα3 (CAPZA3) and actin-capping protein Zβ (CAPZB) has a role in regulating actin dynamics by preventing loss or addition of G-actin subunits at the ends of F-actin filaments (Wear & Cooper, 2004). A mouse model carrying a missense mutation in *Capza3* gene displayed male infertility and phenotype similar to the one observed in *Cylc*-deficient mice, with morphological defects of the sperm head, flagellum wrapping and retention of cytoplasm (Geyer et al., 2009). Interestingly, both CCIN and CAPZA3 co-localize with CYLC1 and CYLC2 in the calyx of epididymal sperm and are both severely mislocalized upon loss of Cylicins, suggesting that Cylicins have a crucial role in maintenance of the PT structure. Additionally, CYLC1 interacts with FAM209, which is localized in the NE, and with an IAM protein SPACA1 which forms a complex with ACTL7A and is required to anchor the acrosome to the PT and NE (Castaneda et al., 2021; Fujihara et al., 2012; Jin et al., 2024). In *Cylc1*$^{-/y}$ mice, the interaction between SPACA1 and ACTL7A was weakened, causing the detachment of the acrosome from the NE (Jin et al., 2024). These results suggest that CYLC1 acts as a molecular glue of the acrosome to the nuclear envelope by interacting with both NE and IAM (**Figure 66, Figure 67**).

Molecular interaction partners of CYLC2 still remain unknown, however, its specific localization pattern during spermiogenesis and in mature sperm, as well as the mislocalization of CCIN and CAPZA3 upon its loss, indicate that CYLC2 might be required for the proper calyx structure. **Figure 66** depicts current knowledge about the involvement of Cylicins in the cytoskeletal network of murine sperm head. Acrosome is tightly connected to the NE by a protein network consisting of SPACA1, ACTL7A (and other testis specific Arps) and CYLC1 connecting the complex to nuclear membrane protein FAM209. Upon loss of both CYLC1, the connection between acroplaxome and NE is disrupted, causing the loss of connection between SPACA1-ACTL71 complex and FAM209 and leading to acrosome detachment from the nucleus (**Figure 66**). The role of CYLC2 in the periacrosomal region and its involment in the PT protein network remain to be elucidated and thus are not depicted in the graphical illustration. Next, the results strongly indicate that in the postacrosomal part of the PT, CYLC1 and CYLC2 stabilize the calyx proteins CCIN and CAPZA3. *Cylc*-deficiency causes mislocalization of these proteins and the loss of calyx structure (**Figure 66**).

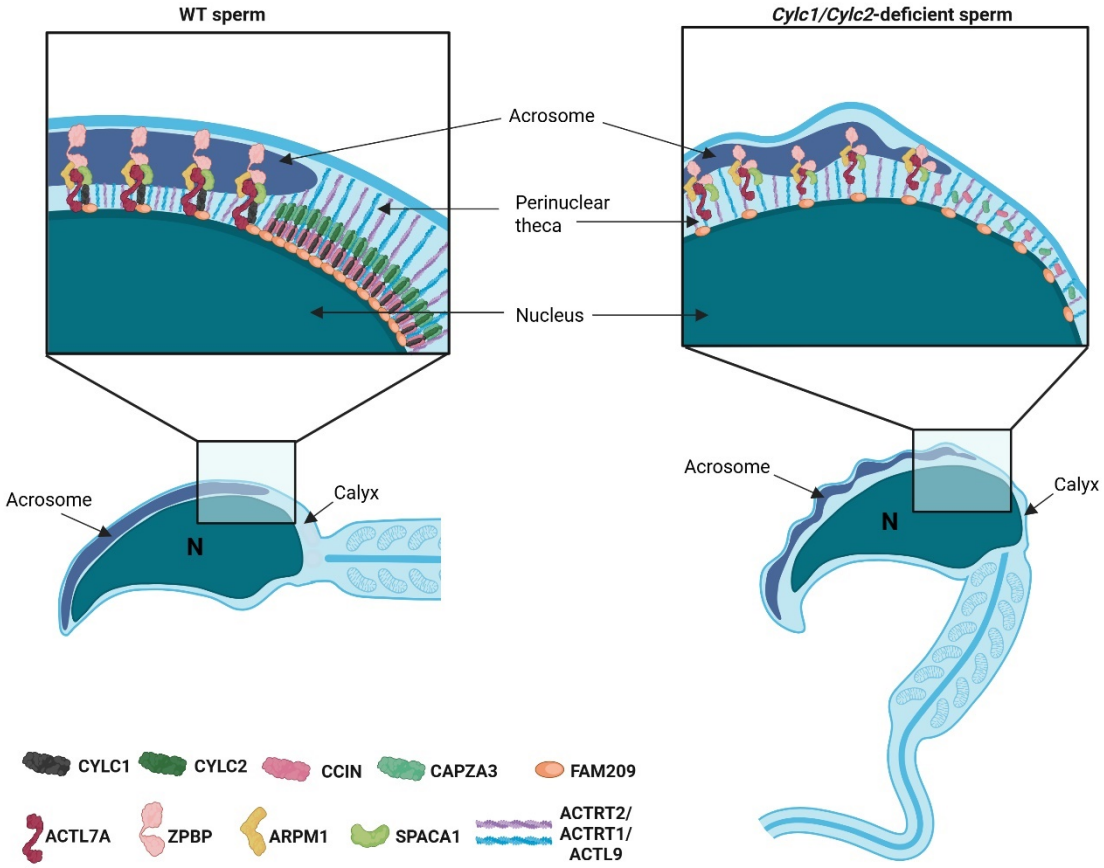

Figure 66: CYLC1 and CYLC2 are essential components of sperm PT. Graphical representation depicting protein networks within the PT of WT and *Cylc*-deficient murine sperm. Destabilized PT structure is shown, leading to acrosome detachment from the nucleus and disruption of the calyx region upon loss of CYLC1 and CYLC2. Created with Biorender.com

During spermiogenesis *Cylc*-deficiency results in excessive manchette elongation, its delayed disassembly, along with a formation of abnormal gaps between acroplaxome and manchette at the level of the perinuclear ring. The delay in manchette disassembly could be caused by the malfunctions of the intra-manchette transport (IMT) of proteins during spermatid elongation. This was observed in different mouse models deficient for IMT proteins such as HOOK1 (Mendoza-Lujambio, 2002), CEP131 (Hall et al., 2013) and IFT88 (Kierszenbaum et al., 2011). Furthermore, anomalies of the head-tail connection, flipping of the sperm head and coiling of the flagellum detected in *Cylc2*$^{-/-}$ males are also observed in *Hook1*-deficient mice (Kazuhiko Mochida et al., 1999). The manchette localizes on the caudal portion of elongating spermatids while calyx occupies the caudal region of mature sperm, suggesting that calyx proteins might be involved in IMT prior to manchette disassembly. As Cylicins do not localize within the tail of WT sperm, and the sperm axonemes appear unaffected by *Cylc*-deficiency, altered sperm motility in *Cylc1*$^{-/y}$*Cylc2*$^{+/-}$, *Cylc1*$^{-/y}$*Cylc2*$^{-/-}$ and *Cylc2*$^{-/-}$ mice as well as the

irregular flagellar beat observed are likely secondary effects caused by defective sperm head morphology, disrupted head-tail connecting piece and delayed manchette removal.

As demonstrated by the infertility and sperm morphological defects observed in a patient carrying variants in both *Cylc* genes, CYLC1 and CYLC2 are required for human spermiogenesis and fertility as well. CYLC1 was absent in the calyx of patient´s mature sperm indicating a functional impact of the missense variant in *CYLC1* gene on the CYLC1 protein. Furthermore, CCIN localization was impaired in patient´s sperm, suggesting a similar role of *Cylc* in PT structural maintenance in both rodents and primates. Interestingly, while in the MERGE German cohort including 2030 infertile men, only one patient carrying variants in both *CYLC* genes was found, WES performed on a Chinese cohort of >500 infertile men with teratozoospermia identified 19 individuals carrying a variant in *CYLC1* gene (Jin et al., 2024). All 19 identified patients with CYLC1 variants displayed abnormal sperm morphology with deformed or detached acrosomes (Jin et al., 2024). Of note, the sperm of a patient carrying variants in both CYLC genes managed to fertilize the egg using ICSI, however, no pregnancy was achieved following the cryo-embryo transfer Schneider, Kovacevic et al., 2023. Similarly, Jin et al. (2024) reported that ICSI, but not IVF can be a promising fertility treatment for men carrying variants in *CYLC1*. Additionally, a combination of ICSI with assisted oocyte activation (AOA) lead to better fertilization rate, suggesting that CYLC1 deficiency in humans might affect oocyte activation (Jin et al., 2024). The underlying cause for this might involve PLCζ - an oocyte activation factor which triggers Ca^{2+} oscillations required for the first divisions of the fertilized oocyte and embryo development (Yoon et al., 2008). In sperm from a patient carrying variants in *CYLC1* and *CYLC2* genes, PLCζ is mislocalized, likely causing an oocyte activation deficiency (OAD) which can be overcome by a combined ICSI-AOA treatment.

Taken together, the results suggest that CYLC1 and CYLC2 are required for the regular sperm development and the sperm head morphology by acting as a molecular glue involved in a complex 3D structure, along with other PT proteins, keeping the acrosome tightly connected to the nuclear envelope. While several interaction partners of CYLC1 have been already identified, further studies are required to elucidate the interactions of CYLC2 and the exact molecular mechanism of the complex PT-protein network in murine and human sperm.

6.2. ARPM1 is required for acrosome development and sperm function in mice

Arpm1 is highly conserved among species and expressed exclusively in the male germ line during spermiogenesis in mouse and human (Kovacevic et al., 2025). *Arpm1*-deficient mouse lines were established and analyzed in detail. Fertility analysis revealed that *Arpm1*-deficiency leads to male subfertility in mice, with reduced epididymal sperm count and viability. The most prominent effect of *Arpm1*-deficiency was defective acrosome development starting at Cap phase and leading to abnormal acrosomes in epididymal sperm.

In this study, a previously demonstrated interaction between ARPM1 and PFN3 was confirmed (Hara et al., 2008). *Pfn3*-deficient mouse line was established and analyzed previously in our lab, demonstrating male subfertility (Umer et al., 2021), similarly to what´s observed upon loss of ARPM1. However, effects caused by the loss of PFN3 seem to be more pronounced compared to defects observed in *Arpm1*-deficiency. *Pfn3*-deficient mice display impaired sperm motility due to misshapen flagella, incomplete cytoplasm eviction and abnormal manchette structure, in addition to defects of the acrosome development which were observed in *Arpm1*$^{-/-}$ mice as well. Both *Pfn3*- and *Arpm1*-deficiency caused impaired *cis*- and *trans*-Golgi trafficking in round spermatids, as shown by the disruption of GM130 and TGN46 respectively, leading to alterations of acrosome biogenesis. However, while in *Arpm1*-deficient mice, these defects are first observed at Cap phase of acrosome biogenesis, in *Pfn3*-deficient testes, they occur earlier, during Golgi phase of acrosome development (Umer et al., 2021). Slightly different protein expression patterns were observed as well, with PFN3 being detected at earlier stages of spermiogenesis compared to ARPM1 (**Figure 9, Supplementary Figure S8**) (Guo et al., 2018a; Lukassen et al., 2018b). Furthermore, a loss of ARPM1 was observed in *Pfn3*-deficient mice (Umer et al., 2021), while in *Arpm1*-deficient testis tissues and epididymal sperm, levels of PFN3 were dramatically reduced, suggesting that PFN3 and ARPM1 act as a complex and are not stable separately. However, as traces of PFN3 were still detected in *Arpm1*$^{-/-}$ mice and the protein was not completely depleted, our current hypothesis is that PFN3 might also interact with ARPM1 related proteins such as ACTRT1 or ACTRT2 and might be partially stabilized upon loss of ARPM1. The additional defects observed in *Pfn3*-deficient mice that were not observed in *Arpm1*$^{-/-}$ males are effects independent of ARPM1.

Next, aside from PFN3, ARPM1 interacts with testis enriched members of Arp family that localize in the PT, namely ACTRT1, ACTRT2 and ACTL7A. Of note, ACTRT1 and ACTL7A are part of a complex cytoskeletal scaffold required for the structure and development of the sperm head and acrosome (Xin et al., 2020; Zhang et al., 2022b). *Actrt1*-deficient male mice are subertile with acrosome abnormalities (Zhang et al., 2022b). On the other hand, *Actl7a*-deficient mice display male infertility with more severe morphological defects affecting sperm

head shape and acrosome integrity . Interestingly, ACTRT1 and ACTL7A have been found to interact among themselves and with ACTL9 (Dai et al., 2022; Zhang et al., 2022b). Furthermore, ACTL7A interacts with further PT-proteins CCIN (Zhang et al., 2022a), CYLC1 (Jin et al., 2024) and SPACA1 (Chen et al., 2021) acting as a central component of the protein network of the PT. Since we demonstrated that ARPM1 co-precipitates with ACTL7A and its interaction partner ACTRT1 as well as ACTRT2, it is an integral part of the PT cytoskeletal scaffold (**Figure 67, Figure 68**).

Another ARPM1 interaction partner identified in this study is ZPBP which localizes in the acrosome and is required for binding and penetration of the zona pellucida – the extracellular matrix that surrounds the oocyte, making the fertilization possible (Lin et al., 2007). In *Arpm1*-deficient sperm, ZPBP is present but mislocalized in epididymal sperm, suggesting that ARPM1 is required to tether ZPBP in its proper localization. This mislocalization of ZPBP likely contributes to the subfertility of *Arpm1*$^{-/-}$ male mice *in vitro* and *in vivo*. Interestingly, SPEM2, which is an interaction partner of ZPBP and required for sperm development, acrosome biogenesis and cytoplasm eviction, did not co-precipitate with ARPM1 (Li et al., 2024) (**Figure 67**). This indicates that SPEM2 and ARPM1 might have similar but independent roles in stabilizing ZPBP.

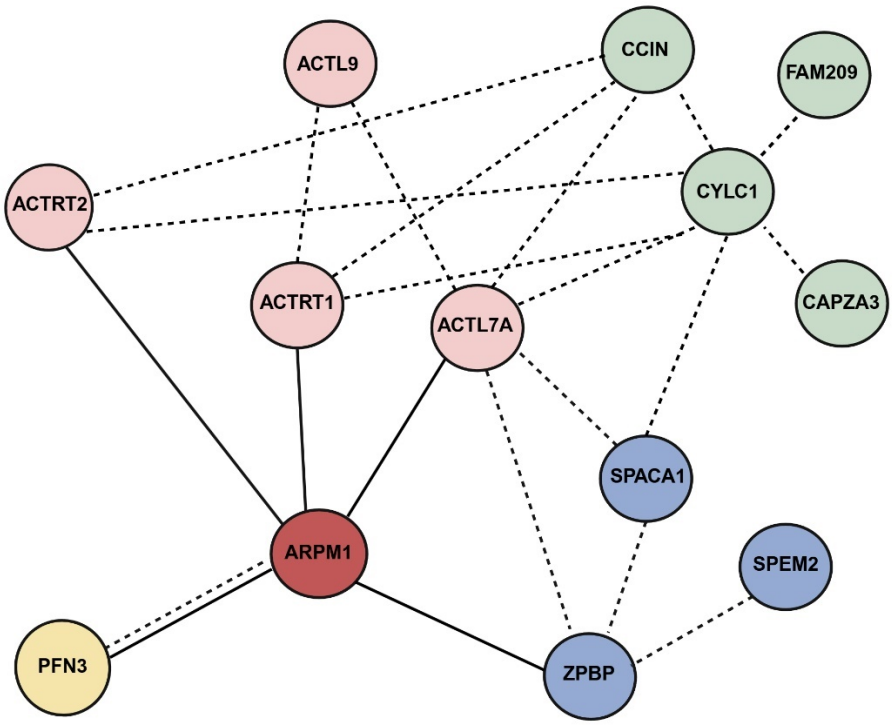

Figure 67: ARPM1 interaction network. String depicts protein interactions of ARPM1. Cytoskeletal proteins belonging to PT scaffold are depicted: ARPM1 (red), members of Arp-complex (light pink), other PT cytoskeletal proteins (green). PFN3 is depicted in yellow while ZPBP and its interactors are shown in blue, to indicate different complexes that include ARPM1. Full line: interactions shown in this study; dashed line: previously published interactions. Created with Biorender.com

The results of this study suggest that ARPM1 is a component of Actin-related core of the protein network within PT, along with ACTL7A, ACTRT1 and ACTL9. Furthermore, it tethers ZPBP to its proper localization. Upon loss of ARPM1, acroplaxome is destabilized, causing the mislocalization of ACTL7A and ZPBP (**Figure 68**). Finally, ARPM1 is required to stabilize PFN3 which regulates *cis*- and *trans*-Golgi networking during spermiogenesis (**Figure 67, Figure 68**).

ARPM1 belongs to the same superfamily and shares sequence similarities with its interaction partners ACTRT1 and ACTRT2 (Goodson & Hawse, 2002). RNA expression data from mouse testis indicates that *Arpm1*, *Actrt1* and *Actrt2* are expressed from round spermatids to compacted sperm, however, the amount of *Actrt2* transcripts seem to be roughly 10 times higher compared to *Arpm1* or *Acrtrt1* (**Supplementary figure S9**). Similarly, Human Testis Atlas data show that all three Arps are expressed in round spermatids, elongating spermatids and sperm (Supplementary figure S9) (Guo et al., 2018). In humans, *ACTRT1* has the lowest expression while *ARPM1* peaks in round and elongating spermatids and it´s less expressed in compacted sperm. Interestingly, *ACTRT2* has the highest expression levels in haploid germ cells, persisting in compacted sperm (**Supplementary figure S9**). Overlapping expression pattern and subfertility observed in *Arpm1*- and *Actrt1*-deficient male mice might indicate to their potentially redundant roles. To continue elucidating the roles of Arps in sperm development and function, *Actrt2*-deficient mice were established and are currently under analysis in our lab. To test weather ACTRT2 partially compensates for the loss of ARPM1 in mice, we are currently establishing an *Arpm1/Actrt2*-double deficient mouse line. Additionally, CoIP of testicular protein extracts followed by Mass Spectrometry analysis could reveal the overlapping interaction partners between ARPM1 and the other sperm-specific Arps.

Finally, human patients carrying variants in *ACTL7A* or *ACTRT1* genes were identified, displaying infertility and defects of the sperm head and acrosome (Dai et al., 2022; Y. Zhang et al., 2023). Patients with *ARPM1* variants were not reported yet. *Arpm1* gene sequence is strongly conserved across species, suggesting that it might have an essential function in humans as well. Thus, variants in *ARPM1* might lead to sub- or infertility in humans as well.

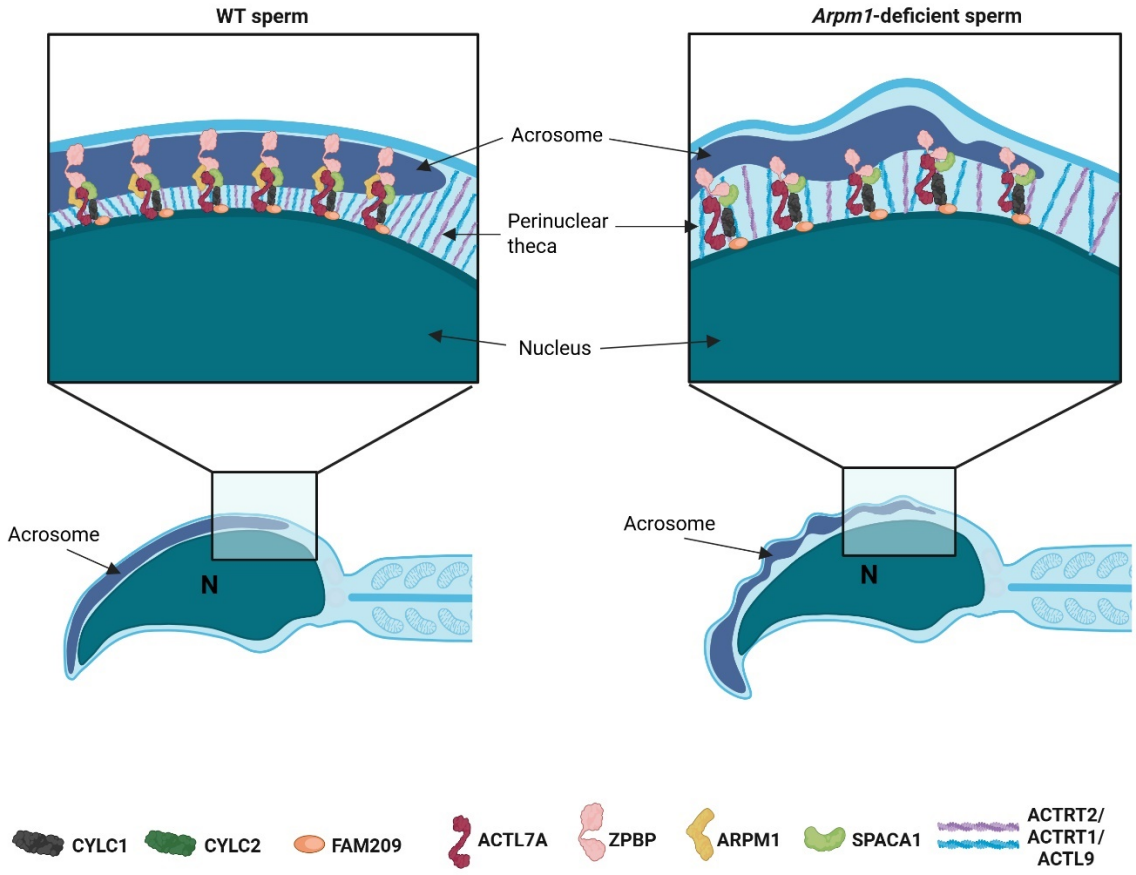

Figure 68: ARPM1 is a part of the PT scaffold. Graphical representation depicting protein networks within the PT of WT and *Arpm1*-deficient murine sperm. Destabilized PT structure is shown, leading to acrosome detachment from the nucleus and misplacement of ZPBP. Created with Biorender.com

7. BIBLIOGRAPHY

Adzhubei, I. A., Schmidt, S., Peshkin, L., Ramensky, V. E., Gerasimova, A., Bork, P., Kondrashov, A. S., & Sunyaev, S. R. (2010). A method and server for predicting damaging missense mutations. *Nature Methods*, *7*(4), 248–249. https://doi.org/10.1038/nmeth0410-248

Amann, R. P. (2008). The Cycle of the Seminiferous Epithelium in Humans: A Need to Revisit? *Journal of Andrology*, *29*(5), 469–487. https://doi.org/10.2164/jandrol.107.004655

AUSTIN, C. R. (1952). The 'Capacitation' of the Mammalian Sperm. *Nature*, *170*(4321), 326–326. https://doi.org/10.1038/170326a0

Avidor-Reiss, T., Carr, A., & Fishman, E. L. (2020). The sperm centrioles. *Molecular and Cellular Endocrinology*, *518*, 110987. https://doi.org/10.1016/j.mce.2020.110987

Baudat, F., & de Massy, B. (2007). Regulating double-stranded DNA break repair towards crossover or non-crossover during mammalian meiosis. *Chromosome Research*, *15*(5), 565–577. https://doi.org/10.1007/s10577-007-1140-3

Berruti, G., & Paiardi, C. (2011). Acrosome biogenesis. *Spermatogenesis*, *1*(2), 95–98. https://doi.org/10.4161/spmg.1.2.16820

Blessing, C. A., Ugrinova, G. T., & Goodson, H. V. (2004). Actin and ARPs: action in the nucleus. *Trends in Cell Biology*, *14*(8), 435–442. https://doi.org/10.1016/j.tcb.2004.07.009

Bülow, M. von, Rackwitz, H.-R., Zimbelmann, R., & Franke, W. W. (1997). CP β3, a Novel Isoform of an Actin-Binding Protein, Is a Component of the Cytoskeletal Calyx of the Mammalian Sperm Head. *Experimental Cell Research*, *233*(1), 216–224. https://doi.org/10.1006/excr.1997.3564

Castaneda, J. M., Shimada, K., Satouh, Y., Yu, Z., Devlin, D. J., Ikawa, M., & Matzuk, M. M. (2021). FAM209 associates with DPY19L2, and is required for sperm acrosome biogenesis and fertility in mice. *Journal of Cell Science*, *134*(21). https://doi.org/10.1242/jcs.259206

CHANG, M. C. (1951). Fertilizing Capacity of Spermatozoa deposited into the Fallopian Tubes. *Nature*, *168*(4277), 697–698. https://doi.org/10.1038/168697b0

CHAUVIÈRE, M., MARTINAGE, A., DEBARLE, M., SAUTIÈRE, P., & CHEVAILLIER, P. (1992). Molecular characterization of six intermediate proteins in the processing of mouse protamine P2 precursor. *European Journal of Biochemistry*, *204*(2), 759–765. https://doi.org/10.1111/j.1432-1033.1992.tb16691.x

Chen, P., Saiyin, H., Shi, R., Liu, B., Han, X., Gao, Y., Ye, X., Zhang, X., & Sun, Y. (2021). Loss of SPACA1 function causes autosomal recessive globozoospermia by damaging the acrosome–acroplaxome complex. *Human Reproduction*, *36*(9), 2587–2596. https://doi.org/10.1093/humrep/deab144

Clermont, Y., & Leblond, C. P. (1959). Differentiation and renewal of spermatogonia in the monkey, Macacus rhesus. *American Journal of Anatomy*, *104*(2), 237–273. https://doi.org/10.1002/aja.1001040204

Dacheux, J.-L., Dacheux, F., & Druart, X. (2016). Epididymal protein markers and fertility. *Animal Reproduction Science*, *169*, 76–87. https://doi.org/10.1016/j.anireprosci.2016.02.034

Dai, J., Chen, Y., Li, Q., Zhang, T., Zhou, Q., Gong, F., Lu, G., Zheng, W., & Lin, G. (2022). Pathogenic variant in *ACTL7A* causes severe teratozoospermia characterized by bubble-shaped acrosomes and male infertility. *Molecular Human Reproduction*, *28*(8). https://doi.org/10.1093/molehr/gaac028

de Kretser, D. M., Loveland, K. L., Meinhardt, A., Simorangkir, D., & Wreford, N. (1998). Spermatogenesis. *Human Reproduction*, *13*(suppl 1), 1–8. https://doi.org/10.1093/humrep/13.suppl_1.1

Desai, A., & Mitchison, T. J. (1997). MICROTUBULE POLYMERIZATION DYNAMICS. *Annual Review of Cell and Developmental Biology*, *13*(1), 83–117. https://doi.org/10.1146/annurev.cellbio.13.1.83

Fawcett, D. W., & Phillips, D. M. (1969). The fine structure and development of the neck region of the mammalian spermatozoon. *The Anatomical Record*, *165*(2), 153–183. https://doi.org/10.1002/ar.1091650204

Ferrer, P., Upadhyay, S., Ikawa, M., & Clement, T. M. (2023). Testis-specific actin-like 7A (ACTL7A) is an indispensable protein for subacrosomal-associated F-actin formation, acrosomal anchoring, and male fertility. *Molecular Human Reproduction*, *29*(3). https://doi.org/10.1093/molehr/gaad005

Fu, J., Wang, Y., Fok, K. L., Yang, D., Qiu, Y., Chan, H. C., Koide, S. S., Miao, S., & Wang, L. (2012). Anti-ACTL7a antibodies: a cause of infertility. *Fertility and Sterility*, *97*(5), 1226-1233.e8. https://doi.org/10.1016/j.fertnstert.2012.02.023

Fujihara, Y., Satouh, Y., Inoue, N., Isotani, A., Ikawa, M., & Okabe, M. (2012). SPACA1-deficient male mice are infertile with abnormally shaped sperm heads reminiscent of globozoospermia. *Development*, *139*(19), 3583–3589. https://doi.org/10.1242/dev.081778

Gervasi, M. G., & Visconti, P. E. (2017). Molecular changes and signaling events occurring in spermatozoa during epididymal maturation. *Andrology*, *5*(2), 204–218. https://doi.org/10.1111/andr.12320

Geyer, C. B., Inselman, A. L., Sunman, J. A., Bornstein, S., Handel, M. A., & Eddy, E. M. (2009). A missense mutation in the Capza3 gene and disruption of F-actin organization in spermatids of repro32 infertile male mice. *Developmental Biology*, *330*(1), 142–152. https://doi.org/10.1016/j.ydbio.2009.03.020

Goodson, H. V., & Hawse, W. F. (2002). Molecular evolution of the actin family. *Journal of Cell Science*, *115*(13), 2619–2622. https://doi.org/10.1242/jcs.115.13.2619

Goudarzi, A., Shiota, H., Rousseaux, S., & Khochbin, S. (2014). Genome-Scale Acetylation-Dependent Histone Eviction during Spermatogenesis. *Journal of Molecular Biology*, *426*(20), 3342–3349. https://doi.org/10.1016/j.jmb.2014.02.023

Govin, J., Escoffier, E., Rousseaux, S., Kuhn, L., Ferro, M., Thévenon, J., Catena, R., Davidson, I., Garin, J., Khochbin, S., & Caron, C. (2007). Pericentric heterochromatin reprogramming by new histone variants during mouse spermiogenesis. *The Journal of Cell Biology*, *176*(3), 283–294. https://doi.org/10.1083/jcb.200604141

Guo, J., Grow, E. J., Mlcochova, H., Maher, G. J., Lindskog, C., Nie, X., Guo, Y., Takei, Y., Yun, J., Cai, L., Kim, R., Carrell, D. T., Goriely, A., Hotaling, J. M., & Cairns, B. R. (2018a). The adult human testis transcriptional cell atlas. *Cell Research*, *28*(12), 1141–1157. https://doi.org/10.1038/s41422-018-0099-2

Guo, J., Grow, E. J., Mlcochova, H., Maher, G. J., Lindskog, C., Nie, X., Guo, Y., Takei, Y., Yun, J., Cai, L., Kim, R., Carrell, D. T., Goriely, A., Hotaling, J. M., & Cairns, B. R. (2018b). The adult human testis transcriptional cell atlas. *Cell Research*, *28*(12), 1141–1157. https://doi.org/10.1038/s41422-018-0099-2

Hall, E. A., Keighren, M., Ford, M. J., Davey, T., Jarman, A. P., Smith, L. B., Jackson, I. J., & Mill, P. (2013). Acute Versus Chronic Loss of Mammalian Azi1/Cep131 Results in Distinct Ciliary Phenotypes. *PLoS Genetics*, *9*(12), e1003928. https://doi.org/10.1371/journal.pgen.1003928

Hamilton, L. E., Lion, M., Aguila, L., Suzuki, J., Acteau, G., Protopapas, N., Xu, W., Sutovsky, P., Baker, M., & Oko, R. (2021). Core Histones Are Constituents of the Perinuclear Theca of Murid Spermatozoa: An Assessment of Their Synthesis and Assembly during Spermiogenesis and Function after Gametic Fusion. *International Journal of Molecular Sciences*, *22*(15), 8119. https://doi.org/10.3390/ijms22158119

Hansen, J., Rassmann, S., Jikeli, J., & Wachten, D. (2018). SpermQ–A Simple Analysis Software to Comprehensively Study Flagellar Beating and Sperm Steering. *Cells*, *8*(1), 10. https://doi.org/10.3390/cells8010010

Hara, Y., Yamagata, K., Oguchi, K., & Baba, T. (2008). Nuclear localization of profilin III–ArpM1 complex in mouse spermiogenesis. *FEBS Letters*, *582*(20), 2998–3004. https://doi.org/10.1016/j.febslet.2008.07.058

Heid, H. W., Figge, U., Winter, S., Kuhn, C., Zimbelmann, R., & Franke, W. W. (2002). Novel Actin-Related Proteins Arp-T1 and Arp-T2 as Components of the Cytoskeletal Calyx of the Mammalian Sperm Head. *Experimental Cell Research*, *279*(2), 177–187. https://doi.org/10.1006/excr.2002.5603

HELLER, C. H., & CLERMONT, Y. (1964). KINETICS OF THE GERMINAL EPITHELIUM IN MAN. *Recent Progress in Hormone Research*, *20*, 545–575.

Hess, H., Heid, H., & Franke, W. (1993). Molecular characterization of mammalian cylicin, a basic protein of the sperm head cytoskeleton. *The Journal of Cell Biology*, *122*(5), 1043–1052. https://doi.org/10.1083/jcb.122.5.1043

Hess, H., Heid, H., Zimbelmann, R., & Franke, W. W. (1995). The Protein Complexity of the Cytoskeleton of Bovine and Human Sperm Heads: The Identification and Characterization of Cylicin II. *Experimental Cell Research*, *218*(1), 174–182. https://doi.org/10.1006/excr.1995.1145

Ikawa, M., Inoue, N., Benham, A. M., & Okabe, M. (2010). Fertilization: a sperm's journey to and interaction with the oocyte. *Journal of Clinical Investigation*, *120*(4), 984–994. https://doi.org/10.1172/JCI41585

Jeffrey B. Kerr, & David De Kretser. (2010). *Endocrinology* (6th ed.).

Jin, H.-J., Fan, Y., Yang, X., Dong, Y., Zhang, X.-Z., Geng, X.-Y., Yan, Z., Wu, L., Ma, M., Li, B., Lyu, Q., Pan, Y., Liu, M., Kuang, Y., & Chen, S.-R. (2024). Disruption in CYLC1 leads to acrosome detachment, sperm head deformity, and male in/subfertility in humans and mice. *ELife*, *13*. https://doi.org/10.7554/eLife.95054.2

Kazuhiko Mochida, Laura L. Tres, & Abraham L. Kierszenbaum. (1999). Structural and biochemical features of fractionated spermatid manchettes and sperm axonemes of the Azh/Azh mutant mouse. *Gamete Biology*.

Khawar, M. B., Gao, H., & Li, W. (2019). Mechanism of Acrosome Biogenesis in Mammals. *Frontiers in Cell and Developmental Biology*, *7*. https://doi.org/10.3389/fcell.2019.00195

Kierszenbaum, A. L., Rivkin, E., & Tres, L. L. (2003). Acroplaxome, an F-Actin–Keratin-containing Plate, Anchors the Acrosome to the Nucleus during Shaping of the Spermatid Head. *Molecular Biology of the Cell*, *14*(11), 4628–4640. https://doi.org/10.1091/mbc.e03-04-0226

Kierszenbaum, A. L., Rivkin, E., & Tres, L. L. (2011). Cytoskeletal track selection during cargo transport in spermatids is relevant to male fertility. *Spermatogenesis*, *1*(3), 221–230. https://doi.org/10.4161/spmg.1.3.18018

Kierszenbaum, A. L., Rivkin, E., Tres, L. L., Yoder, B. K., Haycraft, C. J., Bornens, M., & Rios, R. M. (2011). GMAP210 and IFT88 are present in the spermatid golgi apparatus and participate in the development of the acrosome–acroplaxome complex, head–tail coupling apparatus and tail. *Developmental Dynamics*, *240*(3), 723–736. https://doi.org/10.1002/dvdy.22563

Kovacevic, A., Ordziniak, E., Umer, N., Arevalo, L., Hinterlang, L. D., Ziaeipour, S., Suvilla, S., Merges, G. E., & Schorle, H. (2025). *Actin-related protein M1 (ARPM1) required for acrosome biogenesis and sperm function in mice*. https://doi.org/10.1101/2025.03.27.645694

Krausz, C., & Riera-Escamilla, A. (2018). Genetics of male infertility. *Nature Reviews Urology*, *15*(6), 369–384. https://doi.org/10.1038/s41585-018-0003-3

Leblond, C. P., & Clermont, Y. (1952). DEFINITION OF THE STAGES OF THE CYCLE OF THE SEMINIFEROUS EPITHELIUM IN THE RAT. *Annals of the New York Academy of Sciences*, *55*(4), 548–573. https://doi.org/10.1111/j.1749-6632.1952.tb26576.x

Lécuyer, C., Dacheux, J.-L., Hermand, E., Mazeman, E., Rousseaux, J., & Rousseaux-Prévost, R. (2000). Actin-Binding Properties and Colocalization with Actin During Spermiogenesis of Mammalian Sperm Calicin1. *Biology of Reproduction*, *63*(6), 1801–1810. https://doi.org/10.1095/biolreprod63.6.1801

Li, C., Shen, C., Xiong, W., Ge, H., Shen, Y., Chi, J., Zhang, H., Tang, L., Lu, S., Wang, J., Fei, J., & Wang, Z. (2024). Spem2, a novel testis-enriched gene, is required for spermiogenesis and fertilization in mice. *Cellular and Molecular Life Sciences*, *81*(1), 108. https://doi.org/10.1007/s00018-024-05147-w

Lin, Y.-N., Roy, A., Yan, W., Burns, K. H., & Matzuk, M. M. (2007). Loss of Zona Pellucida Binding Proteins in the Acrosomal Matrix Disrupts Acrosome Biogenesis and Sperm Morphogenesis. *Molecular and Cellular Biology*, *27*(19), 6794–6805. https://doi.org/10.1128/MCB.01029-07

Longo, F. J., Krohne, G., & Franke, W. W. (1987). Basic proteins of the perinuclear theca of mammalian spermatozoa and spermatids: a novel class of cytoskeletal elements. *The Journal of Cell Biology*, *105*(3), 1105–1120. https://doi.org/10.1083/jcb.105.3.1105

Lüders, J., & Stearns, T. (2007). Microtubule-organizing centres: a re-evaluation. *Nature Reviews Molecular Cell Biology*, *8*(2), 161–167. https://doi.org/10.1038/nrm2100

Luense, L. J., Donahue, G., Lin-Shiao, E., Rangel, R., Weller, A. H., Bartolomei, M. S., & Berger, S. L. (2019). Gcn5-Mediated Histone Acetylation Governs Nucleosome Dynamics in Spermiogenesis. *Developmental Cell*, *51*(6), 745-758.e6. https://doi.org/10.1016/j.devcel.2019.10.024

Lukassen, S., Bosch, E., Ekici, A. B., & Winterpacht, A. (2018a). Characterization of germ cell differentiation in the male mouse through single-cell RNA sequencing. *Scientific Reports*, *8*(1), 6521. https://doi.org/10.1038/s41598-018-24725-0

Lukassen, S., Bosch, E., Ekici, A. B., & Winterpacht, A. (2018b). Single-cell RNA sequencing of adult mouse testes. *Scientific Data*, *5*(1), 180192. https://doi.org/10.1038/sdata.2018.192

Lüpold, S., & Pitnick, S. (2018). Sperm form and function: what do we know about the role of sexual selection? *Reproduction*, *155*(5), R229–R243. https://doi.org/10.1530/REP-17-0536

Mascarenhas, M. N., Flaxman, S. R., Boerma, T., Vanderpoel, S., & Stevens, G. A. (2012). National, Regional, and Global Trends in Infertility Prevalence Since 1990: A Systematic Analysis of 277 Health Surveys. *PLoS Medicine*, *9*(12), e1001356. https://doi.org/10.1371/journal.pmed.1001356

Mendoza-Lujambio, I. (2002). The Hook1 gene is non-functional in the abnormal spermatozoon head shape (azh) mutant mouse. *Human Molecular Genetics*, *11*(14), 1647–1658. https://doi.org/10.1093/hmg/11.14.1647

Montellier, E., Boussouar, F., Rousseaux, S., Zhang, K., Buchou, T., Fenaille, F., Shiota, H., Debernardi, A., Héry, P., Curtet, S., Jamshidikia, M., Barral, S., Holota, H., Bergon, A., Lopez, F., Guardiola, P., Pernet, K., Imbert, J., Petosa, C., … Khochbin, S. (2013). Chromatin-to-nucleoprotamine transition is controlled by the histone H2B variant TH2B. *Genes & Development*, *27*(15), 1680–1692. https://doi.org/10.1101/gad.220095.113

Ng, P. C. (2003). SIFT: predicting amino acid changes that affect protein function. *Nucleic Acids Research*, *31*(13), 3812–3814. https://doi.org/10.1093/nar/gkg509

Oakberg, E. F. (1956). A description of spermiogenesis in the mouse and its use in analysis of the cycle of the seminiferous epithelium and germ cell renewal. *American Journal of Anatomy*, *99*(3), 391–413. https://doi.org/10.1002/aja.1000990303

Oakberg, E. F. (1971). Spermatogonial stem-cell renewal in the mouse. *The Anatomical Record*, *169*(3), 515–531. https://doi.org/10.1002/ar.1091690305

O'Donnell, L., & O'Bryan, M. K. (2014). Microtubules and spermatogenesis. *Seminars in Cell & Developmental Biology*, *30*, 45–54. https://doi.org/10.1016/j.semcdb.2014.01.003

Oko, R., & Maravei, D. (1994). Protein Composition of the Perinuclear Theca of Bull Spermatozoa1. *Biology of Reproduction*, *50*(5), 1000–1014. https://doi.org/10.1095/biolreprod50.5.1000

Oko, R., & Sutovsky, P. (2009). Biogenesis of sperm perinuclear theca and its role in sperm functional competence and fertilization. *Journal of Reproductive Immunology*, *83*(1–2), 2–7. https://doi.org/10.1016/j.jri.2009.05.008

Phillips, B. T., Gassei, K., & Orwig, K. E. (2010). Spermatogonial stem cell regulation and spermatogenesis. *Philosophical Transactions of the Royal Society B: Biological Sciences*, *365*(1546), 1663–1678. https://doi.org/10.1098/rstb.2010.0026

Pogany, G. C., Corzett, M., Weston, S., & Balhorn, R. (1981). DNA and protein content of mouse sperm. *Experimental Cell Research*, *136*(1), 127–136. https://doi.org/10.1016/0014-4827(81)90044-6

Potelle, S., Morelle, W., Dulary, E., Duvet, S., Vicogne, D., Spriet, C., Krzewinski-Recchi, M.-A., Morsomme, P., Jaeken, J., Matthijs, G., De Bettignies, G., & Foulquier, F. (2016). Glycosylation abnormalities in Gdt1p/TMEM165 deficient cells result from a defect in Golgi manganese homeostasis. *Human Molecular Genetics*, *25*(8), 1489–1500. https://doi.org/10.1093/hmg/ddw026

Richards, S., Aziz, N., Bale, S., Bick, D., Das, S., Gastier-Foster, J., Grody, W. W., Hegde, M., Lyon, E., Spector, E., Voelkerding, K., & Rehm, H. L. (2015). Standards and guidelines for the interpretation of sequence variants: a joint consensus recommendation of the American College of Medical Genetics and Genomics and the Association for Molecular Pathology. *Genetics in Medicine*, *17*(5), 405–424. https://doi.org/10.1038/gim.2015.30

Rousseaux- Prévost, R., Lécuyer, C., Drobecq, H., Sergheraert, C., Dacheux, J.-L., & Rousseaux, J. (2003). Characterization of boar sperm cytoskeletal cylicin II as an actin-binding protein. *Biochemical and Biophysical Research Communications*, *303*(1), 182–189. https://doi.org/10.1016/S0006-291X(03)00317-6

Russell, L. D., Ettlin, R. A., Hikim, A. P. S., & Clegg, E. D. (1993). Histological and Histopathological Evaluation of the Testis. *International Journal of Andrology*, *16*(1), 83–83. https://doi.org/10.1111/j.1365-2605.1993.tb01156.x

Russell, L. D., Russell, J. A., MacGregor, G. R., & Meistrich, M. L. (1991). Linkage of manchette microtubules to the nuclear envelope and observations of the role of the manchette in nuclear shaping during spermiogenesis in rodents. *American Journal of Anatomy*, *192*(2), 97–120. https://doi.org/10.1002/aja.1001920202

Schafer, D. A., & Schroer, T. A. (1999). Actin-Related Proteins. *Annual Review of Cell and Developmental Biology*, *15*(1), 341–363. https://doi.org/10.1146/annurev.cellbio.15.1.341

Schneider, S., Balbach, M., Jan F. Jikeli, Fietz, D., Nettersheim, D., Jostes, S., Schmidt, R., Kressin, M., Bergmann, M., Wachten, D., Steger, K., & Schorle, H. (2016). Re-visiting the Protamine-2 locus: deletion, but not haploinsufficiency, renders male mice infertile. *Scientific Reports*, *6*(1), 36764. https://doi.org/10.1038/srep36764

Schneider, S., Kovacevic, A., Mayer, M., Dicke, A.-K., Arévalo, L., Koser, S. A., Hansen, J. N., Young, S., Brenker, C., Kliesch, S., Wachten, D., Kirfel, G., Strünker, T., Tüttelmann, F., & Schorle, H. (2023). Cylicins are a structural component of the sperm calyx being indispensable for male fertility in mice and human. *ELife*, *12*. https://doi.org/10.7554/eLife.86100.3

Schneider, S., Shakeri, F., Trötschel, C., Arévalo, L., Kruse, A., Buness, A., Poetsch, A., Steger, K., & Schorle, H. (2020). Protamine-2 Deficiency Initiates a Reactive Oxygen Species (ROS)-Mediated Destruction Cascade during Epididymal Sperm Maturation in Mice. *Cells*, *9*(8), 1789. https://doi.org/10.3390/cells9081789

Sha, Y., Liu, W., Li, L., Serafimovski, M., Isachenko, V., Li, Y., Chen, J., Zhao, B., Wang, Y., & Wei, X. (2021). Pathogenic Variants in ACTRT1 Cause Acephalic Spermatozoa Syndrome. *Frontiers in Cell and Developmental Biology*, *9*. https://doi.org/10.3389/fcell.2021.676246

Skinner, B. M., Rathje, C. C., Bacon, J., Johnson, E. E. P., Larson, E. L., Kopania, E. E. K., Good, J. M., Yousafzai, G., Affara, N. A., & Ellis, P. J. I. (2019). A high-throughput method for unbiased quantitation and categorization of nuclear morphology. *Biology of Reproduction*, *100*(5), 1250–1260. https://doi.org/10.1093/biolre/ioz013

Sutovsky, P., Manandhar, G., Wu, A., & Oko, R. (2003). Interactions of sperm perinuclear theca with the oocyte: Implications for oocyte activation, anti-polyspermy defense, and assisted reproduction. *Microscopy Research and Technique*, *61*(4), 362–378. https://doi.org/10.1002/jemt.10350

Teixidó-Travesa, N., Roig, J., & Lüders, J. (2012). The where, when and how of microtubule nucleation – one ring to rule them all. *Journal of Cell Science*. https://doi.org/10.1242/jcs.106971

Tiwari, N., Graham, M., Liu, X., Yue, X., Zhu, L., Meshram, D., Choi, S., Qian, Y., Rothman, J. E., & Lee, I. (2019). Golgin45-Syntaxin5 Interaction Contributes to Structural Integrity of the Golgi Stack. *Scientific Reports*, *9*(1), 12465. https://doi.org/10.1038/s41598-019-48875-x

Topfer-Petersen, E. (1999). Carbohydrate-based interactions on the route of a spermatozoon to fertilization. *Human Reproduction Update*, *5*(4), 314–329. https://doi.org/10.1093/humupd/5.4.314

Tres, L. L., & Kierszenbaum, A. L. (1975). Transcription during Mammalian Spermatogenesis with Special Reference to Sertoli Cells. In *Hormonal Regulation of Spermatogenesis* (pp. 455–478). Springer US. https://doi.org/10.1007/978-1-4613-4440-7_32

Truett, G. E., Heeger, P., Mynatt, R. L., Truett, A. A., Walker, J. A., & Warman, M. L. (2000). Preparation of PCR-Quality Mouse Genomic DNA with Hot Sodium Hydroxide and Tris (HotSHOT). *BioTechniques*, *29*(1), 52–54. https://doi.org/10.2144/00291bm09

Umer, N., Arévalo, L., Phadke, S., Lohanadan, K., Kirfel, G., Sons, D., Sofia, D., Witke, W., & Schorle, H. (2021). Loss of Profilin3 Impairs Spermiogenesis by Affecting Acrosome Biogenesis, Autophagy, Manchette Development and Mitochondrial Organization. *Frontiers in Cell and Developmental Biology*, *9*. https://doi.org/10.3389/fcell.2021.749559

Utiger, R. D. (2024). *Encyclopedia Britannica*.

Vander Borght, M., & Wyns, C. (2018). Fertility and infertility: Definition and epidemiology. *Clinical Biochemistry*, *62*, 2–10. https://doi.org/10.1016/j.clinbiochem.2018.03.012

VISCONTI, P. E., GALANTINO-HOMER, H., MOORE, G. D., BAILEY, J. L., NING, X., FORNES, M., & KOPF, G. S. (1998). The Molecular Basis of Sperm Capacitation. *Journal of Andrology*, *19*(2), 242–248. https://doi.org/10.1002/j.1939-4640.1998.tb01994.x

Wang, J., Zhang, J., Sun, X., Lin, Y., Cai, L., Cui, Y., Liu, J., Liu, M., & Yang, X. (2021). Novel bi-allelic variants in *ACTL7A* are associated with male infertility and total fertilization failure. *Human Reproduction*, *36*(12), 3161–3169. https://doi.org/10.1093/humrep/deab228

Wear, M. A., & Cooper, J. A. (2004a). Capping protein: new insights into mechanism and regulation. *Trends in Biochemical Sciences*, *29*(8), 418–428. https://doi.org/10.1016/j.tibs.2004.06.003

Wear, M. A., & Cooper, J. A. (2004b). Capping protein: new insights into mechanism and regulation. *Trends in Biochemical Sciences*, *29*(8), 418–428. https://doi.org/10.1016/j.tibs.2004.06.003

WHO laboratory manual for the examination and processing of human semen (6th ed.). (2021).

Winters, B. R., & Walsh, T. J. (2014). The Epidemiology of Male Infertility. *Urologic Clinics of North America*, *41*(1), 195–204. https://doi.org/10.1016/j.ucl.2013.08.006

Wyrwoll, M. J., Temel, Ş. G., Nagirnaja, L., Oud, M. S., Lopes, A. M., van der Heijden, G. W., Heald, J. S., Rotte, N., Wistuba, J., Wöste, M., Ledig, S., Krenz, H., Smits, R. M., Carvalho, F., Gonçalves, J., Fietz, D., Türkgenç, B., Ergören, M. C., Çetinkaya, M., … Tüttelmann, F. (2020). Bi-allelic Mutations in M1AP Are a Frequent Cause of Meiotic Arrest and Severely Impaired Spermatogenesis Leading to Male Infertility. *The American Journal of Human Genetics*, *107*(2), 342–351. https://doi.org/10.1016/j.ajhg.2020.06.010

Wyrwoll, M. J., van der Heijden, G. W., Krausz, C., Aston, K. I., Kliesch, S., McLachlan, R., Ramos, L., Conrad, D. F., O'Bryan, M. K., Veltman, J. A., & Tüttelmann, F. (2024). Improved phenotypic classification of male infertility to promote discovery of genetic causes. *Nature Reviews Urology*, *21*(2), 91–101. https://doi.org/10.1038/s41585-023-00816-0

Xin, A., Qu, R., Chen, G., Zhang, L., Chen, J., Tao, C., Fu, J., Tang, J., Ru, Y., Chen, Y., Peng, X., Shi, H., Zhang, F., & Sun, X. (2020). Disruption in *ACTL7A* causes acrosomal ultrastructural defects in human and mouse sperm as a novel male factor inducing early embryonic arrest. *Science Advances*, *6*(35). https://doi.org/10.1126/sciadv.aaz4796

Yanagimachi, R. (2011). Mammalian Sperm Acrosome Reaction: Where Does It Begin Before Fertilization? *Biology of Reproduction*, *85*(1), 4–5. https://doi.org/10.1095/biolreprod.111.092601

Yoon, S.-Y., & Fissore, R. A. (2007). Release of phospholipase C ζand [Ca2+]i oscillation-inducing activity during mammalian fertilization. *Reproduction*, *134*(5), 695–704. https://doi.org/10.1530/REP-07-0259

Yoon, S.-Y., Jellerette, T., Salicioni, A. M., Lee, H. C., Yoo, M., Coward, K., Parrington, J., Grow, D., Cibelli, J. B., Visconti, P. E., Mager, J., & Fissore, R. A. (2008). Human sperm devoid of PLC, zeta 1 fail to induce Ca2+ release and are unable to initiate the first step of embryo development. *Journal of Clinical Investigation*, *118*(11), 3671–3681. https://doi.org/10.1172/JCI36942

Zakrzewski, P., Lenartowska, M., & Buss, F. (2021). Diverse functions of myosin VI in spermiogenesis. *Histochemistry and Cell Biology*, *155*(3), 323–340. https://doi.org/10.1007/s00418-020-01954-x

Zhang, X.-Z., Wei, L.-L., Jin, H.-J., Zhang, X.-H., & Chen, S.-R. (2022). The perinuclear theca protein Calicin helps shape the sperm head and maintain the nuclear structure in mice. *Cell Reports*, *40*(1), 111049. https://doi.org/10.1016/j.celrep.2022.111049

Zhang, X.-Z., Wei, L.-L., Zhang, X.-H., Jin, H.-J., & Chen, S.-R. (2022). Loss of perinuclear theca ACTRT1 causes acrosome detachment and severe male subfertility in mice. *Development*, *149*(12). https://doi.org/10.1242/dev.200489

Zhang, Y., Tang, J., Wang, X., Sun, Y., Yang, T., Shen, X., Yang, X., Shi, H., Sun, X., & Xin, A. (2023). Loss of ACTL7A causes small head sperm by defective acrosome-acroplaxome-manchette complex. *Reproductive Biology and Endocrinology*, *21*(1), 82. https://doi.org/10.1186/s12958-023-01130-5

Zhou, R., Wu, J., Liu, B., Jiang, Y., Chen, W., Li, J., He, Q., & He, Z. (2019). The roles and mechanisms of Leydig cells and myoid cells in regulating spermatogenesis. *Cellular and Molecular Life Sciences*, *76*(14), 2681–2695. https://doi.org/10.1007/s00018-019-03101-9

Zhou, X., Liu, Z., Jia, W., Hou, M., & Zhang, X. (2022). Actl7a deficiency in mice leads to male infertility and fertilization failure. *Biochemical and Biophysical Research Communications*, *623*, 154–161. https://doi.org/10.1016/j.bbrc.2022.07.065

8. APPENDIX

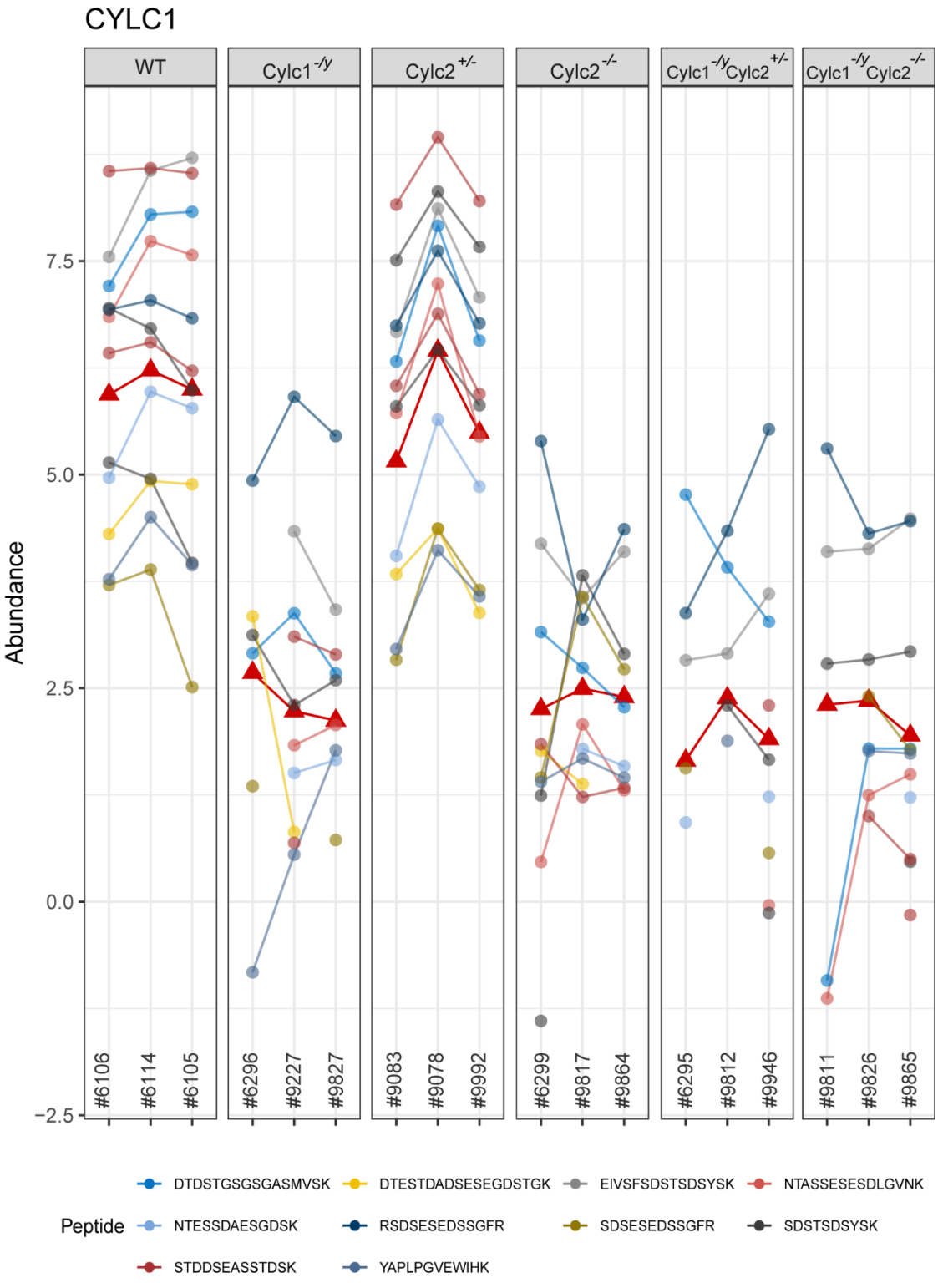

Figure S1: Protein abundance of CYLC1 in *Cylc*-deficient sperm. Different peptides corresponding to CYLC1 are detected in cytoskeletal protein lysates from WT, *Cylc1*$^{-/y}$, *Cylc2*$^{+/-}$, *Cylc2*$^{-/-}$, *Cylc1*$^{-/y}$ *Cylc2*$^{+/-}$ and *Cylc1*$^{-/y}$ *Cylc2*$^{-/-}$ sperm.

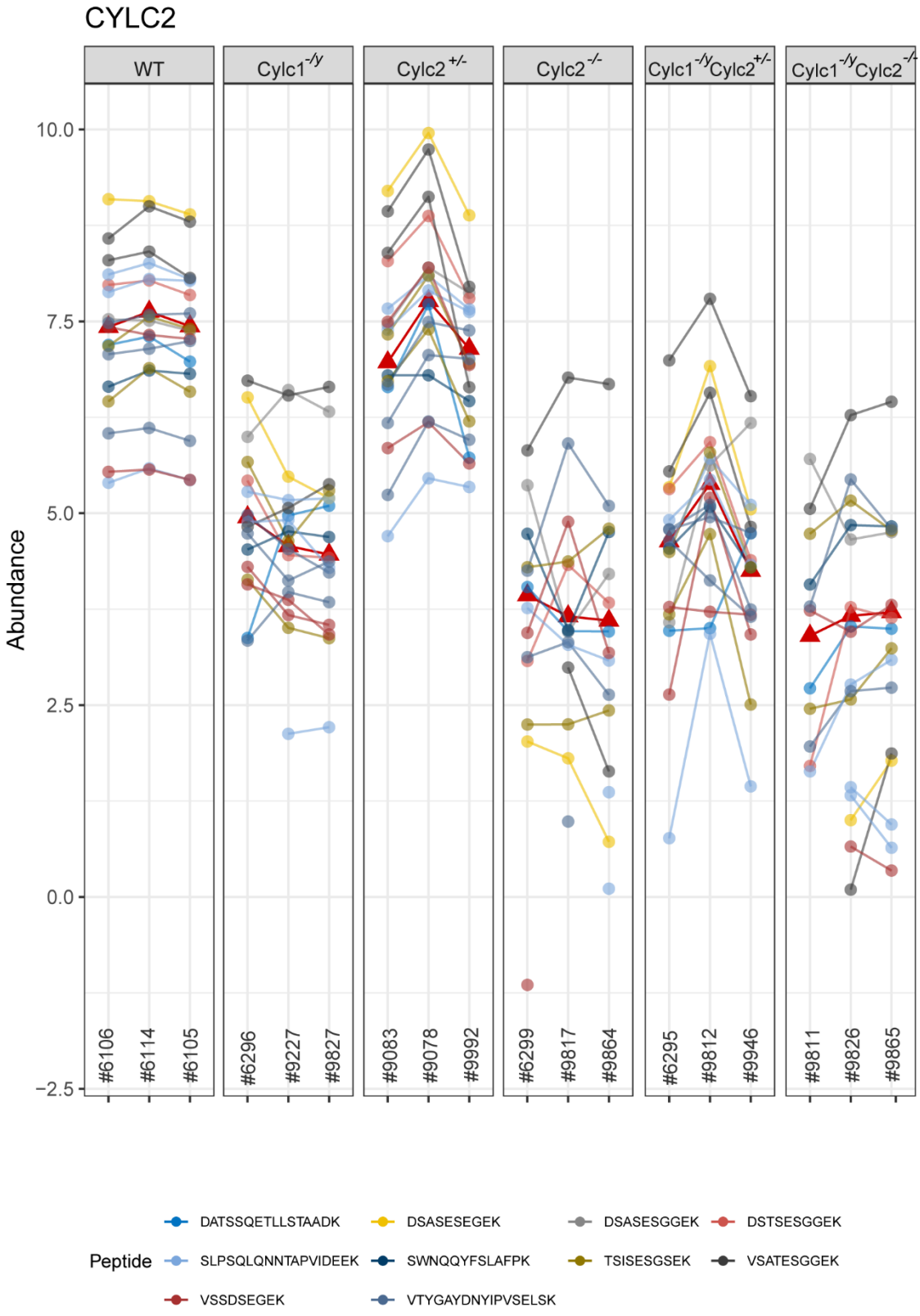

Figure S2: Protein abundance of CYLC2 in *Cylc*-deficient sperm. Different peptides corresponding to CYLC1 are detected in cytoskeletal protein lysates from WT, *Cylc1*$^{-/y}$, *Cylc2*$^{+/-}$, *Cylc2*$^{-/-}$, *Cylc1*$^{-/y}$ *Cylc2*$^{+/-}$, and *Cylc1*$^{-/y}$*Cylc2*$^{-/-}$ sperm.

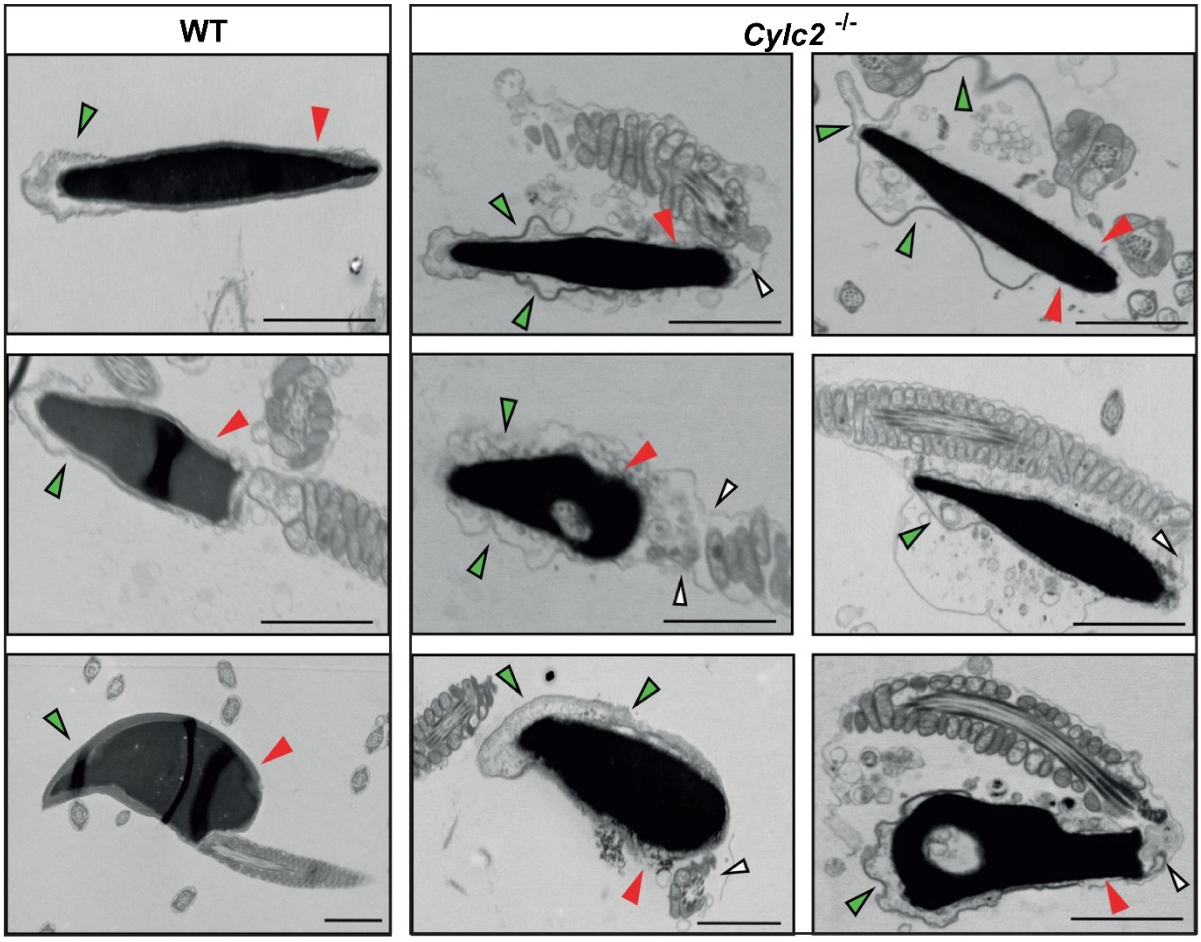

Figrue S3: TEM micrographs of WT and *Cylc2*$^{-/-}$ sperm. Acrosomes are depicted with green arrow heads. Red arrow heads indicate calyx structure which is disrupted in *Cylc2*$^{-/-}$ sperm. White arrow heads point to breakage in the neck region and head-tail connection in *Cylc2*$^{-/-}$ sperm. Scale bar: 1 µm. Modified from Schneider, Kovacevic et al., 2023

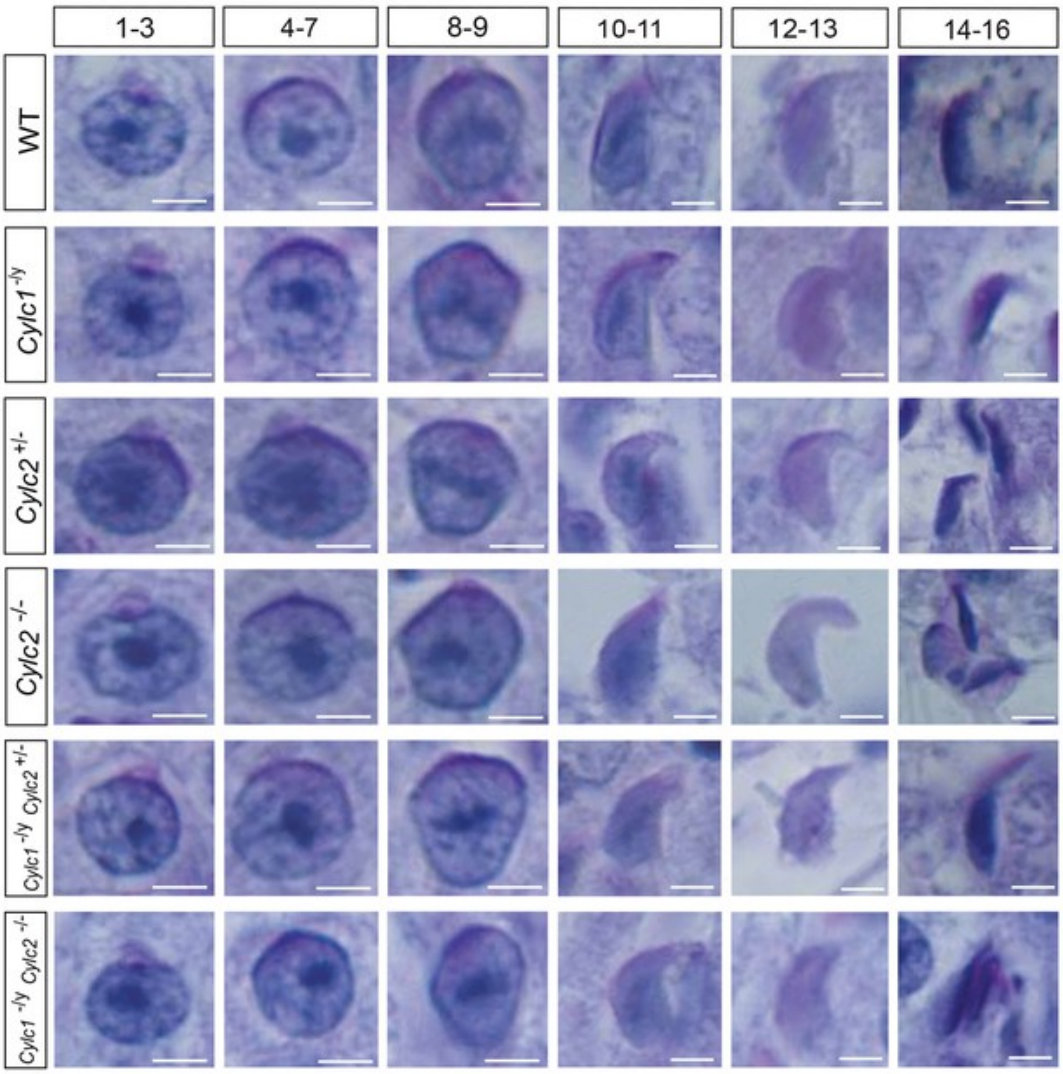

Figrue S4: PAS staining of individual spermatids from *Cylc*-deficient mice. Periodic acid Schiff (PAS) staining of testicular tissue sections from WT, *Cylc1*$^{-/y}$, *Cylc2*$^{+/-}$, *Cylc2*$^{-/-}$, *Cylc1*$^{-/y}$ *Cylc2*$^{+/-}$, and *Cylc1*$^{-/y}$ *Cylc2*$^{-/-}$ male mice. Representative spermatids from step 1 to step 16 of spermiogenesis are shown. Scale bar: 3 µm. Modified from Schneider, Kovacevic et al., 2023.

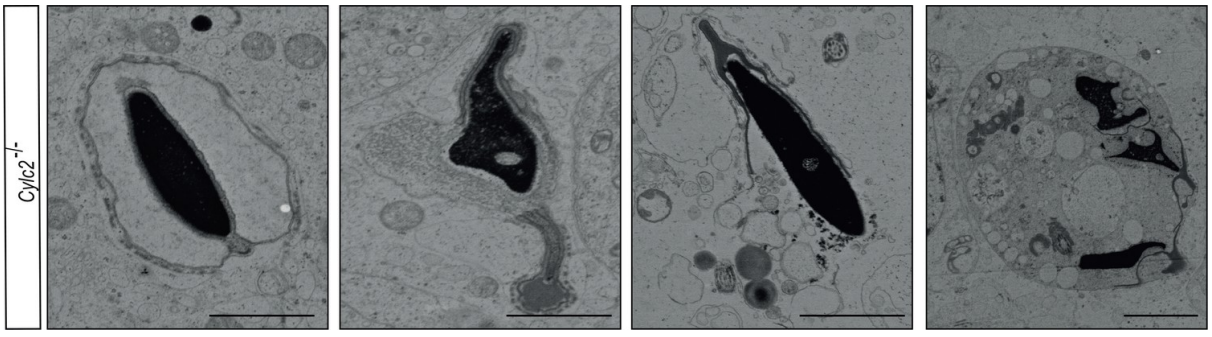

Figrue S5: TEM micrographs of degrading damaged spermatids in testis tissue of *Cylc2*$^{-/-}$ mice. Severely damaged and degrading spermatids were observed at the basal membrane of seminiferous tubule, often engulfed in phagosomes. Scale bar: 5 µm. Modified from Schneider, Kovacevic et al., 2023.

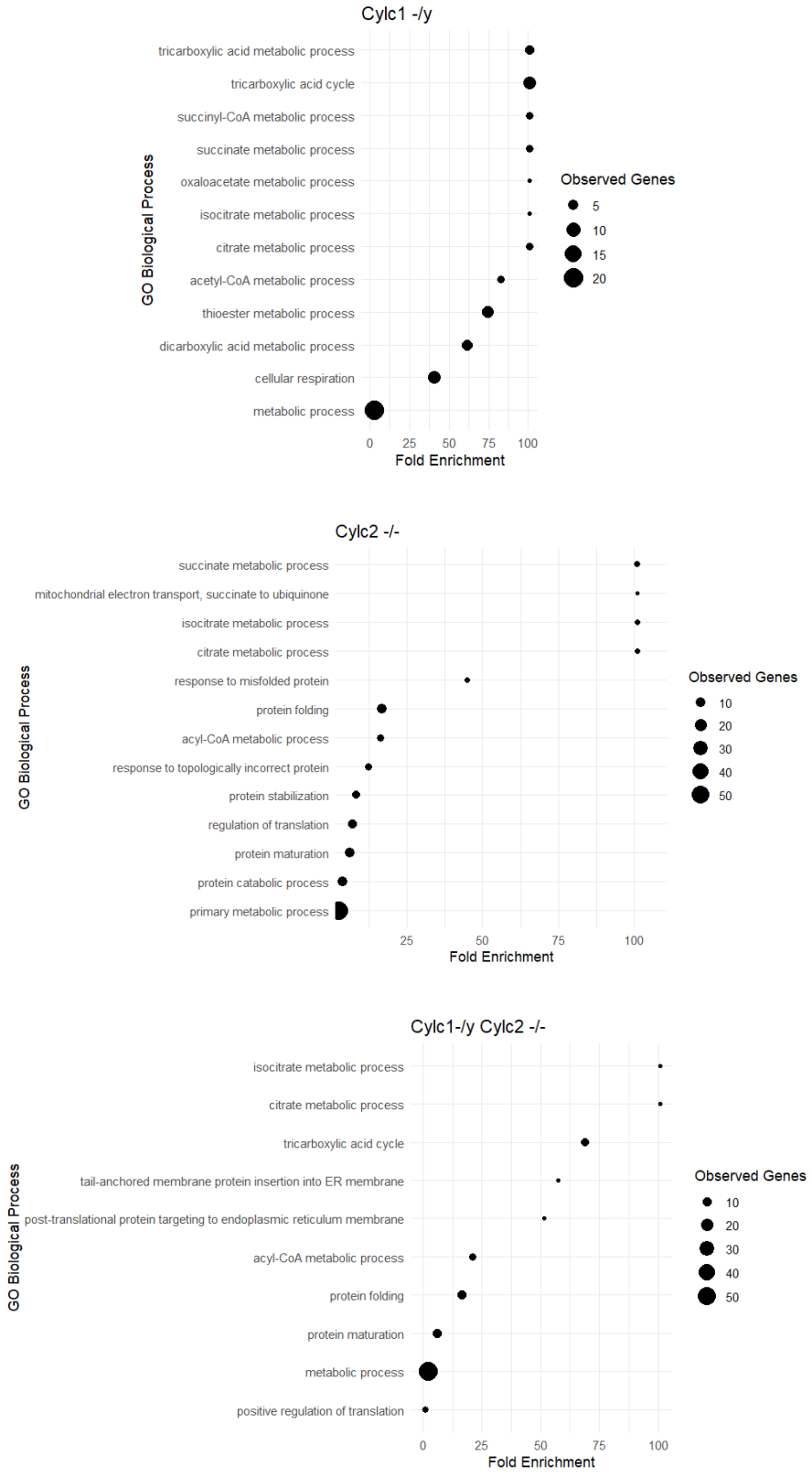

Figure S6: Enrichment analysis of 100 most significantly enriched proteins in *Cylc*-deficient sperm. GO term enrichment analysis of significantly enriched proteins in *Cylc1*$^{-/y}$, *Cylc2*$^{-/-}$ and *Cylc1*$^{-/y}$ *Cylc2*$^{-/-}$ sperm. Y-axis depicts different biological processes while x-axis shows Fold Enrichment. The size of the dots represents the observed protein count in each cellular compartment. Measurements were performed by Dr. Marc Sylvester; Bioinformatics data analysis was performed by Dr. Andreas Buness and Dr. Farhad Shakeri.

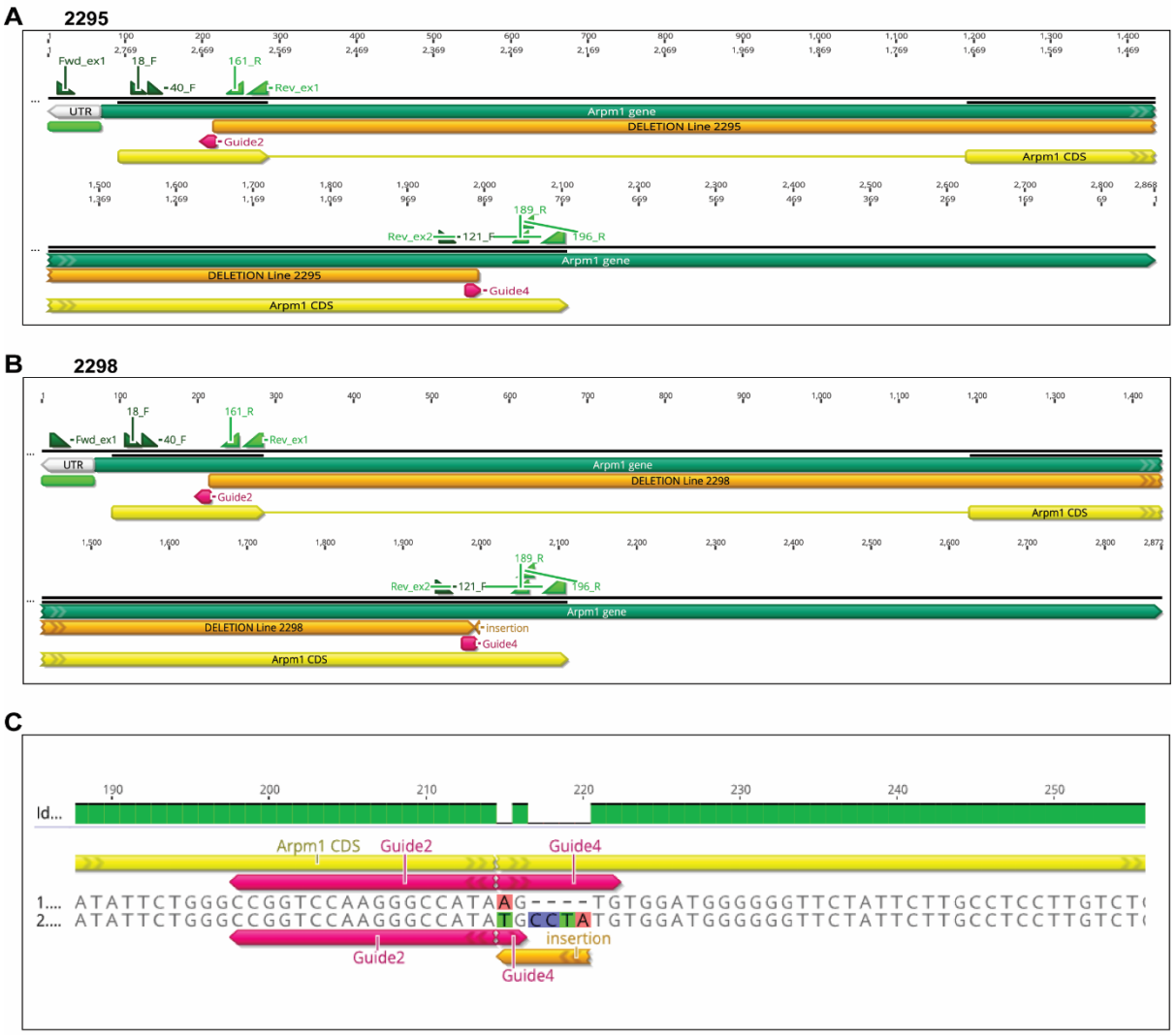

Figrue S7: Schematic representation and comparison of ARPM1 amino acid sequence generated in Δ2295 and Δ2298 mouse lines. A) *Arpm1* gene sequence from Δ2295 line (yellow) compared to WT *Arpm1* gene sequence (green). Deleted region is depicted in orange. Primers used for genotyping PCR and PCR on cDNA (green), as well as guide sequences (red) are shown in respective positions. **B**) *Arpm1* gene sequence from Δ2299 line (yellow) compared to WT *Arpm1* gene sequence (green). Deleted region is depicted in orange. Primers used for genotyping PCR and PCR on cDNA (green), as well as guide sequences (red) are shown in respective positions. **C**) Differences in amino acid sequence between Δ2295 line (upper row) and Δ2298 line (lower row). Guide sequences are shown in magenta, while orange bar indicates an insertion found in Δ2298 line.

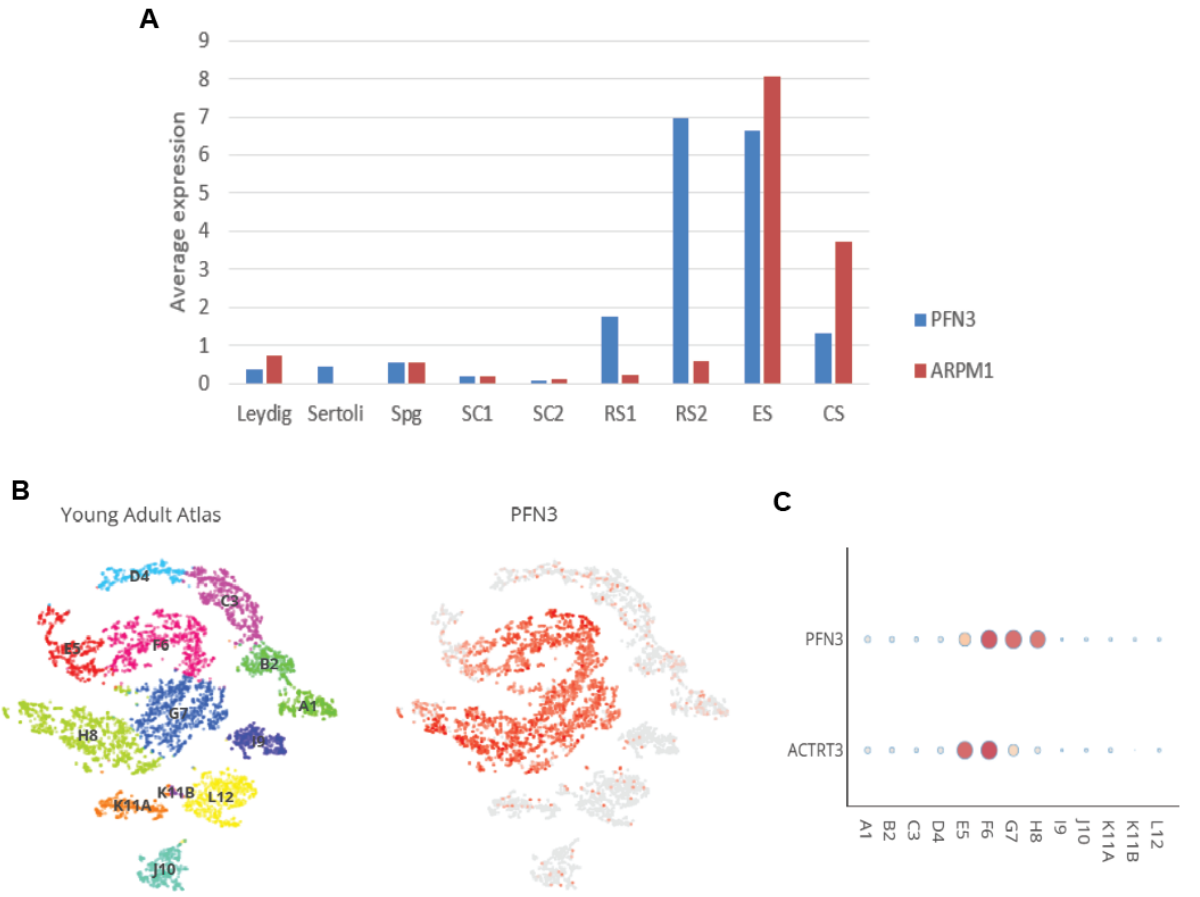

Figure S8: *Pfn3* is expressed earlier than *Arpm1* in mouse testis. Average expression of *Arpm1* and *Pfn3* in different testicular cell populations in mouse: Spg: spermatogonia, SC1: Spermatocyte 1; SC2: Spermatocyte 2, RS1: round spermatid 1; RS2: round spermatid 2; ES: elongating spermatid, CS: compacted sperm. Source: Lukassen et al., 2018. **B)** Expression pattern of PFN3 across different cell populations of human testis. A1: spermatogonial stem cells (SSCs), B2: differentiating spermatogonia, C3: early primary spermatocytes, D4: late primary spermatocytes, E5: round spermatids, F6: elongating spermatids, G7: sperm “1” H8: sperm “2”. Red indicates high expression while gray indicates low or no expression. Similarly, dot color and size in the dot plot are related to the average expression. Data extracted from *Human Testis Atlas* database (Guo et al., 2018a). **C**) Comparison of expression patterns of PFN3 and ACTRT3 (ARPM1) across different cell populations of human testis. A1: spermatogonial stem cells (SSCs), B2: differentiating spermatogonia, C3: early primary spermatocytes, D4: late primary spermatocytes, E5: round spermatids, F6: elongating spermatids, G7: sperm “1” H8: sperm “2”. Red indicates high expression while gray indicates low or no expression. Similarly, dot color and size in the dot plot are related to the average expression. Data extracted from *Human Testis Atlas* database (Guo et al., 2018a).

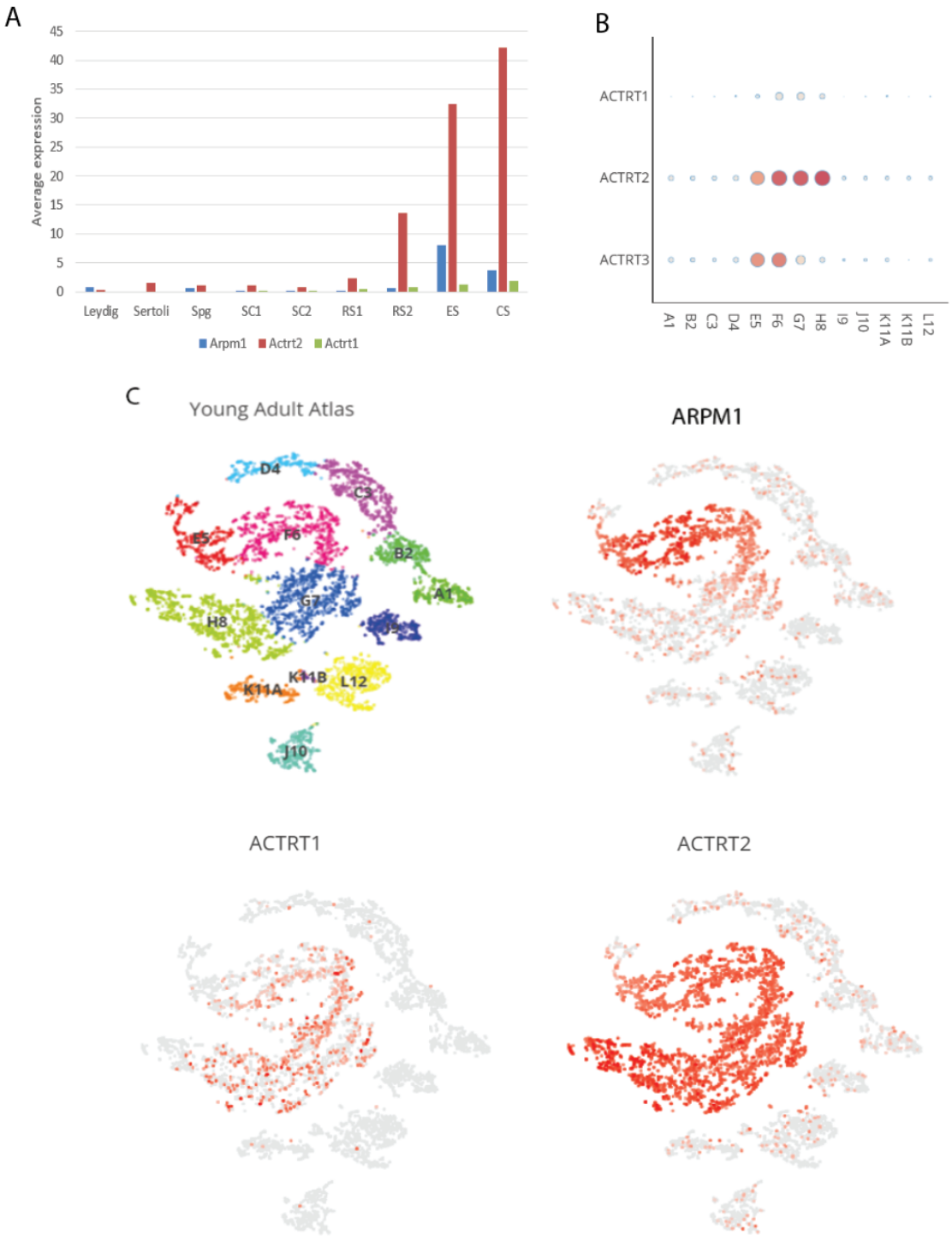

Figure S9: Average expression of different Arps in mouse and human testis. Average expression of *Arpm1, Actrt1* and *Actrt2* in different testicular cell populations in mouse: Spg: spermatogonia, SC1: Spermatocyte 1; SC2: Spermatocyte 2, RS1: round spermatid 1; RS2: round spermatid 2; ES: elongating spermatid, CS: compacted sperm. Source: Lukassen et al., 2018. **B)** Comparison of expression patterns of *ACTRT3* (*ARPM1*), *ACTRT1* and *ACTRT2* across different cell populations of human testis. A1: spermatogonial stem cells (SSCs), B2: differentiating spermatogonia, C3: early primary spermatocytes, D4: late primary spermatocytes, E5: round spermatids, F6: elongating spermatids, G7: sperm "1" H8: sperm "2". Red indicates high expression, gray indicates low or no expression. Dot color and size in the dot plot are related to the average expression. C) Expression pattern of ARPM1, ACTRT1 and ACTRT2 across different cell populations of human testis. Data extracted from *Human Testis Atlas* database (Guo et al., 2018a).

9. ACKNOWLEDGMENTS

At the end of this thesis, I would like to express my gratitude to all those who contributed in their own way to make this work possible.

First and foremost, I would like to thank my doctoral supervisor (*Doctorvater*) Prof. Dr. Hubert Schorle, for giving me the opportunity to join his lab after only one video call. I´m grateful for your patience and guidance throughout the ups and downs of this journey and for being the most impactful figure in my career so far. I´m grateful for all the opportunities to express my ideas and share my excitement about my research topic with you and the rest of the lab.

I´d like to thank PD. Dr. Gregor Kirfel for a successful collaboration accompanied by small lectures of German grammar. I´m thankful to Prof. Dr. Oliver Gruß and Prof. Dr. Matthias Geyer for valuable input during my PhD and for agreeing to be a part of my examination committee.

I´m grateful to Prof. Dr. Timo Strünker and Prof. Dr. Frank Tüttelmann from the University of Münster, along with their lab members, for a successful collaboration and fruitful discussions at conferences.

Above all, I´m grateful to all the Schorle Lab members that were there during the four years of my PhD. A huge thank you to Dr. Simon Schneider who trusted me with taking over the Cylicin project and for being the best partner in crime. I wouldn´t be where I am today without the guidance, supervision and friendship of Dr. Lena Arevalo and Dr. Gina Merges who were my points of reference whenever I struggled with experiments or life in general. Thank you for having my back always and for showing me that scientific research is teamwork. I´m also grateful to Gina and Simon for proof-reding my thesis and publications. My immense gratitude goes to Gaby Beine for wiping my tears away countless times and for making me laugh even more often. I´m thankful for Aylin Hansen, Greta Zech, Eva Ordziniak and Annalena Liesen for being fabulous lab partners and gossip companions. I´m grateful to Angela Egert Andrea Jäger and Ahman Chebli for always taking care of my mice with dedication and precision. Thanks to other Schorle Lab members who were a part of my journey: Dr. Naila Umer, Dr. Kai Funke, Christoph Wiesejahn and Mar Domingo Lopez, and to Master´s students who I supervised: Eva Ordziniak, Sara Suvilla, Leo Hinterlang and Dario Feibel for their contributions to this thesis. This all wouldn´t be possible without an amazing work atmosphere of the Schorle Lab – THANK YOU.

I´d like to thank Dr. Hannes Beckert, Dr. Marc Sylvester, Dr. Andreas Bunnes and Dr. Farhad Shakeri, members of Microscopy, Mass Spectrometry and Bioinformatics Core Facilities of the University of Bonn, whose work has greatly improved my research.

I would like to thank my friends for always supporting all my dreams and sharing good and bad days. I´m grateful to Hena, who I met during my first weeks in Bonn and who soon became a lifetime friend. I´m grateful to Katarina, who´s next to my family, the only constant person in my life since the high school classroom.

Last but not least, I´m grateful for my family: to my mom for her love, support and motivation whenever I needed an extra push; to my dad for all the laughs and his casual belief that I could do whatever I intend to; to my sister for every now and then reminding me of our childhood and bringing me down to Earth by remembering where I come from, and to my baby brother who´s not so much a baby anymore, for showing me that all the love of the world can come from one person. Thank you for all your sacrifices during the past 10 years of my academic career, I promise to always do my best to make you proud. Volim vas.

Thank you. Danke. Hvala.